STUDIES OF GAS–LIQUID FLOW IN BENDS

by

Albina Maria de Sá Ribeiro

Thesis submitted for the degree of

Doctor of Philosophy (Chemical Engineering)

School of Chemical Engineering
University of Birmingham

December 1993

ABSTRACT

The present investigation is concerned primarily with air–water flow in a horizontal 0.032 m ID tube, and the influence of a 90° horizontal bend on the flow characteristics. Visualisation studies using high speed still photography and cine film, and entrainment and drop size measurements were conducted before and after the bend. Entrained mass fluxes were determined from film flow measurements carried out using the film removal technique, while the drop size distributions were measured with a laser diffraction technique. During these measurements the pressure in the test section was held between 1.0–1.4 bar, and at ambient temperature.

Prior to the horizontal flow study, drop size and film flow rates were measured for vertical air–water flow in a 0.01026 m ID tube. This extended the work of Jepson (1992) who reported the effect of gas density and surface tension on film flow rate, drop size and deposition mass transfer coefficient. Modifications to the equipment described by Jepson (1992) allowed an extension of the measurements to higher flow conditions.

The visualisation study was taken across flow conditions that include stratified, annular and pseudo–slug flow regimes. Still photographs show the presence of air bubbles entrained in the liquid film, and the creation of liquid drops at the crest of roll waves. Drops were seen to be entrained from the liquid film by both bag break–up and ligament break–up mechanisms. At the bend, the phenomenon of film inversion was seen to occur. Also, a secondary flow existing in the gas phase at the bend can be responsible for a swirl movement observed in the liquid film, in which at the upper part of the tube the liquid was pulled from the outer wall of the bend to the top of the tube in an anti–clockwise, cork screwing fashion. In the lower half, the liquid film was drawn from the outer wall towards the bottom of the tube in a clockwise motion. From the cine films, information on drop velocity was also extracted. This showed the axial drop velocity to be constant over the time frame of analysis. No significant correlation was found between the drop size and the axial drop velocity.

The entrainment results in the horizontal tube showed that for stratified/annular conditions the entrained liquid mass flux increases with liquid flow rate (for a fixed gas flow rate), and in some instances plateau conditions were reached. However, for the pseudo–slug regime the level of entrainment falls considerably. For the whole range of flow conditions studied, the entrained liquid mass flux increases with superficial gas velocity, except for G_L = 10 kg/m^{2}s where the amount of entrainment is constant. The reduction in entrained liquid mass flux after the bend above certain flow conditions, is caused by drops depositing on the outside wall of the bend.

For the flow conditions under study, the Sauter mean diameter varies between 60–110 μm. Gas velocity has a strong influence on drop size, ie, the higher the gas velocity the smaller the drop size. The effect of liquid flow rate is somewhat more complex. At the lower liquid flow rates, drop size seems to be controlled by the entrainment mechanisms, while at the higher liquid flows drop coalescence has a dominant effect. The influence of the 90° bend on the drop size distribution was to increase the diameter of the drops. Both the entrained liquid mass flux and drop size were found to be lower for horizontal annular flow than in vertical flow, for the same flow conditions and tube diameter.

The measurements carried out for air–water flow in the vertical 0.01026 m ID tube, showed the entrained mass flux to increase with both gas and liquid flow rates. For the flow conditions analysed, the Sauter mean diameter varies between 26–45 μm. Drop size was seen to be influenced by gas and liquid flow rates, following similar trends to those observed during the horizontal study.

ACKNOWLEDGEMENTS

I wish to thank my supervisors, Dr T. R. Bott and Dr D. M. Jepson for their suggestions, guidance and advice through every stage of this work. The financial support by the AEA Technology at Harwell, and the managing of this project by Mr. S Dawson is also acknowledged.

The help received from the Harwell Laboratory Technical staff is deeply appreciated, especially the following:

Eur. Ing. P. Lovegrove and the Technical Services Section for the design and construction of the rig.

Mr D. Benn for his help with the instrumentation.

The Harwell Photographic Group for carrying out the photographic work.

Mr N. Evans for his help in analysing the cine films.

In addition, the time given by the Instituto Superior de Engenharia do Porto to carry out this project is recognized, with my special thanks to Dr F. Morgado and Dr L. Vasconcelos.

Finally, I would like to thank my husband John and my parents for their encouragement and help during the course of this research.

CONTENTS

LIST OF FIGURES

LIST OF TABLES

1. INTRODUCTION

Two-phase, gas-liquid flow occurs widely in the power generation, process and offshore industries. To understand and control two-phase flow behaviour and its heat and mass transfer characteristics, it is necessary to understand the hydrodynamics of the system.

This chapter will provide the reader with a broad understanding of the fundamentals of two-phase, gas-liquid flow. In particular, those relating to vertical upflow and horizontal flows as these have direct relevance to this study.

1.1. Gas-Liquid Flow in Straight Pipes

Gas-liquid flow can adopt various geometric configurations known as flow patterns. These are governed by the physical properties of the system, the gas/liquid ratio, the flow conditions and the flow geometry.

1.1.1. Vertical Flow

In vertical upflow, five main flow patterns exist (Figure 1.1). These are:

- **Bubbly flow** : In bubbly flow the gas phase is distributed as discrete bubbles within a continuous liquid phase. As the gas flow rate is increased, the number of bubbles increases and collisions therefore occur more often. This accounts for a rise in bubble coalescence. Griffith and Snyder (1964) suggested that the bubbly/slug transition occurred at a void fraction of about 0.25-0.30.
- **Slug flow** : In slug flow the gas moves upwards in large bullet-shaped bubbles which occupy virtually the entire cross-section of the tube. These bubbles are surrounded by a thin falling film of liquid, and separated by regions of liquid where small gas bubbles are distributed. As the gas velocity is increased the slug/churn transition is approached.
- **Churn flow** : Increases in the gas velocity cause the liquid slug to become unstable, break and fall. This liquid merges with the approaching slug, while the gas from the collapsed bubbles merge. The reformed slug then resumes its upwards motion until it becomes unstable and falls once again. The oscillatory nature of the liquid flow is typical of churn flow.
- **Annular flow** : Annular flow is characterised by a central core of fast flowing gas and a slower moving liquid film that travels around the pipe wall. The shearing action of the gas at the interface generates small amplitude waves on the liquid surface, known as ripples. By increasing flow conditions beyond critical gas and

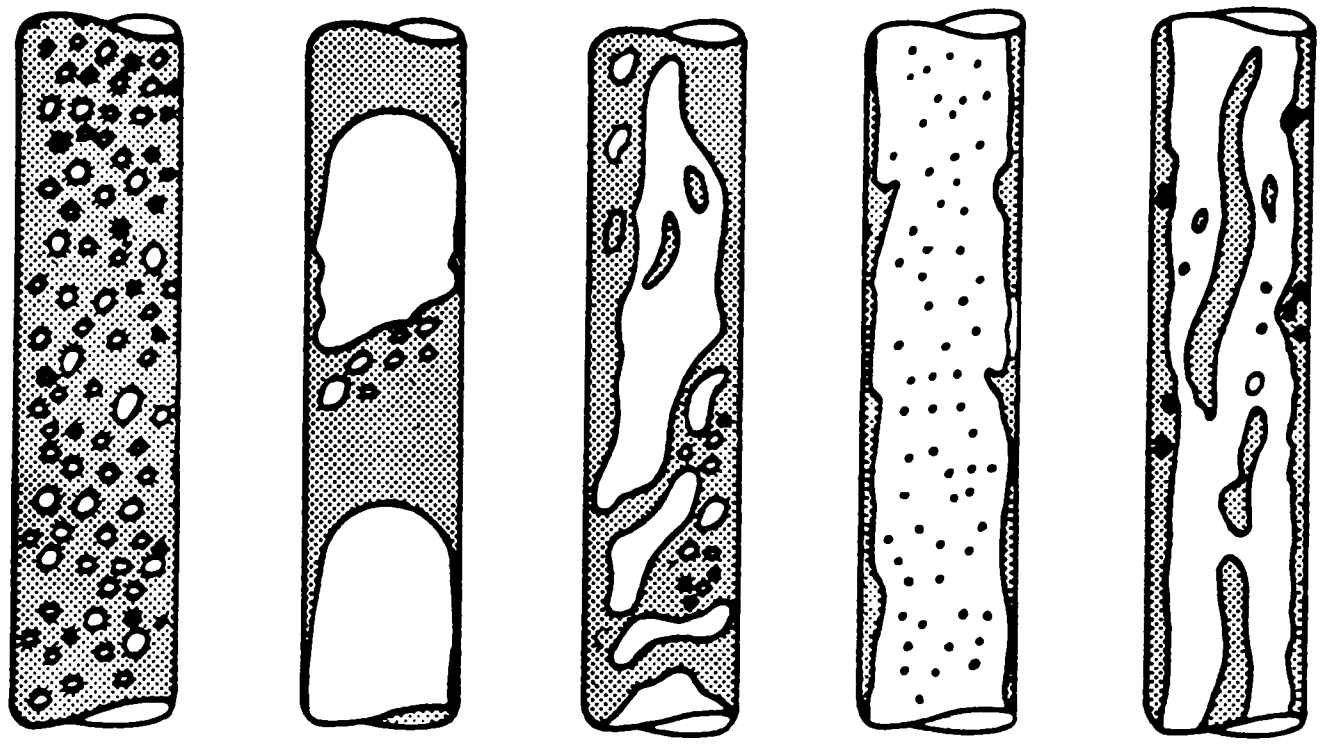

Figure 1.1 Flow patterns for gas–liquid upflow.

liquid flow rates, large amplitude surges or disturbance waves appear. Liquid is torn from the surface of these waves giving rise to drop entrainment in the gas core. The deposition of these drops maintains the liquid film.

As the liquid flow is increased the drop concentration in the gas core rises. Eventually, these drops agglomerate to form large lumps (wisps) of liquid. The resulting flow pattern is known a **wispy–annular flow.**

1.1.2. Horizontal Flow

In horizontal conditions, gravity introduces an asymmetry into the flow: the density difference between the phases causes the liquid to travel preferentially along the bottom of the tube. Hewitt (1982) identified several flow patterns, shown in Figure 1.2.

- **Bubbly flow** : As with vertical bubbly flow, the high degree of turbulence in the liquid phase causes the gas to be distributed as discrete bubbles within a liquid continuum. Buoyant forces however, cause the bubbles to flow along the upper part of the tube.

  At lower liquid flows, where the turbulent mixing is less pronounced, Taitel and Dukler (1976) suggested that the buoyant forces dominate. This causes the bubbles to rise and agglomerate to form gas plugs.

- **Plug flow** : Horizontal plug flow is similar to vertical slug flow, but gravity effects cause the gas plugs to move along the top of the tube.

- **Stratified flow** : In stratified flow the liquid travels along the bottom of the pipe whilst the gas passes over it. At low gas and liquid flows the interface is smooth (**smooth stratified flow**). At higher gas velocities the shearing action of the gas at the interface generates small 2–D waves (**wavy stratified flow**). At even higher gas velocities, large amplitude waves are seen on the liquid surface. Liquid is torn from the surface of these waves giving drop entrainment in the gas. The deposition of these drops may partially wet the top of the tube and eventually form rivulets. By increasing the liquid flow the slug flow regime is approached.

- **Slug flow** : Slug flow is characterised by the intermittent appearance of frothy slugs of liquid which bridge the entire pipe section and move at almost the gas velocity.

  Pressure fluctuations typify this flow, here the gas pressure behind the slug is greater than that in front of the slug.

- **Pseudo–slug flow** : This flow pattern occurs near the annular/slug, stratified/slug and stratified/annular flow transitions.

  Pseudo–slug flow is characterised by the presence of liquid disturbances which have the appearance of slugs, but which do not give the identifying pressure

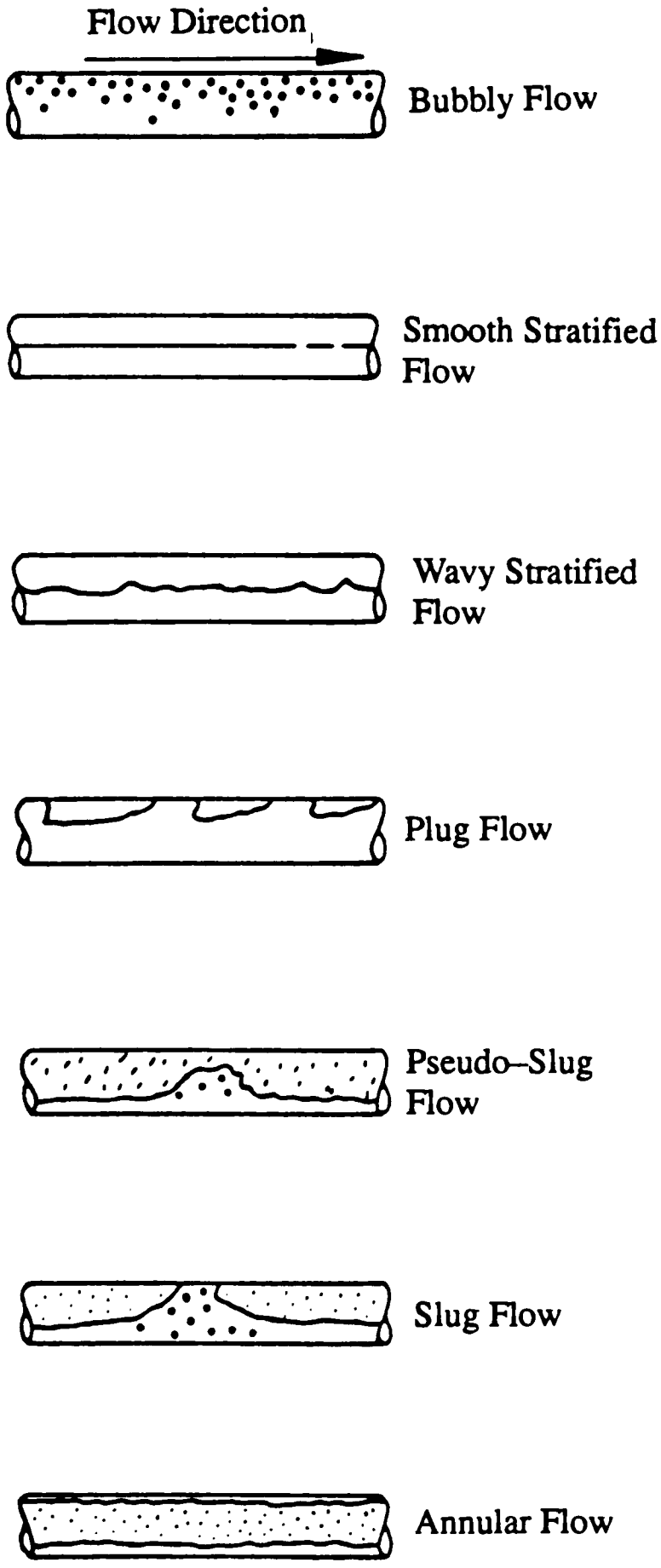

Figure 1.2 Flow pattterns for horizontal gas–liquid flow. •

pattern a slug does and do not travel at the gas velocity. These disturbances can touch the top of the tube momentarily, but do not block the entire pipe section. In this way pressure build–up behind the pseudo–slug is prevented.

- **Annular flow** : At yet higher gas rates the liquid slug is pierced by a gas core and the flow becomes essentially annular. At extreme gas flow rates horizontal annular flow can be approximated to vertical annular flow, but at low gas flows the film is thicker at the bottom of the tube.

  Taitel and Dukler (1976) suggest that the transition from stratified to either slug or annular flow depends uniquely on the liquid height, h, of the stratified layer. They suggest that when this height is above the pipe centre line slug flow will develop, on the other hand if $h/d_t < 0.5$, annular flow will result.

1.2. Flow Pattern Maps

In many practical situations the flow cannot be observed. In these cases the flow regime must be predicted. Visual observations have shown that different flow patterns occur at different flow conditions (e.g. flow rates, physical properties, flow geometry etc.). These observations are usually presented on flow pattern maps which mark the boundaries between flow regimes. Such maps are generally two–dimensional and tend to adopt simple coordinate systems. Examples of some common flow pattern maps for vertical and horizontal flows are discussed below.

1.2.1. Vertical Flow

For vertical upflow, several different flow pattern maps have been proposed. Of particular interest because of its simplicity is that due to Hewitt and Robert (1969) (Figure 1.3). They used high speed flash photography and simultaneous X–radiography to evaluate the structure of an air–water flow. Their data are plotted in terms of the superficial momentum flux of the gas ($\varrho_G\, U_{SG}{}^2$) and the superficial momentum flux of the liquid ($\varrho_L\, U_{SL}{}^2$). Whalley (1987) stated that this map performs reasonably well for air–water and steam–water systems over a range of pressures in small diameter tubes.

1.2.2. Horizontal Flow

For horizontal flow, Baker (1954) proposed a map in which (G_G / λ) and $(G_L\, \psi \lambda / G_G)$ are used as coordinates. G_G and G_L are, respectively, the gas and the liquid mass fluxes and λ and ψ are fluid property correction factors, defined as:

$$\lambda = \left(\frac{\varrho_G}{\varrho_A}\right)\left(\frac{\varrho_L}{\varrho_W}\right)^{\frac{1}{2}} \tag{1.1}$$

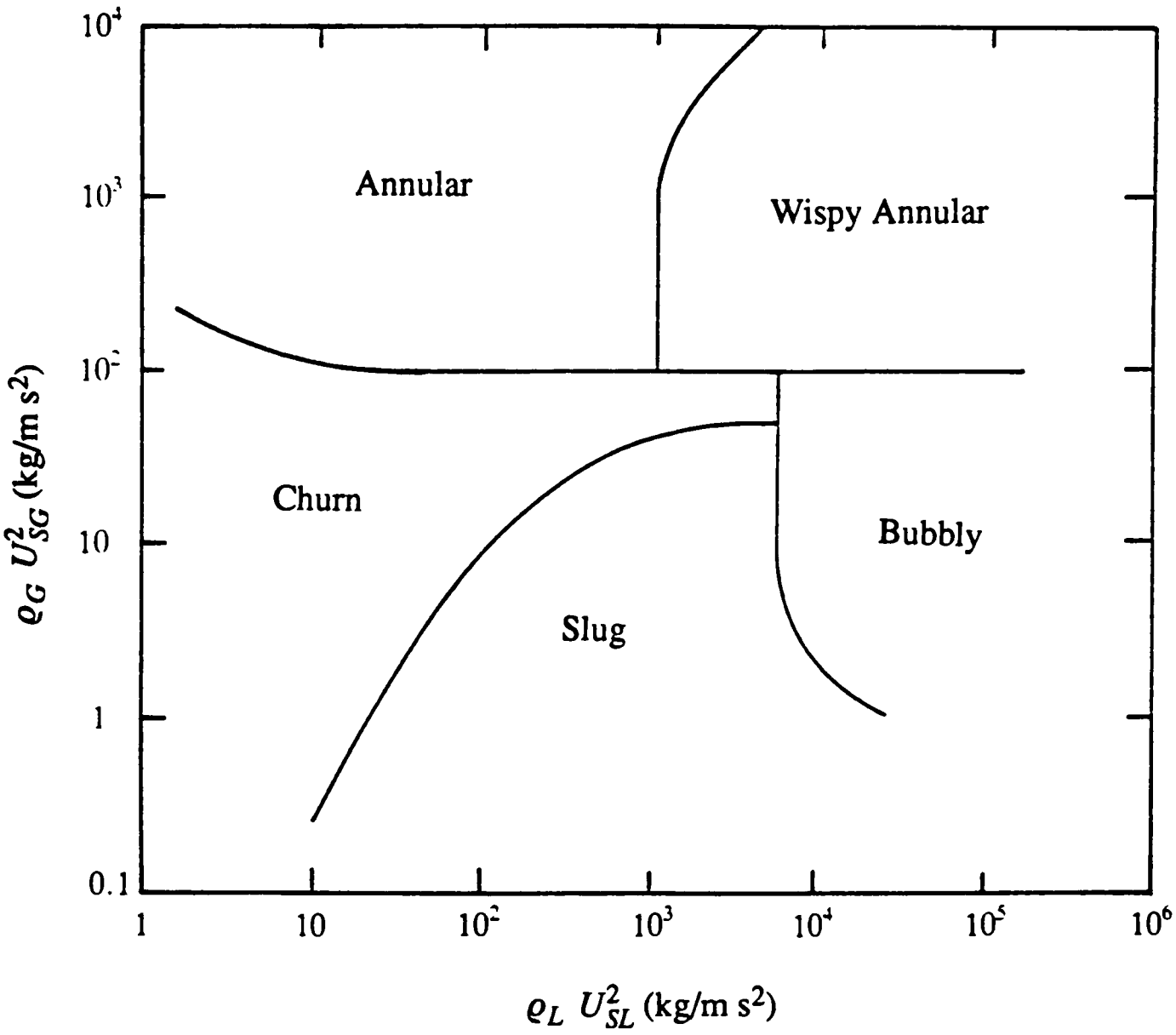

Figure 1.3 Flow pattern map for vertical upflow (Hewitt and Roberts (1969)).

and

$$\psi = \frac{\sigma_W}{\sigma}\left[\frac{\mu_L}{\mu_W}\left(\frac{\varrho_W}{\varrho_L}\right)^2\right]^{\frac{1}{3}} \tag{1.2}$$

where $\varrho_A, \varrho_G, \varrho_W$ and ϱ_L represent the densities of the air, gas, water and liquid, μ_W and μ_L are the water and liquid viscosities, and σ is the surface tension and σ_W is the surface tension for an air–water system. These correction factors were introduced to adjust for non air–water systems.

The Baker flow pattern map (Figure 1.4) is suitable for use with air–water and oil–gas mixtures in small diameter tubes ($d_t < 0.05$ m), as mentioned by Whalley (1987).

Hoogendoorn (1959) investigated the flow patterns formed by air–water and air–oil mixtures in horizontal pipes with inner diameters ranging from 0.024 m to 0.14 m. The author found that the influence of liquid viscosity and pipe diameter on the transition between the different flow patterns was very small. Hoogendoorn presented his results in a flow pattern map in which the velocity of the mixture (U_M) is plotted against the gas percentage by volume (C_G). U_M is related to the liquid and gas superficial velocities by:

$$U_M = U_{SG} + U_{SL} \tag{1.3}$$

while C_G is defined as

$$C_G = \frac{U_{SG}}{U_{SG} + U_{SL}} \times 100 \quad (\%) \tag{1.4}$$

This coordinate system, however, restricts the wavy–stratified and annular region to a very small area on the map, therefore it is difficult to use it in the present study.

Scott (1963) using the data of Hoogendoorn (1959) and Govier and Omer (1962) suggested a modification in the Baker map. In the new diagram the transition boundaries are broad bands rather than well defined lines.

Mandhane et al (1974) tested existing flow pattern maps against a data bank of flow pattern observations, covering a wide range of flow conditions and physical properties in horizontal flow. They also proposed a new map using as coordinates the superficial liquid velocity (U_{SL}) and the superficial gas velocity (U_{SG}). The basic map was developed with air–water data (Figure 1.5), but it is possible to extend its use to other fluid systems.

Mandhane et al did not include a diameter effect on their map. However, they did check their map against data obtained in tubes with different diameters. Their map was shown to work

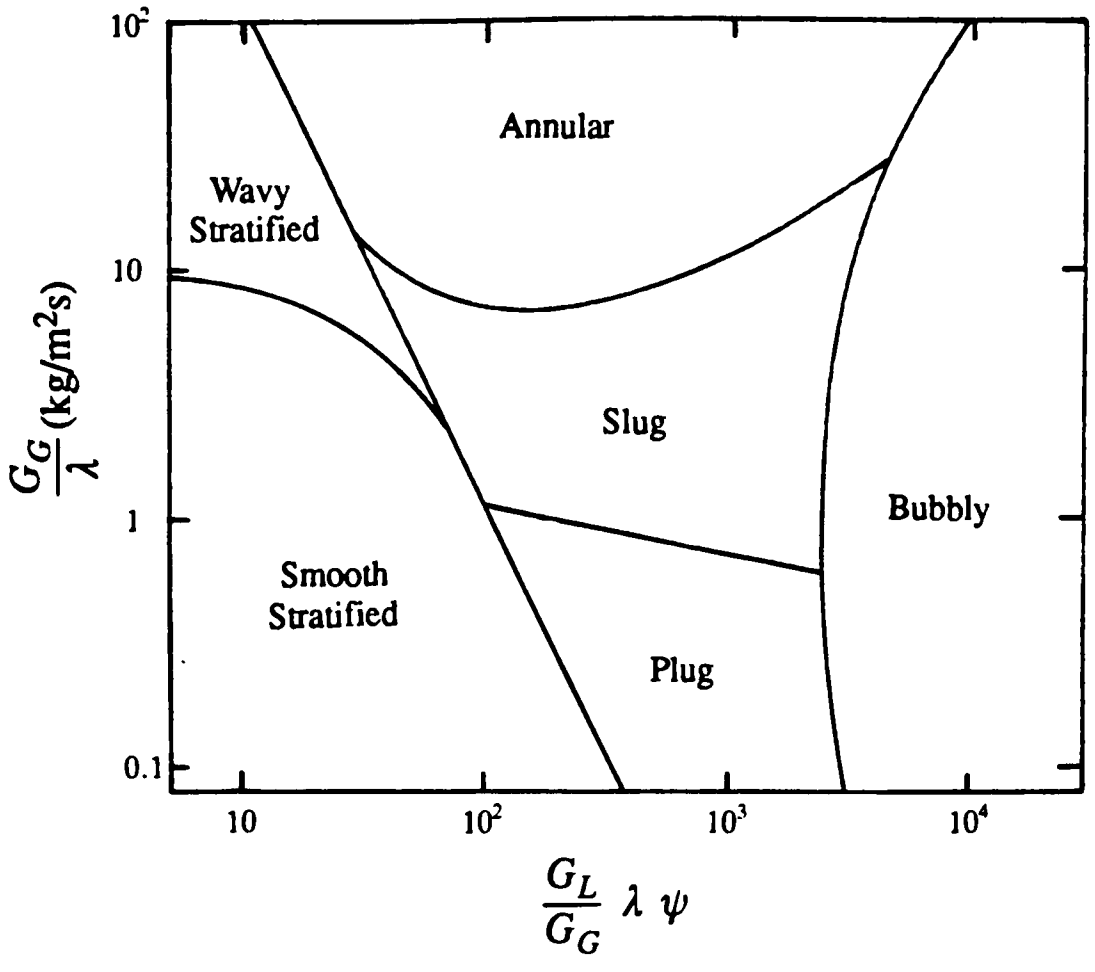

Figure 1.4 Flow pattern of Baker (1954).

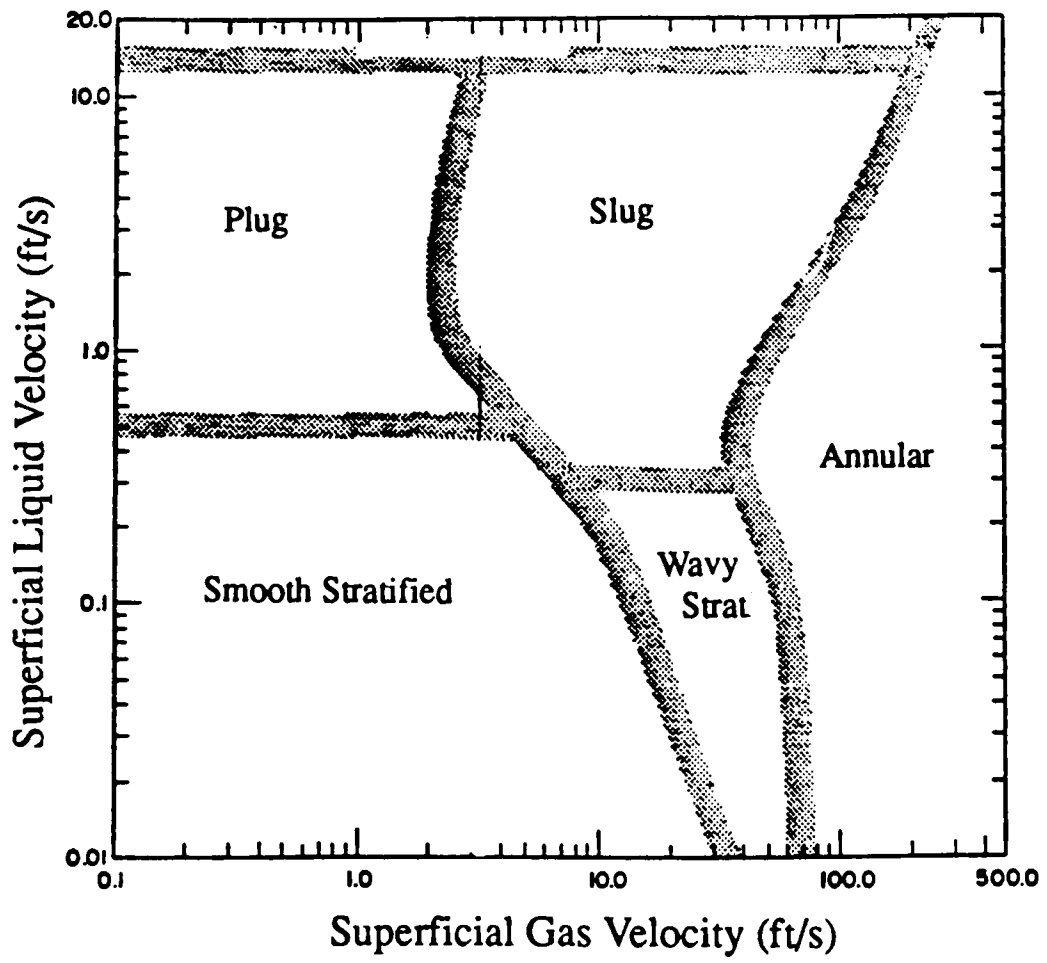

Figure 1.5 Flow pattern map proposed by Mandhane et al (1974).

well for tubes up to 0.05 m in diameter, although, even for larger diameters, the accuracy of the map was good when compared with the overall accuracy of other maps.

All the maps presented so far have been constructed from visual observations. A different approach to represent flow pattern maps was developed by Taitel and Dukler (1976). They presented a semi-theoretical model which predicts the relationship between the variables that affect flow regime transitions: gas and liquid flow, physical properties and tube diameter.

The parameters considered emerge as dimensionless groups:

$$X = \left[\frac{(\frac{dp}{dz})_L}{(\frac{dp}{dz})_G}\right]^{\frac{1}{2}} \tag{1.5}$$

$$T = \frac{|(\frac{dp}{dz})_L|}{(g\ (\varrho_L - \varrho_G))^{\frac{1}{2}}} \tag{1.6}$$

$$Fr = \frac{G_G}{(\varrho_G\ (\varrho_L - \varrho_G)\ d_t\ g)^{\frac{1}{2}}} \tag{1.7}$$

$$K = Fr\left(\frac{G_G\ d_t}{\mu_L}\right)^{\frac{1}{2}} \tag{1.8}$$

The Taitel and Dukler method for flow pattern determination in a horizontal tube is presented in Figure 1.6. Hewitt (1982) recommended their method, but pointed out some deficiencies that later results reported by Weisman (1979) have highlighted:

i) Taitel and Dukler correlation for the separated/intermittent flow transitions predicts an effect of liquid viscosity, however data on high viscosity solutions showed no viscosity effect;

ii) the transition intermittent/bubbly showed dependence on surface tension, which is not accounted for in the parameters of Taitel and Dukler:

iii) the assumption that the intermittent/annular flow transition occurred at $h/d_t = 0.5$ was not consistent with experimental results.

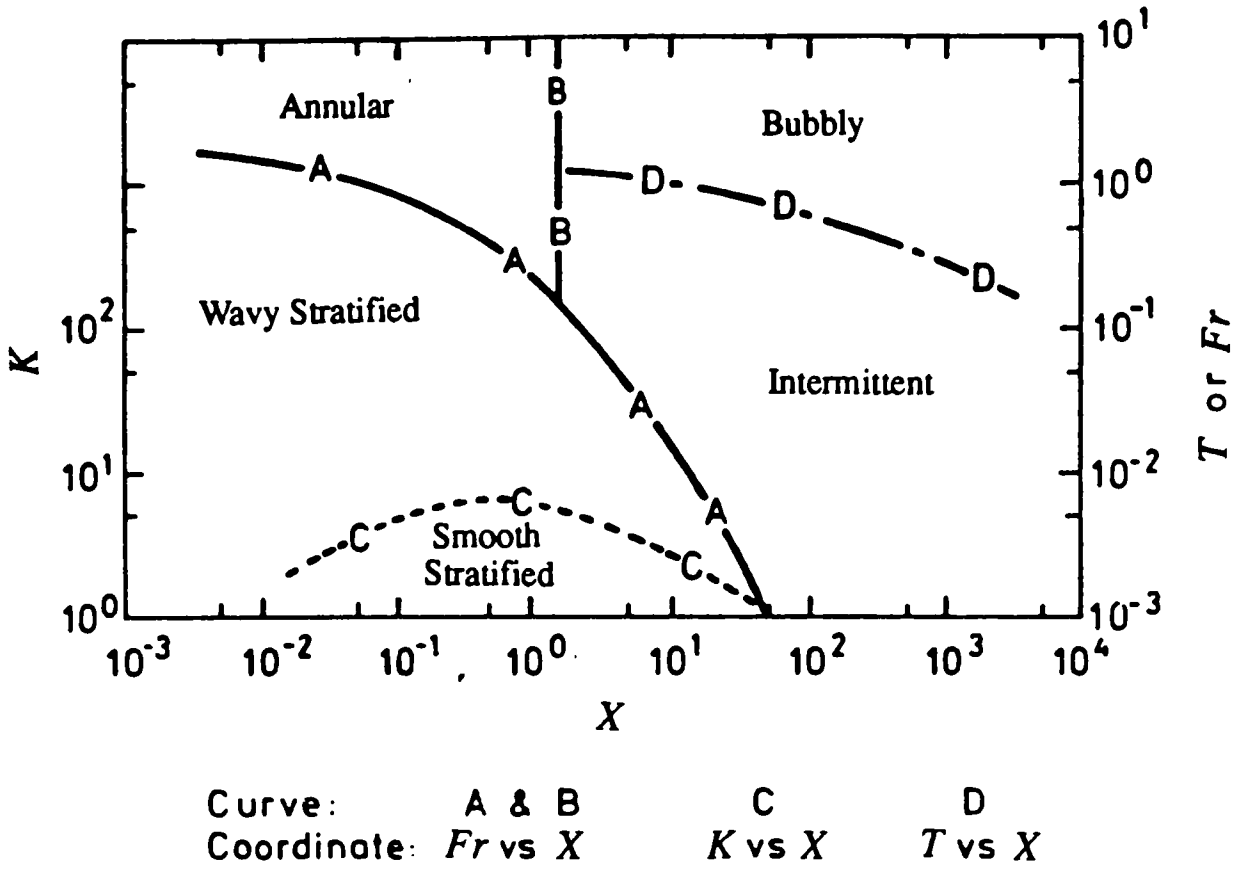

Figure 1.6 Generalized flow regime map for horizontal two–phase flow (Taitel and Dukler (1976)).

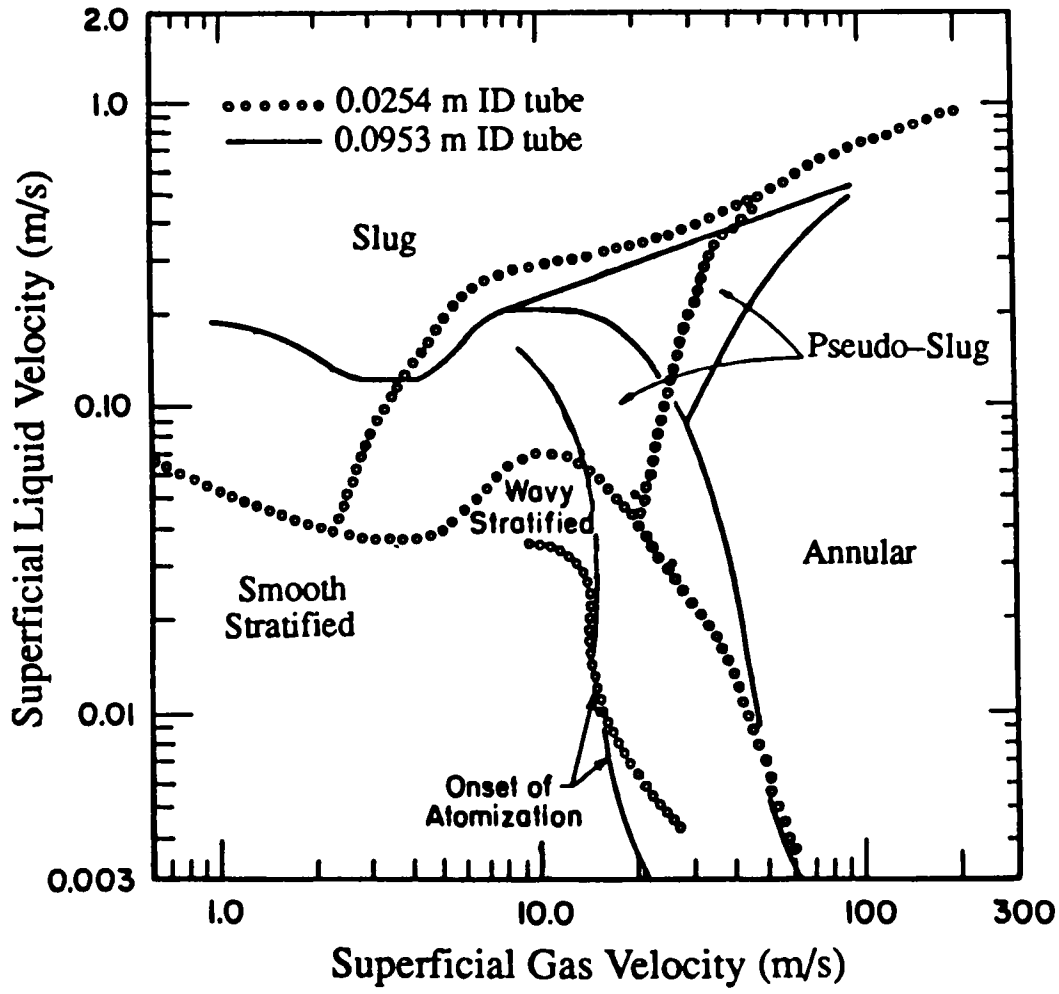

Figure 1.7 Flow pattern map for air–water flowing in 0.0254 m and 0.0953 m ID horizontal tubes (Lin and Hanratty (1987)).

The term 'separated' flow refers to the combination of smooth stratified and wavy stratified flows, and 'intermittent flow' to the combination of plug and slug flows.

More recently, Lin and Hanratty (1987) presented a flow pattern map for horizontal air-water flow in pipes 0.0254 m and 0.0953 m ID at near atmospheric conditions. They examined the influence of pipe diameter on the transition between flow regimes and identified pseudo-slug flow as a discrete flow regime on their flow pattern map (Figure 1.7).

In this study, the flow pattern map by Lin and Hanratty has been adopted. Apart from being the most recent map developed for air-water, the visualisation experiments (Chapter 3) showed good agreement between the present flow observations and the map, and the flow conditions studied fall within the limits of the map.

The next sections describe in more detail the flow regimes covered in the present investigation and discusses the influence of bends on these flows.

1.3. Stratified Flow

One of the simplest flow patterns in horizontal gas-liquid flow is stratified flow. It is characterised by the liquid flowing in the lower part of the tube and the gas in the upper part. The smooth stratified flow exists at low gas and liquid flow rates, and the gas-liquid interface appears as a smooth surface.

When the gas flow rate is increased for a fixed liquid flow rate, the interface becomes covered with waves. This is the beginning of wavy-stratified flow.

Andritsos and Hanratty (1987) characterised the different types of waves found in stratified air-water flow through tubes of 0.0252 m and 0.0953 m ID. For constant liquid flow rate and increasing gas flow rate, they first observed small amplitude 2-D waves. As the gas velocity was increased, they saw the amplitude of these waves increase and their wavelength decrease. Andritsos and Hanratty called these large amplitude waves, roll waves. Further increase in the gas flow rate, caused drops to be torn from the liquid phase and deposited on the pipe walls. Figure 1.8 illustrates the regime changes and different wave patterns for their air-water experiments in the 0.0252 m ID tube.

For wavy-stratified flow, increases in the gas flow rate causes the liquid film to rise up the sides of the pipe. This is illustrated by the film thickness measurements of Liné et al (1991). Under conditions where entrainment was not observed, they showed a decrease in the film thickness at the bottom of the pipe with increasing gas velocity.

The flow field in the gas is affected not only by the gas Reynolds number, but also by the gas-liquid interfacial structure. Measurements of the gas axial velocity component have indicated that for a relatively smooth interface (up to a surface covered with 2-D waves) the velocity profile is symmetrical. Under these conditions, the interfacial friction factor is similar to the friction factor for a smooth wall.

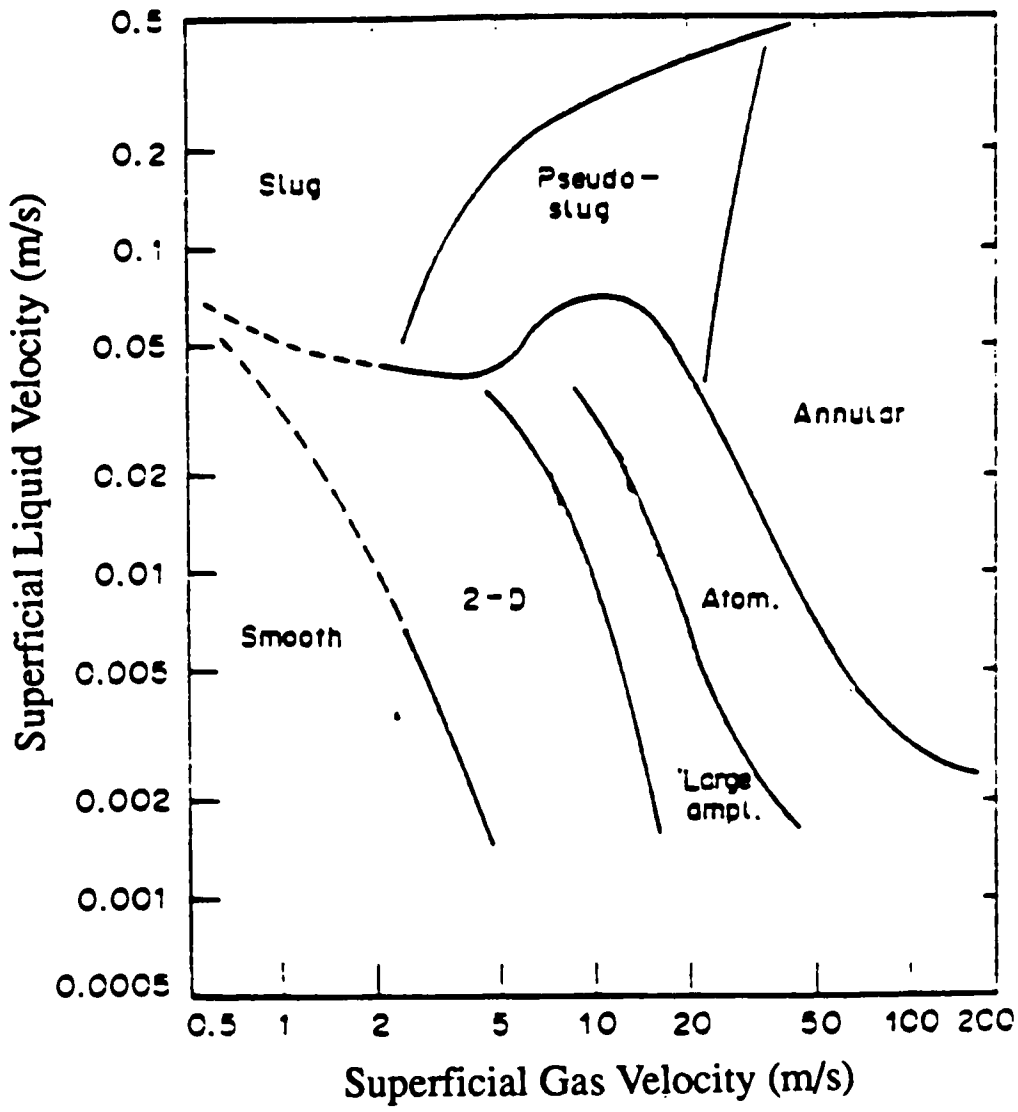

Figure 1.8 Flow regime changes and wave patterns for air–water flow in a horizontal tube 0.0254 m ID.

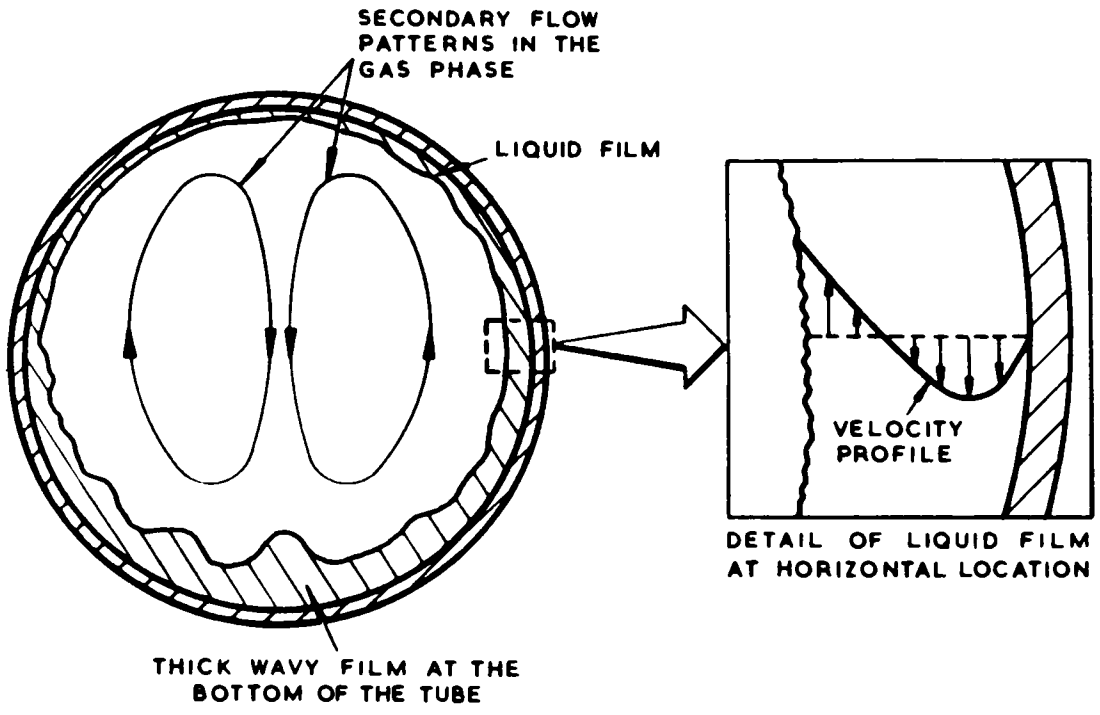

Figure 1.9 Secondary flow mechanism for maintaining the film (Butterworth and Pulling (1972)).

When roll waves exist the axial velocity profile in the gas phase becomes asymmetric with the maximum velocity displaced towards the upper wall. This is illustrated by the experiments of Liné et al (1991) with circular pipes, and by Hanratty and Engen (1957) and Akai et al (1977) with rectangular channels. These observations suggest that, frictionally, the roll waves behave as though they presented a rough solid surface at the gas-liquid interface.

The wavy interface also affects the flow structure in the liquid phase. The visualisation experiment of Akai et al (1977) in a rectangular channel illustrated this fact. By adjusting the liquid Reynolds number below the laminar flow limit and progressively increasing the gas velocity, they were able to show the influence of the waves on a filament of dye injected into the liquid phase.

At low gas flow rates, the dye filament retained its identity. With increasing gas velocity, interfacial waves appear and the dye filament was seen to mix rapidly with the liquid stream. This suggested that the formation of waves introduced turbulence into the liquid film.

Fogwell and Hope (1987) conducted visualisation experiments in horizontal stratified flow using a photochromic dye tracing technique. From this study, they concluded that for smooth stratified flow the velocity profile in the liquid film appeared to be laminar with the characteristic S-shaped profile. This S-shape profile occurred when the velocity of the gas was higher than the velocity of the liquid. With increasing gas and liquid flow rates, waves appeared which enhanced the turbulence in the central section of the S-shaped velocity profile, and induced secondary flows in the liquid film.

The presence of air bubbles entrained in the liquid film was noticed in this study above certain gas and liquid flow rates. This is discussed in the more detail in Chapter 3.

1.4. Stratified to Annular Flow Transition

The transition from stratified to horizontal annular flow is linked to the formation of an annular film covering the whole pipe circumference. Butterworth and Pulling (1972) discussed the mechanisms that sustain the liquid film at the top of the tube. These include:

- **Secondary flow**. Darling and McManus (1968) have shown that circumferential variations in the surface roughness can produce secondary flows in a single-phase turbulent gas flow. In annular flow the gas phase is effectively flowing over a rough surface where the roughness is highest at the bottom of the tube. Because of this, secondary flow patterns would be expected in annular flows. Here the upward flow of the gas near the interface carries part of the liquid film upwards whilst the gravity drives liquid near the wall downwards, as illustrated in Figure 1.9.
- **Entrainment-deposition**. Here, the film at the top of the tube is replenished by the deposition of entrained drops.

- **Wave mixing.** In annular horizontal flow, large roll waves are present. These waves are coherent around the perimeter of the tube, despite the fact that the average velocities in the film are highest at the bottom of the tube. In another paper Butterworth (1972) suggested that this coherence is maintained by strong circumferential mixing in the film. This mixing action can be due to the high levels of turbulence in the roll wave which oppose the film drainage. On the other hand, the mixing can be caused by variations in the pressure under the roll wave due to different curvatures at different points, which promote flow from positions of high pressure to positions of low pressure (Figure 1.10).

- **Wave spreading**. The ripples (i.e. 2-D waves) on the liquid film surface tend to travel faster at the bottom of the tube because the film velocity here is higher. The action of the gas over the film produces a net force with a component in the circumferential direction, as shown in Figure 1.11. This force is expected to transport liquid from the bottom of the tube (region of high film velocity) towards the top of the tube (region of lower film velocity).

Hoogendoorn (1959) described the flow regime transition from stratified to annular flow. based on experiments with air-oil and air-water flow in pipes up to 0.14 m in diameter. The author suggested that the entrainment-deposition mechanism is responsible for the transition.

Butterworth and Pulling (1972) conducted visualisation experiments in a 0.0318 m ID horizontal tube, using a dye injection technique. From these experiments, they concluded that the wave mixing mechanism sustained the liquid film at the top of the tube.

In a recent work, Lin and Hanratty (1987) argued that both the entrainment-deposition and the wave mixing mechanisms played an important role in the stratified/annular transition. Based on experimental observations, the authors reported that for the flow in a 0.0953 m pipe, the transition occurs mainly through deposition of drops. For a pipe 0.0254 m in diameter, this mechanism was dominant for superficial liquid velocities up to 0.015 m/s. At higher liquid flows, the wave mixing mechanism was most important.

1.5. Annular Two-Phase Flow

In annular flow the gas travels in the centre of the tube. The liquid flows as a slower film covering the whole pipe circumference, and also as entrained drops in the gas core. Due to the shearing action of the gas phase, the gas-liquid interface is covered with waves.

In vertical annular flow the film is uniformly distributed around the pipe circumference. In horizontal flow, however, gravity causes the liquid to be drained to the bottom of the pipe. Consequently, the film at the bottom of the tube is thickest. With increasing gas velocity, this asymmetry in the film thickness becomes less pronounced. This is illustrated by the film

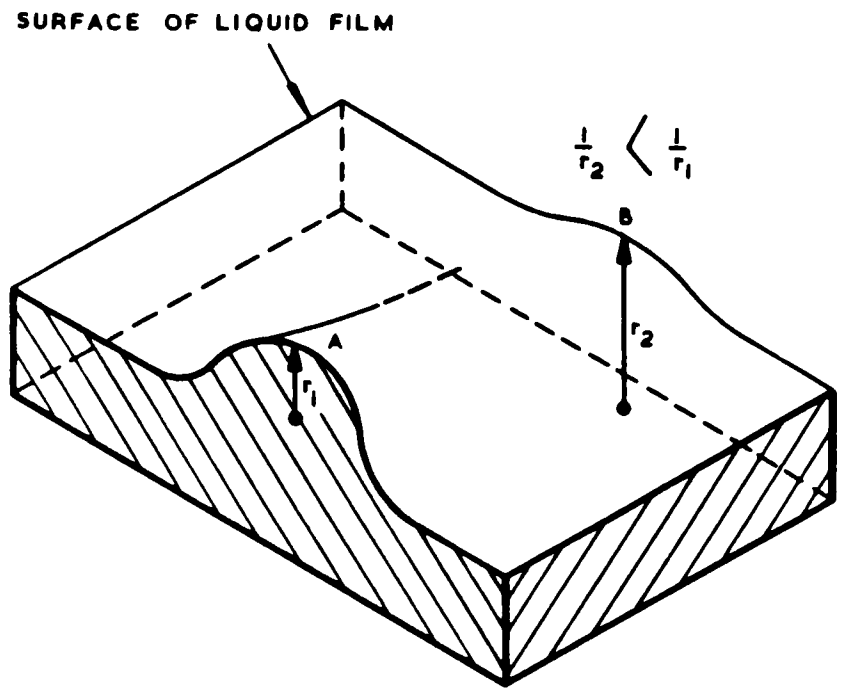

Figure 1.10 Illustration of wave transport configuration for circumferencial transport (Butterworth and Pulling (1972)).

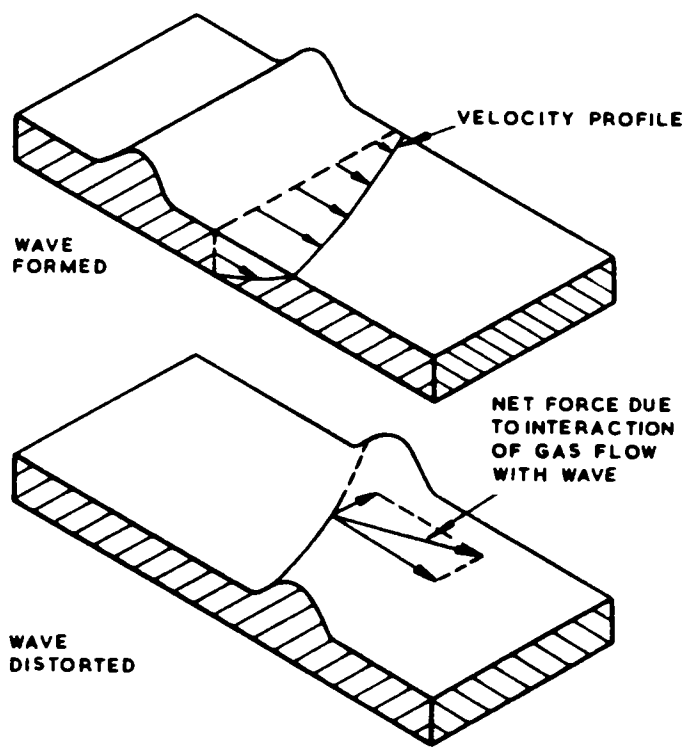

Figure 1.11 Illustration of wave spreading mechanism for circumferencial transport (Butterworth and Pulling (1972)).

thickness measurements of Dallman (1978), Sekoguchi et al (1982), Laurinat (1982), Paras and Karabelas (1990–a) and Jayanti (1990).

Paras and Karabelas (1990–a) studied the annular flow of an air–water mixture in a horizontal tube 0.0508 m ID. They found that at relatively low gas flow rates the wave structure was dominated by large amplitude waves which appeared in the lower part of the tube. As the gas flow rate was increased, these waves progressively covered a greater portion of the tube circumference, and became more symmetrical and more frequent.

Andritsos and Hanratty (1987) observed the wave pattern in horizontal annular flow for tubes of 0.0252 m and 0.0953 m ID. In the small tube at high gas velocities they observed large amplitude waves which took the form of aerated rings that covered the whole pipe circumference. However, for the 0.0953 m tube the waves did not cover the entire pipe circumference, until very high gas velocities of 70 m/s were reached.

Another interesting feature of the liquid film in horizontal annular flow was documented by Jayanti (1990). The author reported the presence of air bubbles in the liquid film, with sizes varying from a fraction of a millimetre to a few millimetres.

1.6. Drop Behaviour

1.6.1. Entrainment

Entrainment is a complex phenomena linked to the appearance of large amplitude waves called roll waves. Beyond critical gas and liquid flow conditions, liquid is torn from the surface of these waves giving rise to drop entrainment in the gas core.

In vertical flow, the onset of entrainment occurs under annular flow conditions, however in horizontal flow entrainment begins during wavy–stratified flow.

For vertical annular flow, Azzopardi (1983) has identified two mechanisms of entrainment from axial view photography. One of the mechanisms termed bag break–up occurs when a roll wave is undercut by the gas to form an open–ended bubble with a thick filament rim (Figure 1.12(a)). The gas pressure inside the bubble builds up until eventually the bubble bursts to form large drops from the rim and smaller drops from the bubble skin. This entrainment mechanism can impart high ejection velocities to the drops.

At higher flows the second mechanism termed ligament break–up predominates. Here, the top of the wave is pulled forward in the form of a ligament. This ligament is torn from the surface and broken–up in the gas stream (Figure 1.12(b)).

Azzopardi (1987) conducted a similar visualisation study for horizontal annular flow. For the flow rates considered, Azzopardi observed the presence of bag break–up and no evidence of

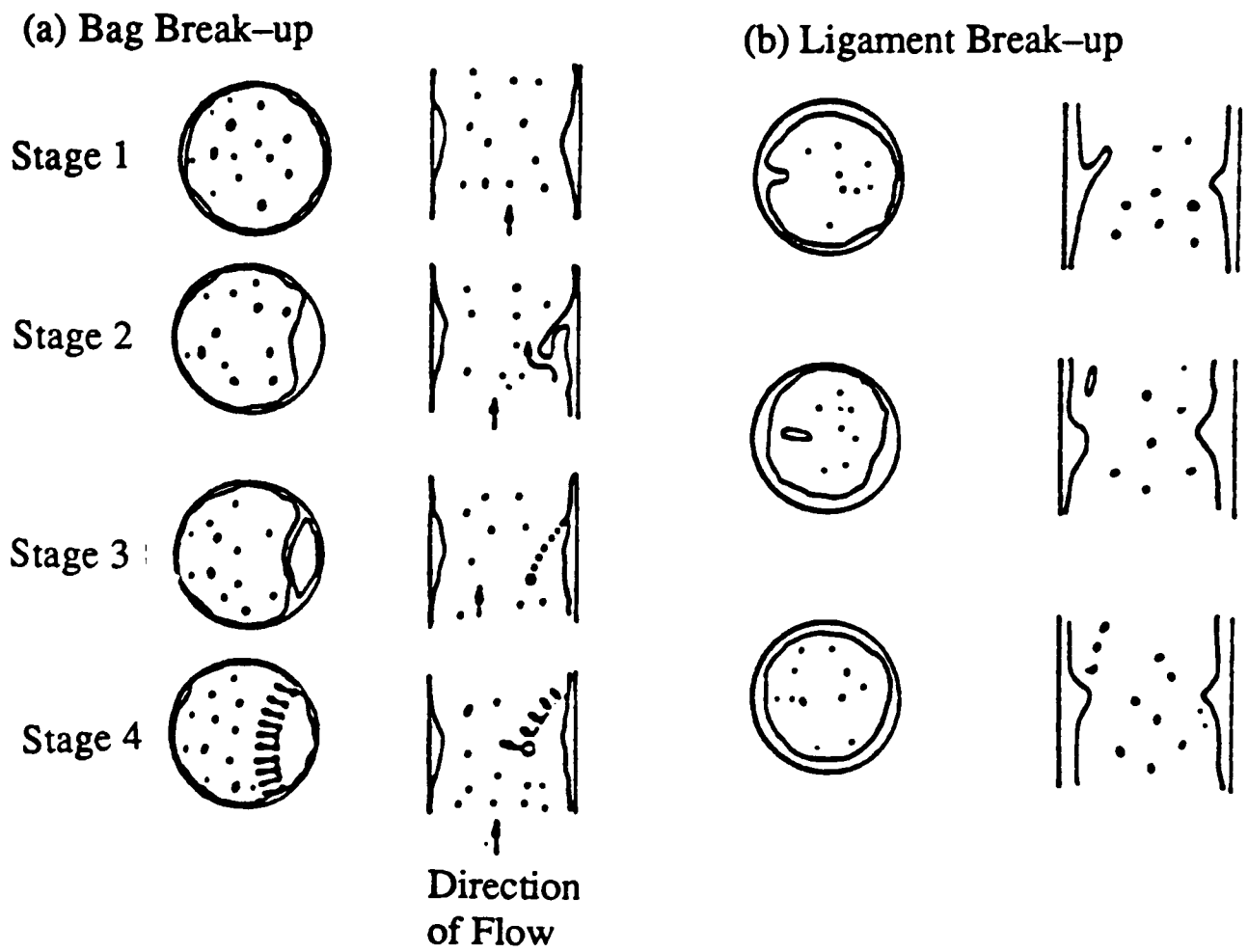

Figure 1.12 Mechanisms of entrainment (Azzopardi (1983)).

ligament break-up was seen. Visualisation studies performed in this work, however, reveal the presence of ligament break-up (see Chapter 3).

In addition, Newitt et al (1954) and Garner et al (1954) suggested that secondary entrainment may occur from the collapse of air bubbles at the gas-liquid interface. For horizontal annular flow, the presence of air bubbles in the liquid film has been reported by Jayanti (1990), and the present work showed air bubbles entrained in the liquid film under wavy-stratified flows. Correspondingly, the release of these bubbles may contribute to liquid entrainment. Secondary entrainment of the liquid can also be caused through drop impaction, as observed by Nigmatulin (1984).

1.6.2. Drop Transport and Deposition

In vertical annular flow drops entrained in the gas will interact with the gas phase turbulence before depositing. Hewitt (1978-a) reviewed these interactions and suggested that the mode of drop transport and deposition is influenced by the drop size. These mechanisms are discussed below:

- **Diffusion**. Drops with diameters less than 0.1 μm interact with the gas phase eddies in the turbulent core. The subsequent deposition of these drops through the laminar boundary region is then limited by Brownian diffusion.
- **Inertia**. Drops with diameters in the range 0.1-10 μm also follow the turbulent motion in the gas stream. However, the inertia these drops gain as a result of the velocity fluctuations in the gas core is sufficient to carry them through the laminar boundary region.
- **Impaction**. Drops with diameters greater than 10 μm fail to respond to the gas phase turbulence and possess sufficient momentum to penetrate the boundary layer region.

In horizontal flow, gravitational settling can have an important influence on the deposition rate. Consequently, the deposition mechanisms can be very different from those seen in vertical flows. In cases where gravitational settling dominates, drop deposition at the bottom of the tube is much larger than at the top.

Azzopardi (1987) illustrated the influence of gravity on drop transport in horizontal tubes by tracing the parabolic trajectories taken by drops.

1.6.3. Deposition and Entrainment Rate

In vertical annular flow, there is a continuous interchange of liquid between the film and the gas core. The deposition rate ($\dot{D}$) defined as the mass flow rate of liquid deposited per unit area of tube wall, is commonly expressed as a mass transfer process in terms of the relationship:

$$\dot{D} = k_D \, C \tag{1.9}$$

where k_D is the overall deposition mass transfer coefficient, and C is the drop concentration in the gas core.

Under equilibrium conditions the rate of deposition ($\dot{D}$) is equal to the rate of entrainment ($\dot{E}$), and thus:

$$\dot{E} = \dot{D} = k_D \, C_e \tag{1.10}$$

where C_e is the equilibrium drop concentration. Assuming no slip between the drops and the gas, C_e is given by:

$$C_e = \frac{G_{LE}}{\left(\frac{G_G}{\varrho_G} + \frac{G_{LE}}{\varrho_L}\right)} \tag{1.11}$$

If $G_G/\varrho_G \gg G_{LE}/\varrho_L$, then:

$$C_e = \frac{G_{LE} \, \varrho_G}{G_G} \tag{1.12}$$

and the rates of entrainment ($\dot{E}$) and of deposition ($\dot{D}$) become:

$$\dot{E} = \dot{D} = k_D \, \frac{G_{LE} \, \varrho_G}{G_G} \tag{1.13}$$

where G_{LE} and G_G are the entrained liquid and gas mass fluxes, and ϱ_L and ϱ_G are the liquid and gas densities. Provided the deposition constant k_D is known and the entrained liquid mass flux can be determined (G_{LE}), the entrainment and deposition rates can be calculated.

1.7. Flow in Bends

Fluid flowing in pipe systems often encounters fittings such as bends. The presence of a bend can modify drastically the conditions of the flow in its upstream and downstream regions.

Most of the investigations in this field have been restricted to single-phase flow, and only a few authors have published results for gas-liquid flows. These works are discussed below.

1.7.1. Single-Phase Flow

Eustice (1911) was one of the first authors to report dye injection experiments to visualize the laminar flow of water in a curved pipe. The tests were conducted in glass tubes, in which the stream motion was traced by the introduction of coloured water through capillary nozzles. For a 90° bend, it was noticed that a dye filament at the axis of the tube moved away towards the outside of the bend, while the fluid near the wall flowed to the centre. These experiments demonstrated the existence of a transverse motion (secondary flow) superimposed on the primary flow, represented in the form of a pair of counter rotating longitudinal vortices (Figure 1.13).

Dean (1927 and 1928) wrote the first theoretical approach on the subject, and since then several works have been reported. A recent study by Dewhurst et al (1990) includes flow measurements using a 3-D LDA system in a square sectioned (0.1 x 0.1 m) 90° vertical bend. Streamwise and secondary velocities obtained by these authors for water flow upstream of the bend and at 80° on the bend, are illustrated in Figure 1.14. The streamwise and secondary velocities are represented as contour plots and vector plots, respectively. At 80°, the peak velocity is seen to be displaced towards the outside of the bend.

Most of the studies with bends have been carried out for single phase flow. Jayanti (1990) presented a review of these works, both under laminar and turbulent conditions. Two-phase flow in bends is discussed in the following sections.

1.7.2. Two-Phase Flow

Two-phase flow patterns observed in a bend are qualitatively the same as those seen in a straight pipe. However bends introduce a developing situation in the flow pattern, whereby the relative positions and local velocities of the two phases are redistributed.

Stuiver (1955) used a high speed photographic technique to study the flow characteristics of an air-water mixture passing through a horizontal 90° and 180° bend. The observations of Stuiver (1955) suggested that many of the entrained drops entering the bend, continued to travel on a straight line and deposited on the outside of the bend.

Banerjee et al (1967) have studied stratified air-water flows in helical coils. They observed a displacement in the maximum film thickness from the bottom of the tube; at low air and water flow rates, the maximum film thickness was located mainly on the outside of the bend, whilst, for high gas velocities and low liquid loadings the maximum film thickness was seen on the inside of the bend. The authors called this phenomenon film inversion, and correlated the position of maximum film thickness by the expression:

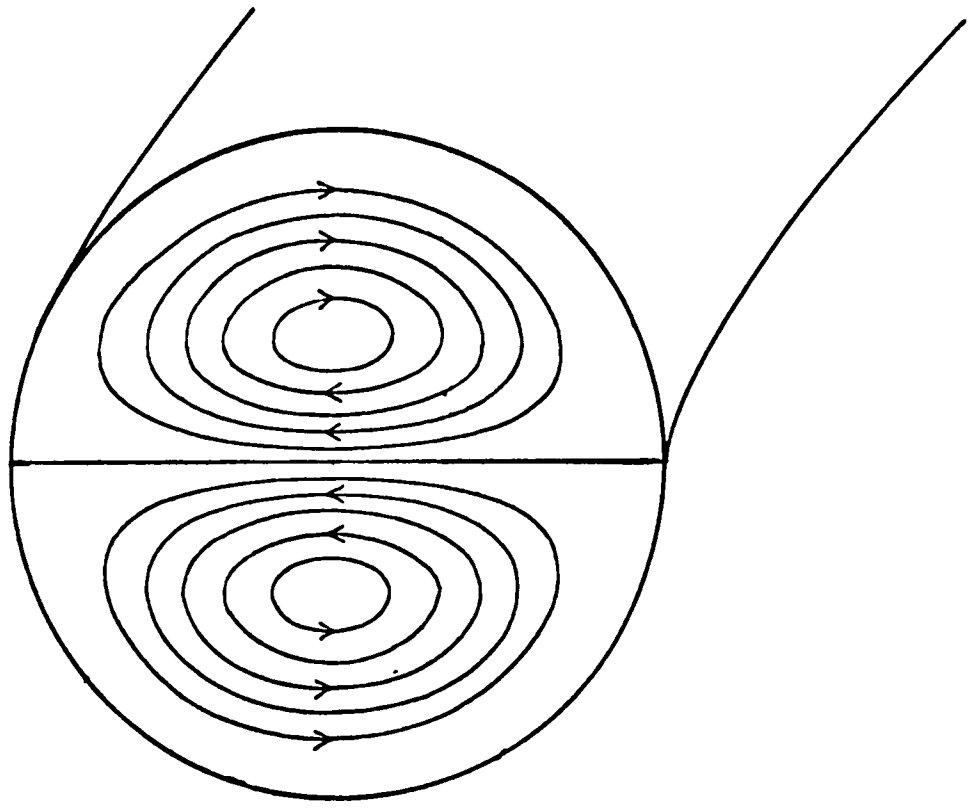

Figure 1.13 Secondary flow pattern.

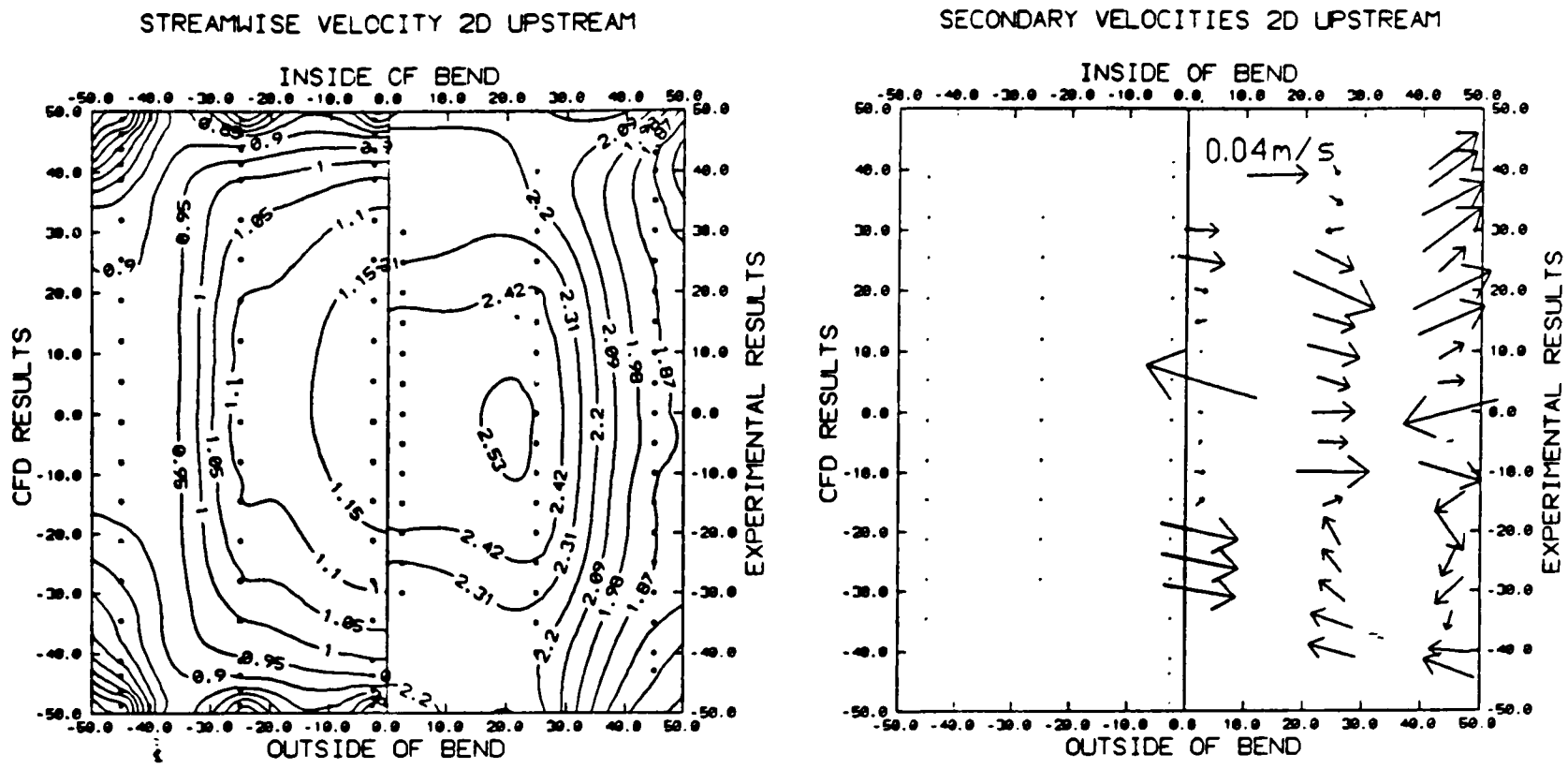

Figure 1.14 Streamwise and secondary velocities for a 90° square bend (Dewhurst et al (1990)).

$$\tan\theta = \frac{R\,\varrho_L\,g}{\varrho_L\,U_{LF}^2 - \varrho_G\,U_{SG}^2} \qquad (1.14)$$

where θ is the angle of displacement (Figure 1.15), R is the radius of curvature of the coil, U_{SG} is the superficial air velocity, and U_{LF} the mean velocity of the film. The same behaviour was observed by Balfour and Pearce (1978) but for annular flow in a 180° horizontal bend, and by Whalley (1980) in a helical coil.

For air–water flow round a vertical bends, Gardner and Neller (1969) suggested that the phase distribution is governed by the competing centrifugal force, which tends to take the liquid to the outside of the bend, and gravity, which causes the water to fall to the inside of the bend.

George (1971) used high speed cine films to observe the flow structure of an air–water mixture passing from a horizontal line into a 180° vertical return bend. These visualisation studies covered several flow patterns and highlighted the influence of the bend on the flow structure.

The influence of a bend on annular flow has been studied by Anderson and Hills (1974) and Maddock et al (1974) for vertical flow, and by Chakrabarti (1976) and Balfour and Pearce (1978) for horizontal flow.

Figure 1.16 shows the film thickness measurements of Anderson and Hills (1976) at several positions around a 180° vertical bend. The increase in film thickness on the inside of the bend was attributed to the action of gravity and to the secondary flow existing in the gas phase. At low liquid flow rates, the authors observed a change from annular to stratified flow in the bend. For the high liquid flow rates, local maxima in the film thickness were seen on the inside and the outside of the bend.

For horizontal annular flow, Chakrabarti (1976) and Balfour and Pearce (1978) also noticed a thickening in the liquid film towards the inside of horizontal bends. Also, for some flow conditions another local maximum in the film thickness profile was found towards the outside of the bend. They attribute the appearance of a thick film on the outside of the bend to the deposition of entrained drops. The deposition of these drops contributes to a reduction in entrainment after the bend, both in vertical and horizontal annular flow.

Anderson and Hills (1974) used a pitot tube to measure the axial gas velocity profile before and after a 180° vertical bend for single and two–phase flows. The results in Figure 1.17 were obtained before the bend. In comparison to the velocity profile for single–phase turbulent flow, the velocity profile for two–phase flow became progressively more peaked in the centre of the tube as the liquid flow was increased. Teixeira (1988) obtained similar results using Laser Doppler Anemometry (LDA) to study the turbulence in annular vertical flow.

Data obtained after the bend (Figure 1.18) show that the maximum gas velocity is displaced from the centre of the tube towards the outside of the bend. This displacement is more

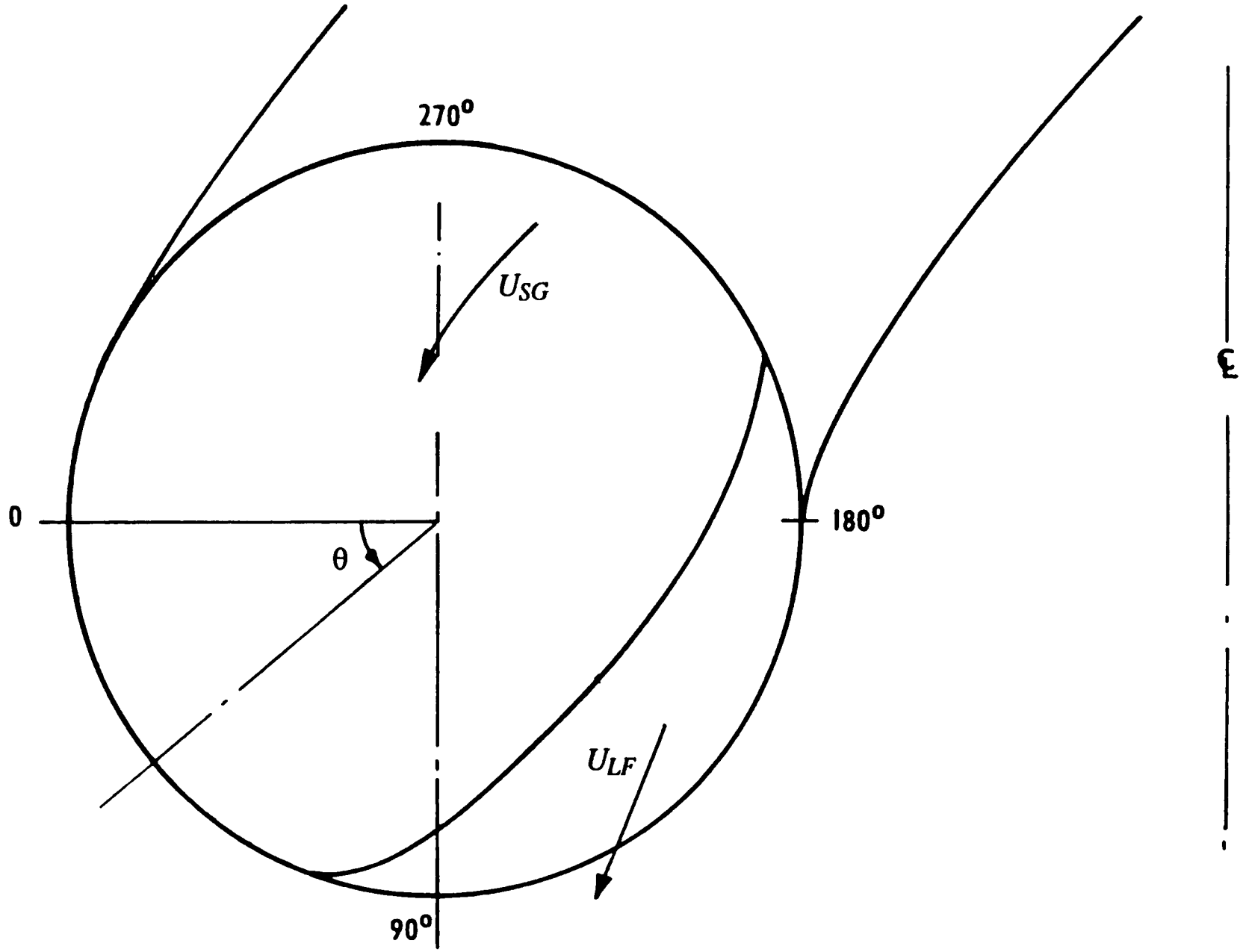

Figure 1.15 Film inversion for stratified flow.

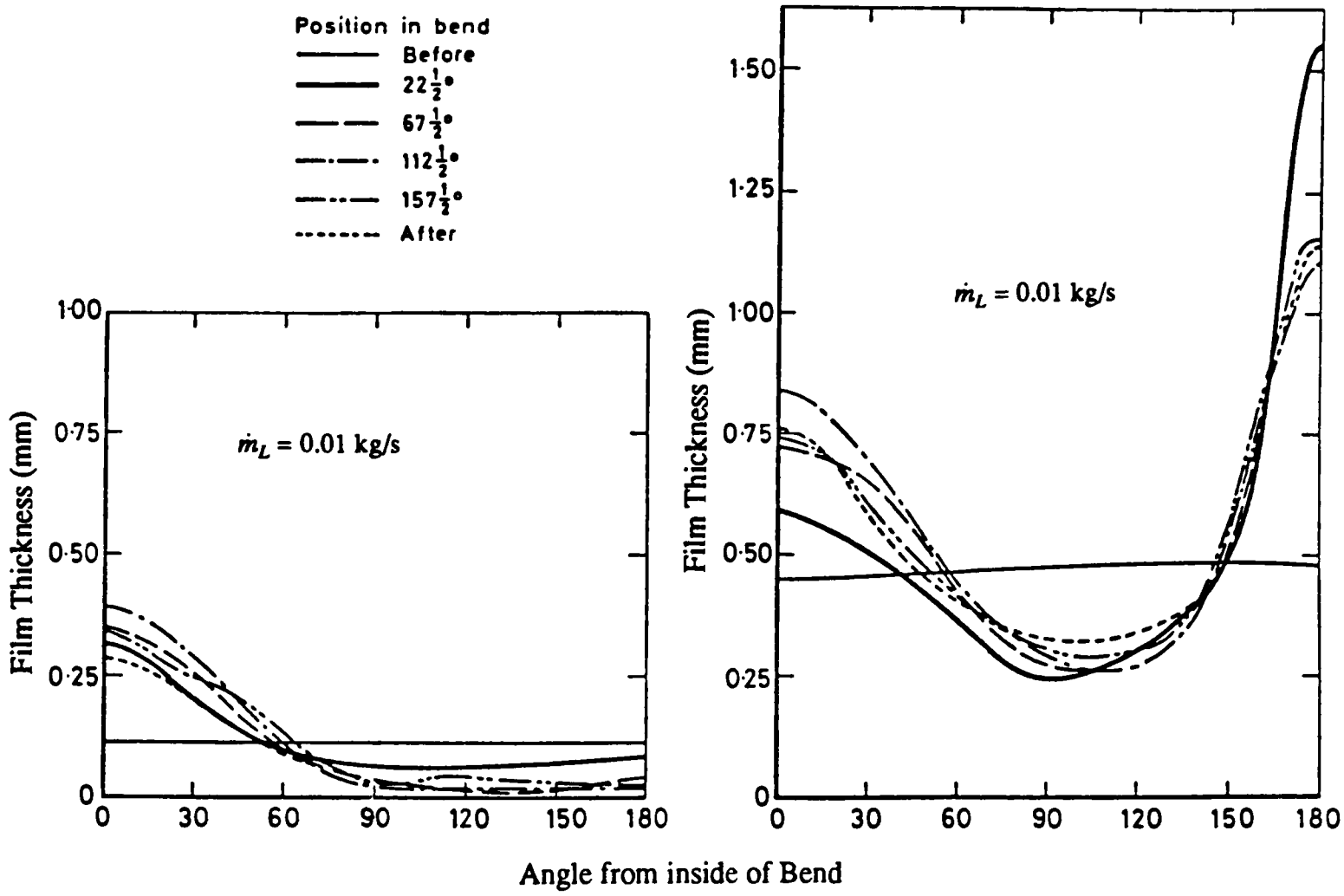

Figure 1.16 Film thickness variations for an air mass flow of 0.032 Kg/s (Anderson and Hills (1974)).

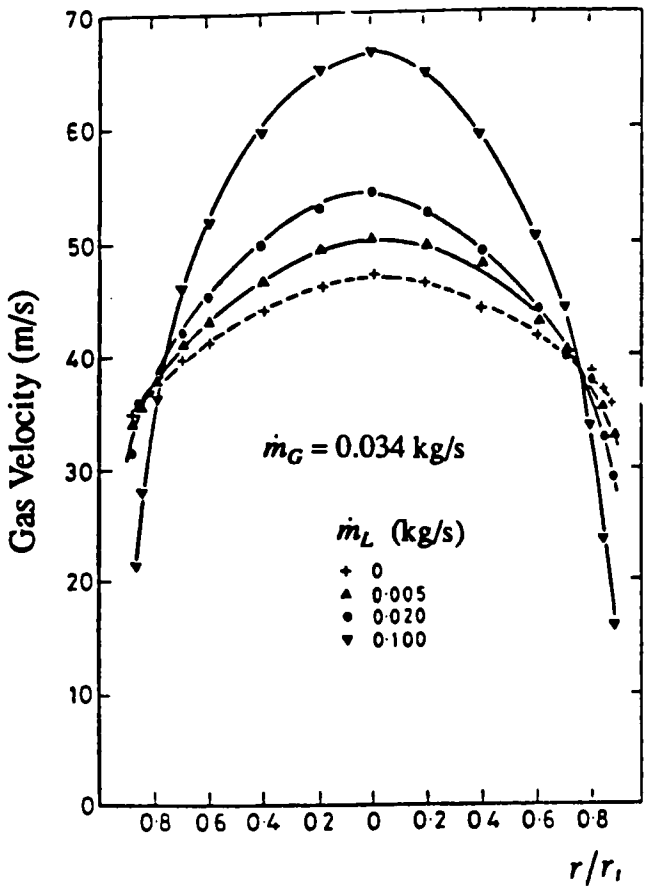

Figure 1.17 Gas velocity profiles before the bend (Anderson and Hills (1974)).

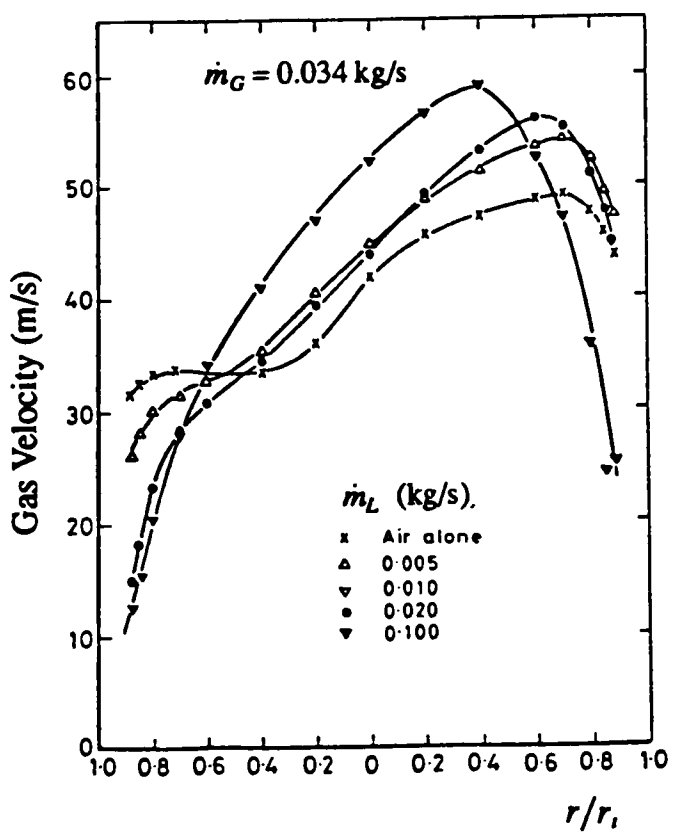

Figure 1.18 Gas velocity profiles after the vertical bend (Anderson and Hills (1974)).

pronounced in single-phase flow and is caused by the secondary flow in the gas. Similar results were reported by Chakrabarti (1976) at the exit of the horizontal bend.

1.8. Outline of the Thesis

The present investigation is concerned primarily with air-water flow in a horizontal 0.032 m ID tube. The influence of a 90° horizontal bend on this flow was studied. As part of this project, a new horizontal rig was designed and constructed (described in section 2.1.). The experiments included flow visualisation using high speed photographic techniques, and measurements of the film flow rate, drop size and drop velocity at locations before and after the bend. Also pressure drop experiments were performed upstream of the bend, in order to access the position of the measuring section before the bend.

Prior to the horizontal flow study, drop size and film flow rates were measured for vertical air-water annular flow in a 0.01026 m ID tube. This extended the work of Jepson (1992) who reported the effect of gas density and surface tension on the film flow rate, drop size and deposition mass transfer coefficient. Modifications to the rig described by Jepson (1992) allowed an extension of the measurements to higher flow conditions. These experiments are reported in **Chapter 7**.

In the next chapter, **Chapter 2**, the flow rigs and measurement techniques are described. For the horizontal study, the location of the measurement point upstream of the bend is discussed. Finally, the flow conditions over which the measurements were conducted are tabulated and justified.

Chapter 3 includes the results of the flow visualisation using high speed still photography and cine film, for horizontal flow. Several photographs are included to illustrate the behaviour of the system and phenomena occurring under different flow conditions.

Chapter 4 is dedicated to the entrainment results obtained in horizontal flow. Published data on entrainment and the new data are tested against several existing correlations.

Chapter 5 presents new drop size data for horizontal two-phase flow and discusses the influence of the gas and liquid flow rates on the drop size. The results are compared against existing drop size correlations. The influence of a 90° horizontal bend on the drop size distribution is discussed.

Chapter 6 deals with drop velocity information. Data were obtained from an analysis of the cine films of the flow before the bend.

Chapter 7, as mentioned before, reports the film flow rate and drop size measurements for vertical annular flow in a 0.01026 m ID tube.

Chapter 8 presents the major conclusions that can be taken from the horizontal and vertical flow studies, and points out future areas of interest.

2. EXPERIMENTAL DETAILS AND TECHNIQUES

This chapter describes the experimental equipment and measurement techniques used during the course of the investigations. Section 2.1 is devoted to the newly constructed Horizontal Two-Phase Flow Rig and measuring techniques applied in the horizontal two-phase flow experiments. Section 2.2 describes the Vertical Upflow Rig and experimental techniques associated with it.

2.1. Horizontal Two-Phase Flow Rig

2.1.1. Flow Apparatus

The experiments in horizontal two-phase flow were carried out with air-water in the Horizontal Two-Phase Flow Rig. This is shown schematically in Figure 2.1, and photographic views are displayed in Figures 2.2, 2.3, 2.4 and 2.5.

Filtered air from the main air supply flows through the feedback pressure regulator PRV1, and is fed to a 0.032 m ID horizontal Perspex tube (at a later stage, all the Perspex tube upstream of the bend was substituted by 0.032 m ID PVC ABS, apart from a section 1.5 m long just before the bend). The valve assembly PRV1 and valve V9 enable the operator to control the air flow introduced into the system. The air flow rate was measured using an orifice plate fitted into a 0.0383 m ID tube, that connects the pressure regulator PRV1 to the entrance of the test tube. The gas mass flow rate is related to the loss in pressure across the orifice, as given by a manometer connected to the pipe by d_t and $d_{t/2}$ tappings, according to the recommendations in BS 1042: Part 1: 1964. For gas flow rates up to 50 kg/m^{2}s the orifice meter used had a diameter of 0.0196 m. For higher gas flows (G_G= 60 kg/m^{2}s and G_G= 70 kg/m^{2}s) it was substituted by another orifice of 0.0254 m diameter.

Demineralised water from the stock tank was metered using one bank of three rotameters. This was fed into the test tube through a porous sintered metal section 0.076 m long, placed 1 m after the entry point of the air. This type of inlet allows a smooth entrance for liquid, minimising the effect of a sudden contact between the phases. The three rotameters were previously calibrated (calibration curves are given in Appendix A) and each one covers a set range of flow conditions: 0–0.038 kg/s, 0–0.091 kg/s and 0–0.18 kg/s, respectively.

A 90° horizontal bend is placed 5.3 m after the water inlet (at ~ 166 d_t) to allow development of the flow regime. Butterworth and Pulling (1973) using a horizontal tube 0.0318 m in diameter, reported that at approximately 120 diameters from the air-water mixing point, measurements indicated fully developed flow.

A photograph of the bend is shown in Figure 2.6. The bend was made by cementing together two blocks of Perspex. The diameter and radius of curvature of the bend were 0.032 m and

THIRD ANGLE PROJECTION

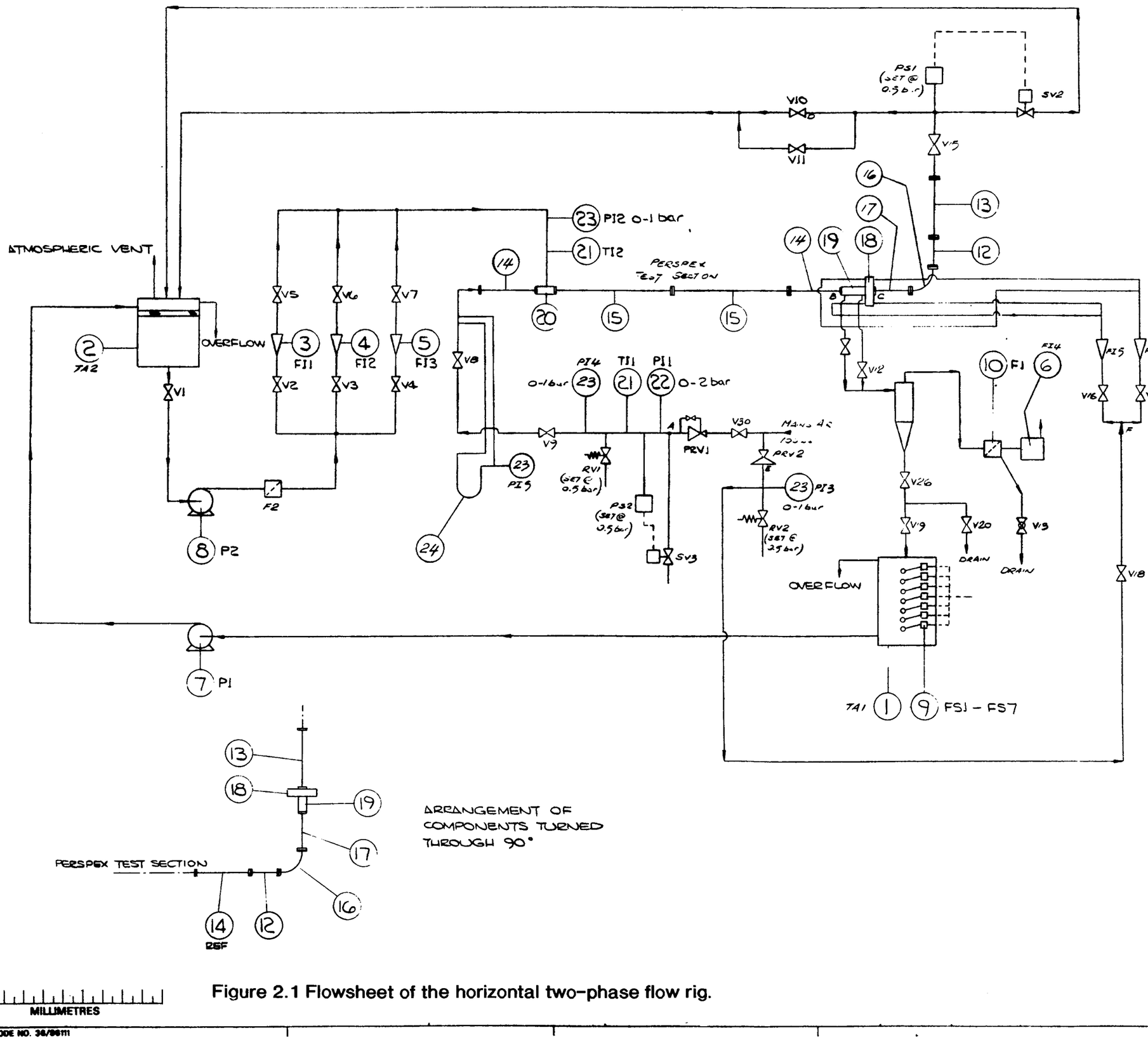

ARRANGEMENT OF COMPONENTS TURNED THROUGH 90°

ITEM NO.	DRG. NO. OR CODE NO.	DESCRIPTION	NO OFF ASSEMBLY a	b	c
1	TA1	TANK, 750 ℓ, POLYPROPYLENE, FORBES	1		
2	TA2	TANK, 1400 ℓ, POLYPROPYLENE, FORBES	1		
3	FI1	ROTAMETER, SERIES 2000, SIZE 10S	1		
4	FI2	ROTAMETER, SERIES 2000, SIZE 14S	1		
5	FI3	ROTAMETER, SERIES 2000, SIZE 18S	1		
6	FI4	GAS METER	1		
7	P1	PUMP - CEKM 370/1 - LOWARA	1		
8	P2	PUMP - 2850 - STUART TURNER	1		
9	FS1-FS7	FLOAT SWITCH	7		
10	FI	FILTER	1		
11	ENGL 00660	CYCLONE	1		
12	"	PIPE SECTION, 340 LG	1		
13	"	PIPE SECTION, 650 LG	1		
14	"	PIPE SECTION, 1000 LG	2		
15	"	PIPE SECTION, 2000 LG	2		
16	GROUP SUPPLY	BEND	1		
17	"	TRANSITION PIECE	1		
18	"	VIEWER	1		
19	ENGL 00660	SINTER	1		
20	ENGL 00706	SINTER	1		
21	TI1 & TI2	THERMOCOUPLE	2		
22	PI1	PRESSURE GAUGE 0-2 bar	1		
23	PI 2 to 5	PRESSURE GAUGE 0-1 bar	4		
24		PODDYMETER	1		
25					
26	PRV1	FEED BACK PILOT OPERATED REGULATOR NORGREN, 11.204.004/11.906.980	1		
27	SV2	SOLENOID VALVE - EVENVALVE	1		
28	SV3	" " — "	1		
29	PS1	PRESSURE SWITCH - BAILEY & MACLEY	1		
30	PS2	" " — "	1		
31	F2	FILTER	1		
32					
33	PRV 2	REDUCING VALVE - R13-400-RNAD - NORGREN	1		
34	RV1	RELIEF VALVE - 3/8" BSP MALE/FEMALE TAPPED - SPIRAX SARCO	1		
35	RV2	RELIEF VALVE - B-4CA-3 - NUPRO	1		
36	FI5 & FI6	GAP METER - GP-50215100 - PLATON	2		
37					
38					
39					
40					

MILLIMETRES

Figure 2.1 Flowsheet of the horizontal two-phase flow rig.

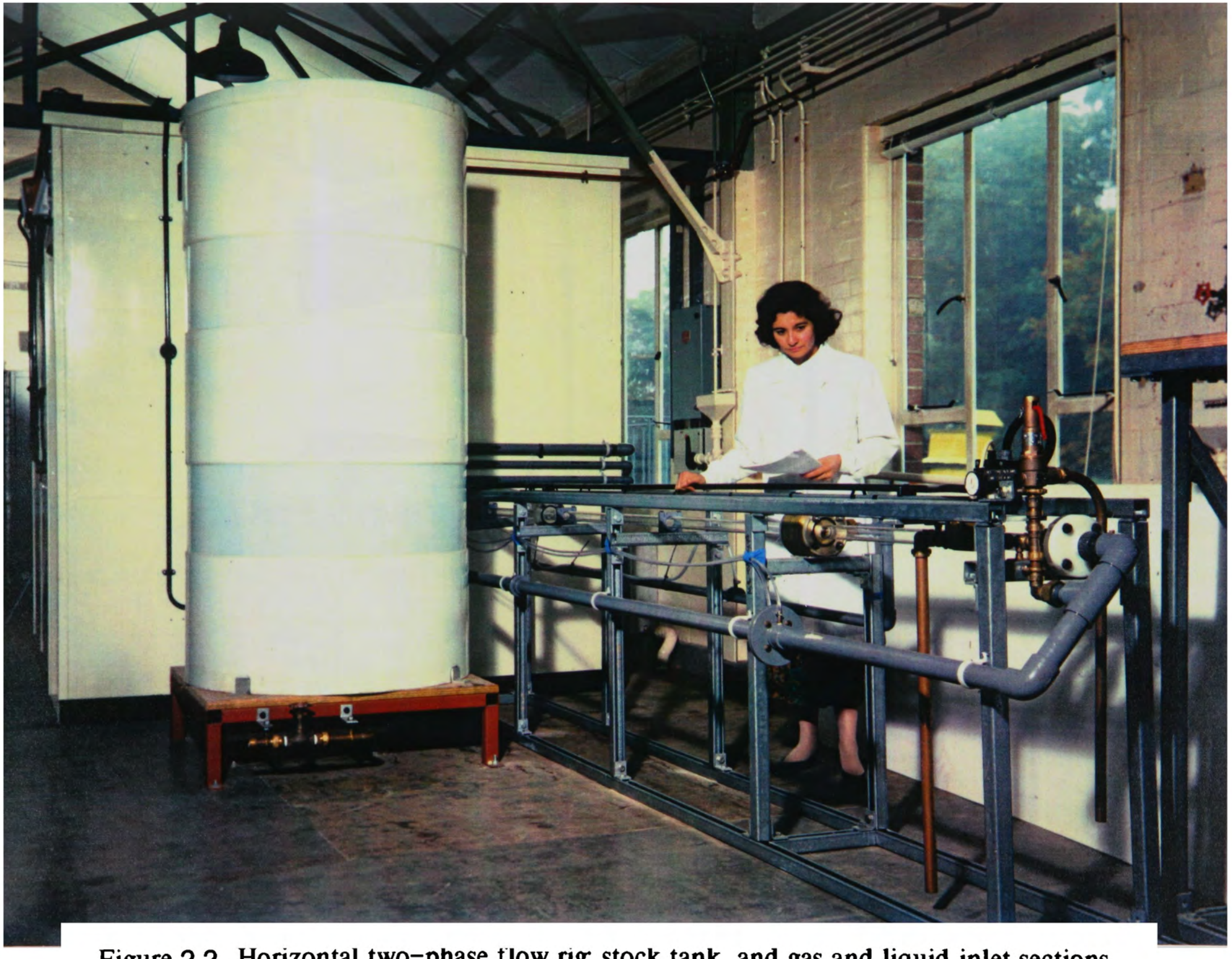

Figure 2.2 Horizontal two-phase flow rig: stock tank, and gas and liquid inlet sections

Figue 2.3 Close view to the instrumentation

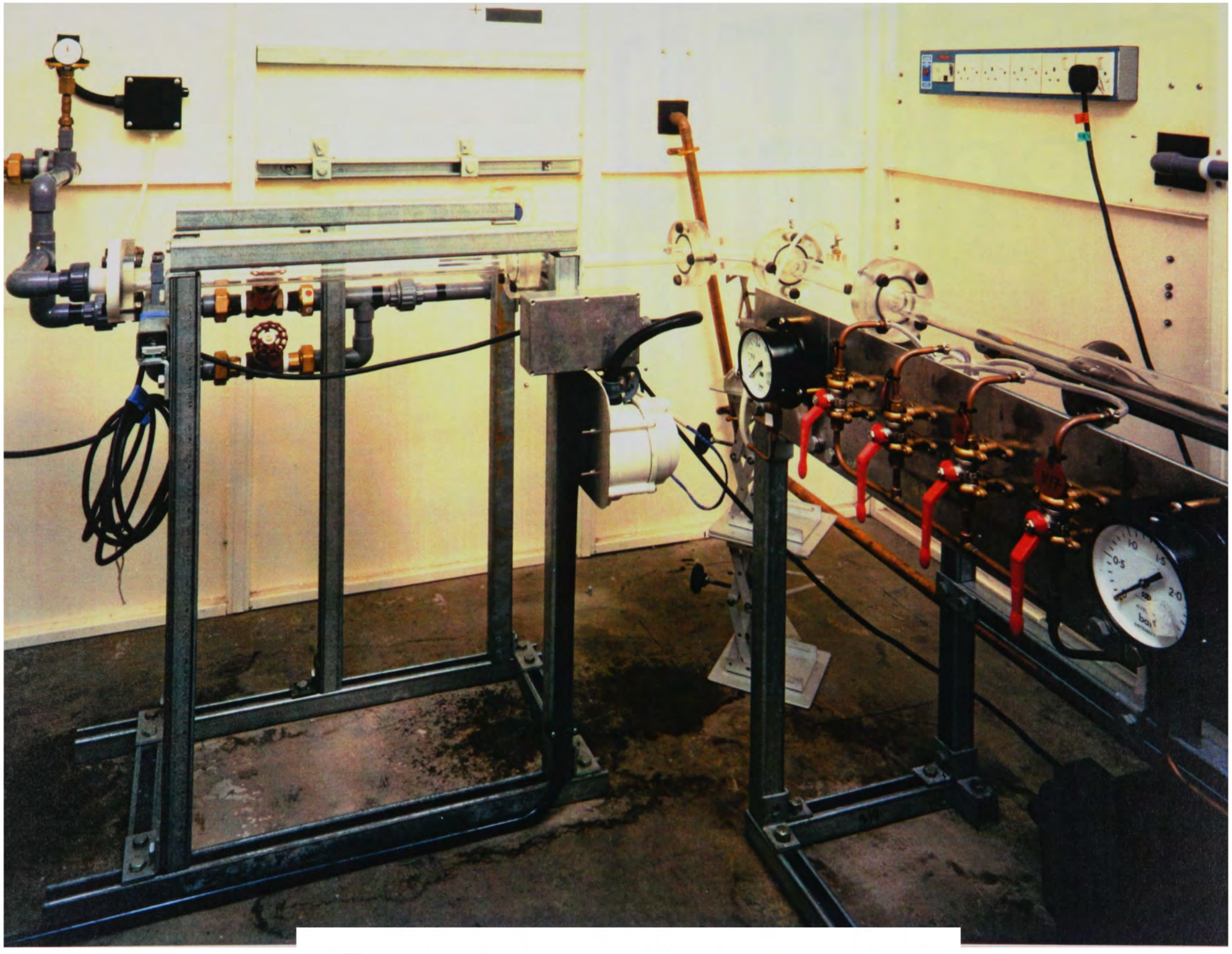

Figure 2.4 Inside the cubicle: test tube and bend

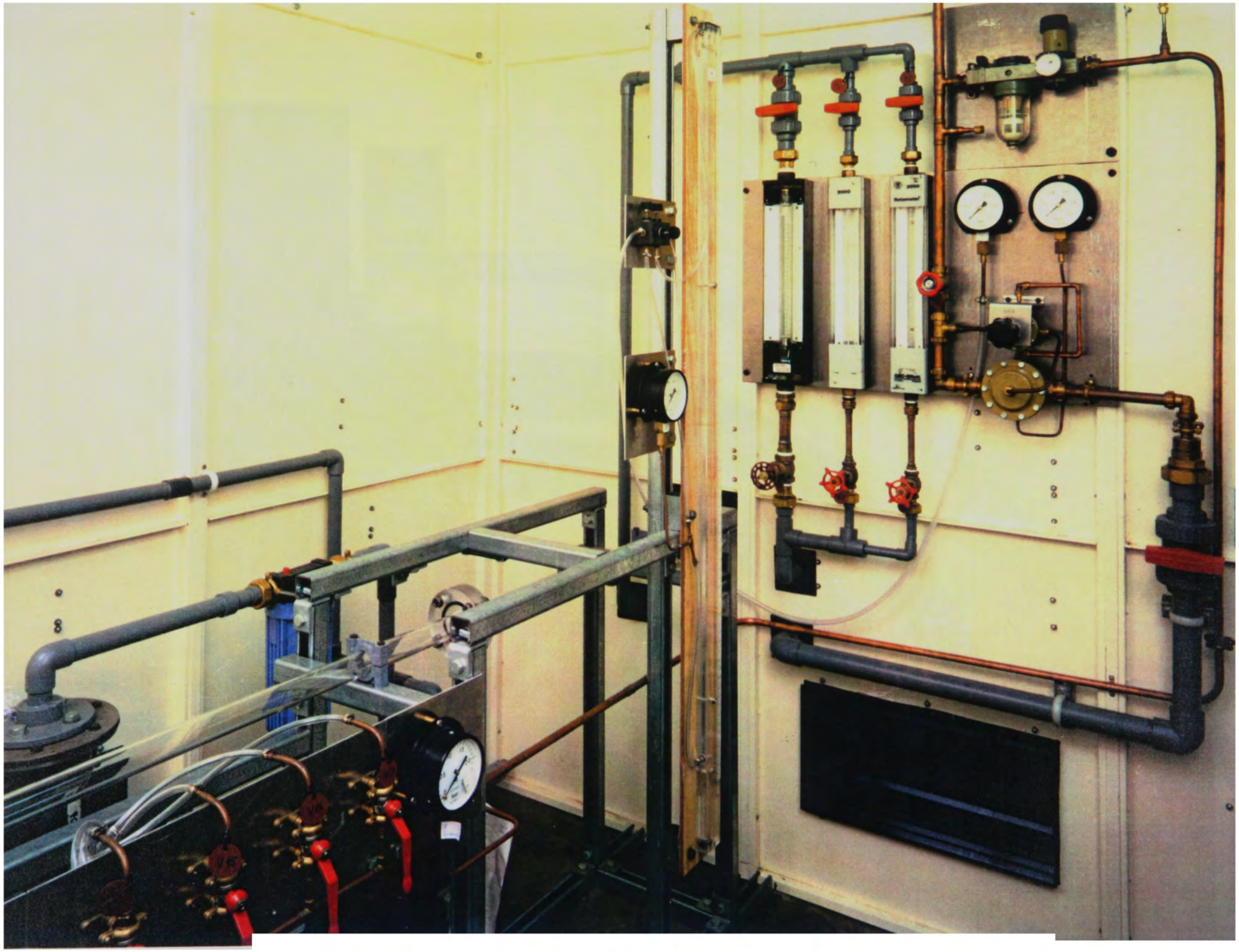

Figure 2.5 Inside the cubicle: gas and liquid flow controls

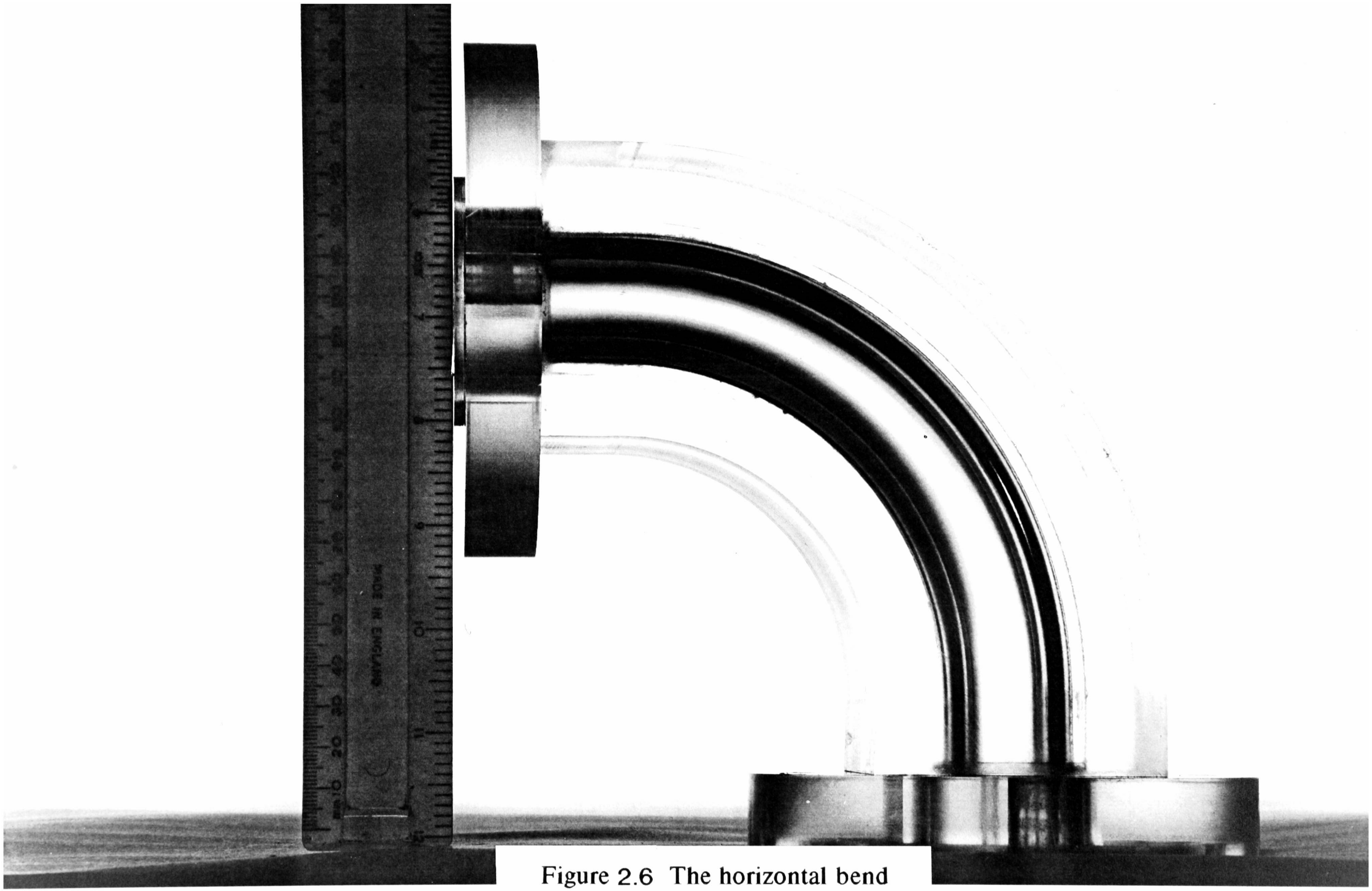

Figure 2.6 The horizontal bend

0.116 m, respectively. Special attention was paid to levelling both the tube and the bend in a horizontal plane, since Taitel and Dukler (1976) reported that the flow regime transition depends on tube inclination.

After the bend, the air–water mixture was returned to the stock tank, where the air was vented to the atmosphere and the water is recirculated.

A set of three thermocouples was used to monitor the temperature of the fluids through the system. The inlet air temperature was measured by a thermocouple inserted downstream of the orifice plate, while another one monitors the temperature of the water just before entering the porous section. Finally, a third was installed at approximately 0.9 m after the bend. The thermocouples were linked to the channels of a digital multimeter and the temperatures were continuously displayed on a monitor. A pressure tapping located 0.27 m upstream of the bend was used to regulate the pressure of the system.

2.1.2. Pressure Drop Measurements Upstream of the Bend

Sekoguchi et al (1968) studied the developing flow phenomena of a two-phase flow mixture near a horizontal bend. The authors found that the pressure distribution around the bend presented an erratic behaviour not only in its downstream position, but also in the region just upstream of the bend.

Taking into account the results of Sekoguchi et al (1968), it was decided to investigate the possible back influence of the bend in the present rig. Also, it was intended to identify the position in the horizontal tube before the bend, where future measurements could be made away from any influence of the bend. For this purpose, a series of pressure drop measurements for single phase (air) and two-phase (air–water) was planned, and a new test section was constructed.

It was made of a 0.032 m Perspex tube and was 1.003 m long, and pressure tappings were drilled every 0.05 m. Due to the large number of tappings it was decided to make measurements only between tappings spaced by at least 0.1 m. The test tube was connected by flanges, and put immediately before the bend with the pressure tappings located at 45° from the top of the tube to the outside of the bend. Due to the mismatch of the bolt holes on the flanges it was not possible to put the tappings at the top of the tube.

The pressure drop between consecutive tappings was measured by means of an inclined manometer model MK4 manufactured by Airflow Developments. In two-phase flow measurements for a gas mass flux of G_G = 40 kg/m^{2}s, pieces of capillary tube approximately 0.12 m long had to be inserted in the pressure leads, to help eliminate the undesirable fluctuations of the liquid levels in the manometer. The presence of capillaries introduced damping into the system, but on the other hand the stabilisation time was greatly increased.

For a gas mass flux of G_G = 10 kg/m^{2}s and a liquid flow of G_L = 70 kg/m^{2}s, the flow regime was stratified with large waves appearing at a certain frequency. Their passage introduced

large fluctuations in the manometer level, that even with the arrangement described above, could not be eliminated. The length of capillary tube in the pressure leads was doubled, but there were still fluctuations that could introduce errors of approximately 30% in the manometer readings. Given the circumstances, it was decided to make no measurements for this set of flow rates.

To investigate a possible circumferential variation of the pressure, another set of measurements was taken with the tappings located at 45° from the top of the tube to the inside of the bend, using the same flow conditions. Finally, the test tube was moved 0.3 m upstream of the bend, by inserting a piece of flanged tube between the bend and the test tube, and again another set of pressure drop measurements was taken.

Pressure drop measurements along the test tube for gas flowing alone in the pipe are tabulated in Tables B1 to B3 (Appendix B), and shown in Figures 2.7(a), (b) and (c), for different circumferential positions of the tappings and location of the test tube in relation to the bend. A close analysis of the graphs indicates that the pressure drop profiles along the tube display similar trends. This means that there is no circumferential variation of the pressure before the bend. Also, as the profile is maintained when the test tube is moved away from the bend, there is no significant influence of the bend upstream of its position for gas flowing alone in the tube.

Analysis of Figures 2.7(a), (b) and (c) confirmed as expected, that pressure drop increases with gas velocity. For air mass fluxes of 10 kg/m^{2}s and 20 kg/m^{2}s the pressure drop is almost constant along the tube, but for G_G = 30 kg/m^{2}s a slight increase in the pressure gradient is noticed between tappings 11–13, and at tappings 3–5 there is a decrease, followed by another increase in pressure drop between tappings 1–3. These abnormal differences in pressure drop were even more pronounced at higher gas mass fluxes (G_G = 40 kg/m^{2}s and G_G = 50 kg/m^{2}s). They can only be attributed to local defects at the tapping points, i.e., the presence of burrs upstream or downstream of the tapping point.

If a burr occurs upstream of the tapping, a stagnation zone is formed and so the fluid has to accelerate locally, in order to compensate the streamline change in direction. Consequently, the static pressure decreases at this point, and causes the pressure drop between the tappings to decrease abnormally. On the other hand, if the burr is downstream of the tapping, the fluid is affected by impaction against the burr, the velocity decreases locally and the static pressure increases.

Pressure drop measurements in two–phase flow along the test tube are given in Tables B4 to B6, and illustrated in Figures 2.8(a), (b) and (c) for G_G = 40 kg/m^{2}s. As in single phase flow, the pressure drop profiles obtained show a similar shape when the test tube was located near the bend for two different circumferential positions of the tappings, and when the test tube was 0.3 m away from the bend. Also, the abnormal pressure drop occurring between certain tappings can be attributed to local defects at these tappings as explained before. For a constant

(a)

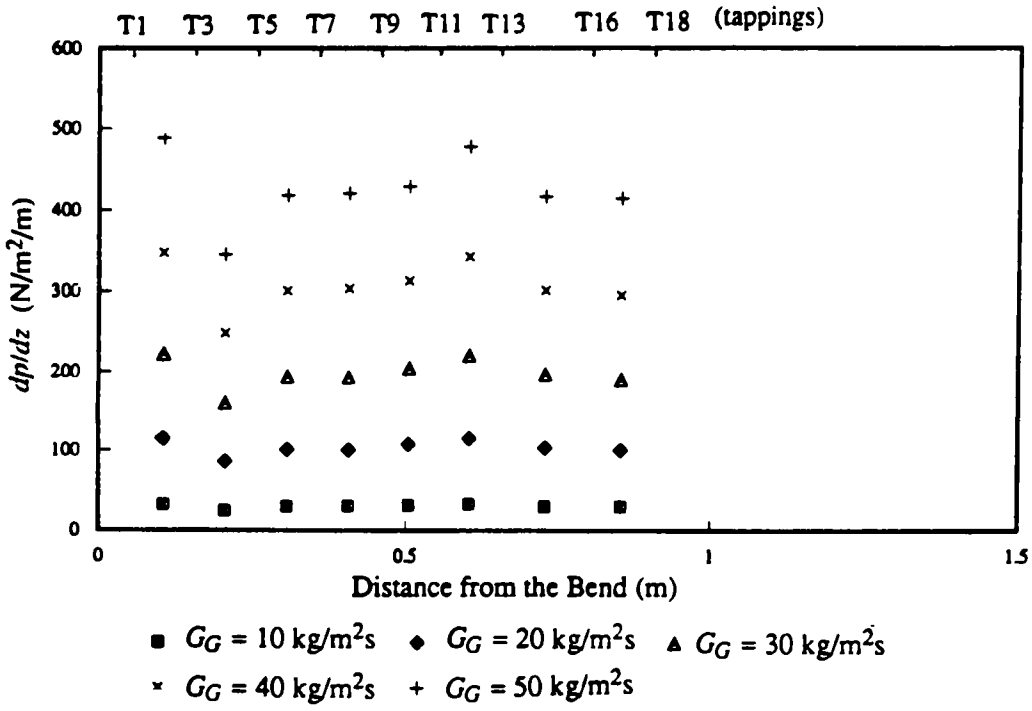

(b)

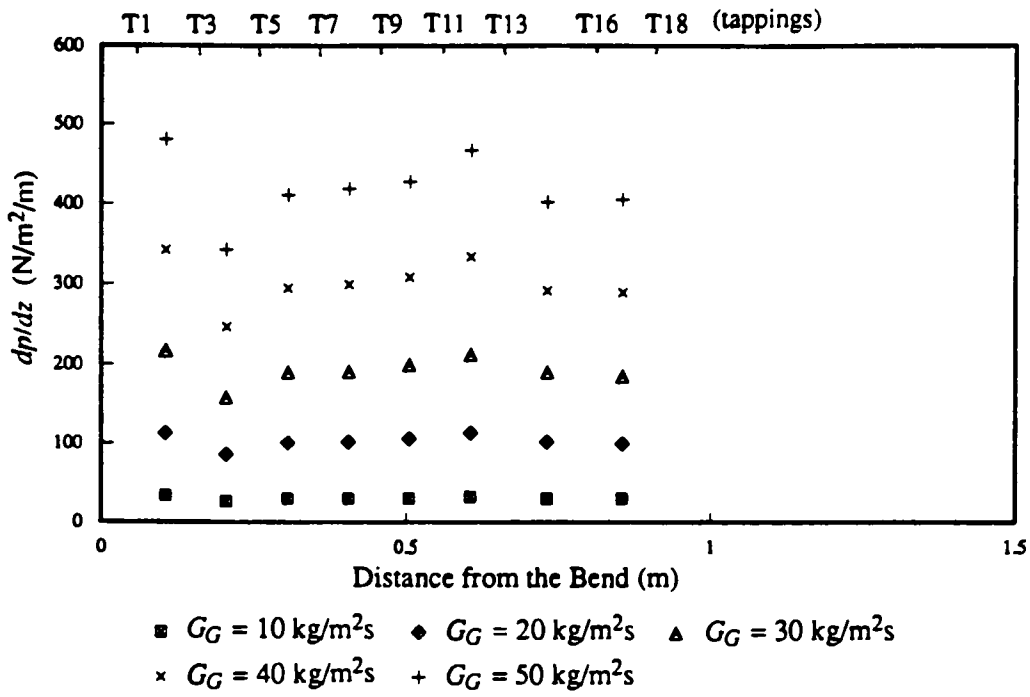

(c)

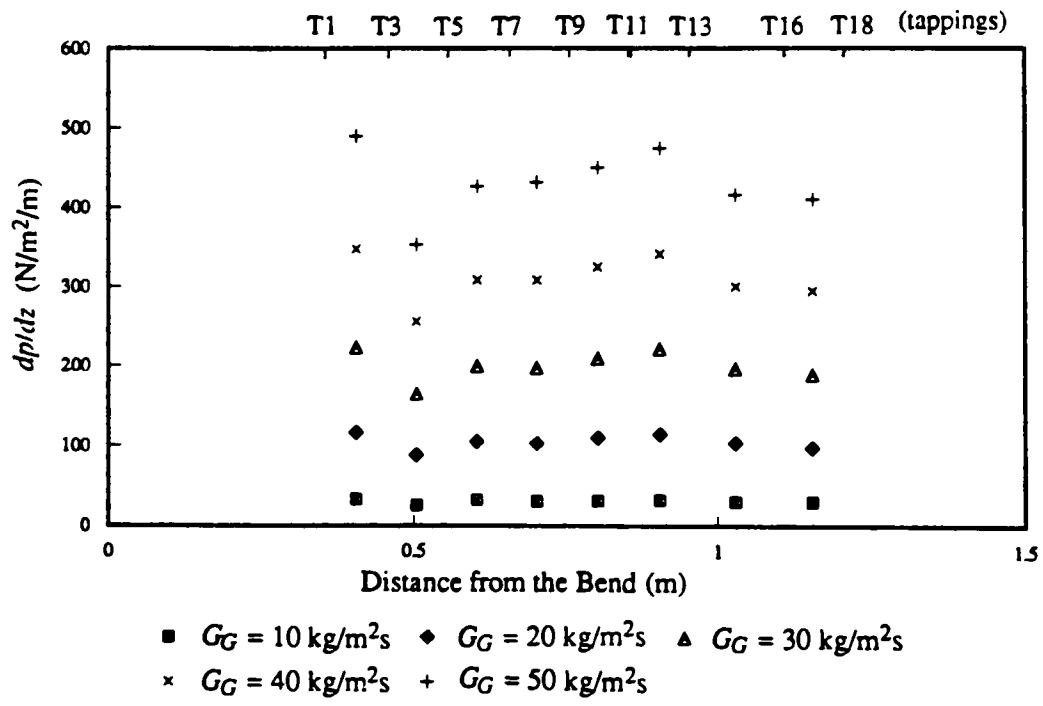

Figure 2.7 Pressure drop profile along the test tube for single phase flow: (a) test tube near the bend and tappings located 45° from the top of the tube to the outside of the bend, (b) test tube near the bend and tappings located at 45° from the top of the tube to the inside of the bend, (c) test tube located at 0.3 m upstream of the bend.

(a)

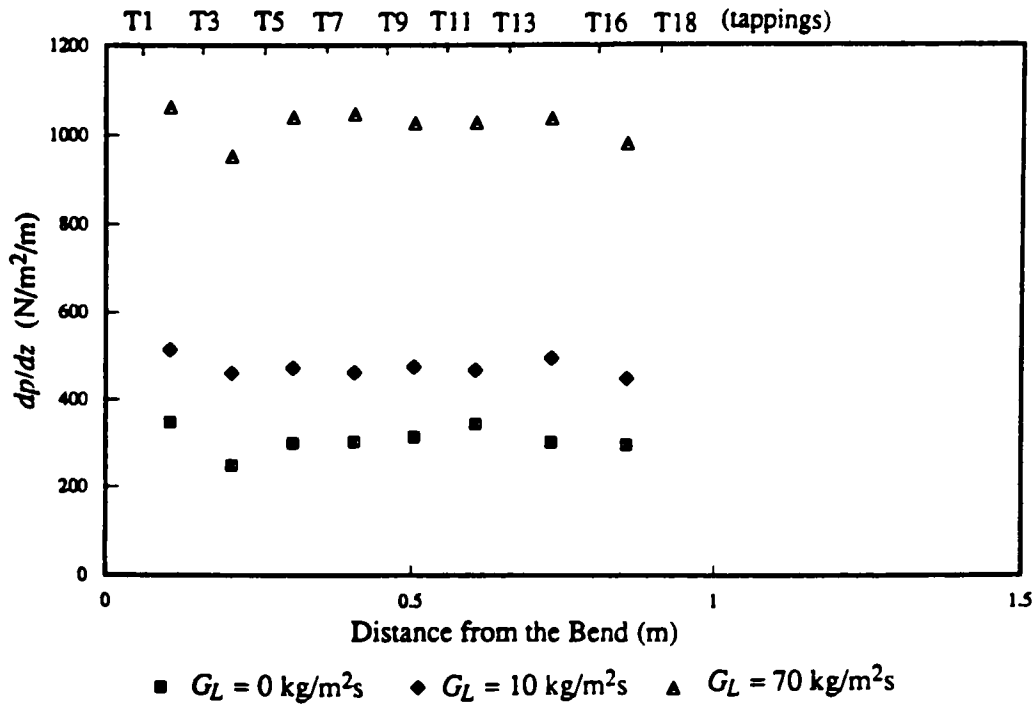

(b)

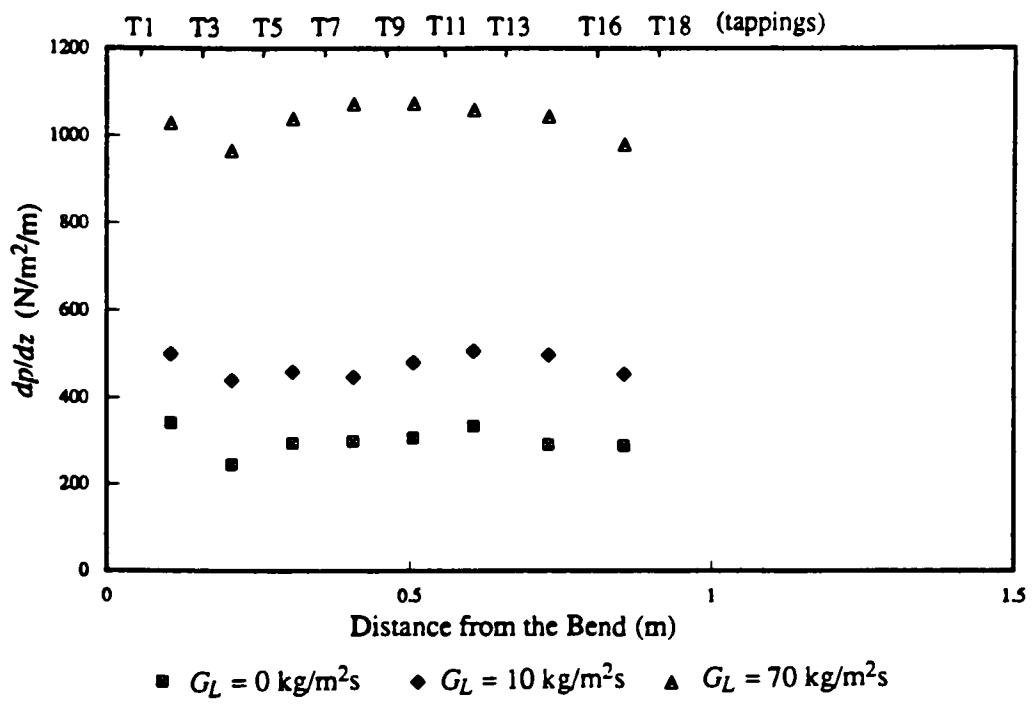

(c)

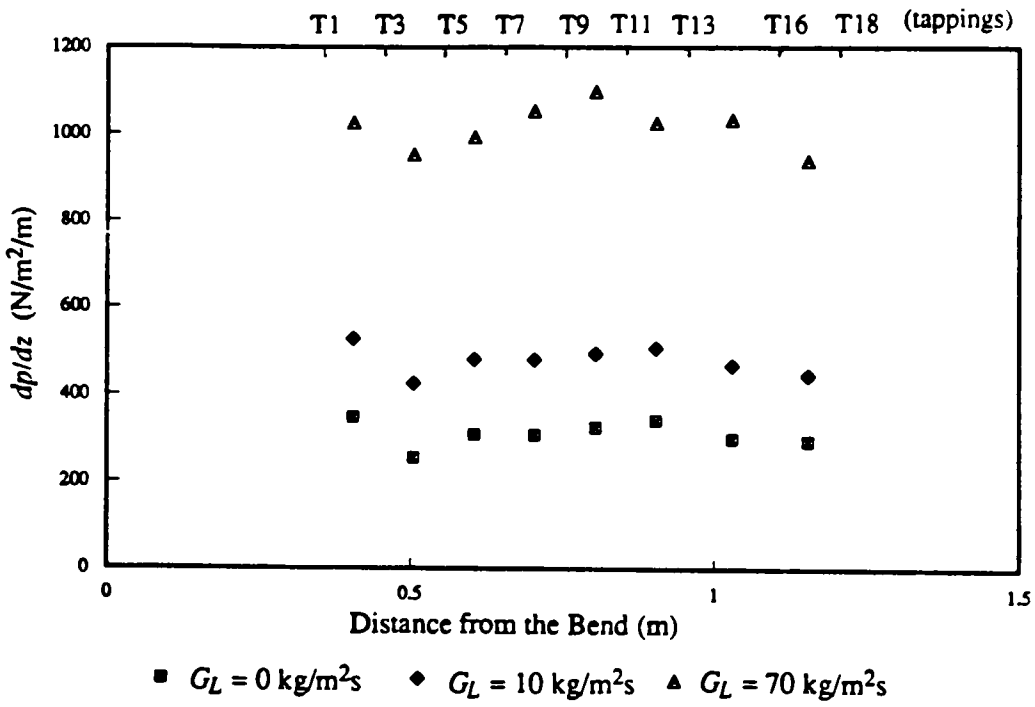

Figure 2.8 Pressure drop profile along the test tube for two–phase flow, at a constant G_G = 40 kg/m²s: (a) test tube near the bend and tappings located 45° from the top of the tube to the outside of the bend, (b) test tube near the bend and tappings located at 45° from the top of the tube to the inside of the bend, (c) test tube located at 0.3 m upstream of the bend.

gas flow of G_G= 40 kg/m^{2}s, pressure drop increases with increasing liquid flow rate. This is expected because the liquid film acts as a roughened wall to the gas flow.

In spite of the studies of Sekoguchi et al (1968), the pressure drop experiments carried out for single and two-phase flow suggest no influence of the bend in its upstream position for the present studies.

2.1.3. Flow Visualisation Experiments

The observation of the various phenomena occurring in two-phase flow can be made by visual inspection through a transparent window. However, when the processes are occurring at high speed the observer does not have a clear picture of what is happening. The use of high speed photography and high speed cine film techniques allows this problem to be overcome.

2.1.3.1. Observation Using a Stroboscope

A stroboscopic light was placed on one side facing the Perspex test tube, and observations of the flow were made looking into the tube from the opposite side. The timing of the stroboscopic light was adjusted for optimum visual clarity of the flow.

2.1.3.2. High Speed Still Photography

High speed still photography was used to observe the flow characteristics of an air-water flow travelling in the horizontal straight pipe, and around the horizontal 90° bend. This technique involves the use of a light pulse of sufficient intensity and short duration to produce a sharp image of the flowing system. Mercury vapour lamps, flash lights, electrical sparks and laser pulses are commonly used.

In the present work, a still camera was used to photograph the two-phase flow before and after the bend, and at four different locations around the bend. For illumination, a flash source was placed opposite the camera. The flash operated at 5 kV which gave a spark duration of about 1 microsecond, with an energy of 5 joule. The shutter of the camera was synchronised with the flash. Photographs were recorded on FP4 film, with an aperture of f.16 and 100 mm Macro lens.

Further photographic work was carried out to photograph the drop flow downstream of the horizontal bend, after removal of the liquid film through a porous wall. The still camera was positioned perpendicular to the flow direction, opposite the flash source. The flash unit used had an input energy of 5 joules with a flash duration of 5 microseconds. The photographs were recorded on Ilford F32 film with an aperture of f/22. The camera was equipped with a 1000 mm Macro lens with extension tubes.

2.1.3.3. High Speed Cine Film

Cine films of the two-phase flow were taken in the horizontal straight pipe upstream of the horizontal bend. Apart from further qualitative information on the flow characteristics, the objective of these experiments was to extract quantitative information on drop size and drop motion. These experiments were restricted to flow conditions where the concentration of entrained drops was low.

The schematic arrangement of the optical equipment is shown in Figure 2.9. The high speed cine camera was positioned facing the Perspex tube. The strobe light head of a Hadland high speed stroboscope was placed opposite the camera. The cine camera was equipped with a 75 mm focal length lens with an aperture of f/5.6. The action of opening the shutter on the camera sent a pulse to the strobe unit, so that the strobe light head was activated.

The pictures were recorded on Ilford HP5 16 mm cine film, at a framing rate of 2000 full frames per second. The films were analysed on a frame by frame basis using a Vanguard cine film analyser.

2.1.4. Liquid Film Flow Measurements

The film flow rate was measured using the film removal technique. This involves extracting the film completely together with a small amount of gas, separating the phases, and measuring the rate of liquid collection.

The test section for liquid film extraction consisted initially of a porous sintered brass section 0.076 m long, having the same internal diameter as the test tube (0.032 m). However, visual observations indicated that for high liquid loadings the thick film at the bottom of the tube was difficult to remove. In order to improve the efficiency of the film removal, another unit was added immediately upstream of the porous metal section. This unit consisted of a perforated plastic tube 0.032 m ID and 0.076 m long. The perforations were drilled in the 160° lower of the tube, symmetrically about the centreline. For high liquid loadings, a visual study and the measurements have shown that the liquid film extraction was improved by adding the extra perforated plastic tube. This unit was only used when the liquid film could not be extracted fully by the metal sintered section alone.

The pressure drop across the porous wall was used to withdraw the liquid film together with a small amount of gas. By adjusting the throttling valves (valves V12 and V14) the amount of gas removed could be varied. The experiment was started with a small aperture in the valve. At this stage, the pressure gradient across the porous wall was not enough to completely decelerate the roll waves over its length, and not all the liquid was removed. As the gas extraction rate was increased, the amount of liquid film removed increased rapidly at first and then reached a plateau. Further opening of the valve resulted in an increase in the gas take-off for a constant liquid withdrawal.

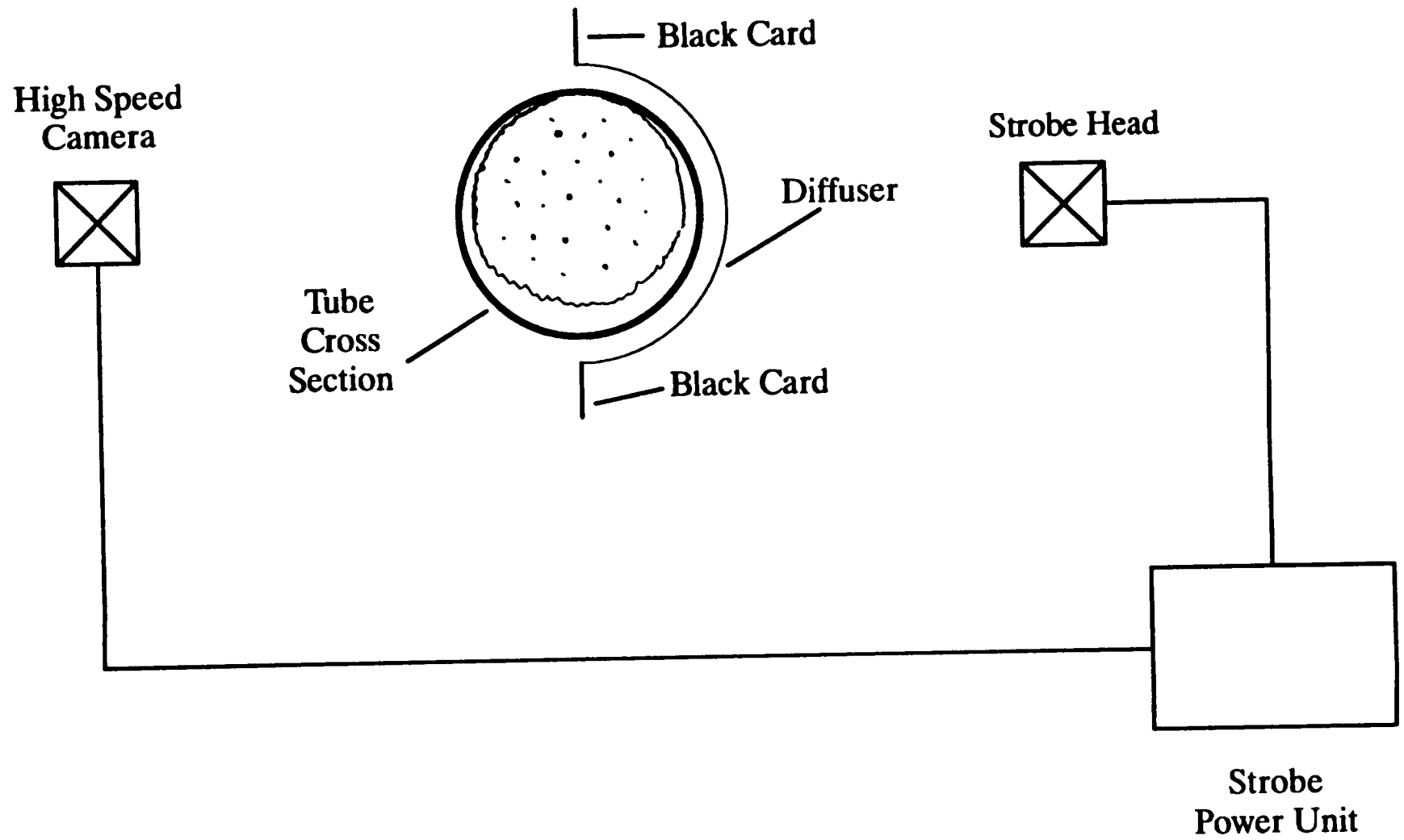

Figure 2.9 Schematic arrangement of the optical system for the high speed cine films.

The liquid film was estimated from the plateau level. Figures 2.10(a), (b) and (c) show typical performance curves obtained using the procedure described above. In all runs, the amount of gas withdrawn with the liquid was kept below 6% of the total gas flow.

Several authors have discussed various methods of film collection. Moeck (1969) concluded that a permeable wall section (notably a porous sintered section) could be used to extract the entire layer travelling on the pipe wall and characterize the average liquid film. Hewitt and Lovegrove (1976) reported that the best method to measure liquid film flow rate would be a porous wall suction rather than a slot technique, although they mentioned that some limitations could occur, particularly at high liquid flow rates.

Experimentally this porous wall technique has been widely used: Brown (1978), Azzopardi et al (1980), Willets (1987) and Jepson (1992) in vertical flow, and Dallman (1978) and Laurinat (1982) in horizontal flow.

2.1.5. Drop Size Measurements

Drop size measurements were performed using a laser diffraction technique developed by Swithenbank et al (1976), and produced commercially by Malvern Instruments Limited. This method was first applied to drop sizing in annular vertical upflow by Azzopardi et al (1978).

2.1.5.1. Light Diffraction

Laser light scattering is a very flexible sizing technique which enables measurements of the size distribution of one material dispersed in another, provided that the refractive indices of the dispersed and continuous phases are different, and the continuous phase is transparent to the light wavelength.

When a laser beam strikes a particle, part of the light is diffracted into small forward angles. If the diffracted light is collected by a detector formed by a series of concentric annular rings, the energy falling at one ring bounded by radii s_1 and s_2 is given by (Swithenbank et al (1976)):

$$L_{s_1 s_2} = E'\left[\left(J_0^2\left(\frac{2\pi\ r_p\ s_1}{\lambda'\ f}\right) - J_1^2\left(\frac{2\pi\ r_p\ s_1}{\lambda'\ f}\right)\right) - \left(J_0^2\left(\frac{2\pi\ r_p\ s_2}{\lambda'\ f}\right) - J_1^2\left(\frac{2\pi\ r_p\ s_2}{\lambda'\ f}\right)\right)\right] \qquad (2.1)$$

where E' is the energy falling on the particle, J_1 and J_0 are Bessel functions of the first kind of order 1 and 0 respectively, r_p is the particle radius, λ' is the wavelength of the incident beam, and f is the focal length of the collecting lens.

If several particles of different size are present simultaneously the diffracted energies are summed up for each of the detector rings, and these can be represented in matrix form by:

(a)

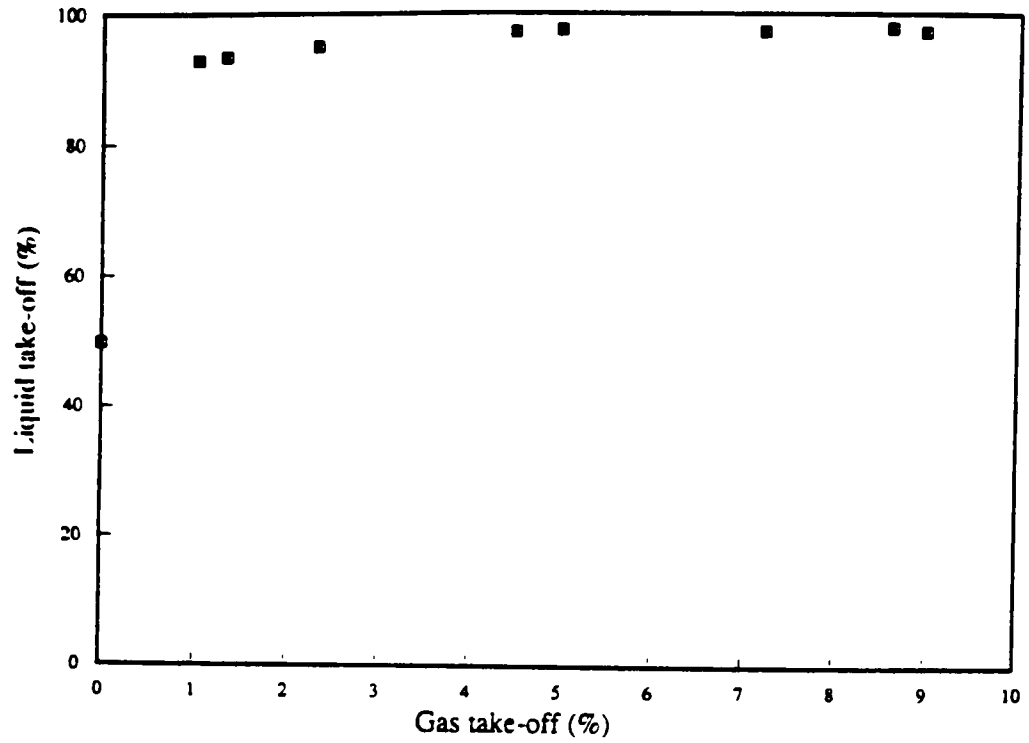

(b)

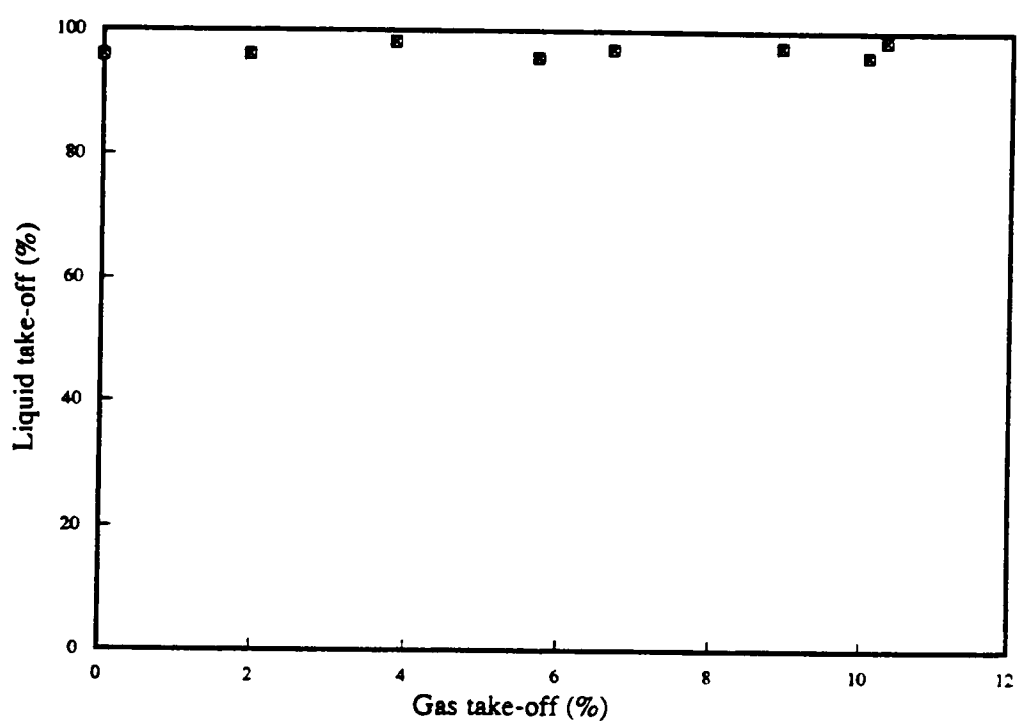

(c)

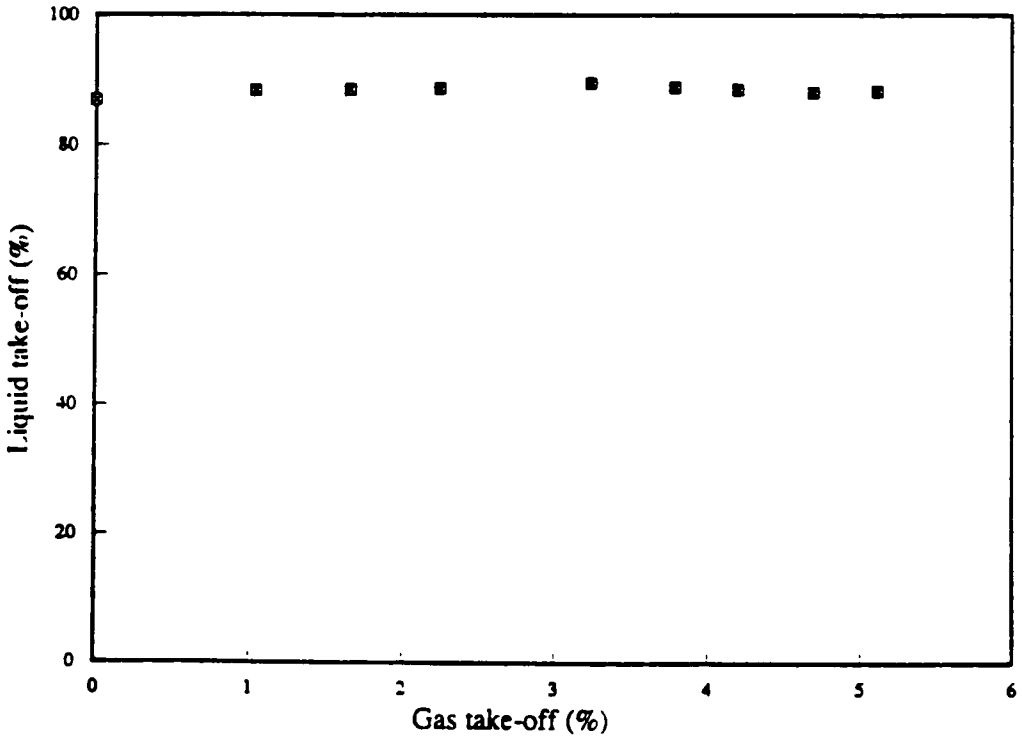

Figure 2.10 Film flow rate measurement sinter technique for various flow conditions: (a) $G_G = 20\ kg/m^2s$ and $G_L = 30\ kg/m^2s$, (b) $G_G = 20\ kg/m^2s$ and $G_L = 110\ kg/m^2s$, (c) $G_G = 40\ kg/m^2s$ and $G_L = 70\ kg/m^2s$.

$$L(I) = T'(I,J) \ . \ W(J) \tag{2.2}$$

where $T'(I,J)$ is the matrix of coefficients which define the light energy distribution curves for each particle, and $W(J)$ is the size distribution. To solve equation (2.2) in relation to the size distribution $W(J)$ it is necessary to invert the matrix $T'(I,J)$. However, in the case of the light scattering matrix this is very difficult to do, and another approach is taken.

To start the analysis, a size distribution is estimated based on the measured light energy data ($L(I)_{mea}$), and a new light energy distribution is calculated ($L(I)_{cal}$) using equation (2.2). The residual difference is calculated as:

$$\log_{10} \left(\sum \ (\ L(I)_{mea} - L(I)_{cal} \ ) \right) \tag{2.3}$$

The difference between $L(I)_{mea}$ and $L(I)_{cal}$ is used to correct the initial solution and a new set of light energy data is calculated. The iterative process is continued until the residual difference is minimised. This method is known as model independent analysis.

The Malvern Particle Sizer is also able to perform a two parameter model analysis, in which a distribution function is assumed for $W(J)$. The parameters are then iteratively adjusted until the residual difference (2.3) is minimised. Three types of distribution functions can be used: Rosin–Rammler, Normal and Log–Normal. These are discussed in the next section.

2.5.1.2. Drop Size Distribution Functions

In gas–liquid two–phase flow when drops are entrained into the gas, the size of these drops varies from a minimum (D_{min}) to a maximum diameter (D_{max}) depending on the flow conditions. The drop size distribution is usually characterised by a histogram, where the number or volume of drops whose diameters range between $D-\Delta D/2$ and $D+\Delta D/2$ are plotted against drop diameter.

If the ΔD is made sufficiently small, the histogram takes the form of a frequency distribution curve, provided that the sampled drops are characteristic of the population. In addition to representing the drop size by a probability distribution function, a cumulative distribution may be used. This type of curve shows the fraction of the total number/volume of drops present in the system below a given diameter. A number of mathematical functions have been proposed for representing size distributions based either on probability or empirical considerations. The Malvern software allows the user to fit the drop size results using three distribution functions. These are listed below.

- **Rosin–Rammler distribution.** This distribution was developed by Rosin and Rammler (1933). It is described by:

$$F_v = \exp - \left(\frac{D}{\overline{X}}\right)^{\overline{N}} \tag{2.4}$$

where F_v is the fraction of the total volume contained in drops of diameter less than D (volume undersize distribution) and $\overline{X}$ and $\overline{N}$ are constants. $\overline{X}$ is a representative diameter and $\overline{N}$ provides a measure of the spread of drop sizes.

- **Normal distribution.** It is based on the random occurrence of a given drop size. The volume frequency distribution is described by the equation:

$$f_v = \frac{1}{\overline{N}\sqrt{2\pi}} \exp - \left[\frac{(D - \overline{X})^2}{2\overline{N}^2}\right] \tag{2.5}$$

where $\overline{X}$ is the sample mean and $\overline{N}$ the standard deviation of the sampled drops.

- **Log-Normal distribution**. Some particle distributions follow a Log-Normal distribution. In this type of function the logarithm of the drop diameters is used as a variable. The volume frequency (f_v) is given by a modification of equation (2.5) as:

$$f_v = \frac{1}{\ln(\overline{N})\sqrt{2\pi}\ D} \exp - \left[\frac{[\ln(D) - \ln(\overline{X})]^2}{2(\ln(\overline{N}))^2}\right] \tag{2.6}$$

The $\overline{X}$ parameter measures the geometric mean of the distribution and $\overline{N}$ the geometric standard deviation.

In many instances it is more convenient to use average diameters rather than the complete drop size distribution. In general, the mean drop diameter ($\overline{D}_{mn}$) is defined as:

$$\overline{D}_{mn} = \left[\frac{\int_{D_{min}}^{D_{max}} D^m\ n(D)\ dD}{\int_{D_{min}}^{D_{max}} D^n\ n(D)\ dD}\right]^{\frac{1}{m-n}} \tag{2.7}$$

where the diameter of the sampled drops is supposed to vary from a minimum value (D_{mim}) to a maximum (D_{max}). An example is the Sauter mean diameter which occurs when $m = 3$ and $n = 2$ in equation (2. 7). $\overline{D}_{32}$ is a measure of the ratio of the total volume of drops in the system to the total surface area of the drops. The most important mean diameters and their fields of

application are listed in Table 2.1 taken from Mugele and Evans (1951)).

TABLE 2.1–MEAN DIAMETERS AND THEIR APPLICATIONS

m	*n*	Symbol	Name of mean diameter	Field of application
1	0	$\overline{D}_{10}$	Linear	Comparisons, evaporations
2	0	$\overline{D}_{20}$	Surface area	Surface area controlling, e.g., absorption
3	0	$\overline{D}_{30}$	Volume	Volume controlling, e.g., hydrology
2	1	$\overline{D}_{21}$	Surface diameter	Adsorption
3	1	$\overline{D}_{31}$	Volume diameter	Evaporation, molecular diffusion
3	2	$\overline{D}_{32}$	Sauter	Efficiency studies, mass transfer, reaction
4	3	$\overline{D}_{43}$	De Brouckere	Combustion equilibrium

By constructing cumulative volume distributions it is possible to calculate volume median diameters. Various possibilities include, for example:

- $\overline{D}_{v0.1}$ is the drop diameter such that 10% of total liquid volume is in drops of smaller diameter.
- $\overline{D}_{v0.5}$ is the drop diameter such that 50% of total liquid volume is in drops of smaller diameter.

2.1.5.3. The Malvern 2600 Particle Sizer

The Malvern 2600 Particle Sizer used in the present work is shown schematically in Figure 2.11. It comprises a 2 mw He/Ne laser beam which is used to illuminate the drop sample. The drops scatter some of the incident light at angles which are characteristic of their size, forming a series of diffraction patterns, each consisting of concentric bright and dark fringes.

A Fourier optical system is placed after the sample, and is used to focus the diffracted and undiffracted light onto a detector. The detector is formed by a set of 31 semicircular photosensitive elements, each of which is associated with a characteristic drop size range. The detector is scanned for a pre-selected number of times, and the signals are processed by a microcomputor.

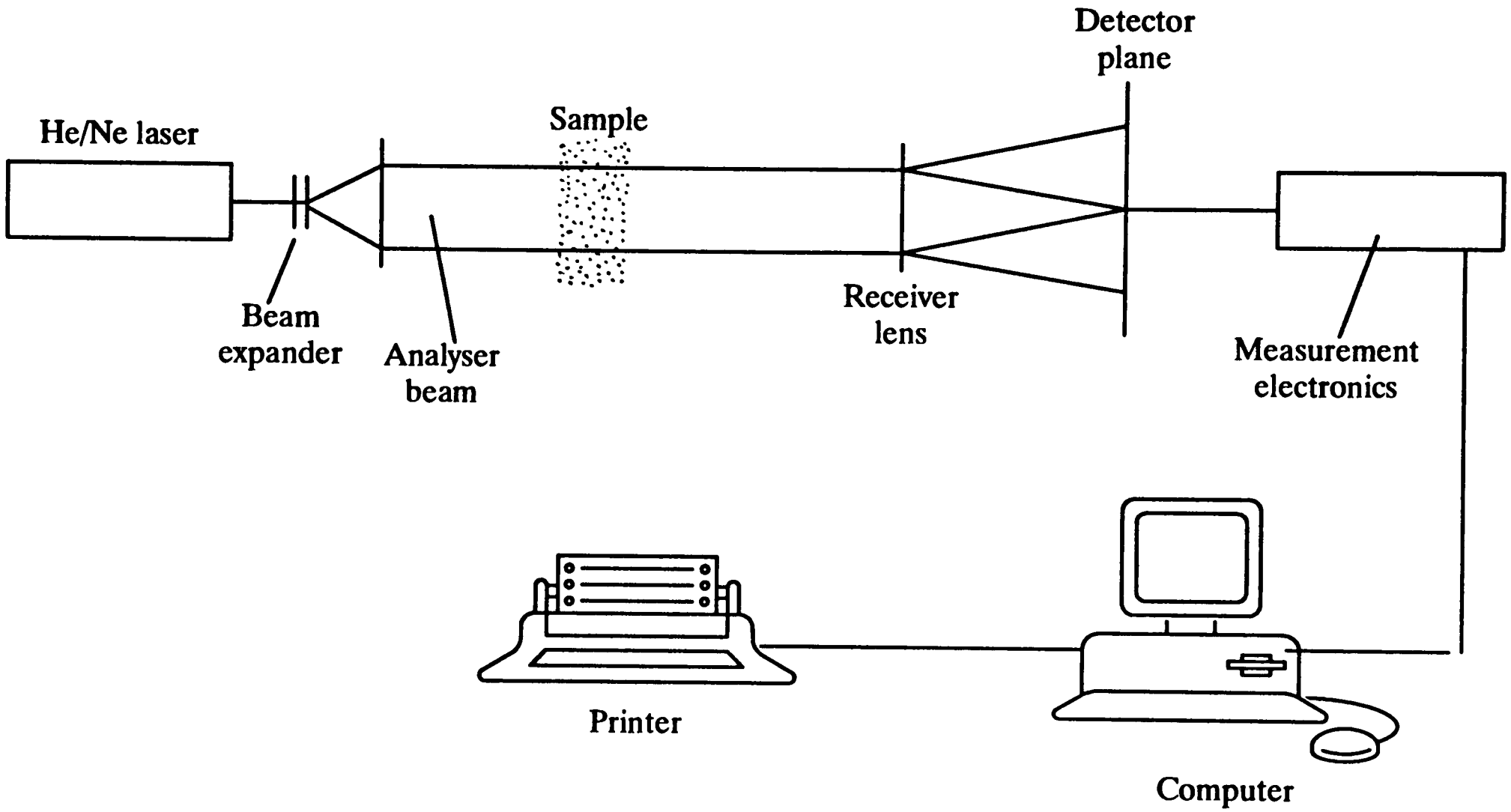

Figure 2.11 Schematic representation of the Malvern 2600 Particle Sizer.

The Malvern apparatus measures drop sizes in a limited range, and as it is based on Fraunhofer diffraction, only applies to drops whose diameter is larger than the wavelength of the incident beam (λ' = 633 nM). The instrument is provided with different lenses: 63, 100, 300, 600, 800 and 1000 mm focal length which are associated with particle ranges of 1.2–118 μm, 1.9–188 μm, 5.8–564 μm, 11.6–1128 μm, 15.5–1503 μm and 19.4–1880 μm, respectively. For the lenses of focal length 63, 100 and 300 mm the manufacturers of the Malvern Instrument recommend the laser beam to be expanded to 9 mm. For focal lenses of 600, 800 and 1000 mm the recommendation is to use the long bed option and the 18 mm beam expander.

2.1.5.4. Test Section

One of the problems encountered when using the Malvern apparatus for drop sizing in annular flow, is that the laser beam should pass undisturbed in and out of the gas core. Several methods to gain access to the gas core were discussed by Jepson (1992). In the present study the technique employed by Teixeira (1988) and Jepson (1992) in vertical flow was applied to horizontal flow.

The method involves completely removing the liquid film through a porous wall (see liquid film flow measurements) just before the two–phase mixture flows through the optical section. The distance between the film removal and the drop size measurement point should be kept to a minimum to prevent new film formation.

Previous studies by Butterworth (1972) and Paras and Karabelas (1990–b) in horizontal annular flow, in which vertical drop fluxes were measured, have shown that there is an increase in the concentration of drops at the bottom of the pipe. As the Particle Sizer does a spatial sampling of the flow (i.e., gives the size distribution of drops contained within a volume for a set period of time) and in order to obtain a more realistic size distribution, the sizing unit was mounted on a vertical stand to take account of drop stratification. This will be discussed further in section 2.1.5.5.

As there are no data on drop sizes in horizontal annular flow, it was decided to start the experiments with the 300 mm lens in combination with the 9 mm beam expander. The drop size test section previously used by Teixeira (1988) was installed in the horizontal rig upstream of the bend. This test section built in Perspex is shown in Figure 2.12.

Two flat glass windows are positioned at opposite sides of the unit, and are clamped to the Perspex block by retaining plates. Air jets are fed across the windows to prevent splattering of drops. A lip had to be inserted in the lower access port for the laser, to prevent accumulated drops at the edge of the hole falling onto the bottom window. The height of this wall was approximately 0.003 m, and is thought not to interfere with the flow.

This arrangement worked well for gas mass fluxes of 55 kg/m^{2}s to 70 kg/m^{2}s. However, for a gas mass flux of 50 kg/m^{2}s and below larger drops were seen in the gas core. The size of

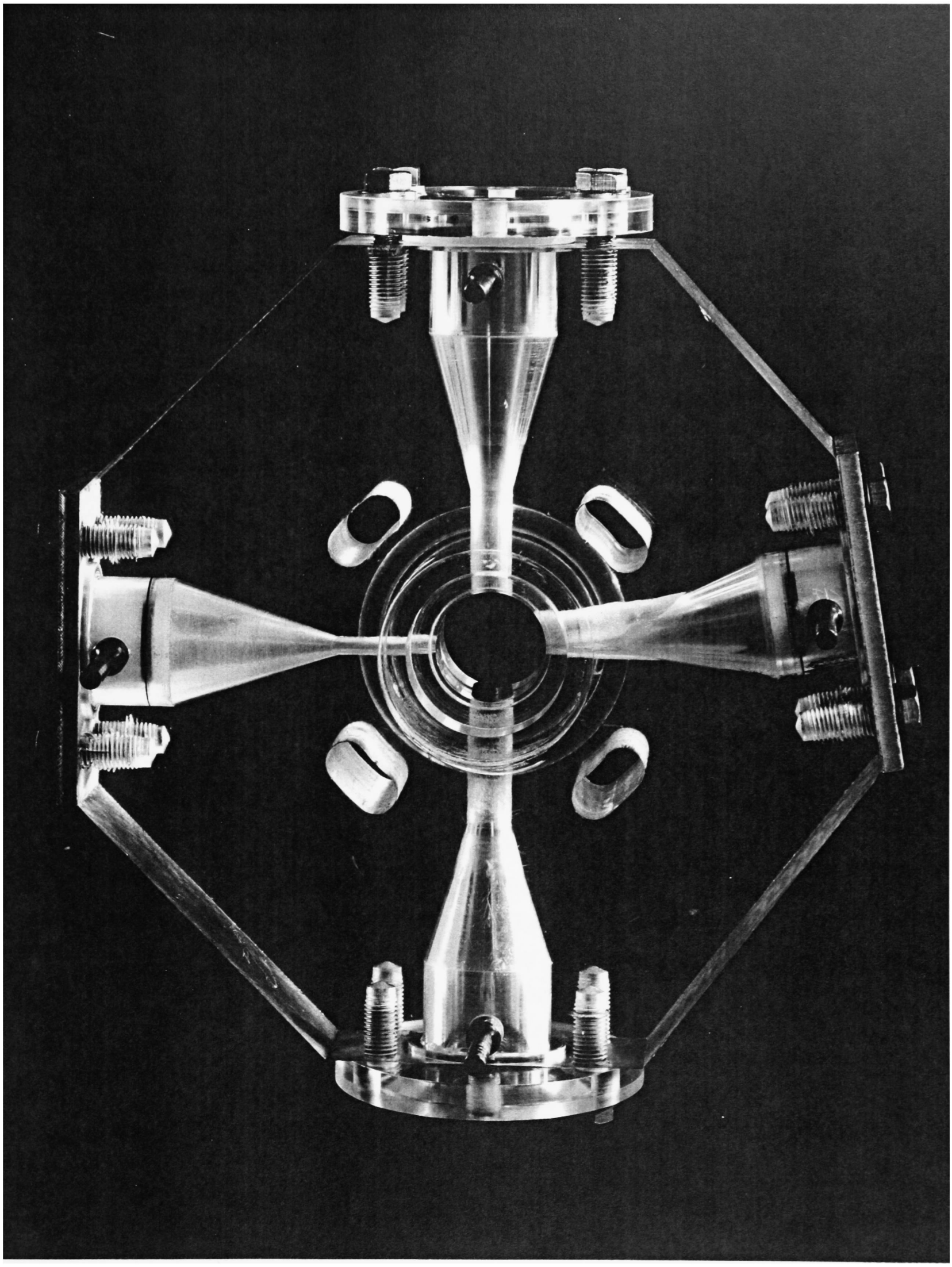

Figure 2.12 Test section used with the laser beam expanded to 9 mm.

these drops fell outside the range of the 300 mm lens. Consequently a higher focal length lens had to be used. The 1000 mm lens was chosen and used in conjunction with the 18 mm beam expander. A new test section had to be constructed to accommodate the 18 mm laser beam (Figure 2.13).

In order to prevent liquid falling on the bottom glass window of this new test section, the following arrangement was made to the lower access port for the laser:

- A thin wall with a height of 0.007 m was placed at the top of the hole. This prevented accumulated liquid falling on the window.
- A hollow cone made of very thin sponge was inserted inside the hole, tight against the wall. This sponge was pre-wetted to collect liquid that might impact on the wall or accumulate around the edges of the lip.
- This liquid drained down the sponge to a small reservoir placed just above the bottom glass window. The collected water was removed continuously.

Measurements taken for the same set of flow conditions using the 300 mm lens and the 1000 mm lens with the respective test sections, showed that the Sauter mean diameter obtained was very similar in both cases. This demonstrates that when using the test section built to accommodate the 18 mm laser beam there was no interference in the flow characteristics.

Figure 2.14 shows the Malvern Particle Sizer with the 1000 mm lens set up in the vertical support. The support was constructed to give flexibility of movement in the *xyz* directions of both the transmitter and receiver support plates. This is particularly important in the alignment of the instrument, because the detector has to be perfectly in line with the laser source.

Initial experiments were carried out to identify the influence on drop size of window air purge flow rates and gas take-off through the porous wall. The results are displayed in Figures 2.15(a) and (b), where the Sauter mean diameters were calculated assuming the model independent analysis. Based on these tests, it was decided that drop size measurements should be carried out at the lowest possible gas take-off rate, bearing in mind that the liquid film has to be completely extracted. The graphs indicate a decrease in the Sauter mean with increasing gas take-off rate. It is thought that increasing gas take-off rate can lead to the early deposition of drops, especially the larger drops that travel closer to the bottom of the porous wall.

The window air purge was maintained at around 3% of the total gas flow. The experiments have shown that for this value the drop size distribution was unaffected and the drops were not wetting the test section windows.

2.1.5.5. Measurement Procedure

The laser diffraction technique involves two stages, namely a background measurement and a sample measurement. The background light energy distribution is measured without the

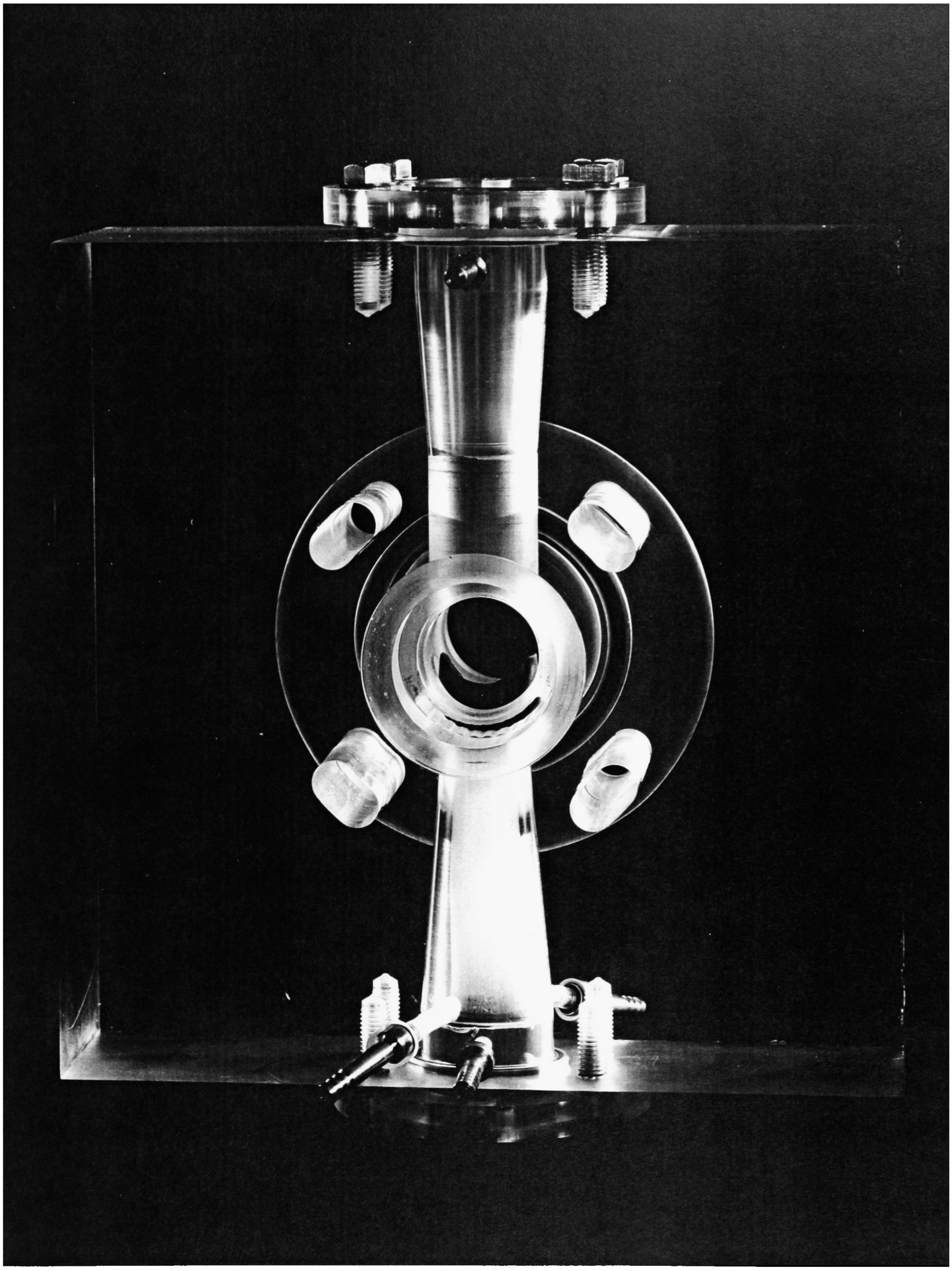

Figure 2.13 Test section used with the laser beam expanded to 18 mm.

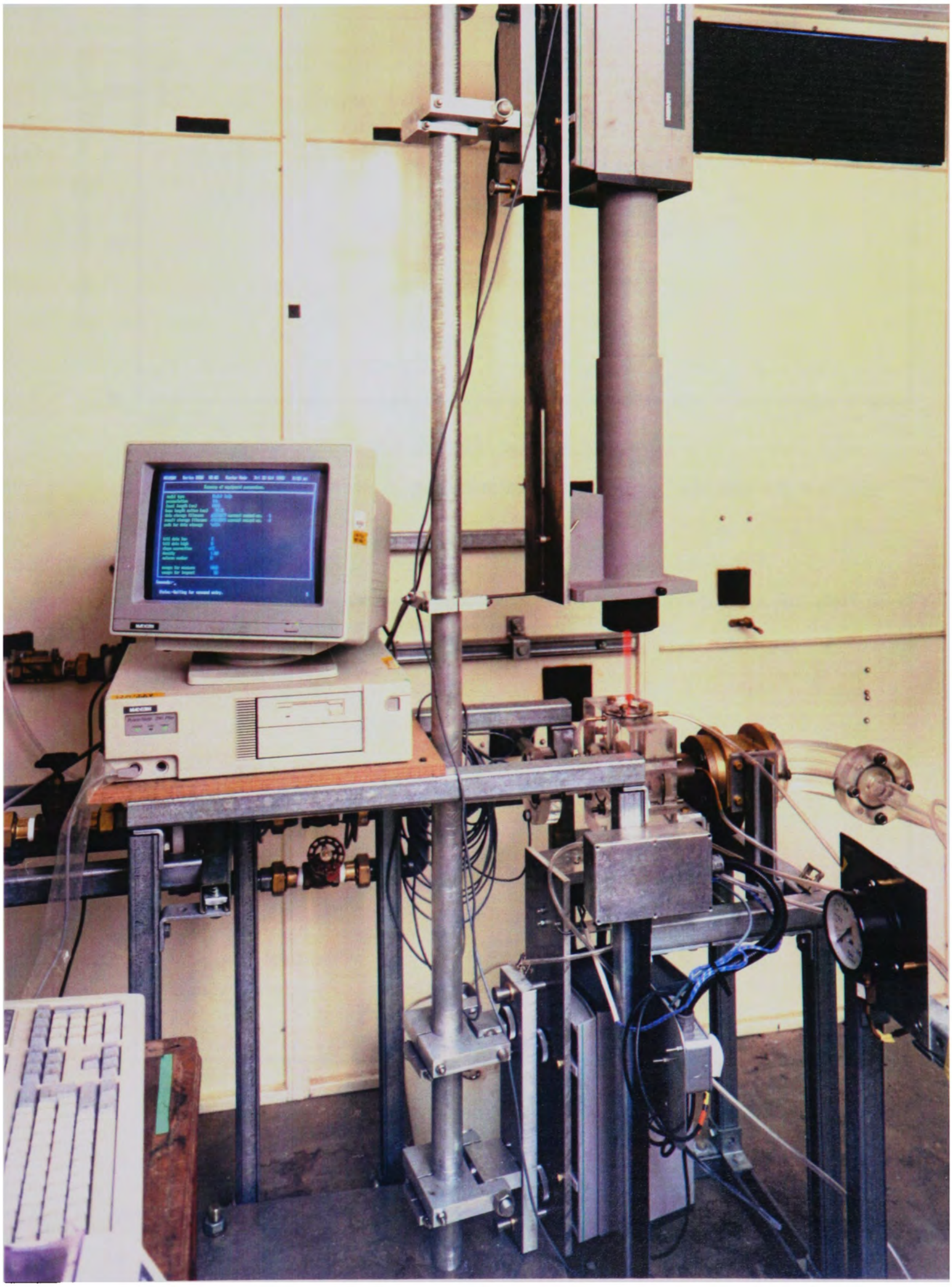

Figure 2.14 Malvern 2600 Particle Sizer set up in the vertical support, using the 1000 mm focal length lens.

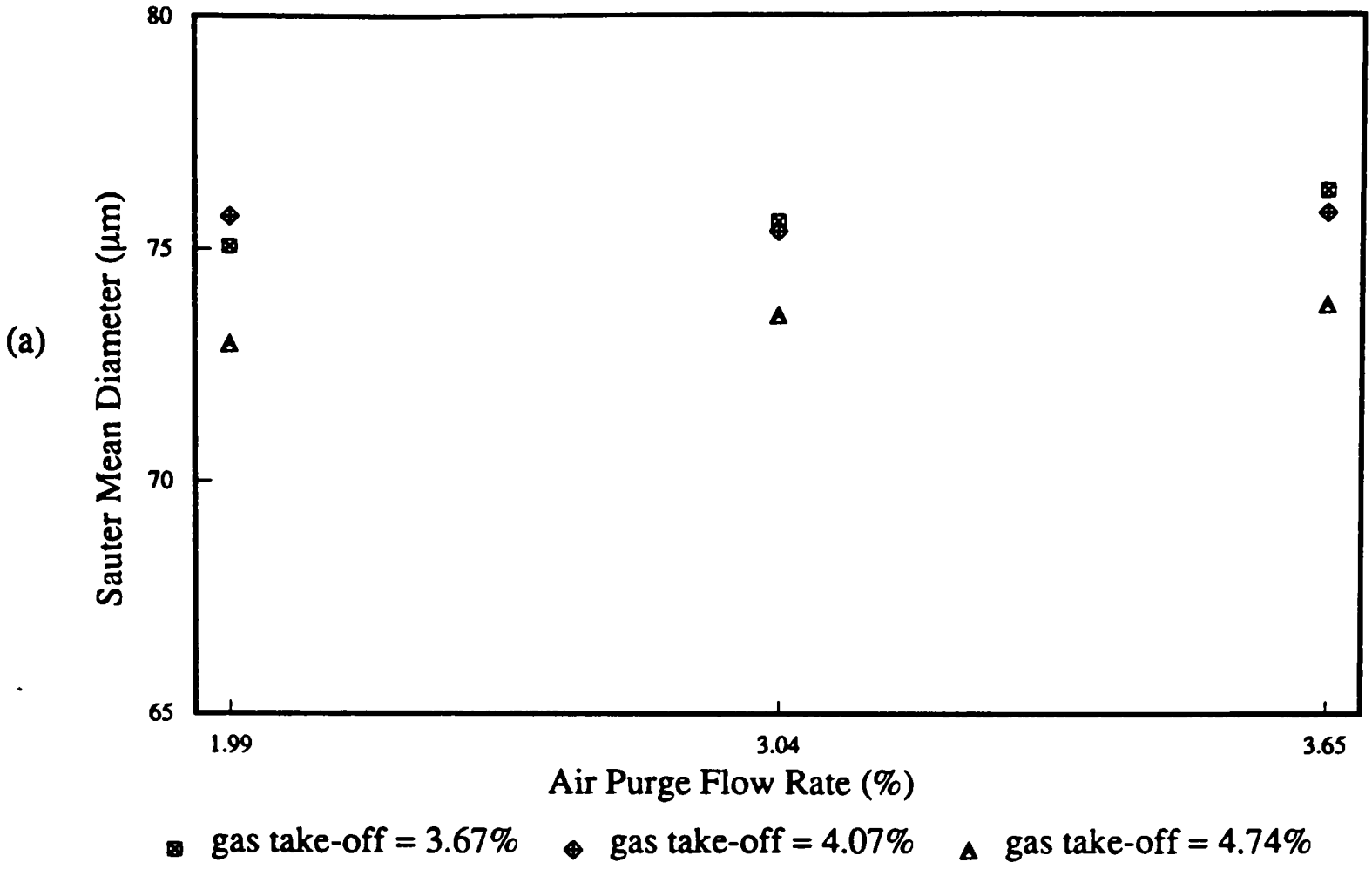

Figure 2.15 Influence of gas take–off rate and window air–purge rate on drop size, for various flow conditions: (a) G_G = 60 kg/m^{2}s and G_L = 70 kg/m^{2}s, (b) G_G = 70 kg/m^{2}s and G_L = 30 kg/m^{2}s

sample present. It should be taken under similar conditions to those used in the sample measurement. In this work, the background light energy distribution was measured under flowing and static conditions, but identical results were obtained. Despite this, the background measurements were always taken under flowing conditions.

Once the gas and liquid flow rates were established in the rig, the sample measurement was carried out. The sample data were obtained by subtracting out the background contribution, and then the resulting drop size distribution was calculated.

The sampling time used during the background and the sample measurement was set at 1000 sweeps, as advised by the manufacturers, Malvern Instruments. A previous study on the influence of sampling time on drop size for fixed flow conditions, showed no variation of drop size when increasing the number of sweeps from 200 to 5000.

During the course of the experimental work, various aspects of the set up were continuously checked:

- Ensuring that the laser beam had a correct shape after passing through the test section and had not been clipped by the walls.
- The laser was correctly aligned with the detector.
- Lenses and glass windows were periodically cleaned. The orientation of the windows relative to the laser beam was adjusted, so that the reflected light did not interfere with the source beam.
- The distance between the sample and the collecting lens was kept within the lens cut off distance. If the system to be measured is positioned too far away from the lens, it is possible that some of the diffracted light will not be collected. This problem is known as vignetting, and will be discussed in the following section.

2.1.5.5. Limitations of The Malvern

The Malvern Particle Sizer can cover a vast range of particle sizes, as discussed previously (section 2.1.5.2.). Being a non-intrusive technique, it does not interfere with the flow and no calibration is necessary. The repeatability of the measurements is within 3%. However, the apparatus presents some limitations in its use.

The theory behind the technique assumes that the particles are spherical and that the diffraction pattern is described by the Fraunhofer diffraction theory. This theory is valid for particles whose diameter is greater than the wavelength of the incident beam. For particles smaller than approximately 1 μm, the diffraction pattern is not only dependent on particle size but also on its optical properties. So, the Fraunhofer diffraction theory is no longer valid, and the Mie scattering theory has to be applied to describe the diffraction pattern. This should not constitute a problem in the present experiments as only a small quantity of the drops present have such small diameters.

Multiple scattering can affect the performance of the Malvern. If the concentration of drops is too high, the light scattered by one drop may be scattered by a second drop before reaching the detector. This will introduce errors in the calculated drop size distribution, i.e. a shift to lower mean drop sizes and broader size distributions. This effect becomes significant when the obscuration (OB) is above 0.5. Obscuration is the percentage of light collected by the sample.

Felton et al (1985) studied the effect of concentration on the particle size distribution of glass beads from 5 μm to 105 μm. The authors developed equations to correct for the effects of multiple scattering. For a Rosin–Rammler distribution, they proposed the following corrections to the distribution parameters $\overline{X}$ and $\overline{N}$ (see section 2.1.5.2):

$$C_{\overline{X}} = 1.0 + (0.036 + 0.4947\ (OB)^{8.997})\ \overline{N}_{ap}^{(1.9 - 3.437(OB))} \tag{2.8}$$

and

$$C_{\overline{N}} = 1.0 + (0.035 + 0.1099\ (OB)^{8.65})\ \overline{N}_{ap}^{(0.35 - 1.45(OB))} \tag{2.9}$$

At low drop concentrations the light energy falling on the detector rings is virtually indistinguishable from the ambient noise level, and large random errors occur. The manufacturers suggest that below an obscuration of 0.05 measurements should not be carried out.

As each lens has a limited aperture for collecting scattered light, it is important that the sample is positioned below a given maximum distance from the lens. If this maximum distance is exceeded, light scattered at large angles may be lost at the outer rings (vignetting), biasing the drop size distribution towards the larger drop sizes. Figure 2.16 illustrates this situation for the maximum scattering (α_M). Dodge (1984) derived the following expression for calculating the maximum distance between the sample and the lens, x :

$$x = f\left(\frac{D_l - D_b}{D_d}\right) \tag{2.10}$$

where f is the lens focal length, D_l is the lens diameter, D_b is the beam diameter and D_d is the detector diameter.

The Malvern sizer analyses a sample over a cylindrical region of the space defined by the laser beam diameter and the path of the beam in the sample. If there is a difference in drop concentration across the space then the line–of–sight measurements can differ from the overall distribution.

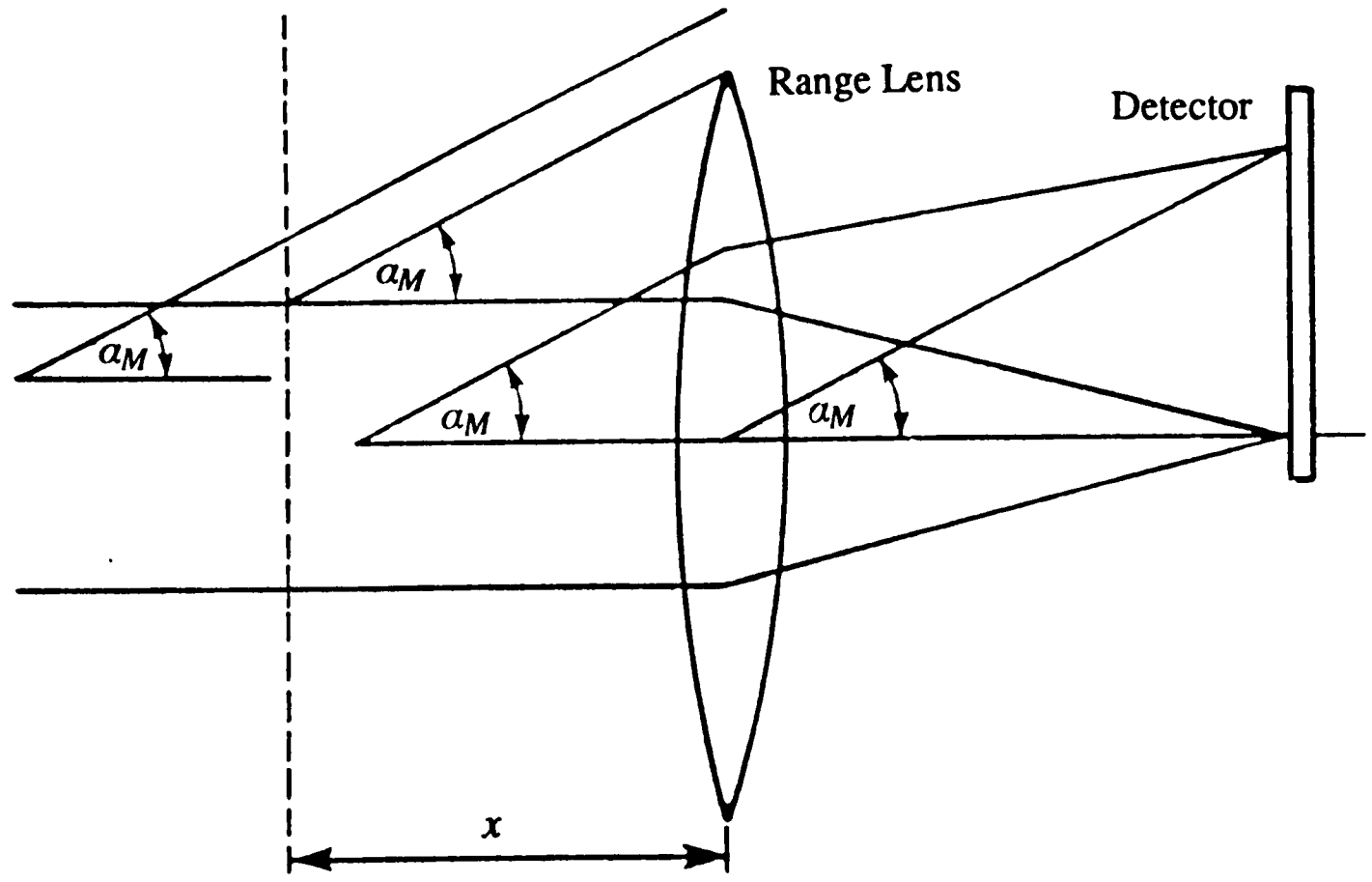

Figure 2.16 Maximum allowable distance for sample position (x).

In horizontal flow, because of gravity there is a definite stratification in drops normal to the flow direction, as shown by the vertical drop flux profiles obtained by Butterworth (1972) (Figure 2.17) and Paras and Karabelas (1990-b) (Figure 2.18(a) and (b)) using pitot tubes. To account for this effect, the laser apparatus was located in a vertical support in order to minimise bias in the measured size distribution.

On the other hand, horizontal drop flux profiles are quite flat. The sudden increase in drop flux near the tube walls in Figure 2.17 has been attributed to the proximity of the probe to the liquid film. Liquid from the tips of waves could have been collected, and counted as drop flux near the wall. So, in this study in spite of having used a 9 mm and 18 mm laser beam in a 0.032 m tube, it is expected that the line-of-sight measurements are not much affected by spatial bias provided the apparatus is set up vertically.

To account for temporal variations in drop concentration due to the passage of disturbance waves, the measurement time was set at 1000 sweeps. As mentioned before, drop size distribution proved to be independent of the sweep number between 200 and 5000.

Finally, it is important to point out that the Malvern instrument samples the number of particles per unit volume of space. So, as slower drops remain longer in the laser beam, the distribution can be biased towards the size of slower drops.

2.1.5.6. Laser Safety

When operating a laser there are some safety precautions that the operator must undertake, depending on the class of laser to be used. The Malvern 2600 Particler Sizer uses a 2mW Helium/Neon laser, that according to BS 4803: 1972 is categorised as a Class IIIA. Appendix C describes the safety procedures adopted during the operation of the Malvern on the Horizontal Two-Phase Flow Rig, and comply with BS 4803.

2.1.6. Operating Conditions

The air and water flow rates were chosen in order to cover the maximum possible range of flow conditions. Systematic variations of the mass flux of both phases were undertaken. The combination of flow rates used include the wavy-stratified, annular and pseudo-slug flow regimes.

The maximum values of gas and liquid flow rates were imposed by the present construction material of the apparatus. According to current safety regulations on pressurised experimental equipment at the Harwell Laboratories (AECP(R) 23 Part 1), the maximum pressure at which the horizontal tube can be operated is 1.5 bar.

Overall, the gas mass flux was varied between 10-70 kg/m^2s and the liquid flow rates between 10-170 kg/m^2s. However, these ranges of flow conditions were not employed for all the experiments. Table 2.2 shows the flow conditions used for each experimental investigation.

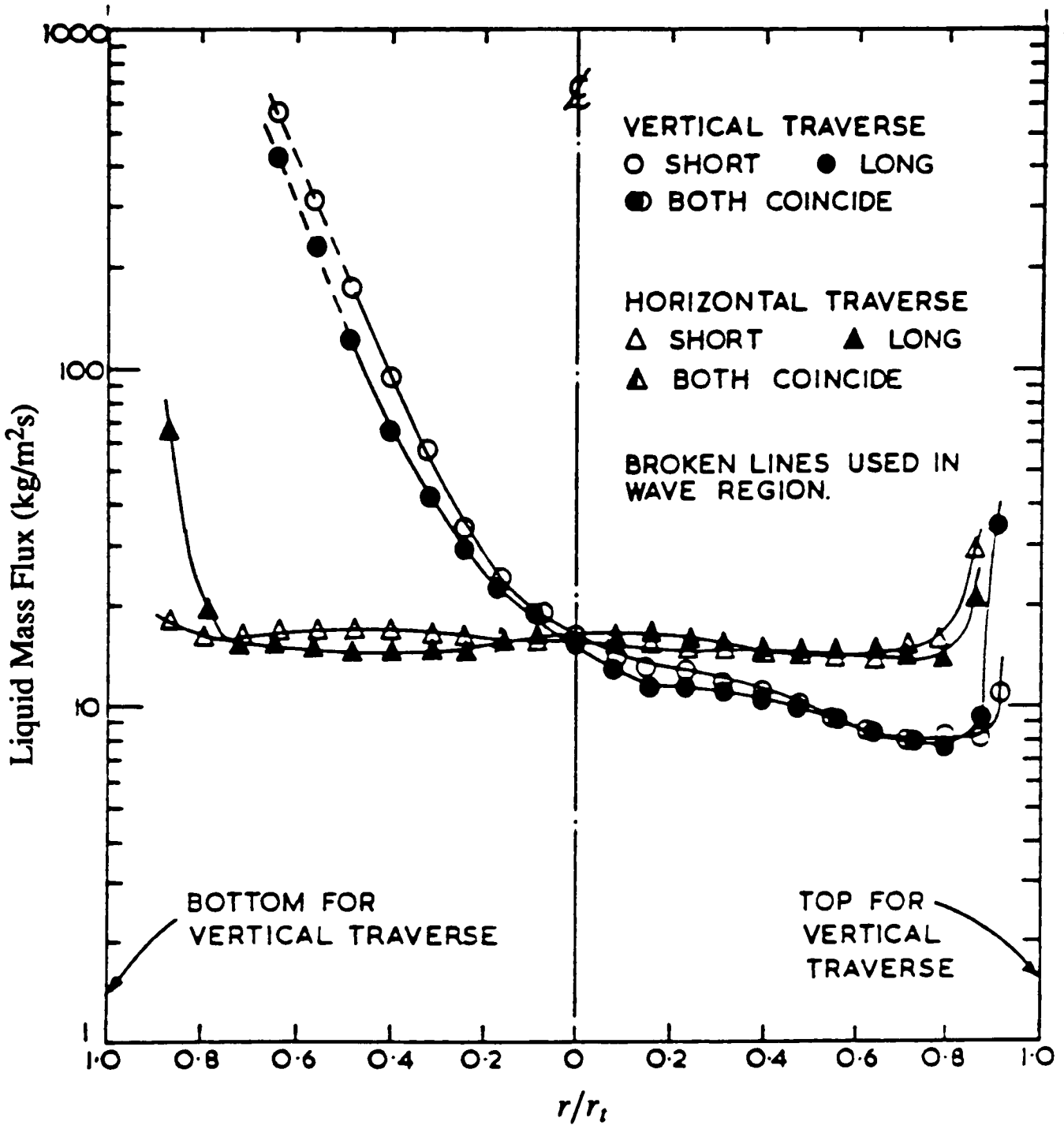

Figure 2.17 Drop flux profiles (horizontal and vertical) obtained by Butterworth (1972) in a horizontal tube 0.0318 m ID, for $G_G = 32$ kg/m^{2}s and $G_L = 159$ kg/m^{2}s.

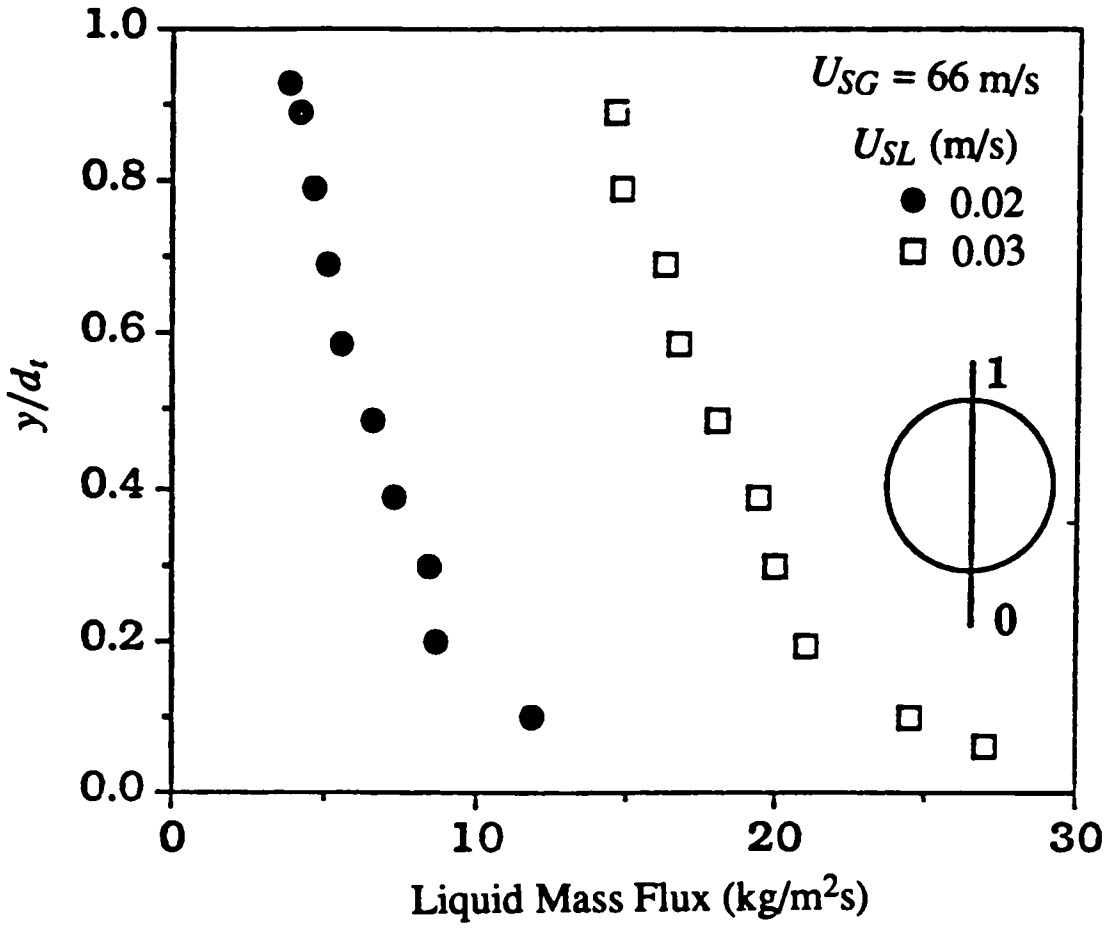

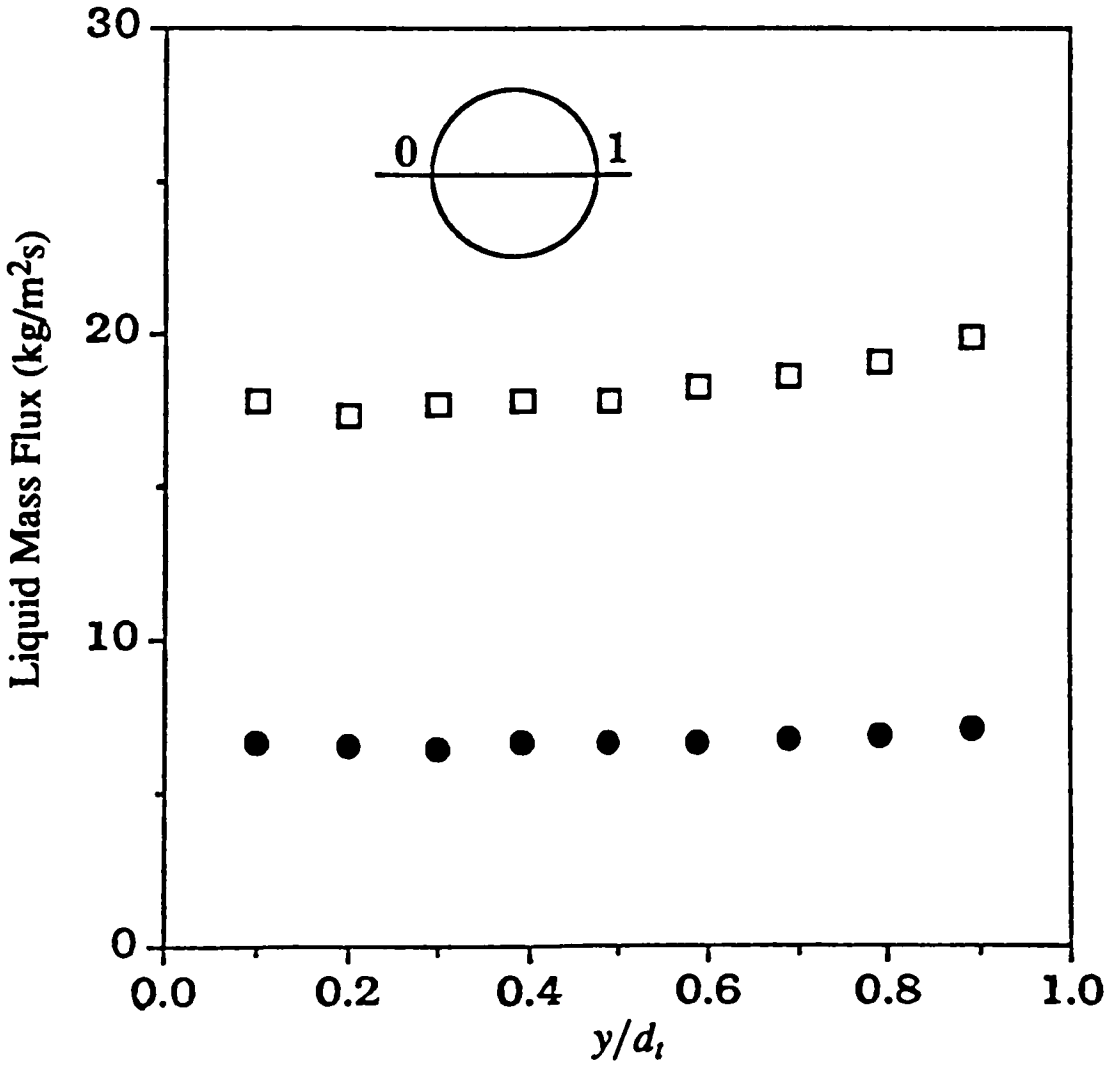

Figure 2.18 Drop flux profiles obtained by Paras and Karabelas (1990–b) in a horizontal tube 0.05 m ID: (a) vertical profiles, (b) horizontal profiles.

TABLE 2.2 – RANGE OF FLOW RATES USED IN THE DIFFERENT MEASUREMENTS

Measurement		G_G (kg/m^{2}s)	G_L (kg/m^{2}s)	Pressure (bar)
Pressure Drop Upstream of the Bend	Single Phase	10–50	–	1.0–1.3
	Two–Phase	10	10	1.0
		40	10 & 70	1.3 & 1.4
Still Photography of Two–Phase Flow		10	10–110	1.0–1.1
		20	10–170	1.1–1.3
		30	10–90	1.2–1.3
		40	10–70	1.3–1.4
		50	10	1.3
Still Photography of the Drop Flow		40	50	1.3
		70	30	1.4
Cine Film		20	10–150	1.1–1.3
		30	10–70	1.2–1.3
		40	10	1.3
		50	10	1.3
Film Flow Measurements		20	10–130	1.3
		30	10–130	1.3
		40	10–130	1.3
		50	10–130	1.3
		60	10–70	1.4
		70	10–70	1.4
Drop Size Measurements before the Bend		40	30–110	1.3
		50	30–110	1.3
		55	20–70	1.4
		60	20–70	1.4
		65	20–70	1.4
		70	20–70	1. 4
Drop Size Measurements after the Bend		40	50–90	1.3
		50	50–90	1.3
		60	30–70	1.4
		70	30–70	1.4

During the pressure drop measurements and visualisation experiments (still photography and cine film) it was not possible to maintain the same operating pressure for the various flow conditions. At the time, valve V15 (Figure 2.1) was not yet incorporated in the rig. At a later stage, for liquid film flow and drop size measurements, it was decided to include valve V15 to enable the operator to maintain a constant pressure in the test section.

Cine films were undertaken at conditions where the concentration of drops in the gas core was low, and drops could be easily followed. However, drop size measurements using the Malvern instrument were not possible at flow rates with low drop concentrations.

Throughout all the experimental work, the pressure in the test section was maintained between 1.0–1.4 bar, and the temperature was approximately 15°C. Teixeira (1988) pointed out that, as both fluids flow together for a considerable distance to achieve a developed condition before they reach the test section, water can be evaporated into the gas core. The author tested the influence of humidity on the physical properties, and found that it has a small effect on air density and viscosity. Table 2.2 lists the physical properties of air and water for the conditions mentioned above, assuming that the air was saturated.

TABLE 2.3 PHYSICAL PROPERTIES OF FLUIDS AT 15°C

Fluids	Pressure (bar)	Density (kg/m^3)	Viscosity (kg/m s)	Surface Tension (N/m)
Air	1.0	1.20	0.0000179	0.07349
	1.1	1.32		
	1.2	1.44		
	1.3	1.56		
	1.4	1.69		
Water		999.13	0.00114	

2.2. Vertical Upflow Rig

2.2.1. Flow Apparatus

The experiments in vertical annular flow were carried out with adiabatic air–water upflow in a rig similar to that described by Jepson (1992). A schematic represention of the equipment is shown in Figure 2.19.

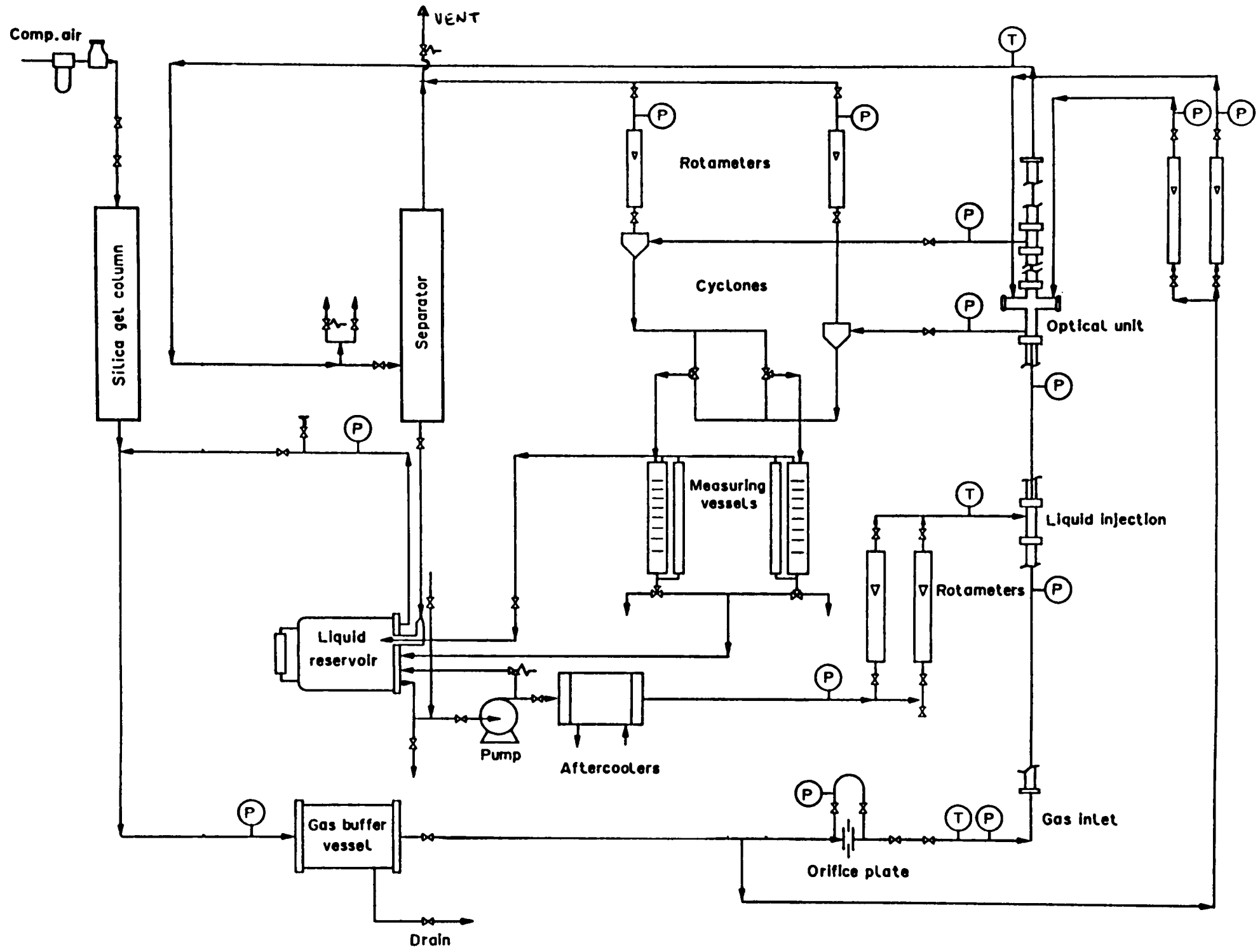

Figure 2.19 Experimental rig used for the vertical annular two–phase study.

Filtered air from the main air supply was introduced at the bottom of a 0.01026 m ID vertical stainless steel tube, after being measured using an orifice plate.

Demineralised water, pumped from the liquid reservoir and metered using calibrated rotameters, was fed into the tube through a porous wall located 0.5 m above the base. The test section for film flow rate and drop size measurements was placed 3 m above the entrance, to allow the development of annular flow conditions.

Above the measuring point the two-phase mixture was separated, the liquid returned to the stock tank and the air released to the atmosphere.

A set of three thermocouples were used to monitor the temperature of the fluid through the system. The inlet air temperature was measured by a thermocouple inserted upstream of the orifice plate, while another monitored the water just before entering the porous wall. A third was installed at the end of the test tube.

2.2.2 Film Flow Measurements

The liquid film flow rate was determined by the film removal technique already discussed in section 2.1.4. The film was completely removed from the test tube through a porous wall 0.076 m long, together with a small amount of gas. The phases were then separated in a cyclone, and the rate of liquid collection was measured.

In the present work the amount of gas taken off was kept below 5% of the total amount of gas. Jepson (1992) found that this had no effect on the measurements of film flow rate and drop size.

2.2.3. Drop Size Measurements

To measure drop sizes, the laser diffraction technique developed by Swithenbank et al (1976) and now commercially available from Malvern Instruments Limited was used. The features of this technique were presented in section 2.1.5.

The Malvern 2600 HSD instrument (a precursor of the Malvern 2600 already discussed in section 2.1.5.3) was used to measure the drop size distribution. This comprised a 3 mW laser beam 7 mm in diameter, which shone through a special test section onto the drop sample. A 300 mm focal length lens (size range between 5.8–564 μm) was used to focus the scattered light onto the Malvern detector unit.

The test section for drop sizing is constructed in brass and is formed by two windows diametrically opposed, that appear at the end of side arms. The windows were purged with compressed air (kept below 5% of the main air flow) to prevent splattering of the drops. Immediately upstream of the optical section the liquid film was completely extracted through a porous wall to provide optical access to the gas core. Figure 2.20 shows the test section and the laser set up used. More details about this test section can be found in Jepson (1992).

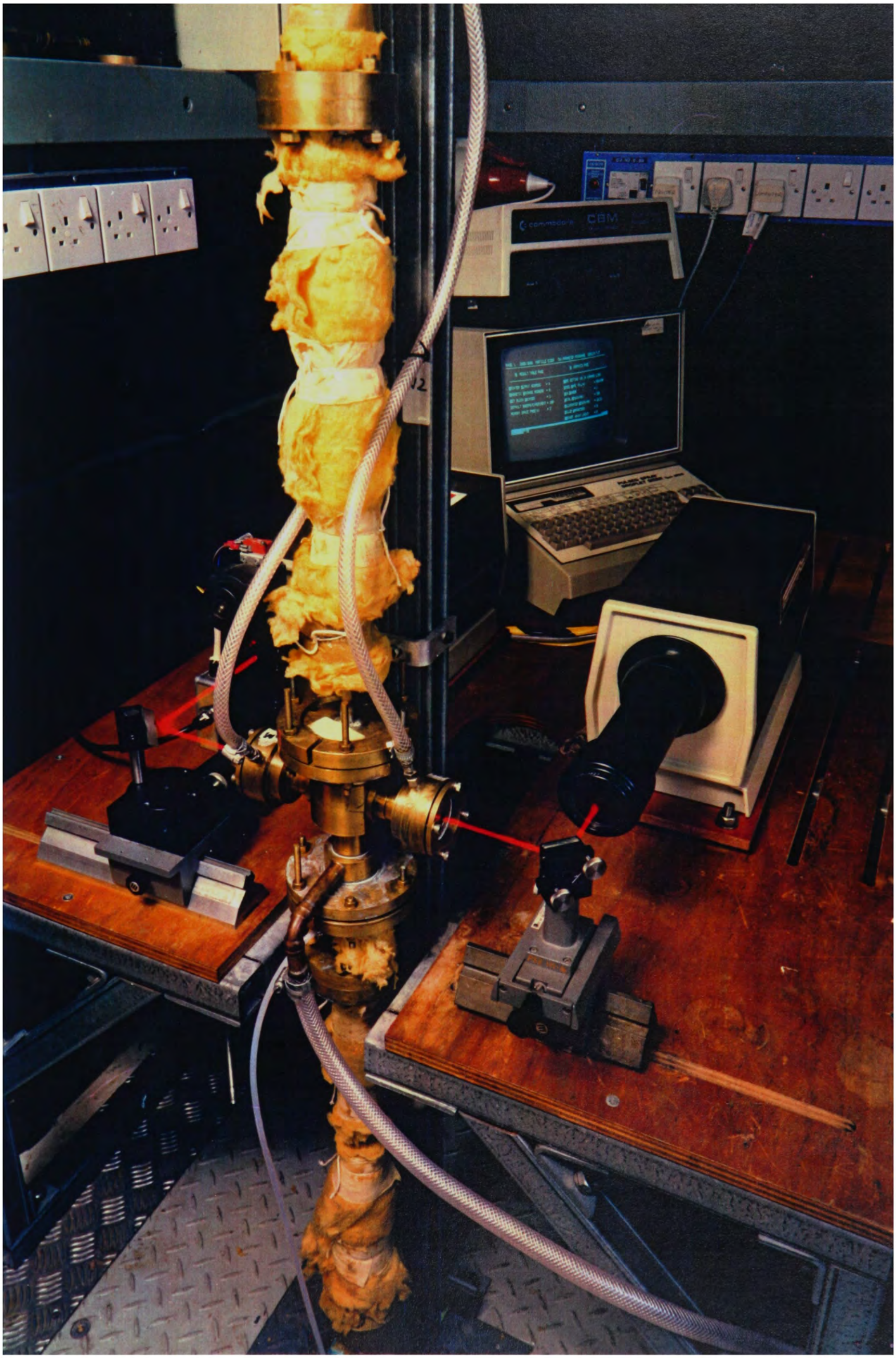

Figure 2.20 Test section and the Malvern 2600 HSD

When processing the data, the computer assumes that the drop sample could be fitted by a Rosin–Rammler distribution. The parameters of this distribution were optimized until the sum of differences between measured and calculated energies is minimized. The applicability of the Rosin–Rammler distribution to represent drop size distributions in vertical annular flow was tested by Azzopardi et al (1978).

2.2.4. Operating Conditions

As mentioned before, modifications were made to the test facility used by Jepson (1992), that allowed an extension of the measurements to higher flow conditions. In the present experiments, the air mass flux was varied between 60–120 kg/m^{2}s, and the liquid mass flux between 40–120 kg/m^{2}s. Systematic variations of the mass flux of both phases were undertaken. All flow conditions studied lay in the annular flow region.

Through all the experimental work, the pressure in the test section was maintained at 1.5 bar, and the temperature was approximately 15°C. For these conditions, the physical properties of the air and water can be extracted from Table 2.3 with the exception of the gas density. For a pressure in the test section of 1.5 bar the air density has a value of 1.81 kg/m^3.

3. VISUALISATION STUDIES IN HORIZONTAL GAS–LIQUID FLOW

3.1. Introduction

The observation of the various phenomena occurring in two–phase flow can be made by visual inspection through a transparent window. However, when the processes are occurring at high speed the observer does not have a clear picture of what is happening. The use of high speed photography and related techniques allows the problem to be overcome by freezing the complicated mechanisms of two–phase flow.

Photographic methods have been widely used in the investigation of two–phase flow. Hewitt and Roberts (1969) established a flow pattern map for vertical gas–liquid flow based on simultaneous X–ray and flash photography. Butterworth and Pulling (1972) used a dye tracing technique to study the horizontal annular flow of an air–water mixture. They injected a dye along the horizontal diameter of the tube and observed its behaviour using high speed cine film. Their observations suggested that the waves play an important role in maintaining the liquid film at the top of the tube. Jayanti (1990) also used high–speed photography and photochromatic dye tracing to study the liquid film characteristics in horizontal annular flow.

Stuiver (1955) used a photographic technique to study the characteristics of air–water flow around 90°and 180° bends. George (1971) conducted visualisation work using a 180° bend set in the vertical plane. Cine films were produced for air–water flow covering different flow patterns. These showed that the bend had a strong influence on the structure of the flow.

From the analysis of the photographic records qualitative as well as quantitative information can be extracted, but quantitative measurements will be subject to errors. Hsu et al (1969) divided these errors into two categories: time and dimensional. The time problem relates to how well the action has been stopped. This time limit is the exposure duration which is linked to the frame speed in cine films, and to the flash duration in still photography. Dimensional problems include optical distortion caused by the curvature of the test tube, thermal gradients in the test area, refraction of the various media between the light source and the photographic camera, and camera alignment. The photographic image has limitations due to the graininess of the film, and due to the blurring of the image by inadequate arrest of the motion.

This chapter discusses the visualisation study performed for air–water flow in a horizontal tube 0.032 m ID, and the influence of a 90° horizontal bend on the flow characteristics. It includes observations of the flow upstream of the bend, at the bend, and downstream of the bend by visual inspection, and using high speed still photography and cine films.

3.2. Flow Characteristics before the Bend

This section covers several features of the air–water flow in a horizontal pipe. Apart from the identification of the flow patterns observed, characteristics of the liquid film are discussed. These include the fraction of the pipe circumference the liquid film occupies in wavy–stratified flow, and the presence of air bubbles entrained in the liquid film. The behaviour of drops travelling in the gas core is also mentioned.

3.2.1. Flow Patterns

The early research on the flow patterns existing in gas–liquid flow was made through visual observation. Photographic studies coupled with other experimental methods, however, have led to the establishment of several distinct flow regimes and flow pattern maps, already described in Chapter 1. The knowledge of these flow patterns is essential in modelling the interactions between the phases.

The range of air–water flow rates investigated in the present study, and the flow patterns observed are presented in Table 3.1. These cover wavy–stratified flow (WS), wavy–stratified flow with atomisation (WS+At), pseudo–slug flow (PS) and annular flow (A). The complete set of still photographs taken before the bend for these flow conditions is presented in Figure D1 (Appendix D). The cine films were taken for the flow conditions which are highlighted in Table 3.1.

TABLE 3.1– FLOW CONDITIONS AND OBSERVED FLOW PATTERNS BEFORE THE BEND

G_L (kg/m^{2}s) / G_G (kg/m^{2}s)	10	30	50	70	90	110	130	150	170
10	WS	WS	WS	WS	WS	WS	–	–	–
20	WS+At	WS+At	WS+At	WS+At	WS+At	PS	PS	PS	PS
30	WS+At	WS+At	WS+At	A	A	–	–	–	–
40	WS+At	A	A	A	–	–	–	–	–
50	WS+At	–	–	–	–	–	–	–	–

The wavy–stratified flow was observed at the lower gas mass flux (G_G = 10 kg/m^{2}s) and for all liquid flow rates studied (G_L = 10–110 kg/m^{2}s). The wavy–stratified flow with atomisation was identified by the presence of drops that had deposited at the top of the tube, and occurred for $G_G \geq 20$ kg/m^{2}s and at low liquid flow rates. The air–water system was considered to travel in annular flow when the liquid film covered the whole pipe circumference.

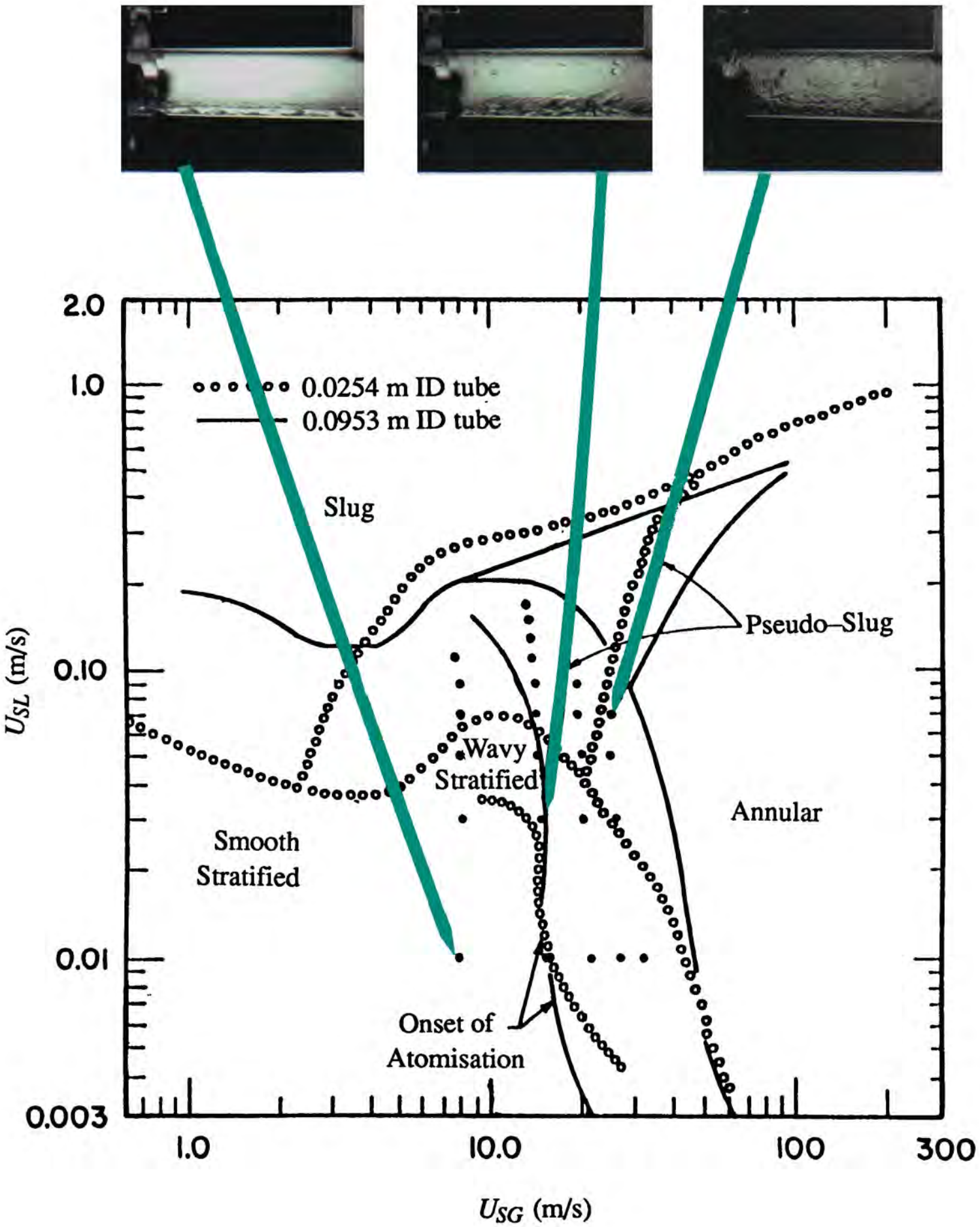

Figure 3.1 Flow regime map by Lin and Hanratty (1987) and flow conditions of the present experiments

The mechanism of film formation in the change from stratified to annular flow can be deduced from the photographs. For a constant liquid flow rate, as the gas velocity is increased, the liquid starts to ride up the sides of the tube. At the same time, drops deposit on the top of the tube. These two mechanisms contribute to the formation of a continuous film around the tube circumference.

Experimental evidence showed that the pseudo–slug flow regime occurred for $G_G = 20\,kg/m^2s$ and $G_L > 110\,kg/m^2s$. As mentioned by Lin and Hanratty (1987), the pseudo–slug regime resembles annular flow in that a film covering the whole pipe circumference is formed. However, it is also characterised by the appearance of large disturbances like slugs, but which do not give the identifying pressure pattern a slug does, and do not travel at the gas velocity. A pseudo–slug was captured in the cine film taken at $G_G = 20\,kg/m^2s$ and $G_L = 150\,kg/m^2s$. It shows a highly aerated disturbance which momentarily touches the top of the tube. The entrainment measurements conducted for $G_G = 20\,kg/m^2s$ and $G_L = 130\,kg/m^2s$ (see Chapter 4) showed the entrained mass flux to fall considerably at these flow conditions. It is believed this reduction in the entrainment level is due to a change in the flow pattern to pseudo–slug.

Figure 3.1 illustrates the flow conditions of this study on the flow pattern map of Lin and Hanratty (1987). Together with this diagram are some typical photographs of air–water flowing at wavy–stratified flow, wavy–stratified flow with atomisation, and annular flow obtained in the present study.

3.2.2 Wetted Perimeter in Wavy–Stratified Flow

The cine films carried out for gas mass fluxes of $G_G = 20$–$50\,kg/m^2s$ and at a liquid mass flux of $G_L = 10\,kg/m^2s$, and for $G_G = 20\,kg/m^2s$ and $G_L = 30\,kg/m^2s$ confirmed that in all cases the wavy–stratified flow with atomisation was seen.

From the height the liquid film spread over the pipe wall, the fraction of wetted perimeter was calculated. It was assumed that the film rise was the same at both sides of the tube, and that the area occupied by the drops deposited at the top of the tube was negligible. The results, plotted in Figure 3.2, show the fraction of wetted perimeter (F) increasing with gas Reynolds number (Re_G), for a constant liquid flow of $G_L = 10\,kg/m^2s$. The additional experiment carried out at $G_G = 20\,kg/m^2s$ and $G_L = 30\,kg/m^2s$, showed an increase in F to 42.7% with increasing liquid mass flux.

Azzopardi and Russell (1984) reported that the fraction of wetted perimeter (F) could be represented as:

$$F = 1 - \frac{6.5\ Ga/La}{\sqrt{\mathrm{Re}_G\ \mathrm{Re}_L}} \qquad \text{for} \quad \frac{\mathrm{Re}_G^{0.6}\ \mathrm{Re}_L^{0.5}}{Ga/La} < 24 \qquad (3.1a)$$

(a)

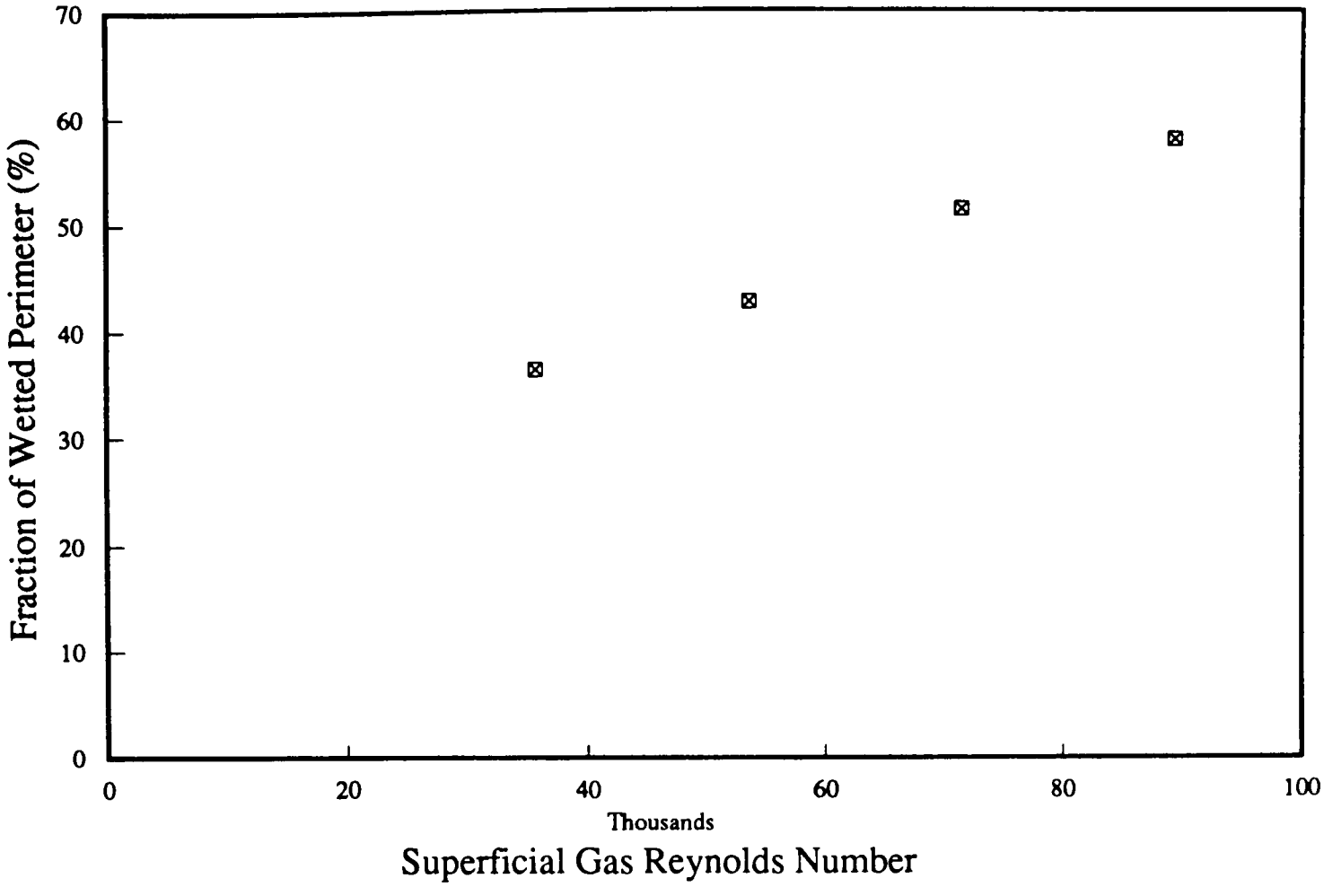

(b)

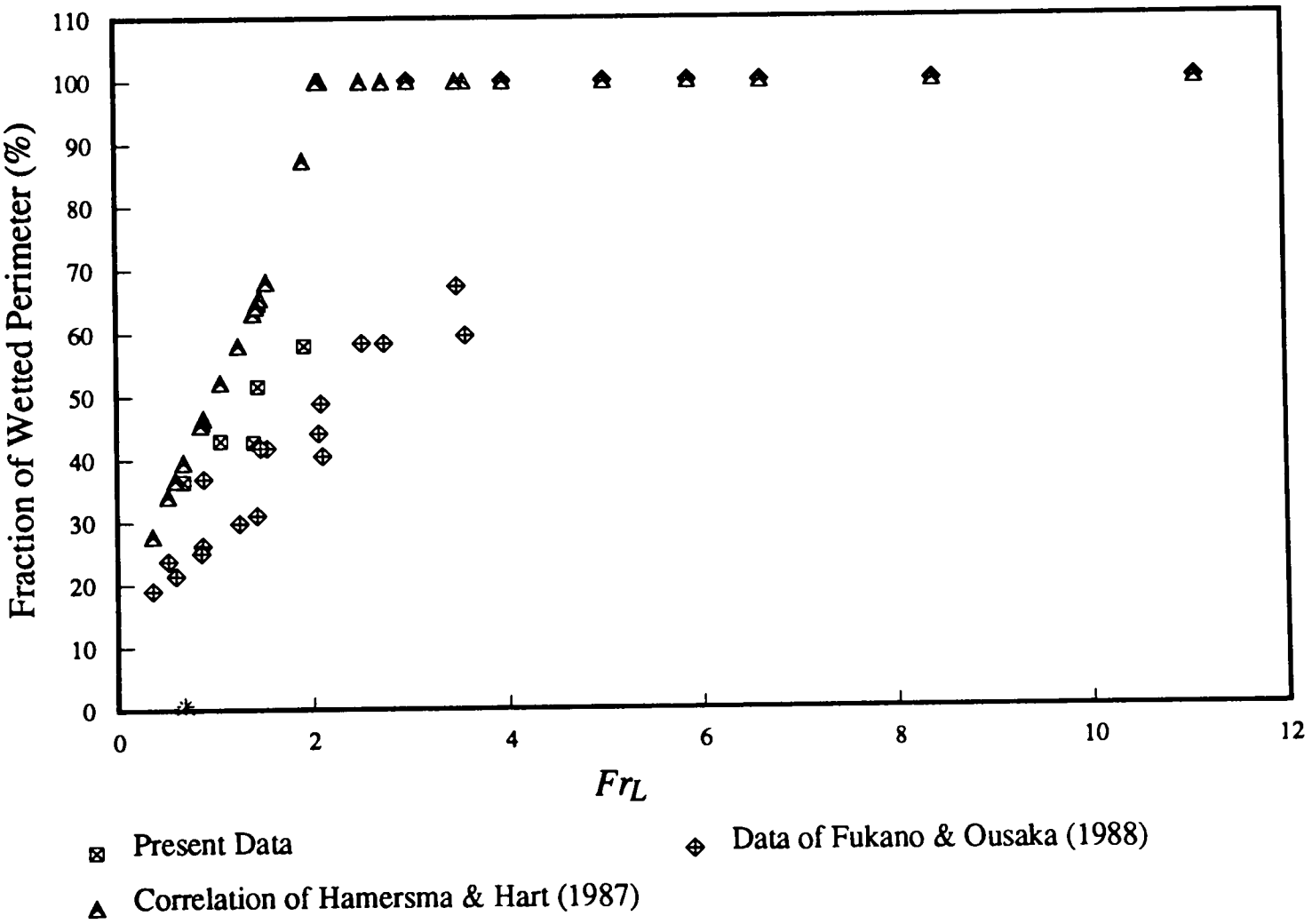

Figure 3.2 Fraction of wetted perimeter: (a) present data as function of the gas Reynolds number for a constant G_L = 10 kg/m^{2}s, (b) comparison of present data and the data of Fukano and Ousaka (1988) with the correlation of Hamersma and Hart (1987).

$$F = 1 - 0.27\ \mathrm{Re}_G^{0.1} \qquad \text{for} \quad \frac{\mathrm{Re}_G^{0.6}\ \mathrm{Re}_L^{0.5}}{Ga/La} > 24 \tag{3.1b}$$

where $Ga/La = d_t^2\ (\varrho_L - \varrho_G)\ g/\sigma$. The authors based their correlation on the work of Rosson and Meyers (1965), who studied the circumferential variation of the heat transfer coefficient for condensation in tubes.

The experimental results and equation (3.1a) show the fraction of wetted perimeter (F) increasing with gas and liquid velocity. Equation (3.1b), however, suggests that the fraction of wetted perimeter is independent of the liquid flow, and decreases with increasing gas velocity. For the flow conditions of the present study $(Re_G^{0.6}\ \mathrm{Re}_L^{0.5})/(Ga/La) > 24$, and so equation (3.1b) should apply, but it predicts a trend opposite to that seen in the data (Figure 3.2(a)).

Hamersma and Hart (1987) proposed a correlation for the fraction of wetted perimeter in terms of a Froude number for the liquid phase, $Fr_L = (\varrho_L/\Delta\varrho)\left(U_{SL}^2/(\varepsilon_L^2\ g\ d_t)\right)$, given by:

$$F = \frac{1}{\pi}\ \arccos\left(1 - C_1\ Fr_L\right) \qquad \text{for}\ C_1\ Fr_L < 2 \tag{3.2a}$$

$$F = 1 \qquad \text{for}\ C_1\ Fr_L \geq 2 \tag{3.2b}$$

where the constant $C_1 \approx 1$. The liquid holdup can be calculated using the equation: $\varepsilon_L = \left(1 + 3.57\ (U_{SG}/U_{SL})^{0.64}\ (\varrho_G/\varrho_L)^{0.28}\ (\mu_G/\mu_L)^{0.07}\right)^{-1}$. Figure 3.2(b) shows the performance of equations (3.2a) and (3.2b) to represent the present data on the fraction of wetted perimeter, and the results of Fukano and Ousaka (1988) obtained in a 0.026 m ID horizontal tube. The present experimental data are closer to the correlation of Hamersma and Hart (1987) compared to the data presented by Fukano and Ousaka (1988).

3.2.3. Presence of Air Bubbles in the Liquid Film

Some of the photographs taken during this study have highlighted a feature of the air–water horizontal flow previously reported by Jayanti (1990): the presence of air bubbles entrained in the liquid film. Figures 3.3 and 3.4 show photographs obtained before the bend for G_G = 20 kg/m^{2}s and G_L = 90 and 150 kg/m^{2}s, respectively. In Figure 3.3, air bubbles are seen to be entrained in the liquid film, their size varying up to a few millimetres. Jayanti (1990) suggested that the air bubbles were created when a wave rolls over itself.

The plate in Figure 3.3 shows a disturbance wave with liquid drops being released at its crest, and air bubbles travelling in the liquid film. This picture confirms that the creation of liquid

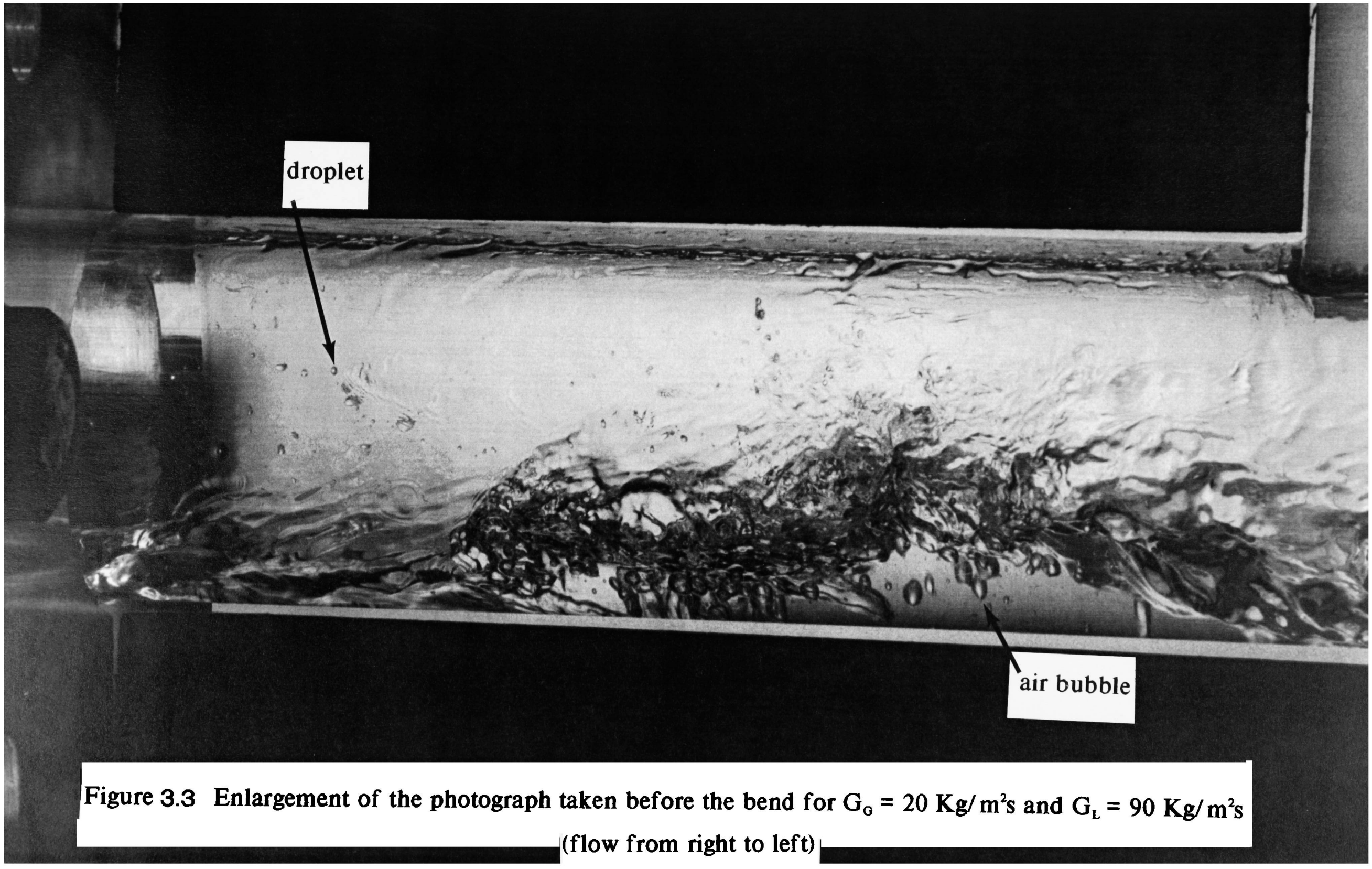

Figure 3.3 Enlargement of the photograph taken before the bend for G_G = 20 Kg/m²s and G_L = 90 Kg/m²s (flow from right to left)

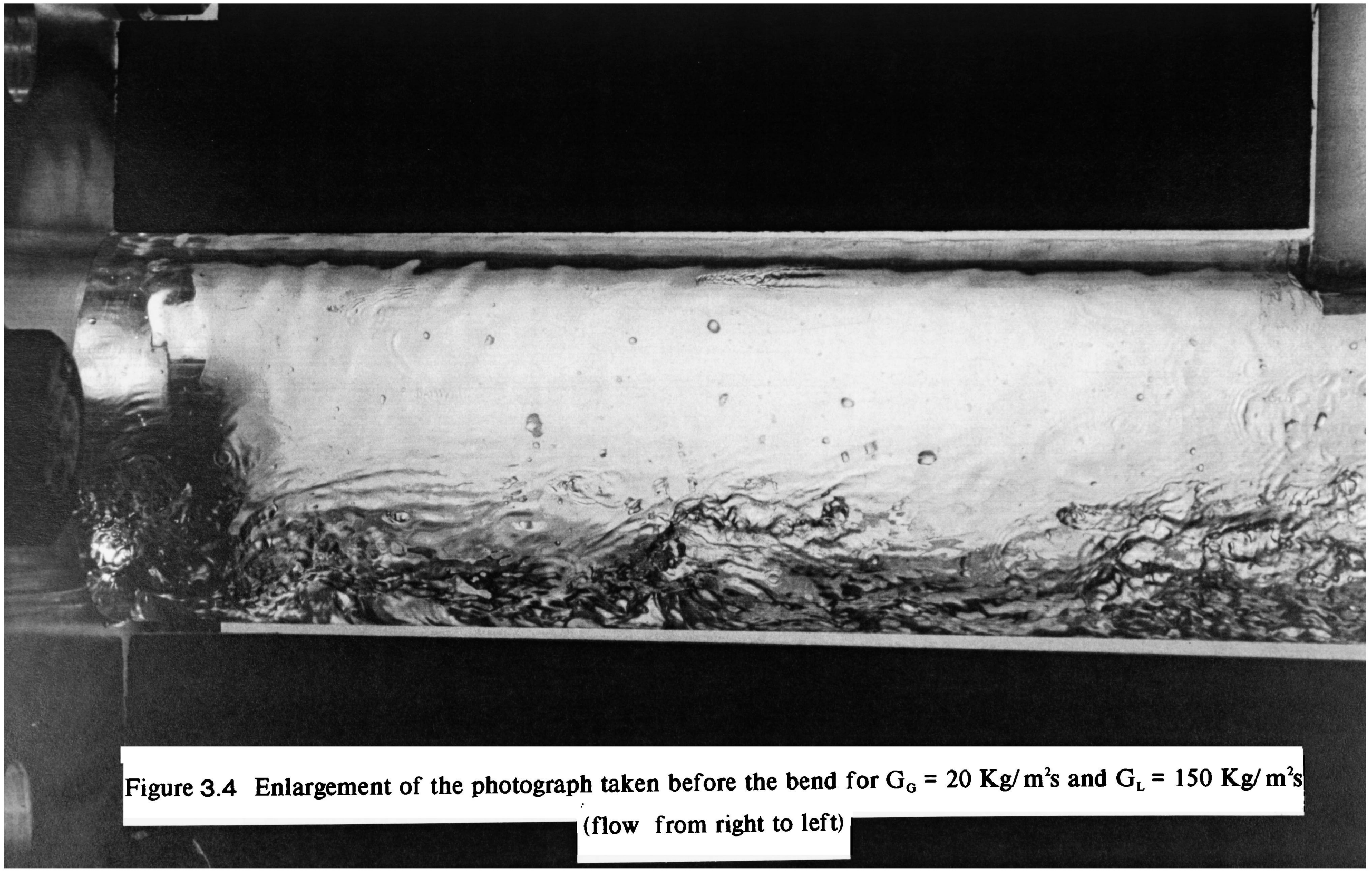

Figure 3.4 Enlargement of the photograph taken before the bend for G_G = 20 Kg/ m²s and G_L = 150 Kg/ m²s (flow from right to left)

drops occurs mainly at the front of the wave. The mechanism of entrainment of the air bubbles is a rolling process, and this occurs at the front of the wave. However, other bubbles are seen to travel towards the rear of the wave. This could mean that after being entrained, the air bubbles were captured by a slower moving layer of the liquid film, and were retarded in relation to the disturbance wave. The release of these air bubbles will probably occur at the back of the wave, and contribute to the entrainment process of liquid drops. The shape of the smaller gas bubbles is nearly spherical, while the larger bubbles appear in an ellipsoid form as a result of the shear action in the liquid film.

From the cine film taken at $G_G = 20$ kg/m^{2}s and $G_L = 150$ kg/m^{2}s it was possible to measure the size of bubbles entrained in the liquid film. The film was analysed using a Vanguard cine film analyser. After calibration of the apparatus against the tube diameter, the size of each bubble in the direction of the tube axis (z), and in the direction normal to the tube axis (y) was measured (z and y are defined according to the frame of reference in Figure 6.2(a)). As many of the bubbles were not spherical, the concept of equivalent bubble diameter (B_{eq}) was introduced. This was assumed as being the diameter of a circle which would have the same area as the ellipsoid projected area of the drop on the plane of measurement, as:

$$B_{eq} = \sqrt{B_z\, B_y} \tag{3.3}$$

where B_z is the diameter of the bubble in z–direction, and B_y is the diameter of the bubble in the y–direction. A total of sixty bubbles were analysed to produce the histogram of bubble size shown in Figure 3.5. The largest entrained bubble that was measured had an equivalent diameter of 2.47 mm, and the minimum size detected corresponds to a limit of 0.4 mm. This, however, may not correspond to the existing minimum size of the bubbles because with the measurement technique employed, bubbles smaller than 0.4 mm could not be measured. For this reason, and also because the sample size is too small to be statistically representative, this data is only qualitatively valid.

The presence of air bubbles in the liquid film was also visually observed for other flow conditions by using a strobe light to 'freeze' the moving flow. This permitted the identification of the flow conditions at which gas bubbles entrained in the liquid film were first observed. The technique was carried out for gas mass fluxes of $G_G = 10$–25 kg/m^{2}s, and liquid mass fluxes between $G_L = 6.2$–50 kg/m^{2}s. For gas flow rates over 25 kg/m^{2}s the flow was too fast to be followed by visual inspection. The observations are summarised in the graph in Figure 3.6, where a boundary line was drawn to identify the onset of bubble entrainment in the liquid film.

In general, the size of the entrained air bubbles in the liquid film appeared to increase as the liquid flow rate increased. However, at this stage it is difficult to say precisely which are the main variables that influence the bubble size. On the one hand, it is possible that the bubble

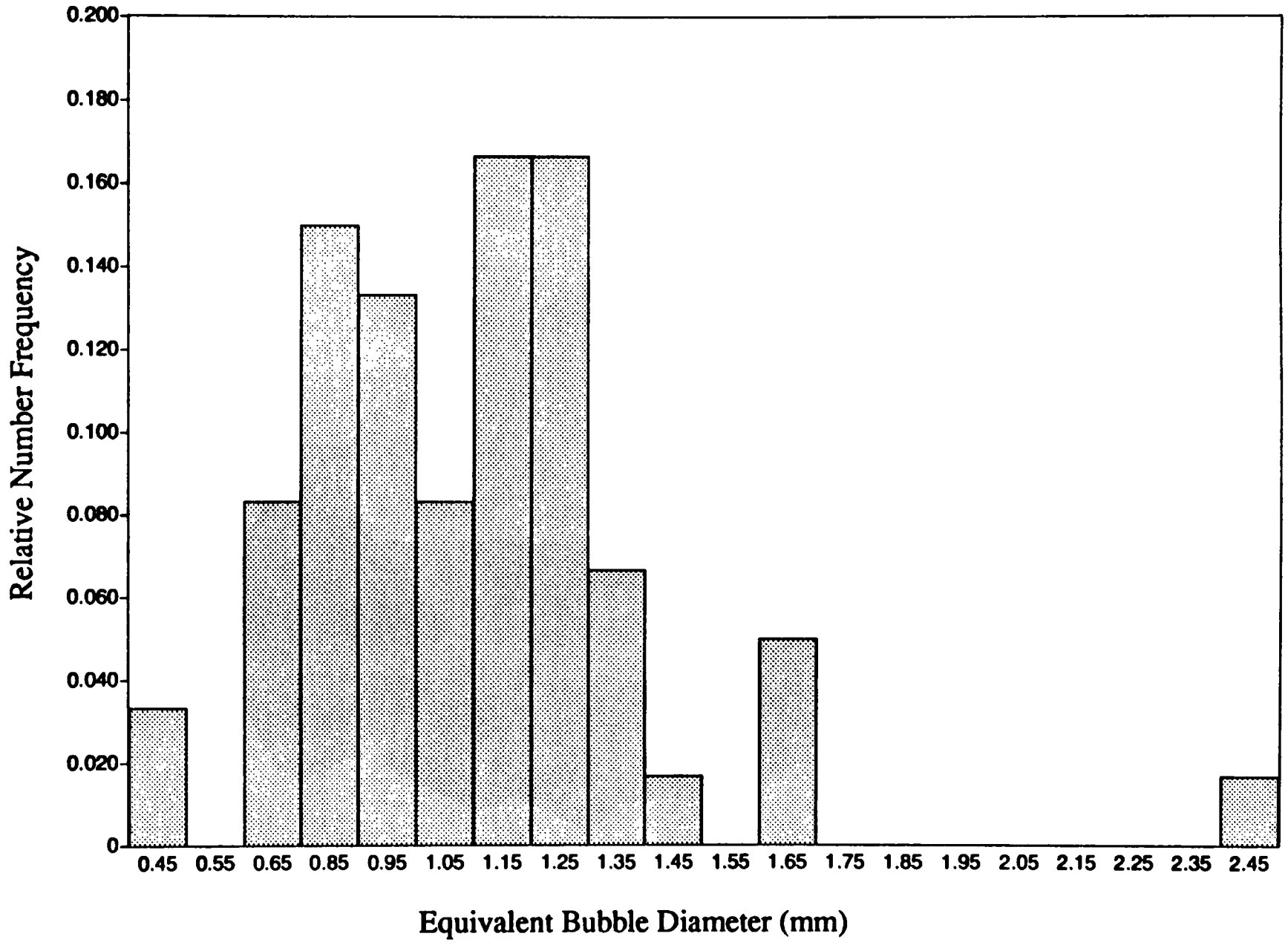

Figure 3.5 Histogram of equivalent bubble diameter for G_G = 20 kg/m^{2}s and G_L = 150 kg/m^{2}s.

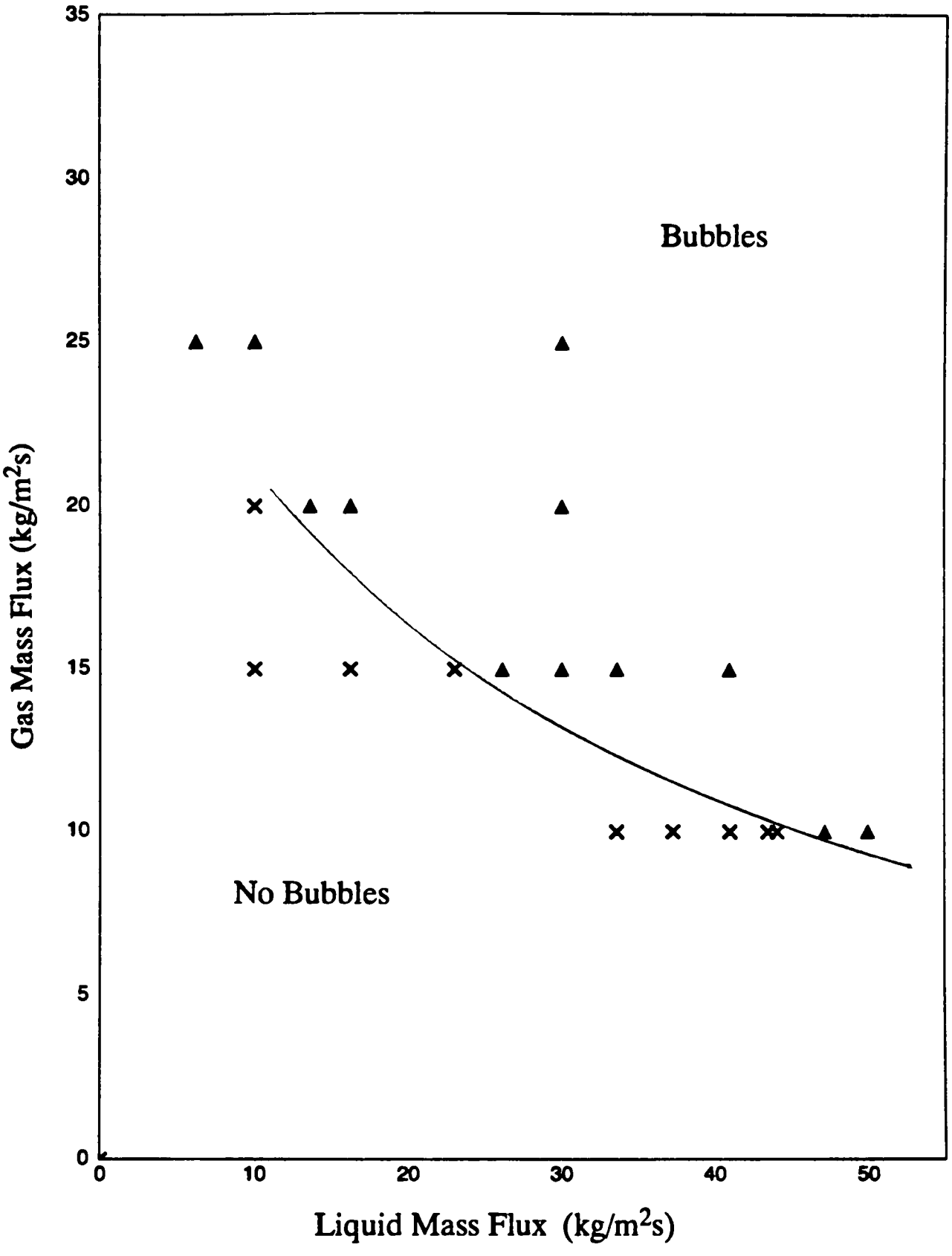

Figure 3.6 Onset of bubble entrainment in the liquid film for air–water in 0.032 m ID horizontal tube.

size may be dependent on the liquid film thickness. On the other hand, the size of the entrained bubbles may be a function of the properties of the waves present on the liquid surface. Smaller bubbles may be created by the break–up of larger ones, and large bubbles may be formed by the coalescence of smaller ones.

3.2.4. Drops Entrained in the Gas Core

The drops that travel in the gas core in two–phase annular flow are created from the large waves present in the liquid film, as illustrated in Figure 3.3. The mechanisms of drop entrainment observed by Azzopardi (1983) for vertical annular flow were discussed in section 1.6.1. According to the author, at low liquid flow rates the main mechanism of drop formation is bag break–up. At higher flows, ligament break–up predominates, which is recognised to produce smaller drops.

In a later paper, Azzopardi (1987) reported that only the bag break–up mechanism was observed in the cine films taken for the flow conditions under study. However, the present cine films which were carried out over a wider range of flow rates, proved that both mechanisms of drop entrainment occur in horizontal flow.

The size of drops was estimated from the still photographs and the cine films taken during this study. From the photograph in Figure 3.4 (taken at G_G = 20 kg/m^{2}s and G_L = 150 kg/m^{2}s) drops as large as 1.5 mm were seen to travel with the gas. Another interesting feature of this photograph is the impingement of a drop seen at the top part of the tube. This was made visible by the formation of a streak along the surface of the liquid film as a result of the impact.

Information on drop size was gathered from the cine films taken at G_G = 20 kg/m^{2}s and liquid mass fluxes of 70, 90 and 130 kg/m^{2}s, and for G_G = 30 kg/m^{2}s and G_L = 70 kg/m^{2}s. At these flow conditions the laser diffraction technique used to determine drop sizes (Chapter 5) could not be applied. The results are presented in Tables B.7 to B.10 (Appendix B), and a typical histogram is shown in Figure 3.7, for G_G = 20 kg/m^{2}s and G_L = 90 kg/m^{2}s. The size of the drops was calculated using the same procedure employed in the estimation of bubble size (see section 3.2.3.), with the exception that every drop was followed for at least five frames. For each drop, the diameter in the tube axis direction (z) and in the direction normal to the tube axis (y) (according to Figure 6.2(a)) were averaged over several frames. An equivalent drop diameter (D_{eq}) was calculated as:

$$D_{eq} = \sqrt{D_z\, D_y} \tag{3.4}$$

where D_z is the average diameter in the z–direction, and D_y is the average diameter in the y–direction.

Several aspects concerning these drop size data should be considered. The error associated with the calculation of D_{eq} (using the propagation of uncertainty analysis described by Owen

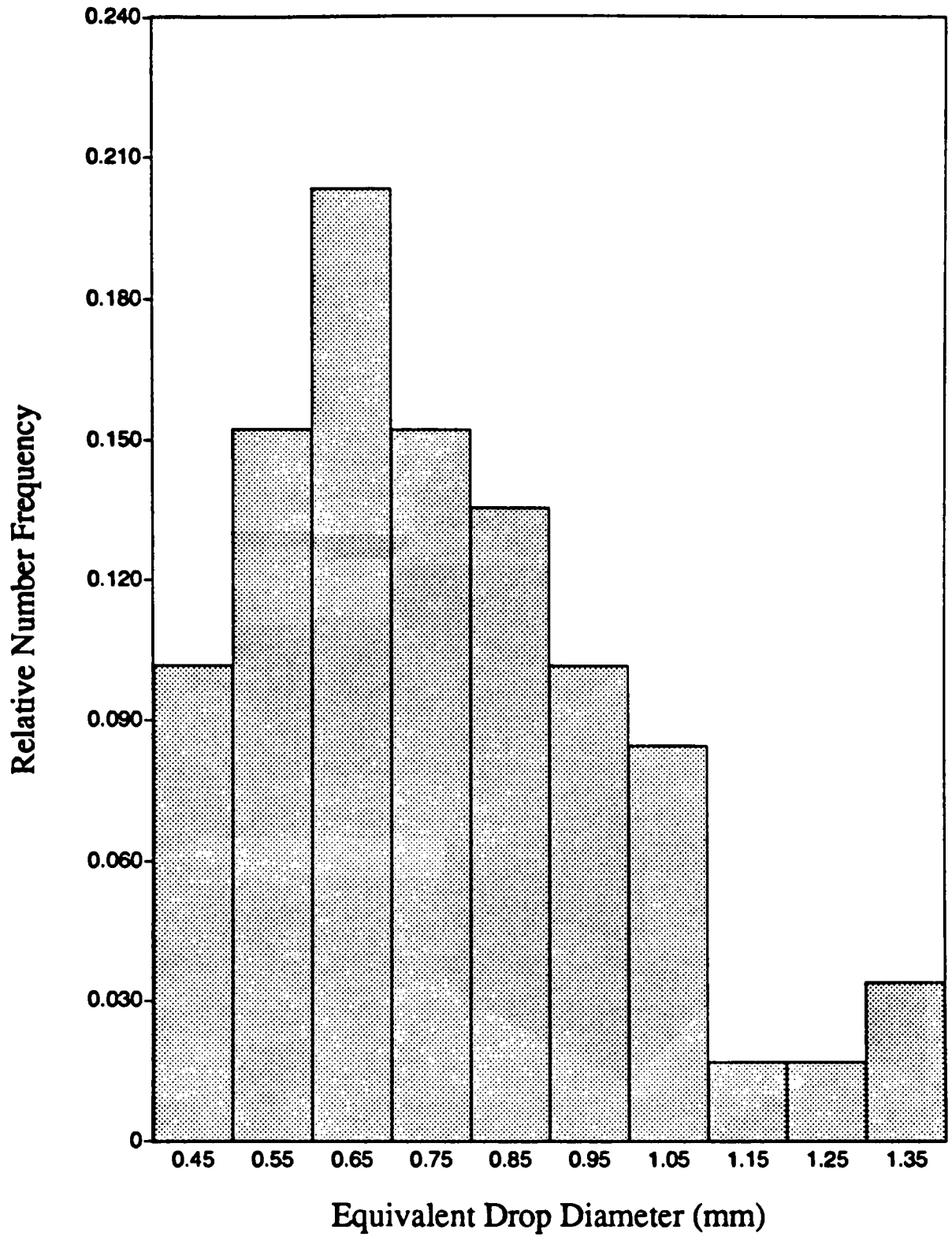

Figure 3.7 Equivalent drop diameter histogram for G_G = 20 kg/m^{2}s and G_L = 90 kg/m^{2}s.

(1986)) is quite high as seen in Tables B.7 to B.10. Also with the measurement technique employed, only drops with diameter higher than 0.4 mm could be tracked. A considerable number of smaller drops should exist in the flow, as the drop size measurements discussed in Chapter 5 have indicated. Finally, only around sixty drops were analysed per film, which makes the sample statistically unrepresentative. In view of this, any conclusions drawn from these results should be taken with care.

3.3. Flow Characteristics at the Bend

The presence of a bend introduces a developing situation in the gas–liquid flow pattern. This section discusses the changes in the flow characteristics of an air–water mixture caused by the effect of a 90° horizontal bend. These features were captured in still photographs taken at four different positions around the bend, and are shown in Figures D2, D3, D4 and D5 (Appendix D).

For gas–liquid stratified and annular flow in a bend, the variation in the liquid film thickness around the pipe circumference is complex. Under conditions where the momentum of the gas phase is higher than the momentum of the liquid phase, the maximum liquid film thickness is seen to be displaced to the inside of the bend. This phenomenon is called film inversion, and was first reported by Banerjee et al (1967) (see section 1.7.2.).

In the present study, film inversion was clearly seen for G_L=10 kg/m^{2}s and G_G =30, 40 and 50 kg/m^{2}s, where the high momentum fluid (the gas in this case) moves to the outside of the bend. At these conditions, the drops travelling in the gas stream were also seen to deposit on the outside of the bend forming a thin liquid film. This film was not connected to the liquid film on the inside of the bend. It was also observed that in the upper half of the tube, the outer thinner film tended to breakdown into rivulets which were pulled to the top of the tube in an anti–clockwise, cork–screwing fashion. This is illustrated in Figure 3.8, for the flow conditions G_G = 30 kg/m^{2}s and G_L = 10 kg/m^{2}s. On the lower half, the thin liquid film was drawn from the outer wall towards the bottom of the tube, in a clockwise motion.

For higher liquid flow rates the thin film did not breakdown. Instead, it combined with the thicker film on the inside of the bend to form an annular film section around the pipe circumference.

This movement of the liquid film/rivulets at the bend may be linked to the appearance of secondary flow in the gas phase (see Figure 1.7.2). Previous studies of the gas velocity at the exit of bends by Chakrabarti (1976) in a horizontal 90°bend, and by Anderson and Hills (1974) in a vertical 180° bend, have shown that the maximum velocity in the gas velocity profile was displaced towards the outside wall of the bend. This was taken as evidence of the presence of a secondary flow in the gas phase at the bend. This secondary flow is thought to be responsible for the swirl motion observed in the visualisation experiments of this study.

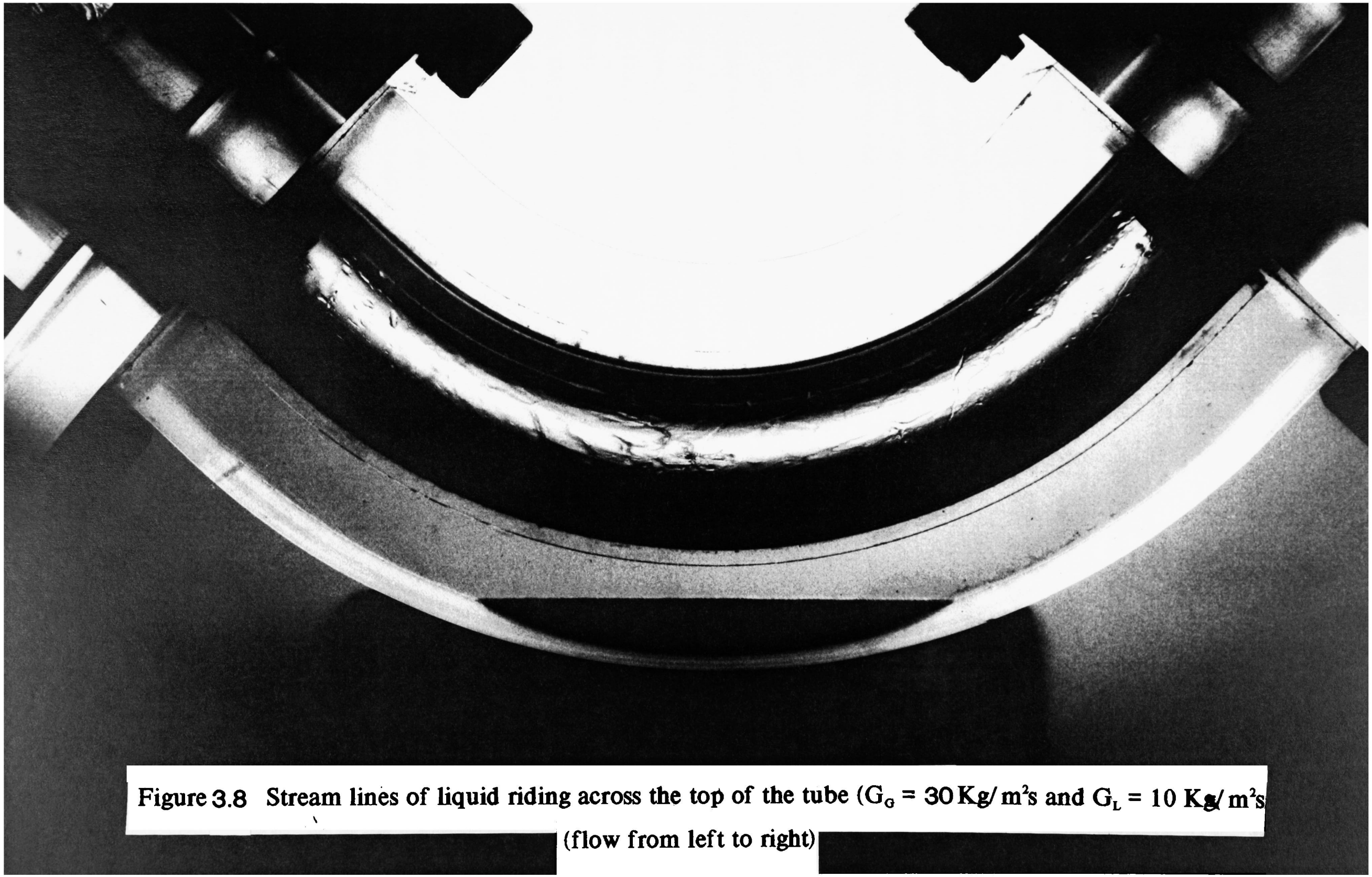

Figure 3.8 Stream lines of liquid riding across the top of the tube (G_G = 30 Kg/ m²s and G_L = 10 Kg/ m²s (flow from left to right)

3.4. Flow Characteristics after the Bend

This section describes observations of the flow carried out downstream of the 90° horizontal bend. Photographs were taken after the bend for the flow conditions mentioned in Table 3.1, and are shown in Figure D6 (Appendix D). In addition, the drop flow was also photographed downstream of the bend, after removal of the liquid film.

It was mentioned in the previous section, that the secondary flow existing in the gas phase was responsible for a swirl movement experienced by the liquid film at the bend, and that for certain wavy–stratified flow conditions, an annular film section was formed around the pipe circumference at the bend. This annular film section was seen to be maintained for a small distance downstream of the bend, before stratified conditions were re–established (Figure 3.10).

The length of the annular section forming after the bend, increased as the liquid flow increased (for a constant gas flow) as shown in the sequence of photographs in Figures 3.9, 3.10 and 3.11. In Figure 3.11, the surface of the pipe downstream of the bend is completely covered with an annular film, but this was seen to be disrupted further along, beyond the edge of the photograph.

The drop size measurements after the bend discussed in Chapter 5, indicated an increase in drop size caused by the presence of the bend. In order to inspect the drop flow, high speed still photographs were taken after the liquid film was removed through a porous wall.

Figure 3.12 shows the photograph of a ruler taken with the same magnification as that used when photographing the drop flow. The minimum division corresponds to 1 mm, which indicates that a magnification factor of five has been used.

Several shots were taken at random for G_G = 40 kg/m^{2}s and G_L = 50 kg/m^{2}s (Figure 3.12 (a) and (b)), and for G_G = 70 kg/m^{2}s and G_L = 30 kg/m^{2}s (Figure 3.14 (a) and (b)). Several considerations can be made from these figures. Comparison of the two photographs taken for the same flow conditions show a variation of drop concentration with time. As drops are mostly formed from roll waves, and these are known to appear with a certain frequency, it is not surprising that drop concentration is not constant. The cine films of this study also confirmed that the number of drops entrained in the gas core always increased near the presence of a large wave.

By comparing Figures 3.13 and 3.14 it can be said that, in general, drop size increases with decreasing gas flow rate. Larger drops are observed in the photographs taken at lower gas flows. These figures also support the drop size measurements after the bend obtained with the laser diffraction technique (Chapter 5). The maximum drop size seen in the photographs is within the range indicated by the drop size distributions.

The photograph in Figure 3.13 (b) has captured evidence of drop coalescence and subsequent separation of two drops. It shows a large drop linked to a smaller one by a thin filament of liquid. At some stage it is likely that these drops have collided, but subsequently have

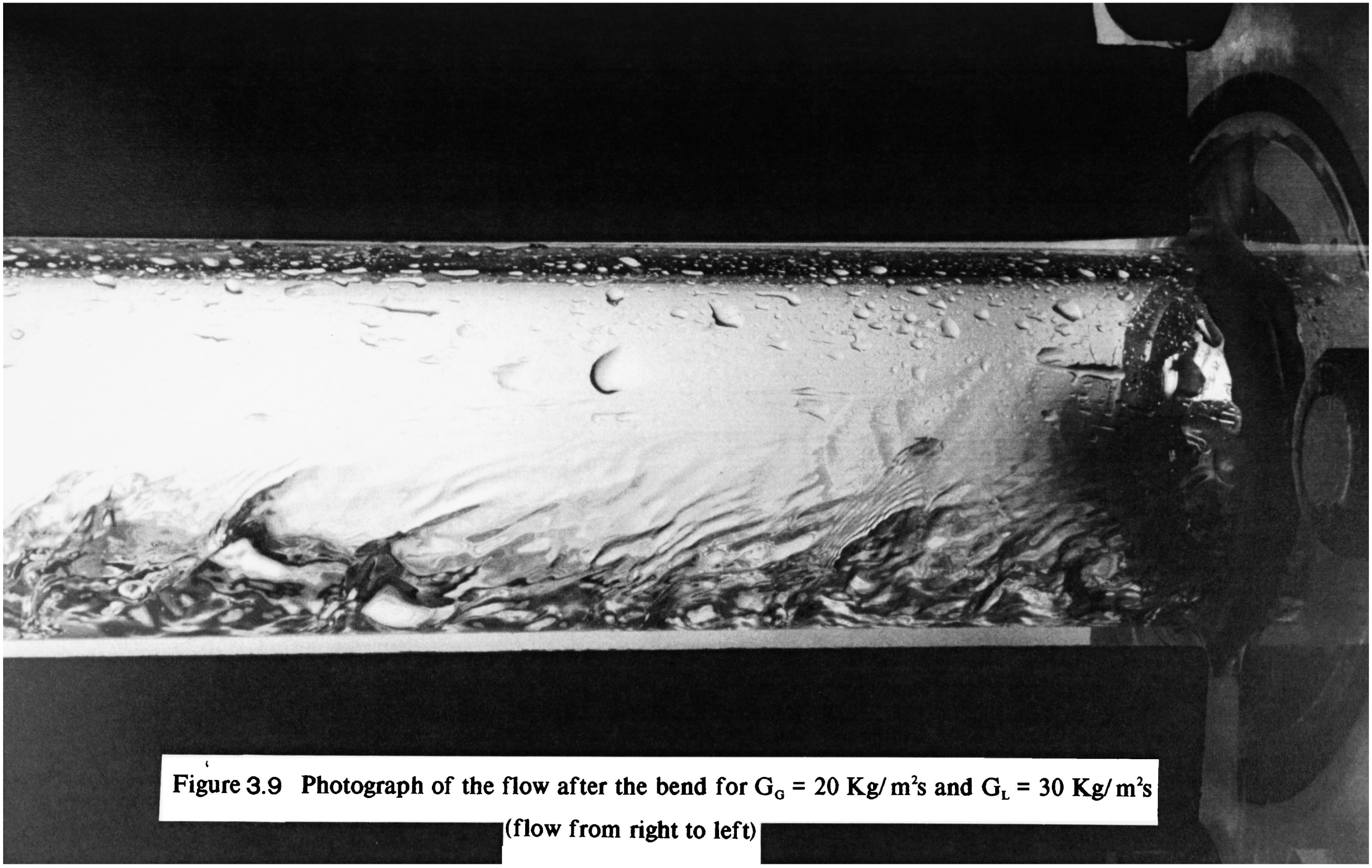

Figure 3.9 Photograph of the flow after the bend for G_G = 20 Kg/ m^2s and G_L = 30 Kg/ m^2s (flow from right to left)

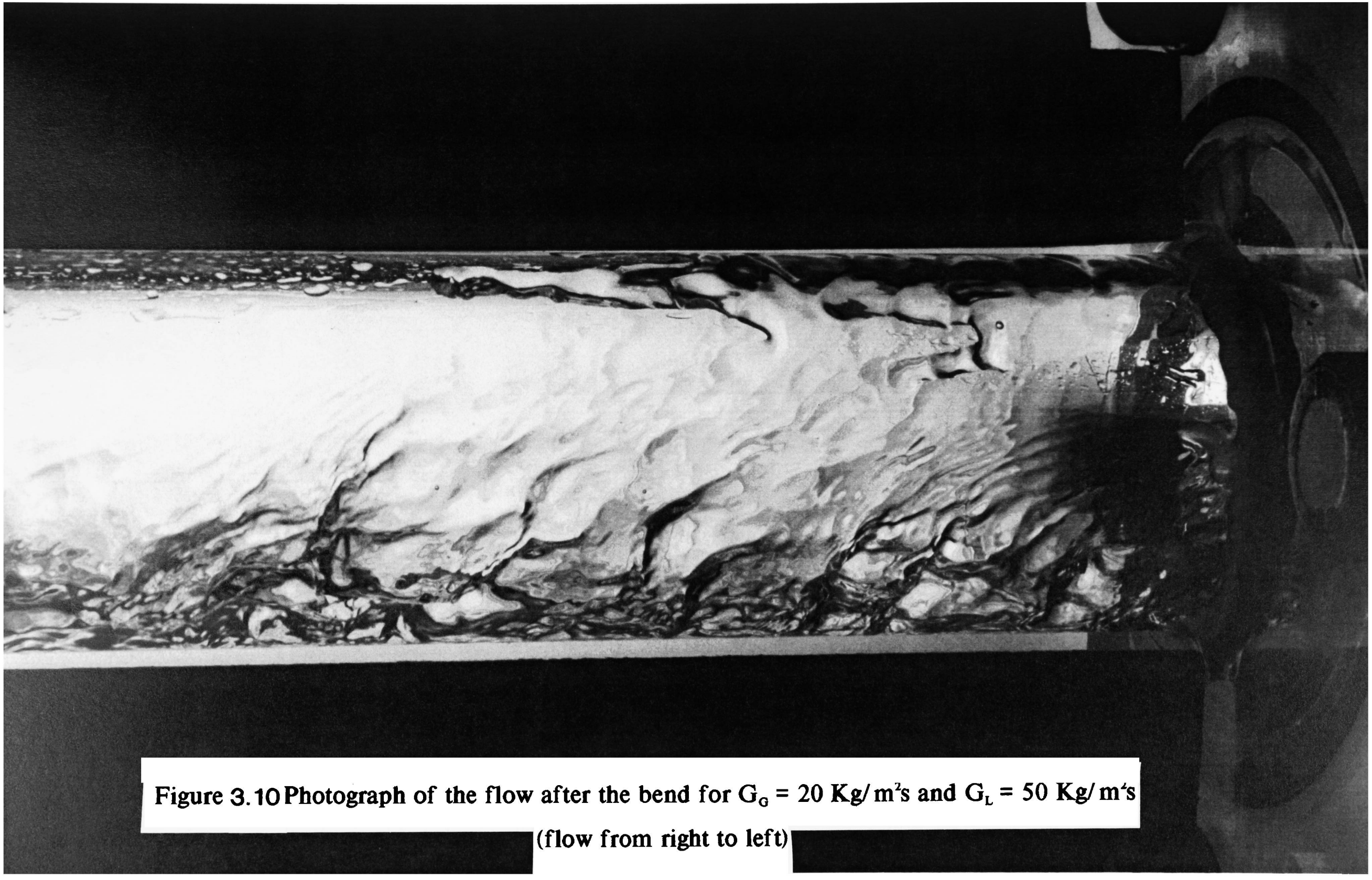

Figure 3.10 Photograph of the flow after the bend for G_G = 20 Kg/m²s and G_L = 50 Kg/m²s (flow from right to left)

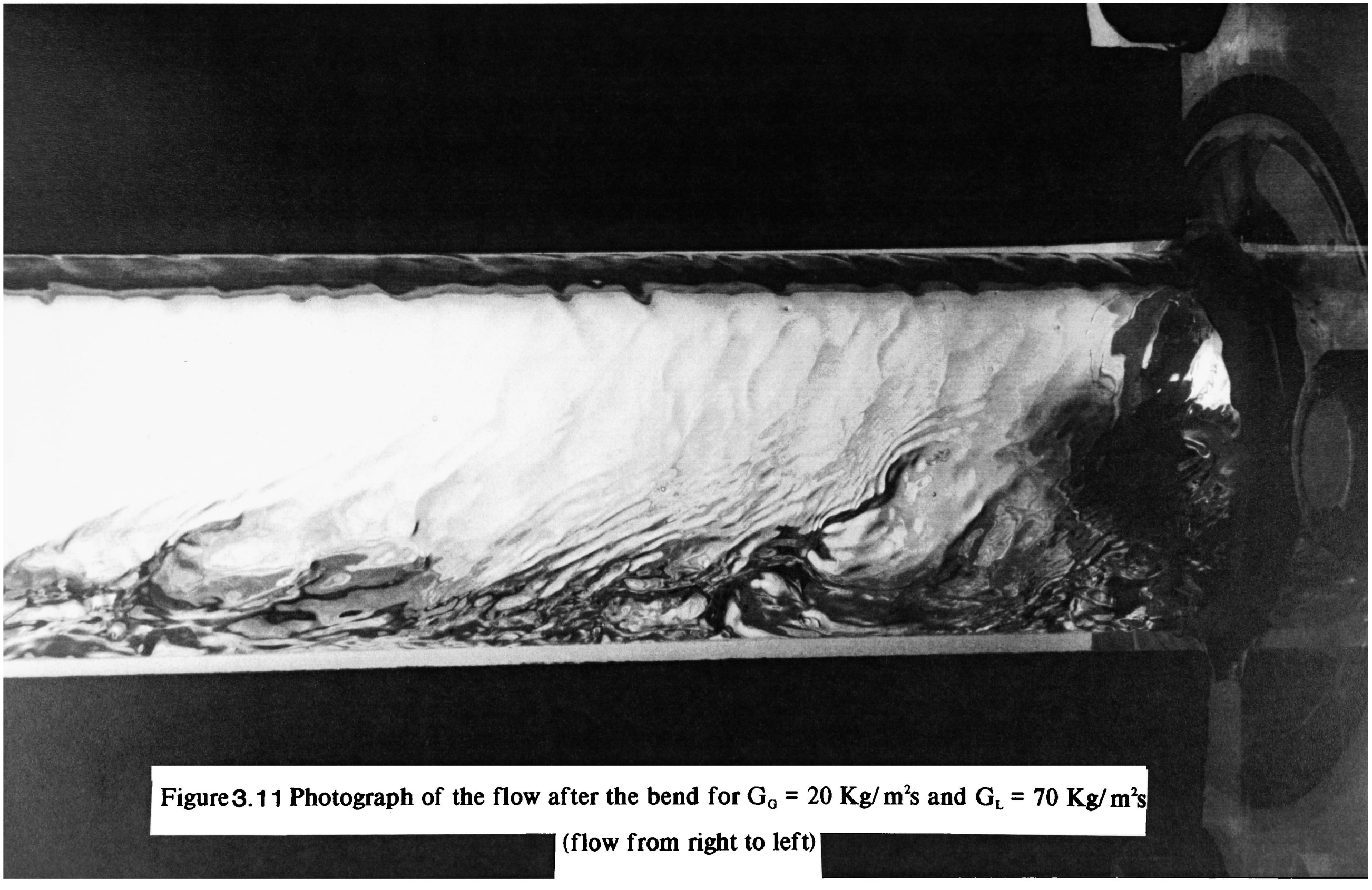

Figure 3.11 Photograph of the flow after the bend for G_G = 20 Kg/m²s and G_L = 70 Kg/m²s (flow from right to left)

Figure 3.12 Magnification used in photographing the drop flow after the bend.

(a)

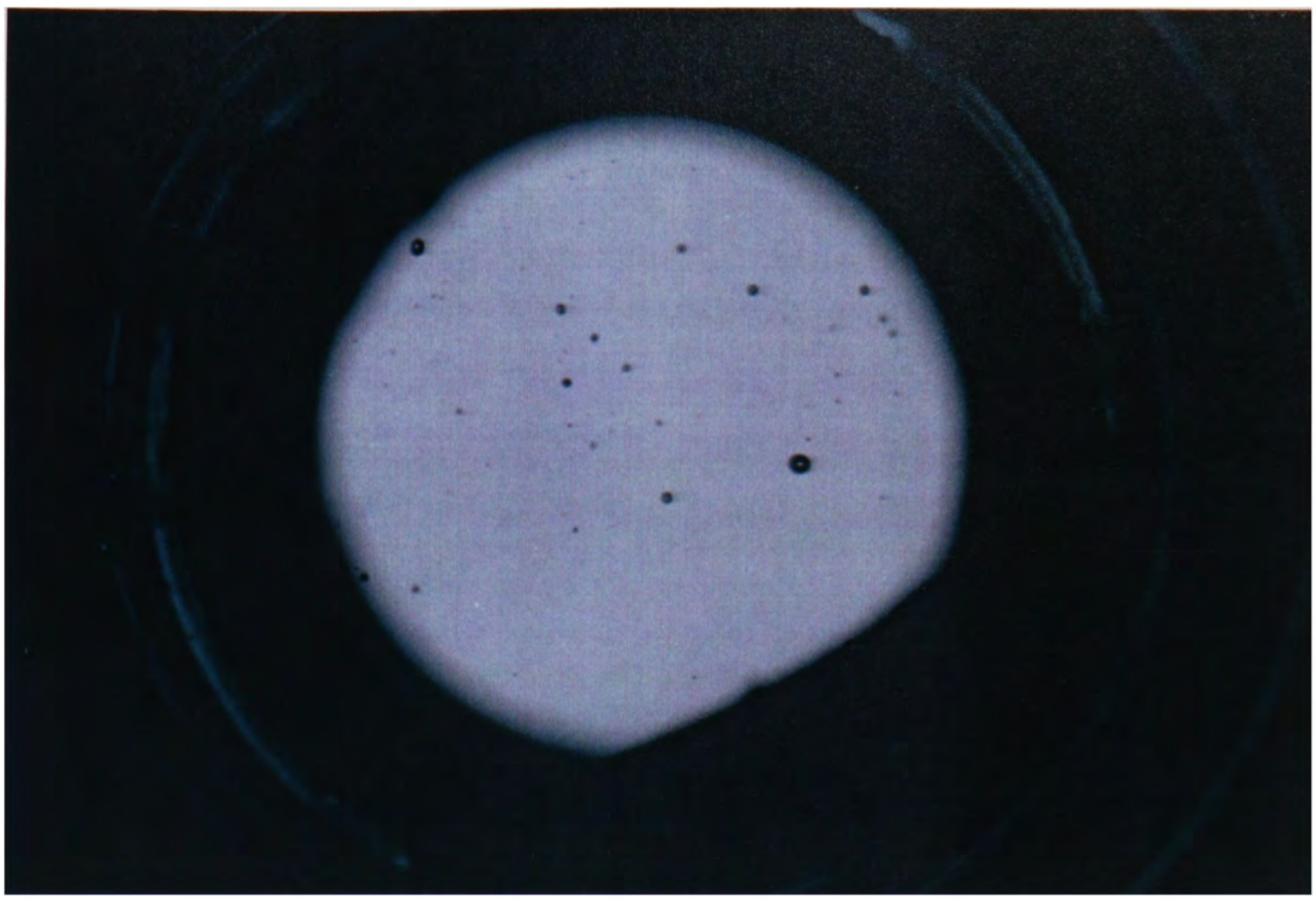

(b)

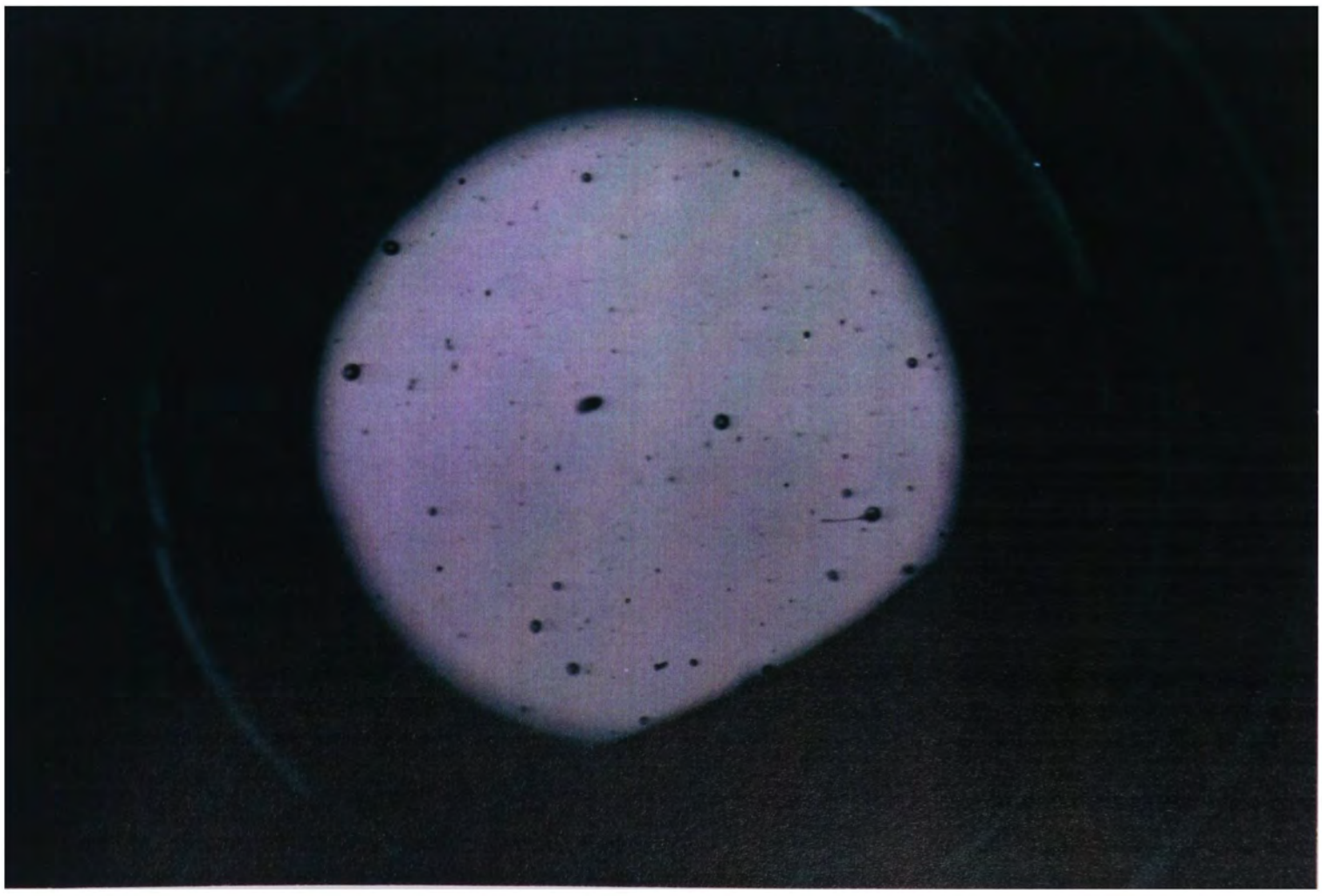

Figure 3.13 Photographs of the drop flow after the bend for G_G = 40 kg/m^{2}s and G_L = 50 kg/m^{2}s.

(a)

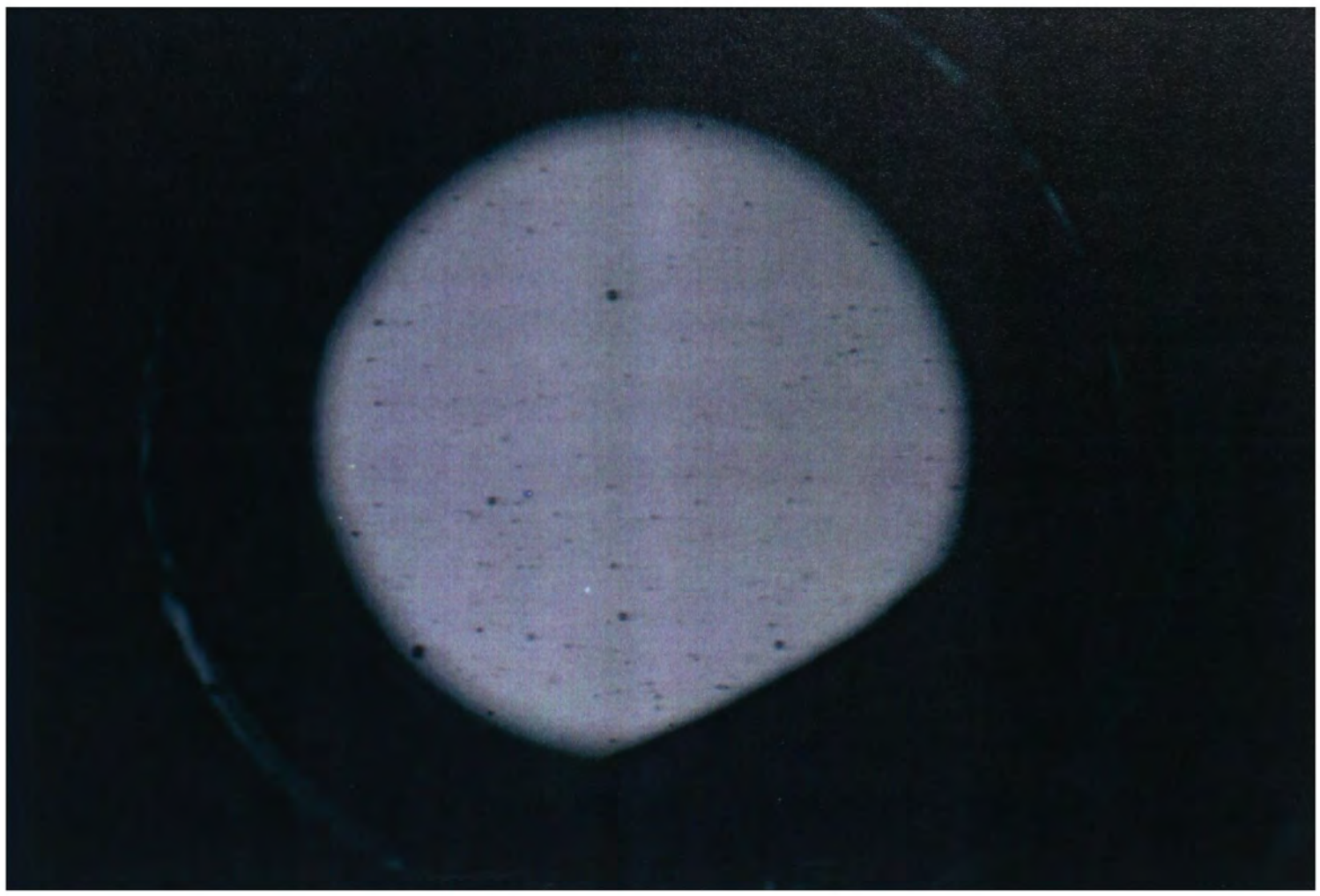

(b)

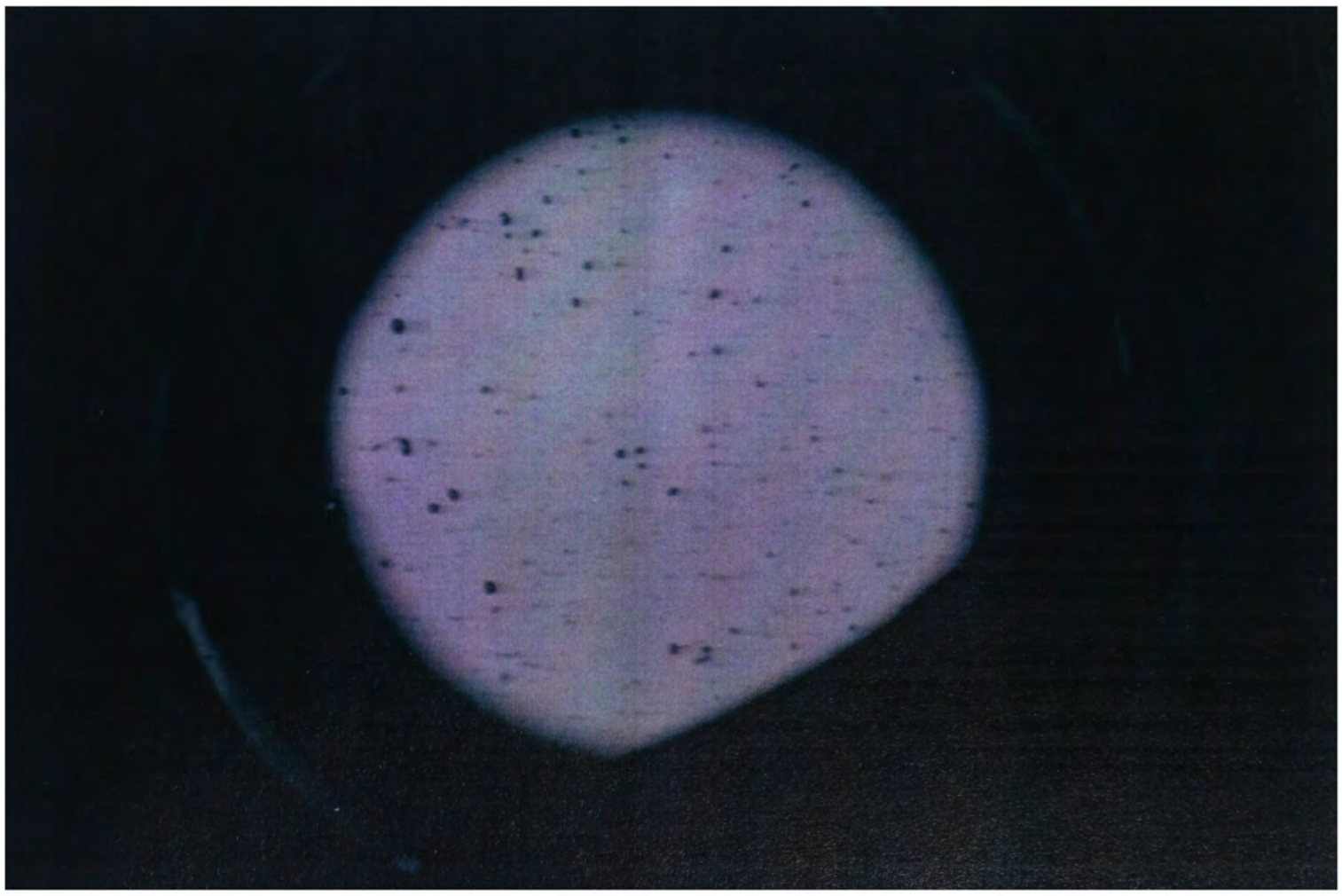

Figure 3.14 Photographs of the drop flow after the bend for G_G = 70 kg/m^{2}s and G_L = 30 kg/m^{2}s.

separated as shown in the photograph. If the conditions had been more favourable, permanent coalescence would have arisen. Drop coalescence can be an important parameter contributing to the increase in drop size observed after the bend.

3.5. Conclusions

The following conclusions can be drawn from the discussion above:

- For the range of air–water flow rates studied, the flow patterns observed were wavy–stratified with and without atomisation, annular and pseudo–slug flow.
- During wavy–stratified flow, the fraction of wetted perimeter increased with both gas and liquid flow rates. The present experimental data are closer to the correlation of Hamersma and Hart (1987) compared to the data presented by Fukano and Ousaka (1988).
- Photographs taken before the bend showed interesting features, such as the presence of air bubbles entrained in the liquid film, and the creation of liquid drops at the crest of a roll wave.
- The size of entrained air bubbles was measured from the cine film taken at G_G = 20 kg/m^{2}s and G_L = 150 kg/m^{2}s. The larger bubbles had an ellipsoid shape, while the smaller ones were almost spherical. The larger bubbles observed had an equivalent diameter of 2.47 mm.
- For the flow conditions of G_G = 10–25 kg/m^{2}s and G_L = 6.2–50 kg/m^{2}s, it was possible to identify the conditions for the onset of the entrainment of air bubbles in the liquid film.
- The present cine films showed that both mechanisms of drop entrainment (bag break–up and ligament break–up) occur in horizontal air–water flow.
- The phenomenon of film inversion reported by Banerjee et al (1967) was observed at the 90° horizontal bend.
- At the horizontal 90° horizontal bend, the liquid film was seen to have a swirl movement, in which at the upper part of the tube the liquid was pulled across from the outer wall of the bend to the top of the tube in an anti–clockwise, cork screwing fashion. In the lower half, the liquid film was drawn from the outer wall towards the bottom of the tube, in a clockwise motion. It is thought that a secondary flow existing in the gas phase can be responsible for this swirl movement of the liquid film at the bend.
- The still photographs of the drop flow taken after the bend, confirm that drop size decreased with increasing gas flow rate. These photographs also support the drop size measurements obtained with the laser diffraction technique (Chapter 5).
- The photographic work after the bend has captured evidence of drop coalescence and subsequent separation of two drops.

4. ENTRAINMENT IN HORIZONTAL TWO–PHASE FLOW

The atomisation of a liquid film by a high velocity gas is of considerable practical importance in many engineering systems, such as the film cooling of jet and rocket engines and the burnout heat flux in nuclear reactors. Separators and evaporators are also equipment units affected by atomisation and entrainment of liquid films.

Beyond critical gas and liquid superficial velocities, the liquid film becomes highly agitated and roll waves appear. Liquid is torn from the surface of these waves giving rise to drop entrainment in the gas, and the liquid film is replenished by drop deposition. This is a dynamic system with a continuous mass transfer of liquid to and from the film. Under equilibrium conditions the rate of drop entrainment is equal to the rate of deposition.

The quantity of liquid entrained in the gas can be described in terms of an entrained liquid fraction *(E)*, which is defined as

$$E = \frac{G_{LE}}{G_L} \tag{4.1}$$

where G_{LE} is the entrained liquid mass flux and G_L is the total liquid mass flux. The entrained fraction (E) can vary from values close to zero up to values approaching unity.

For a constant liquid flow and increasing gas velocity, Dallman (1978) introduced the concept of maximum possible entrainment. The author observed that the quantity of entrained liquid reached a maximum when the liquid film flow rate was approximately equal to the critical film flow rate for the onset of entrainment. Dallman referred to this as the 'fully entrained atomisation region (FEAR)', and at this condition the maximum entrained fraction (E_M) was given by

$$E_M = \frac{G_L - G_{LFC}}{G_L} \tag{4.2}$$

where G_{LFC} is the critical liquid film mass flux below which no more atomisation occurs irrespective of further increases in the gas.

This chapter reviews both experimental and analytical work on the onset of entrainment and liquid entrainment, with special emphasis on horizontal flow. New entrainment data are presented for the horizontal flow of an air–water system in a 0.032 m ID tube. The influence of a horizontal bend on the quantity of liquid entrained in the gas is also studied (see Tables B.11 to B.15 – Appendix B).

4.1. Onset of Entrainment

When gas-liquid flow in a horizontal tube there are flow conditions where the liquid flows as a film along the wall and also as entrained drops in the gas core. However, before liquid atomisation takes place, several transitions occur in the gas-liquid interface according Andritsos and Hanratty (1987). These transitions occurring at the interface have already been discussed in section 1.3, where Figure 1.8 summarises the flow regimes and wave patterns observed by the author for air-water flowing in a 0.0254 m ID horizontal tube.

Another study by Whalley et al (1977) using axial view photography technique revealed that most of the liquid drops are entrained from the roll waves. In the absence of roll waves few drops are seen.

A large number of experimental and analytical studies have been carried out to determine the inception conditions for entrainment. Thorough reviews of these works are given by Hewitt and Hall-Taylor (1970) and Ishii and Grolmes (1975). Table 4.1 lists the experimental work for horizontal flows in pipes and channels.

TABLE 4.1 EXPERIMENTAL WORK ON ONSET OF ENTRAINMENT IN HORIZONTAL TWO-PHASE FLOW

Author	System	Geometry
Kinney et al (1953)	air-water	circular tube d_t=0.0508 & 0.1016 m
Van Rossum (1959)	air-water air-mineral oil 1 air-mineral oil 3 air-gas oil air-kerosine air-water/butanol solutions	rect. channel 0.15 x 0.15 m
Woodmansee & Hanratty (1969)	air-water air-glycerine/water solutions	rect. channel 0.0254 x 0.3048 m
Arruda (1970)	air-water	circular tube d_t=0.0254 & 0.0508 m
Russel & Rogers (1972)	air-water	rect. channel 0.0254 x 0.1524 m
Chang (1973)	air-water/glycerine solutions air-water/isobutanol solutions	rect. channel 0.0254 x 0.1524 m
Mishima & Michiyoshi (1987)	air-water	rect. channel 0.016 x 0.040 m

Existing data for air–water systems are plotted in Figure 4.1, in terms of a critical liquid Reynolds number versus a critical gas velocity. This plot, which identifies the flow conditions for the onset of entrainment, reveals three distinct regions. At large liquid Reynolds numbers the critical gas velocity for the onset of entrainment is virtually constant, corresponding to the minimum gas velocity below which no entrainment occurs irrespective of further increases in the liquid flow. In this region large roll waves may be present, but the momentum of the gas is insufficient to tear liquid from the waves.

Below a certain liquid Reynolds number the critical gas velocity increases rapidly with decreasing liquid flow, defining the curve of critical film flow rate (Figure 4.1). In the intermediate region of the graph, the inception of atomisation is controlled by both gas velocity and liquid flow rate.

Hewitt and Hall–Taylor (1970) pointed out that large discrepancies arise when comparing existing correlations and also experimental data on the onset of entrainment (see Figure 4.1). The authors argued that these discrepancies were caused by using different ways of defining the inception point of atomisation, and by the different techniques used in its detection.

4.1.1. Critical Film Flow Rate

Critical film flow rate is an important parameter linked to the inception of atomisation and also to the concept of maximum entrainment introduced by Dallman (1978). One of the most straightforward methods to measure critical film flow rates for a set of gas velocities, is to slowly increase the liquid flow for each gas velocity and record the liquid flow at which atomisation is first observed. Although good in theory, in practice the process is quite laborious.

An alternative solution, which was adopted by Dallman (1978), is to make an estimate of the critical film flow from a plot of film flow measurements against superficial gas velocities, where at high gas velocities the liquid film approaches a constant value (G_{LFC}), for a given liquid flow. These conditions mark the point at which further entrainment stops irrespective of gas velocity.

Dallman (1978) pointed out the difference between plots of liquid film flow rate versus gas flow rate for vertical and horizontal flow. The graph in Figure 4.2 shows data for vertical upflow taken by Whalley et al (1973) in a 0.0318 m pipe, and Figure 4.3 the entrained liquid flow results of Dallman in a horizontal tube 0.0254 m ID. The author suggested that for horizontal flow the liquid film did not approach a single critical film flow at high gas velocities as in vertical flow, but instead tended to smaller G_{LFC} values as the liquid flow decreased.

From his 'FEAR' studies, Dallman also found that the critical film flow rate per unit perimeter ($\dot{m}_{LFC}/\pi\ d_t$) depended on the concentration of entrained drops in the gas core at the onset of the fully entrained region ($\dot{m}_{LE}/\dot{m}_G$), but as the concentration was increased $\dot{m}_{LFC}/\pi\ d_t$

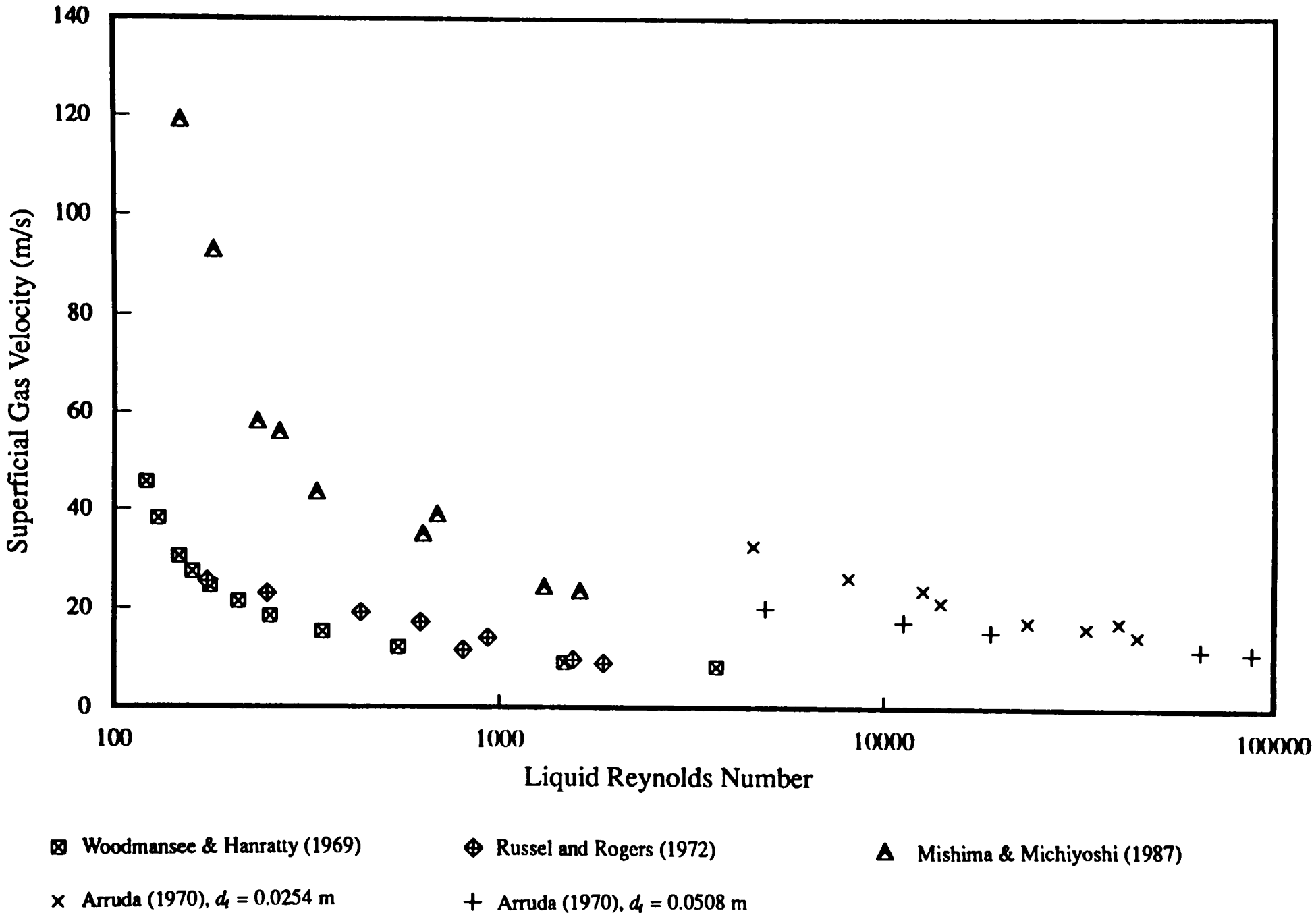

Figure 4.1 Experimental data on onset of atomisation for horizontal air–water flow.

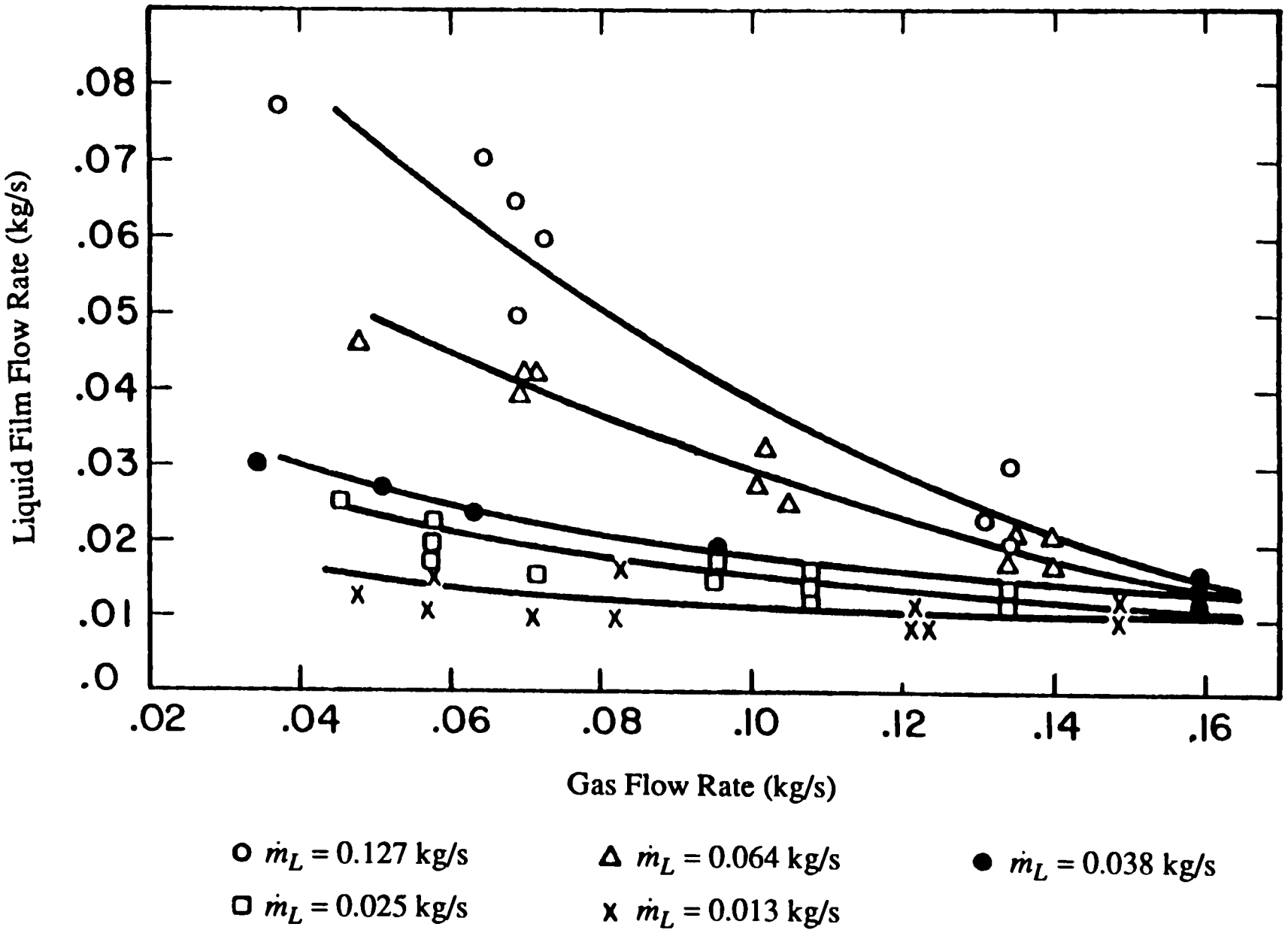

Figure 4.2 Liquid film flow measurements of Whalley et al (1973) for air–water vertical upflow in a 0.0318 m ID tube.

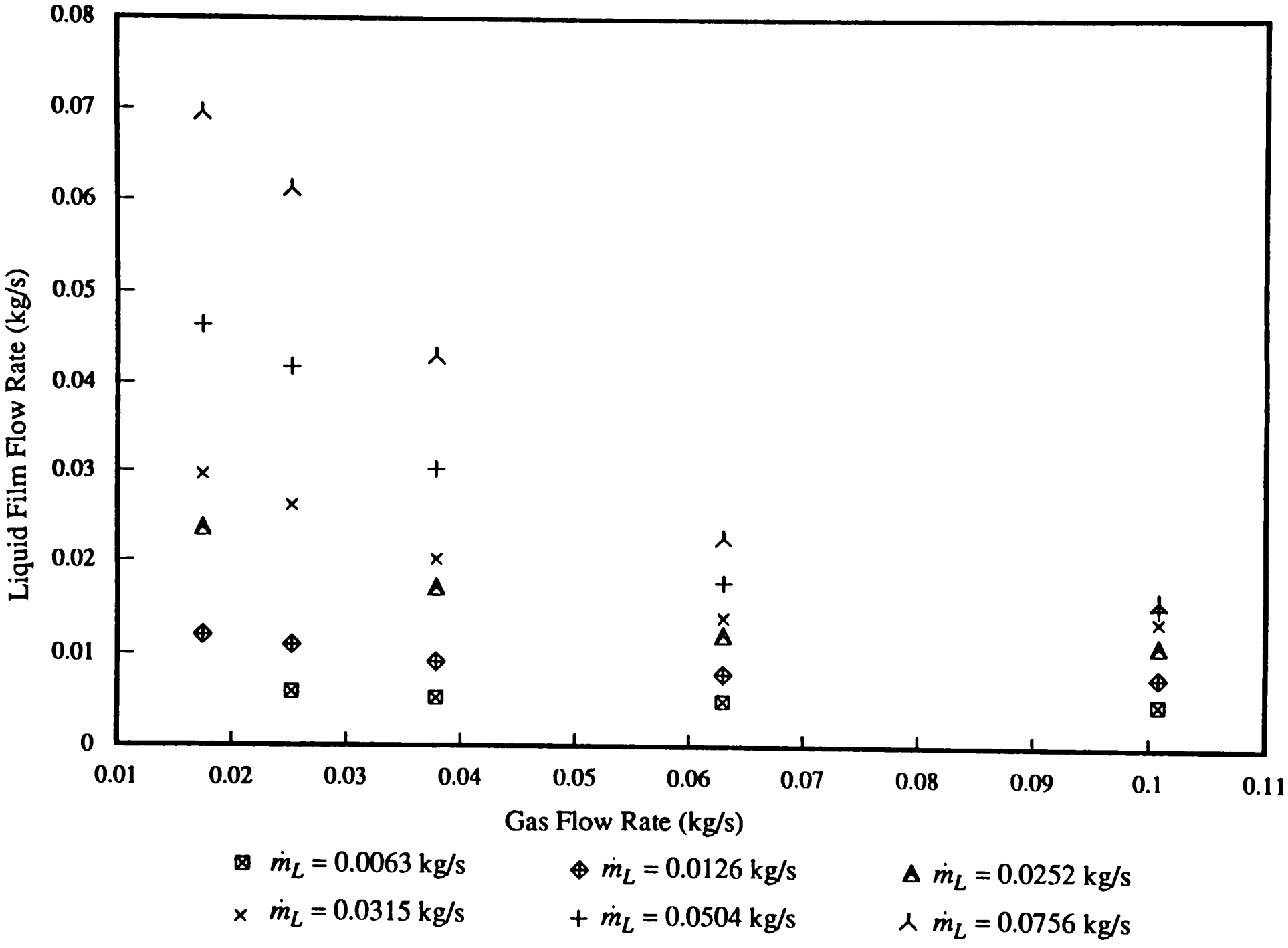

Figure 4.3 Liquid film flow measurements of Dallman (1978) for air–water horizontal flow in a 0.0254 m ID tube.

became a constant (Figure 4.4). This variation of the critical liquid film flow rate with entrained drop concentration was explained as a consequence of the asymmetric distribution of the liquid film thickness in horizontal pipes. Figure 4.4 also indicates the relation between $\dot{m}_{LFC}/\pi\ d_t$ and the entrained drop concentration for the air–water measurements of Laurinat (1982) in a 0.0508 m horizontal tube, and the film flow rate observed by Woodmansee and Hanratty (1969) for the onset of atomisation.

Ishii and Grolmes (1975) developed a criterion for the minimum liquid Reynolds number below which no entrainment occurs. They argued that for full interaction between the gas core and the film, the waves should penetrate the gas boundary layer. The correlation proposed for the minimum liquid Reynolds number for the onset of atomisation was given by:

$$\mathrm{Re}_{LFC} = \left(\frac{y^+}{0.347}\right)^{1.5} \left(\frac{\varrho_L}{\varrho_G}\right)^{0.75} \left(\frac{\mu_G}{\mu_L}\right)^{1.5} \tag{4.3}$$

where the dimensionless distance from the wall $y^+ = 10$.

4.1.2. Critical Gas Velocity

The critical gas velocity (U_{SGC}) defines the point at which entrainment starts for low liquid flow rates. In this section some of the correlations developed for U_{SGC} for horizontal flow are presented.

Van Rossum (1959) correlated his results obtained in a horizontal channel for several fluid systems using various dimensionless groups. In Figure 4.5 the liquid Reynolds number is plotted against the parameter S, where $S=U_{SGC}\ \mu_L/\sigma$, μ_L is the liquid viscosity and σ is the surface tension. It is seen that for each liquid there is a gas velocity below which no atomisation of the film occurs. The author proposed the following empirical rule for the critical gas velocity:

$$U_{SGC}\ (m/s) = \frac{1}{4}\ \sigma\ (dyne/cm) \tag{4.4}$$

This correlation should not be used outside the conditions of Van Rossum's experiments.

Ishii and Grolmes (1975) developed a criterion for the onset of entrainment based on a balance of forces acting at the crest of a roll wave. They considered that entrainment began when the drag force exerted by the gas stream at the crest of the wave was greater than the surface tension force. For low liquid Reynolds numbers (Re_L<160 for horizontal and vertical upflow) the authors considered that drops were formed due to a wave undercut mechanism, also referred to as bag break–up. The correlation for U_{SGC} took the form:

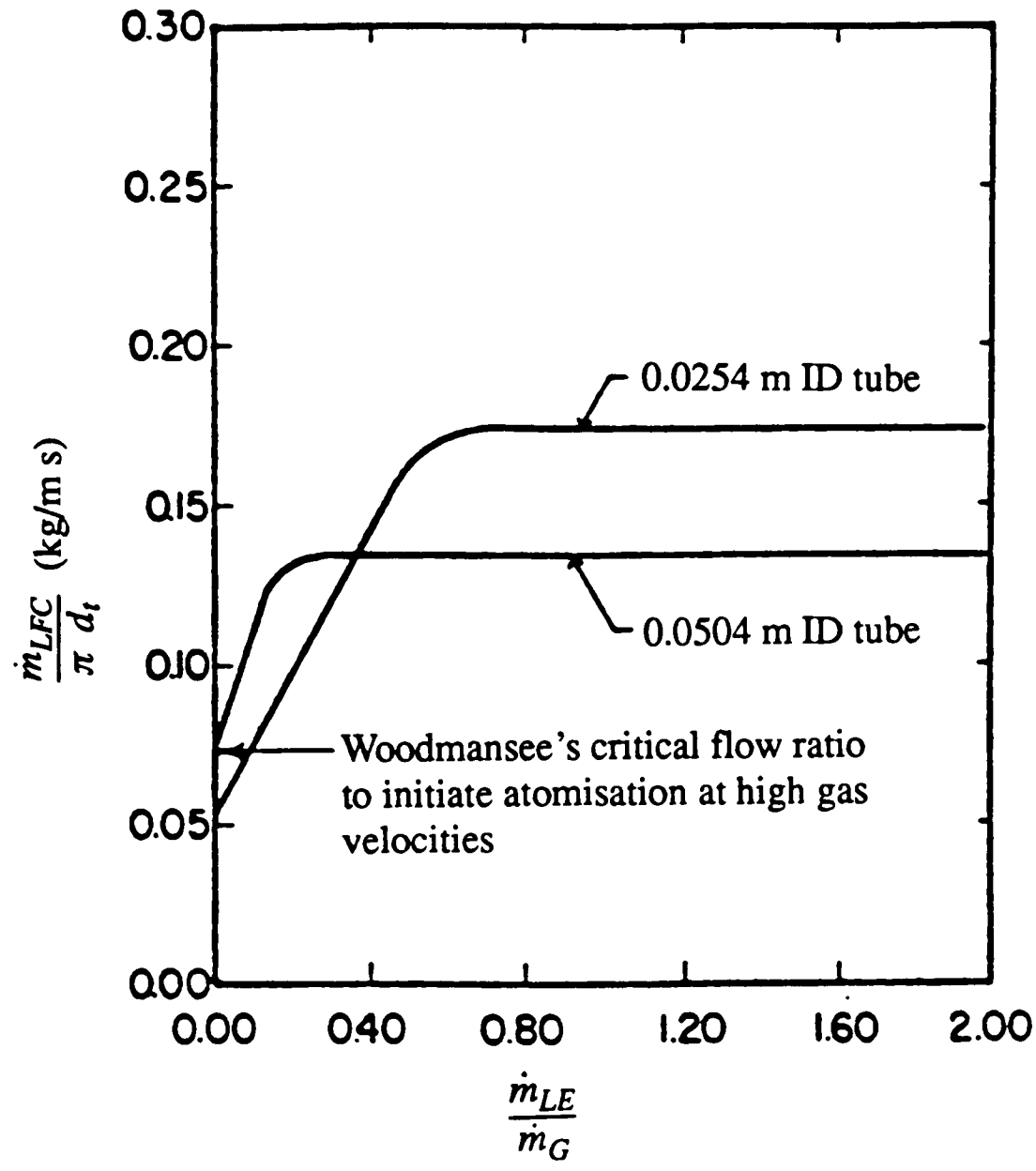

Figure 4.4 Critical liquid film flow rates for air–water flow in horizontal tubes 0.0254 m and 0.0508 m ID (Laurinat (1982)).

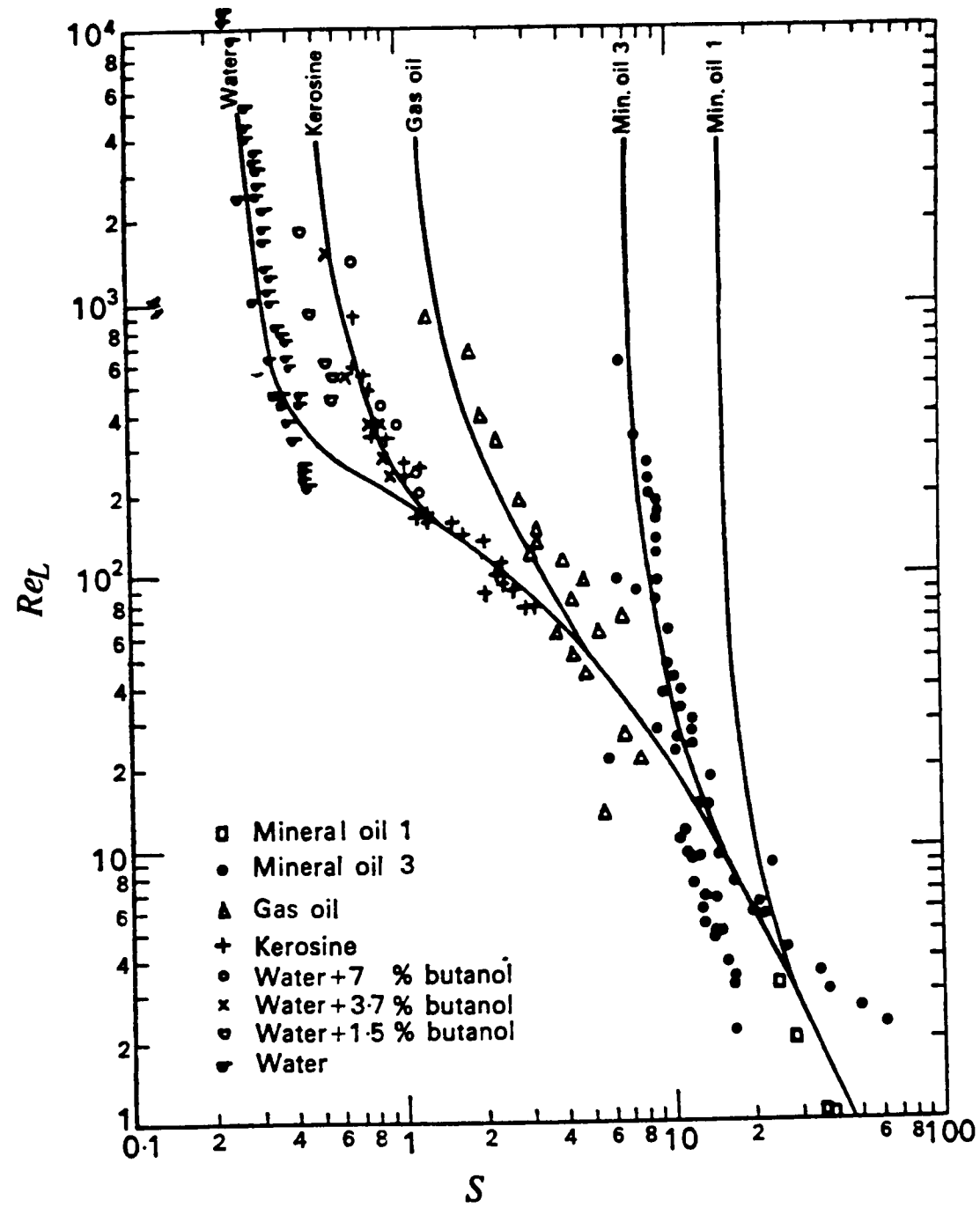

Figure 4.5 Dimensionless correlation for the onset of atomisation as given by Van Rossum (1959).

$$U_{SGC} = 1.5\ \mathrm{Re}_L^{-\frac{1}{2}} \sqrt{\frac{\varrho_L}{\varrho_G}}\ \frac{\sigma}{\mu_L} \tag{4.5}$$

For $160<Re_L<1635$, Ishii and Grolmes assumed that onset of entrainment was due to the mechanism of shearing-off of roll wave crests (also termed ligament break-up). For the transition regime ($160<Re_L<1635$) the critical gas velocity was given by:

$$U_{SGC} = 11.78\ N_\mu^{0.8}\ \mathrm{Re}_L^{-\frac{1}{3}} \sqrt{\frac{\varrho_L}{\varrho_G}}\ \frac{\sigma}{\mu_L} \qquad \text{if } N_\mu \leq \frac{1}{15} \tag{4.6}$$

$$U_{SGC} = 1.35\ \mathrm{Re}_L^{-\frac{1}{3}} \sqrt{\frac{\varrho_L}{\varrho_G}}\ \frac{\sigma}{\mu_L} \qquad \text{if } N_\mu > \frac{1}{15} \tag{4.7}$$

where the viscosity number N_μ is defined as:

$$N_\mu = \frac{\mu_L}{\left(\varrho_L\ \sigma\ \sqrt{\frac{\sigma}{g\ (\varrho_L - \varrho_G)}}\right)^{\frac{1}{2}}} \tag{4.8}$$

and g is the acceleration due to gravity.

For higher liquid flow rates, $Re_L>1635$ the correlations took the form:

$$U_{SGC} = N_\mu^{0.8} \sqrt{\frac{\varrho_L}{\varrho_G}}\ \frac{\sigma}{\mu_L} \qquad \text{if } N_\mu < \frac{1}{15} \tag{4.9}$$

$$U_{SGC} = 0.1146 \sqrt{\frac{\varrho_L}{\varrho_G}}\ \frac{\sigma}{\mu_L} \qquad \text{if } N_\mu > \frac{1}{15} \tag{4.10}$$

Figure 4.6 shows the critical gas velocity for the onset of entrainment calculated using the correlations of Ishii and Grolmes (1975) for air–water flowing in 0.032 m ID horizontal tube. It is seen that for high liquid Reynolds numbers the curve reaches a constant value of 13.7 m/s ($G_G = 21.4$ kg/m^{2}s).

From the visualisation work described in Chapter 3, it was seen that the critical gas velocity for atomisation to occur lies between $G_G = 10$ kg/m^{2}s and $G_G = 20$ kg/m^{2}s. This is supported by the entrainment data which suggests that atomisation is already occurring at $G_G = 20$ kg/m^{2}s, for all the liquid flow rates investigated. Until further experiments are done

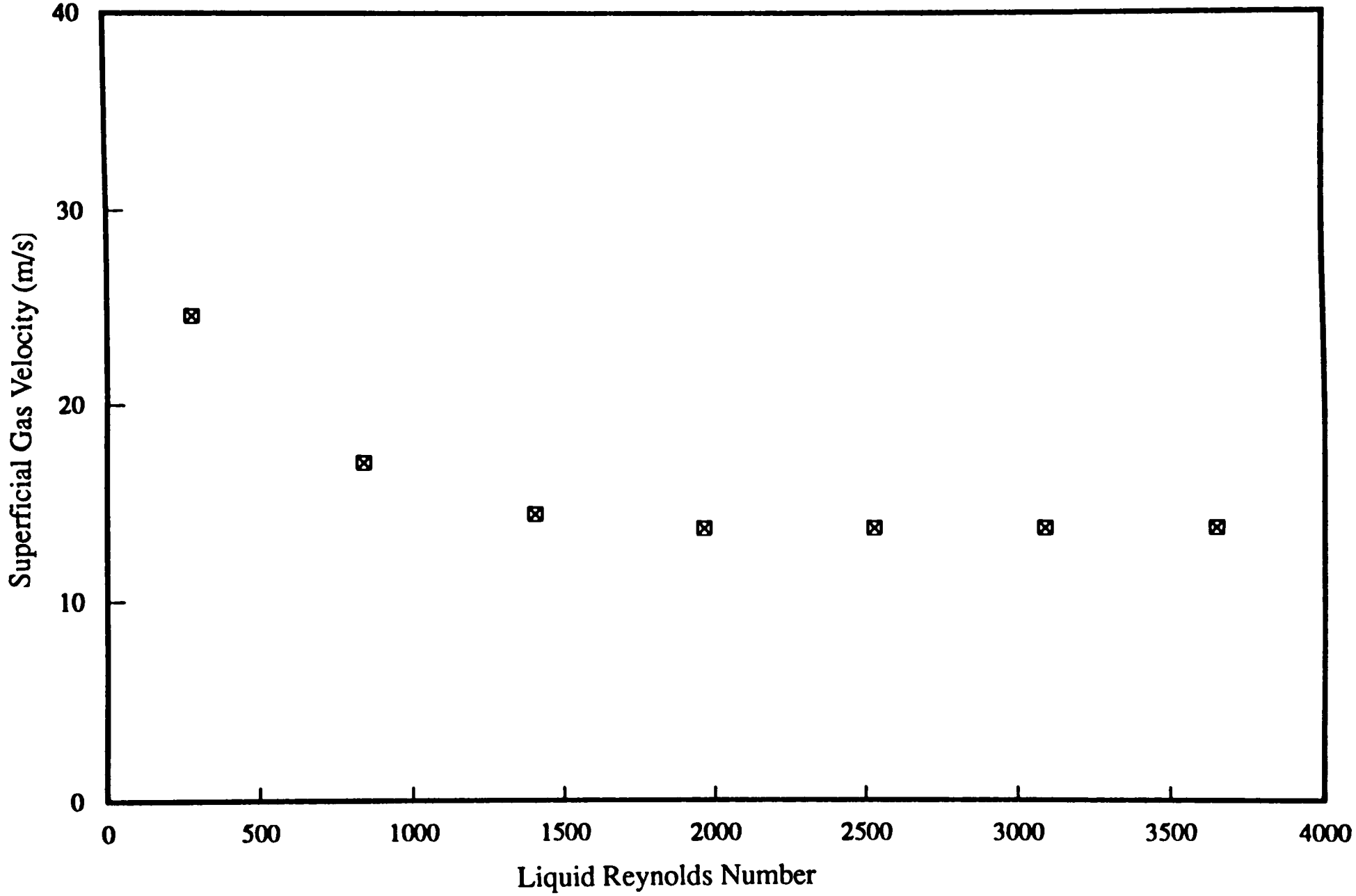

Figure 4.6 Calculated onset of atomisation for air–water horizontal flow in a 0.032 m ID tube, using the correlation of Ishii and Grolmes (1975)

to identify the exact conditions for the onset of entrainment, it can only be concluded that the correlation of Ishii and Grolmes (1975) overpredicts U_{SGC}.

4.2. Entrainment Measurements in Horizontal Flow

The fraction of the liquid flowing as drops can be measured directly by withdrawing samples from the gas stream to determine the drop flux, or calculated by measuring the liquid film mass flux and subtracting this quantity from the total liquid mass flux.

The pitot tube technique was used by Chakrabarti (1976), Williams (1986) and Paras and Karabelas (1991), among others. A transversable sampling probe is moved along the inside diameter of the pipe to collect drops for a given period of time. The total entrained flow is found by integration over the whole cross section of the tube.

One difficulty in applying this technique, is that near the gas–liquid interface the sampling probe tends to collect liquid from the tips of the roll waves, giving erroneous results. However, the problem can be overcome by knowing the exact location of the annular film. To overcome the problem, Williams (1986) used a contact probe that established an electrical circuit when it touched the liquid film. After the location of the film surface, it was possible to position the sampling probe so that it collected only drops.

The experimental determination of the liquid film flow rate includes the film removal method and dye (or other tracer) mixing technique.

In the film removal technique, the liquid film is removed through a slit or porous section, together with a small amount of gas. This technique was discussed in detail in section 2.1.4.

The dye tracer technique is based on the addition to the liquid film of a known flow rate of dye. The product is mixed with the film, its concentration is measured and finally, the film flow rate is determined by a mass balance. This method has some deficiencies due to the slow mixing of the dye. Details of this method are described by Coney and Fisher (1976).

Experimental data on entrainment in horizontal gas–liquid flow in pipes are summarised in Table 4.2. Much of these data were obtained for air–water systems.

The present study includes entrainment measurements in horizontal wavy–stratified and annular air–water flow in a 0.032 m tube, at ambient temperature and at a pressure of 1.3 or 1.4 bar in the measuring section. The film removal technique was used to determine the liquid film flow rate and hence entrained liquid flow.

The influence of the system pressure on the amount of liquid entrained as drops was studied for a gas mass flux of G_G = 60 kg/m^{2}s and liquid mass fluxes of G_L = 10 and 30 kg/m^{2}s. Experiments for both sets of conditions were conducted at a pressure of 1.3 bar and 1.4 bar in the test section. A reduction of 0.015 in the entrained liquid fraction (E) for a 0.1 bar increase in pressure is obtained for G_G = 60 kg/m^{2}s and G_L = 10 kg/m^{2}s, while for

TABLE 4.2 ENTRAINMENT STUDIES IN HORIZONTAL PIPES IN ANNULAR FLOW.

Authors	Tube Diameter (m)	Fluids	Gas Mass Flux (kg/m^2s)	Liquid Mass Flux (kg/m^2s)	Gas Density (kg/m^3)	Tube Lenght (m)	Measurement Technique	Other Measurements
Butterworth (1972)	0.0318	air–water	31.7 & 63.5	158.6 & 317.3	1.7 & 2.7	2.2 & 4.0	Pitot Tube Sampling	•Film Thickness •Pressure Drop
Chakrabarti (1976)	0.0254	air–water	40.1–76.2	44.4–124.3	1.6	2.1	Pitot Tube Sampling	•Film Thickness •Pressure Drop •Gas Axial Velocity
Dallman (1978)	0.0254	air–water	34.3–198.9	12.4–994.7	1.4–4.7	5.8	Pitot Tube Sampling and Porous Sinter	•Film Thickness •Pressure Drop
Laurinat (1982)	0.0508	air–water	28–279	16–476	1.3–2.5	11.7	Pitot Tube Sampling and Porous Sinter	•Film Thickness •Pressure Drop
Guevara and Gotham (1983)	0.0381	steam–water	31–90				Porous Sinter	•Pressure Drop
Williams (1986)	0.0953	air–water	42.8–82.9	30.4–122.8	1.39–1.85	24.8	Pitot Tube Sampling	•Film Thickness
Kitscha et al (1990)	0.0503	air–water	16.8–73.1	29.9–319.4	1.2–1.7	15.4	Pitot Tube Sampling	•Film Thickness •Pressure Drop •Void Fraction
Paras and Karabelas (1991–a)	0.0508	air–water	40–143	20–200	1.27–2.33	15.2	Pitot Tube Sampling	•Film Thickness •Pressure Drop

G_G = 60 kg/m^{2}s and G_L = 30 kg/m^{2}s the reduction on the entrained fraction observed is of 0.022. Charron (1990) studied the influence of the pressure on the entrained liquid fraction in vertical annular flow for the flow rates of G_G = 79.6 kg/m^{2}s and G_L = 67.6 kg/m^{2}s. The author reported a reduction in E of 0.016 per 0.1 bar increase in the pressure, which agrees with the present results.

The liquid film flow data for air–water flow in a horizontal pipe are plotted against liquid mass flux in Figure 4.7, and against the superficial gas velocity in Figure 4.8. The relation between the entrained mass flux and the liquid and the superficial gas velocity are shown in Figures 4.9 and 4.10, respectively. These graphs illustrate that the gas velocity and the liquid mass flux have a strong influence on the entrained liquid flow rate.

Figure 4.7 highlights the linear relationship existing between the liquid film mass flux and the liquid mass flux, observed for the whole range of gas flow rates studied. Figure 4.8 shows the liquid film mass flux (G_{LF}) decreasing with gas velocity except for G_L = 10 kg/m^{2}s, where the film flow rate is constant with increasing gas flow. The decrease in G_{LF} with gas velocity is expected, because the higher the gas velocity the greater the shearing action imposed on the liquid film surface to cause atomisation of the liquid. However, for G_L = 10 kg/m^{2}s it is assumed that the critical liquid film has been achieved, and has an approximate value of 9 kg/m^{2}s.

The effect of liquid mass flux on the entrained liquid mass flux (G_{LE}) is shown in Figure 4.9. For the curves corresponding to constant gas mass flux of G_G = 50, 60 and 70 kg/m^{2}s, G_{LE} increases with G_L. For G_G = 40 kg/m^{2}s a plateau is clearly seen. For the curves obtained at G_G = 20 and 30 kg/m^{2}s after an increase of the entrained liquid flux with G_L, there is a sudden and distinct decrease in G_{LE} occurring at high liquid mass flux conditions.

The reduction in the level of entrainment at these high liquid loadings can be explained by a change in the flow regime occurring at G_G = 20 kg/m^{2}s and G_L = 130 kg/m^{2}s, and at G_G = 30 kg/m^{2}s and G_L = 130 kg/m^{2}s. The location of these flow conditions in the flow pattern map of Lin and Hanratty (1987) (Figure 1.7) indicates that these points are near the pseudo–slug region.

As mentioned before (section 1.1.2.), the pseudo–slug flow pattern is characterised by a continuous film around the whole pipe circumference like annular flow, and by the presence of large disturbances similar in appearance to slugs, but which do not travel at the gas velocity and do not produce the pressure variations a slug does. These disturbances called pseudo–slugs touch the top of the tube wall only momentarily, and do not block the whole cross section of the tube for a long time.

Therefore, if for G_G = 20 kg/m^{2}s and G_L = 130 kg/m^{2}s, and for G_G = 30 kg/m^{2}s and G_L = 130 kg/m^{2}s the air–water mixture is flowing at pseudo–slug flow, the surges that

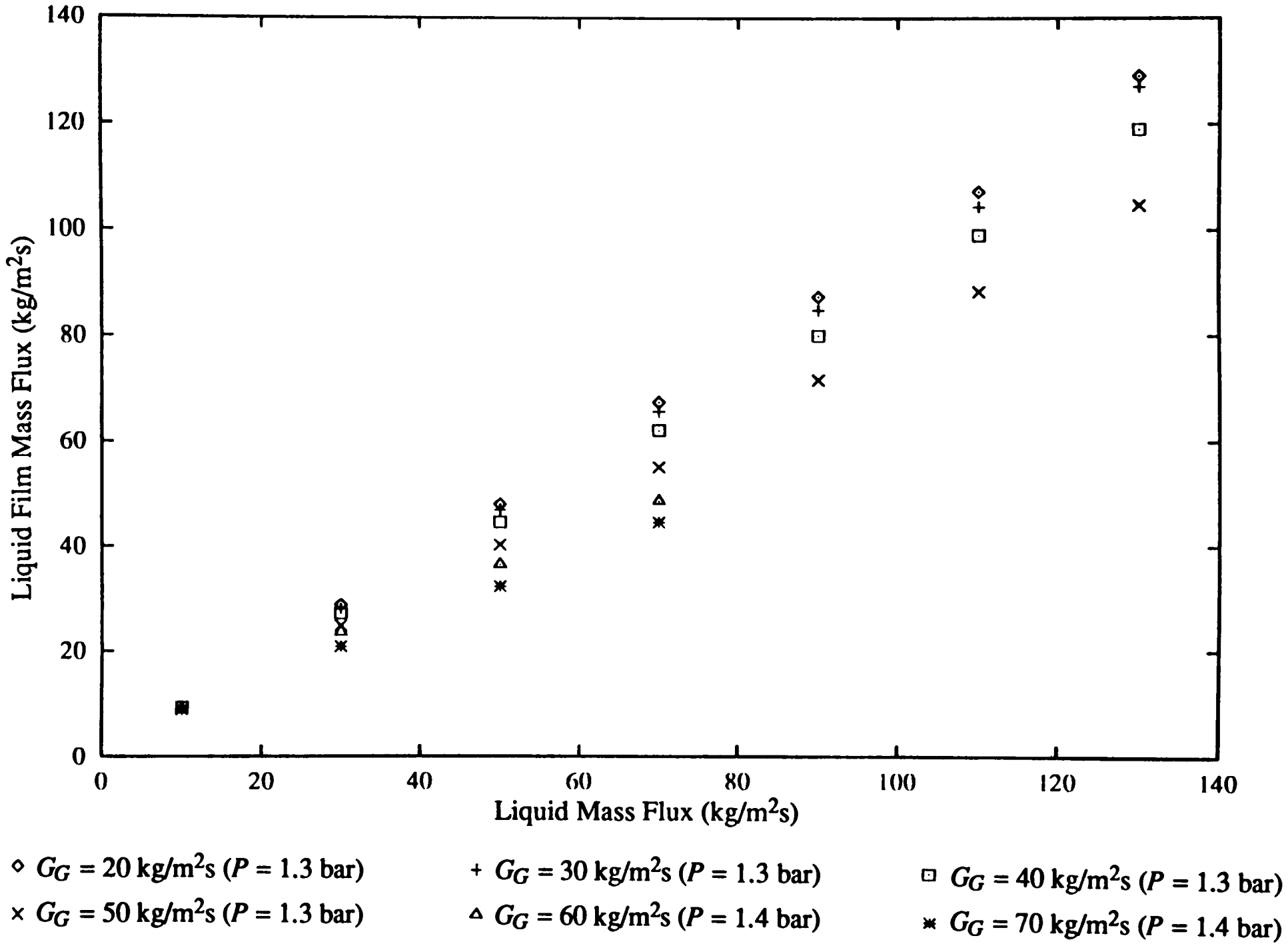

Figure 4.7 Influence of total liquid mass flux on the liquid film mass flux measurements for air–water flow in the 0.032 m ID horizontal tube.

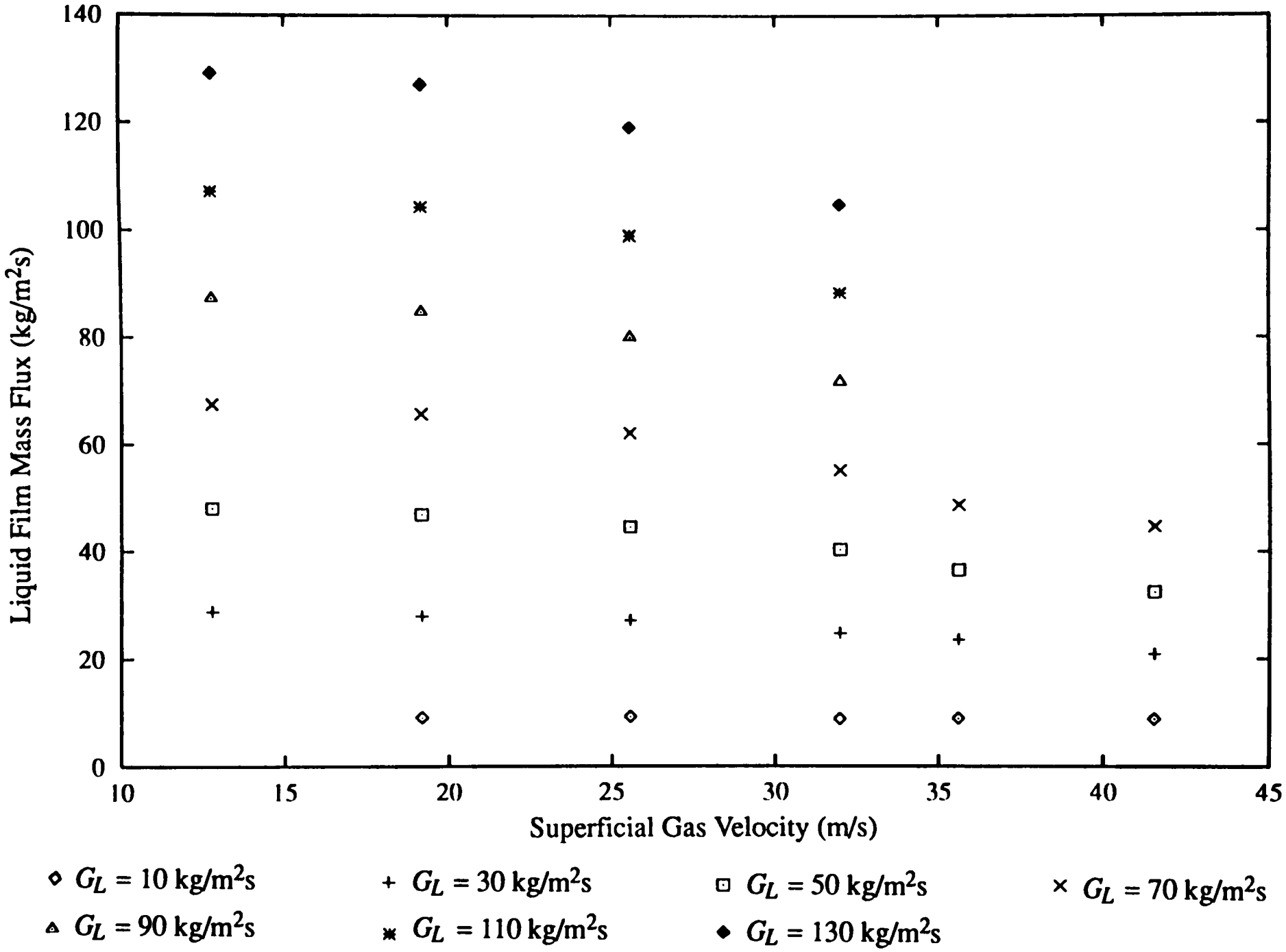

Figure 4.8 Influence of the superficial gas velocity on the liquid film mass flux measurements for air–water flow in the 0.032 m ID horizontal tube.

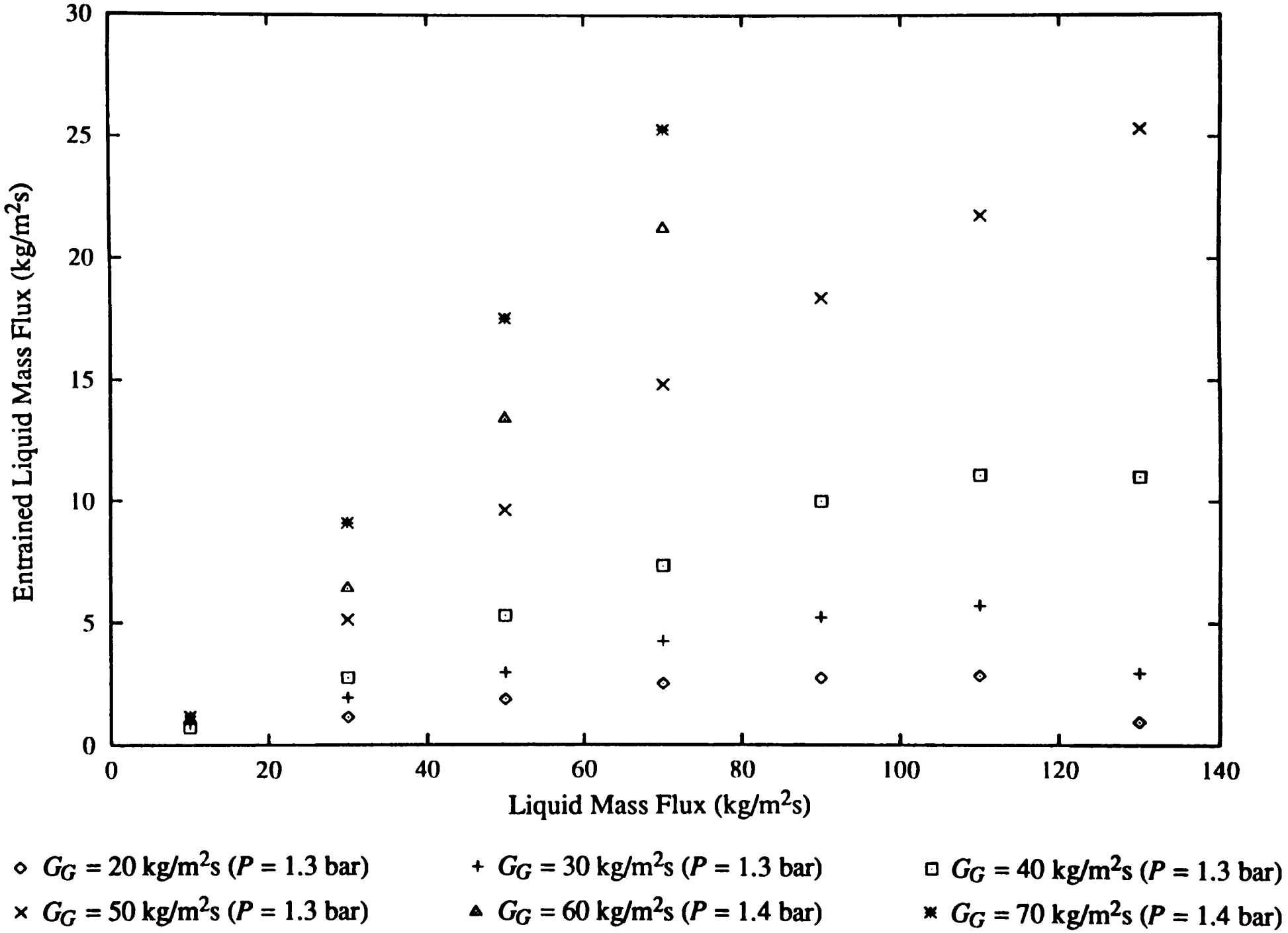

Figure 4.9 Influence of the total liquid mass flux on the entrained liquid mass flux for air–water flow in the 0.032 m ID horizontal tube.

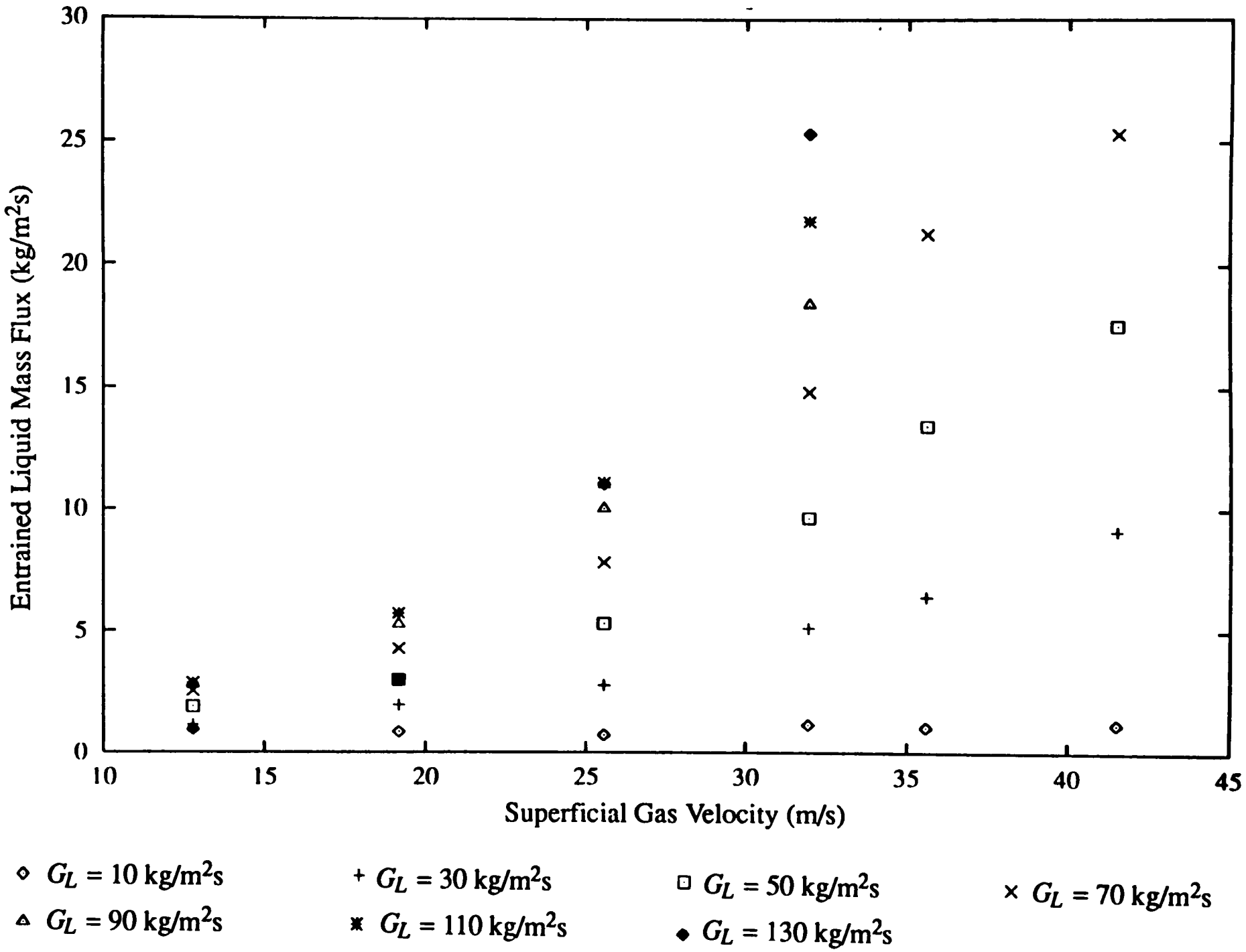

Figure 4.10 Influence of the superficial gas velocity on the entrained liquid mass flux for air–water flow in the 0.032 m ID horizontal tube.

momentarily block the pipe can force the entrained drops to deposit and consequently cause a decrease in entrainment.

Figure 4.10 represents the relation between entrained mass liquid mass flux (G_{LE}) and the superficial gas velocity, at constant liquid flow. For G_L = 10 kg/m^{2}s, G_{LE} has a constant value, for the whole range of gas velocities studied. However, for the other fixed liquid fluxes, G_{LE} increases with gas velocity. In the present set of experiments it was not possible to achieve the fully entrained condition seen by Dallman (1978) due to the limited range of flow conditions studied.

It is of interest to know what effect the orientation of tube has on the amount of liquid entrained. For this purpose, the present data were compared against entrainment measurements obtained under similar conditions in vertical flow. The experiments published by Azzopardi et al (1980) were chosen for this comparison, where the flow conditions were expressed in mass fluxes. As these data were taken at 1.5 bar, while the present measurements were conducted at 1.3 bar or 1.4 bar, the comparison was made in terms of the same superficial gas velocities instead of gas mass fluxes. Also, the flow conditions of Azzopardi et al (1980) did not match the ones used in the present study, and consequently interpolation was necessary. The flow conditions of the this study used for the comparison are: G_G = 50 kg/m^{2}s and G_L = 30–70 kg/m^{2}s (P = 1.3 bar), G_G = 60 kg/m^{2}s and G_L = 30–70 kg/m^{2}s (P = 1.4 bar), G_G = 70 kg/m^{2}s and G_L = 30–70 kg/m^{2}s (P = 1.4 bar). In Figure 4.11 the entrained liquid mass flux in horizontal flow is plotted against the corresponding entrained liquid mass flux in vertical flow for several gas velocities.

Figure 4.11 shows that, in general, the level of entrainment is higher in vertical annular flow than in horizontal annular flow. This may be linked to the difference in the liquid film distribution between vertical and horizontal flow conditions. In vertical annular flow the liquid film is evenly distributed around the pipe circumference, so it is expected that atomisation takes place around the whole area of the liquid film. In horizontal flow, however, the liquid film flow is larger at the bottom of the tube and smaller at the top part. The liquid film flow at the top of the tube may be below the limit for atomisation to occur, limiting the area available for atomisation to the bottom of the tube. It is thought that this difference in the liquid film distribution occurring in horizontal annular flow may explain the difference in the entrained liquid flow between horizontal and vertical flow at the same flow conditions. It is seen in Figure 4.11 that as the gas velocity increases from 25.6 m/s to 41.5 m/s, the curve tends to approach the 45° line. This means that as the gas velocity increases the difference between the entrained liquid fraction in vertical flow and the corresponding entrained fraction in horizontal flow is reduced. At even higher gas velocities, it is expected that the curve will intercept the 45° line. From this point the entrained liquid fraction in both systems may be similar, and the asymmetry existing in horizontal annular flow may be lost.

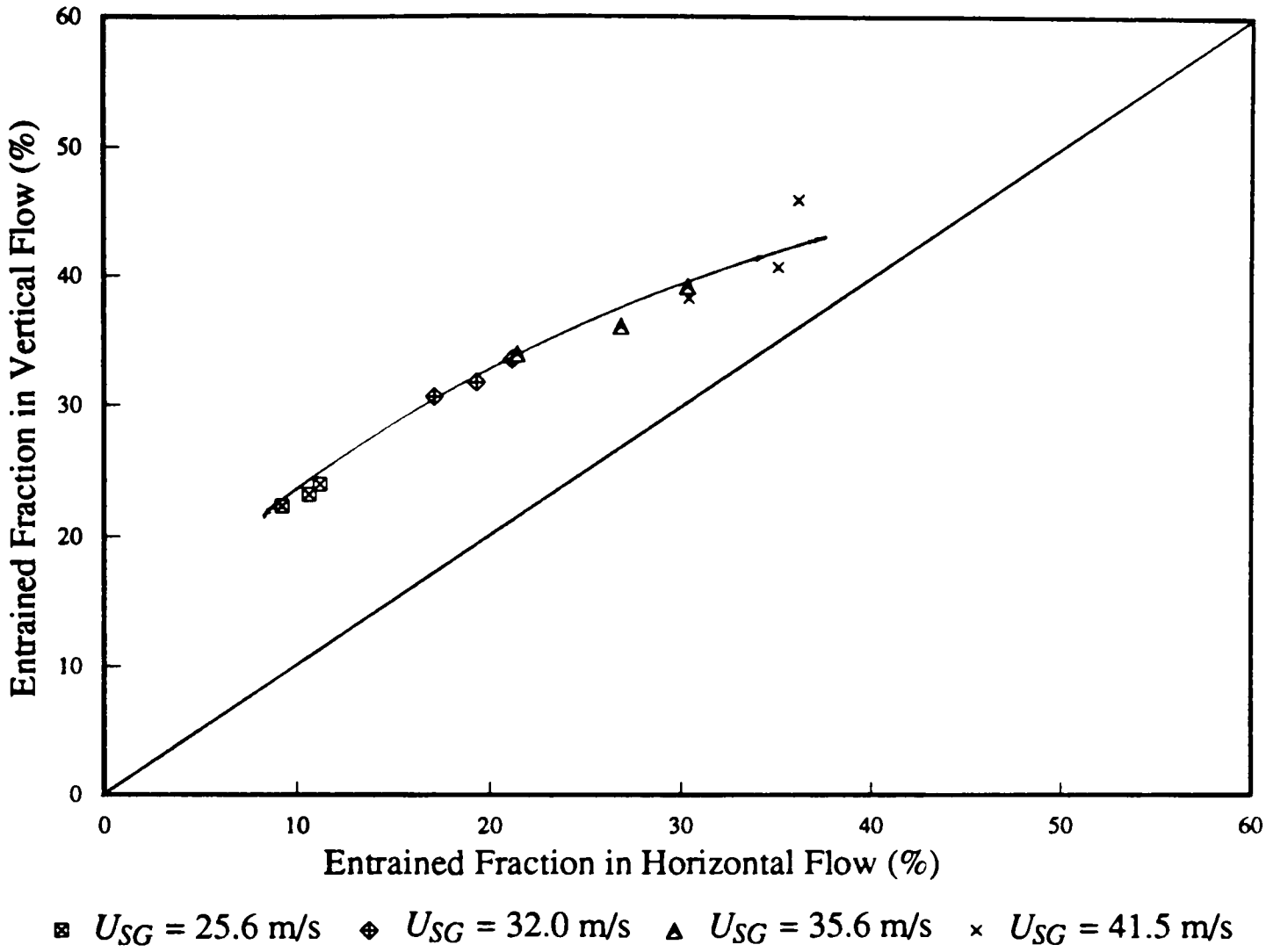

Figure 4.11 Comparison between the entrained fraction obtained in vertical and horizontal flow conditions in a 0.032 m ID tube.

4.3. Entrainment Correlations

To predict accurately important physical phenomena in annular flow, it is essential to understand the mechanisms of entrainment and to know how to correlate the amount of liquid that flows as drops. Several correlations have been proposed, although some are dimensional and therefore limited to a narrow range of flow conditions.

Examples are the correlations of Wicks and Dukler (1960), Paleev and Filipovich (1966) and Hutchinson and Whalley (1972), among others. These and other correlations have been reviewed by Dallman (1978).

In this section more recent entrainment correlations applicable to horizontal flow are discussed and tested against data of the present investigation and from the other studies listed in Table 4.2.

4.3.1. Correlations of Dallman (1978), Laurinat (1982) and Williams (1986)

Dallman (1978) developed a correlation for the entrained fraction based on the assumption that it results from a dynamic balance between the rate of atomisation ($\dot{E}$) from the liquid film and the rate of deposition of drops ($\dot{D}$) from the gas core. The deposition rate is usually represented as a diffusion–like process by:

$$\dot{D} = k_D \, C \cong k_D \frac{\varrho_G \, \dot{m}_{LE}}{\dot{m}_G} \tag{4.11}$$

where k_D is the deposition mass transfer coefficient, C is the drop concentration, and $\dot{m}_{LE}$ and $\dot{m}_G$ are, respectively, the entrained liquid and the gas mass flow rates. It is assumed that there is no slip between the gas and the drops. Under equilibrium conditions $\dot{E} = \dot{D}$, and so

$$E = \frac{\dot{m}_{LE}}{\dot{m}_L} = \frac{\dot{E} \, \dot{m}_G}{\varrho_G \, k_D \, \dot{m}_L} \tag{4.12}$$

The author followed an empirical approach to represent the entrainment rate. Provided that the gas velocity is not close to the critical gas velocity for the onset of entrainment, and that the liquid film mass flow rate ($\dot{m}_{LF}$) is small enough so there is a linear relationship between $\dot{E}$ and $\dot{m}_{LF}$, entrainment rate data for air–water is well represented by the equation:

$$\dot{E} = k_A \, \frac{\dot{m}_{LF} - \dot{m}_{LFC}}{\pi \, d_t} \, (\varrho_G \, \varrho_L)^{\frac{1}{2}} \, U_G^2 \tag{4.13}$$

where k_A is the drop atomisation coefficient, $\dot{m}_{LFC}$ is the critical liquid mass flow rate for the inception of atomisation and d_t is the tube diameter. The actual mean gas velocity U_G used in equation (4.13) can be calculated by:

$$U_G = \frac{4\ \dot{m}_G}{\varrho_G\ \pi\ (d_t - 2m)^2} \tag{4.14}$$

where m is the average thickness of the liquid film.

By substituting equation (4.13) into equation (4.12), the following correlation for entrainment under fully developed conditions in pipes is obtained:

$$E = \left(1 - \frac{\dot{m}_{LFC}}{\dot{m}_L}\right) \frac{(\varrho_G\ \varrho_L)^{\frac{1}{2}}\ U_G^3\ d_t\ (k_A/4k_D)}{1 + (\varrho_G\ \varrho_L)^{\frac{1}{2}}\ U_G^3\ d_t\ (k_A/4k_D)} \tag{4.15}$$

The form of equation (4.15) implies that once the critical gas velocity for the onset of entrainment is exceeded, entrainment has a rapid increase with increasing gas velocity. For high gas velocities the function reaches a limiting condition where the liquid film equals the critical liquid film flow rate ($\dot{m}_{LFC}$). The author was able to correlate well the entrainment data of Cousins et al (1965) for vertical upflow in a 0.0095 m tube.

Dallman (1978) also conducted measurements of the entrained liquid fraction for air–water annular flow in a horizontal tube (see Table 4.2), and compared his results with equation (4.15). The data were shown to exhibit a much faster rise to the fully entrained condition than was predicted by the correlation. Consequently, Dallman abandoned correlation (4.15) and proposed a straightforward empirical relation to represent his data:

$$\frac{E}{1 - \frac{\dot{m}_{LFC}}{\dot{m}_L}} = 3 \times 10^{-6}\ (\varrho_G\ \varrho_L)^{\frac{1}{2}}\ U_G{}^3\ d_t \tag{4.16}$$

valid for $U_G \leq 30$ m/s, whilst the following equation

$$\frac{E}{1 - \frac{\dot{m}_{LFC}}{\dot{m}_L}} = 1 \tag{4.17}$$

is valid for gas velocities greater than 30 m/s.

Laurinat (1982) extended the experimental work of Dallman (1978) to a horizontal tube of ID 0.0504 m. When correlating both his entrainment data carried out for air–water flow in a 0.0504 m tube, and Dallman's results in a 0.0254 m tube, the author found that the best fit to the data was given by the equation:

$$E = \left(1 - \frac{\dot{m}_{LFC}}{\dot{m}_L}\right) \frac{C' \, (\varrho_G \, \varrho_L)^{0.75} \, U_G^{4.5} \, (d_t - 2m)^{1.5}}{1 + C' \, (\varrho_G \, \varrho_L)^{0.75} \, U_G^{4.5} \, (d_t - 2m)^{1.5}} \tag{4.18}$$

where the constant $C' = 3.6 \times 10^{-8} \, s^{4.5}/(kg^{1.5} \, m^{1.5})$. Instead of using the internal diameter of the tube in his correlation, Laurinat used the diameter of the gas core.

Laurinat (1982) also correlated his data with equation (4.15), which Dallman (1978) proved to fit adequately entrainment results for vertical annular flow. However, equation (4.15) failed to correlate the data for horizontal annular flow. Laurinat attributed this to the difference in the drop deposition mechanism between horizontal and vertical annular flow. He further argued that for equation (4.18) to be valid the deposition mass transfer coefficient should vary as:

$$k_D \sim d_t^{-0.5} \, \varrho_G^{-0.25} \, U_G^{-1.5} \tag{4.19}$$

According to McCoy and Hanratty (1977), for small drops in horizontal flow the deposition constant is proportional to the terminal settling velocity of the drops. Assuming that the drops are flowing with the same axial velocity as the gas, the terminal settling velocity could be determined from a momentum balance on the drop, as if the drop was falling in a quiescent gas. The author continued the analysis, considering that if the drag force on the drop was given by the Stokes law then k_D should scale as:

$$k_D \sim \frac{g \, D^2 \, \varrho_L}{\mu_G} \tag{4.20}$$

where D is the drop diameter and μ_G is the gas viscosity.

In the intermediate law region

$$k_D \sim \frac{g^{\frac{5}{7}} \, D^{\frac{8}{7}} \, \varrho_L^{\frac{5}{7}}}{\varrho_G^{\frac{2}{7}} \, \mu_G^{\frac{3}{7}}} \tag{4.21}$$

The drop size was related to other parameters by a result from Tatterson et al (1977):

$$D \sim d_t^{0.5} \left(\frac{\sigma}{\varrho_G \, U_G^2 \, f_{SG}}\right)^{0.5} \tag{4.22}$$

where f_{SG} is the friction factor for a smooth tube ($=0.046\,Re_G^{-0.2}$) and σ is the surface tension.

By substituting (4.22) into (4.20), Laurinat (1982) obtained for the Stokes law range:

$$k_D \sim \left(\frac{d_t}{\varrho_G\, U_G^2}\right)\left(\frac{g\ \sigma\ \varrho_L}{f_{SG}\ \mu_G}\right) \tag{4.23}$$

and for the intermediate law range:

$$k_D \sim \left(\frac{d_t}{\varrho_G\, U_G^2}\right)^{\frac{4}{7}}\left[\frac{g^{\frac{5}{7}}\ \sigma^{\frac{4}{7}}\ \varrho_L^{\frac{3}{7}}}{f_{SG}^{\frac{4}{7}}\ \mu_G^{\frac{3}{7}}}\right]\left(\frac{\varrho_L}{\varrho_G}\right)^{\frac{2}{7}} \tag{4.24}$$

By comparing expressions (4.23) and (4.24) with expression (4.19), the author concluded that only the effect of the velocity on k_D was predicted by the Stokes law settling velocity correction. The effects of pipe diameter and gas density were not predicted correctly.

However, Williams (1986) followed the previous analysis carried out by Laurinat (1982), and substituted expression (4.23) into the equation (4.15) proposed by Dallman (1978). He obtained:

$$E = \left(1 - \frac{\dot{m}_{LFC}}{\dot{m}_L}\right)\frac{C''\ (\varrho_G\ \varrho_L)^{\frac{3}{2}}\ U_G^5\ f_{SG}}{1 + C''\ (\varrho_G\ \varrho_L)^{\frac{3}{2}}\ U_G^5\ f_{SG}} \tag{4.25}$$

where $C'' = 3.6 \times 10^{-11}\ s^5\ m^4/kg^3$.

Williams found a good agreement between this correlation and his entrainment measurements in a 0.0953 m horizontal pipe and the data obtained by Dallman (1978) and by Laurinat (1982) (Figure 4.12). Paras and Karabelas (1991) also reported that their entrainment data were well correlated by the expression of Williams (1986) (Figure 4.13).

The present results were also compared against the correlation of Williams (equation 4.25). The results are presented in Figure 4.14 as calculated entrained fraction against measured entrained fraction. Two assumptions were made in the construction of this graph.

First, to use equation (4.25) it was necessary to calculate the actual gas velocity based on the diameter of the gas core. As no film thickness measurements were taken in the current study, the method proposed by Laurinat et al (1984) to calculate the average film thickness was used. This is described in Appendix E.

Secondly, an assumption was made about the critical film mass flux. For the present measurements (see Figure 4.8) the range of flow conditions makes it difficult to establish

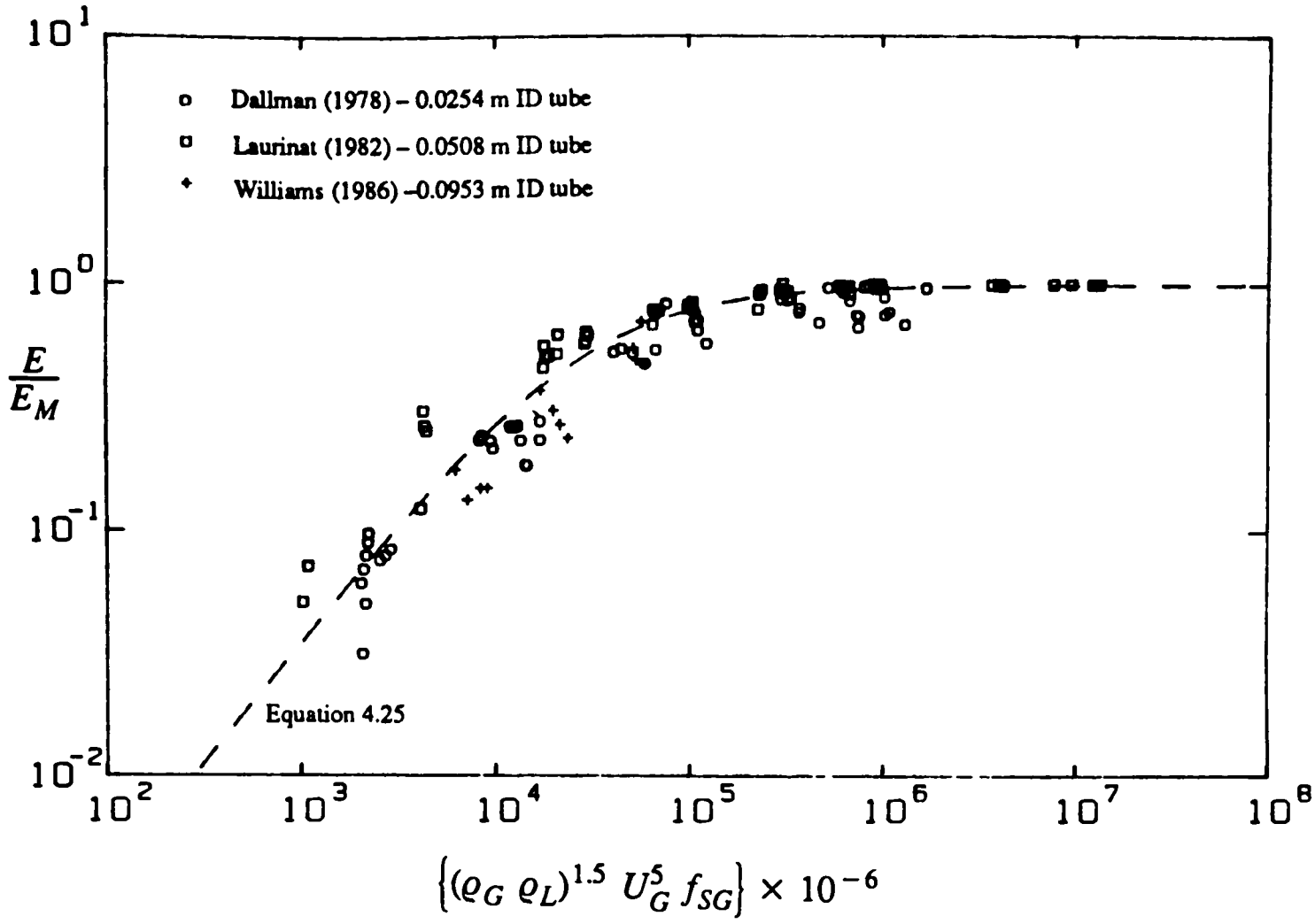

Figure 4.12 Performance of the correlation of Williams (1986) to predict the entrainment data for air–water flow in several tube diameters (Williams (1986)).

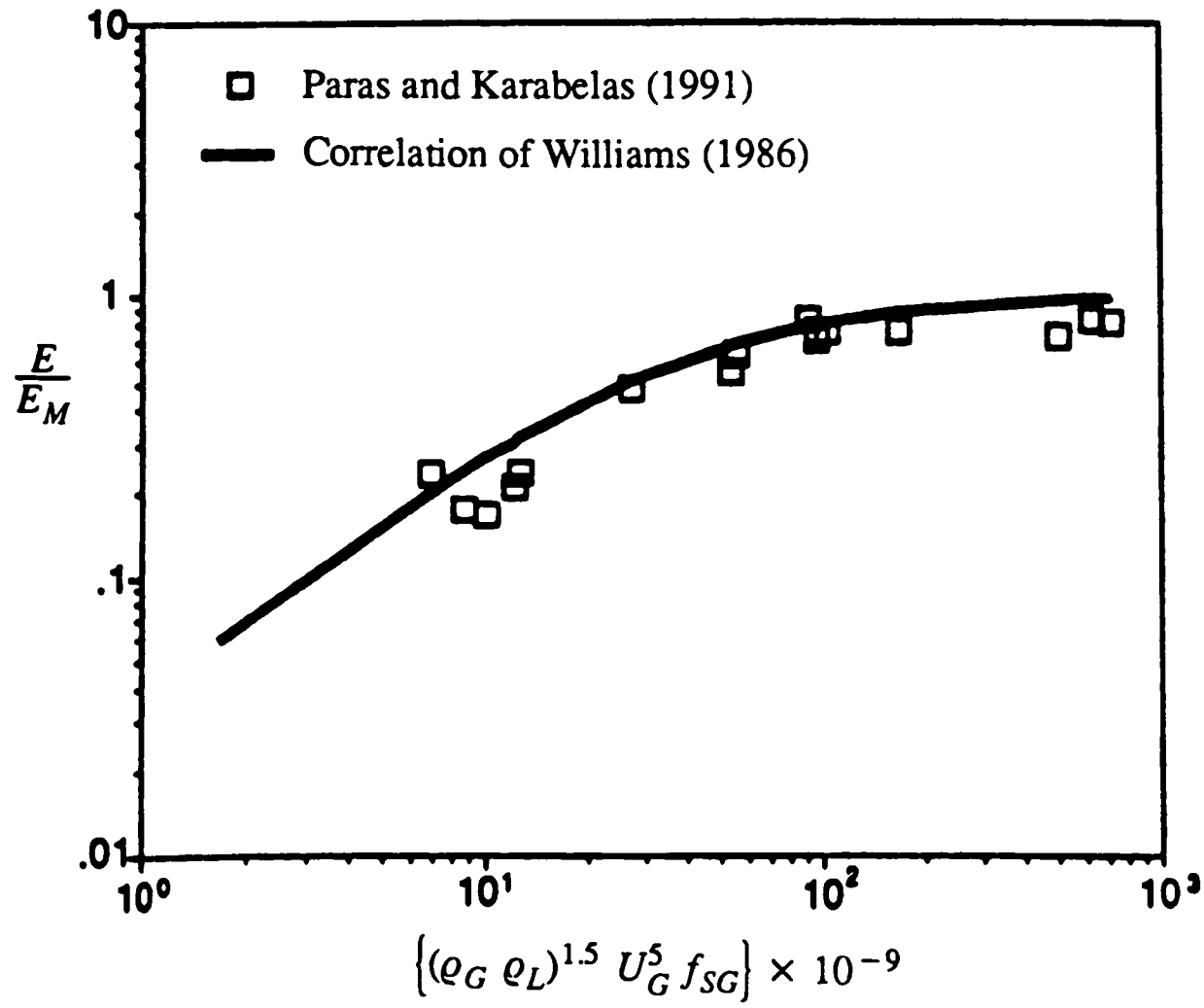

Figure 4.13 Performance of the correlation of Williams (1986) to predict the entrainment data of Paras and Karabelas (1991) (Paras and Karabelas (1991)).

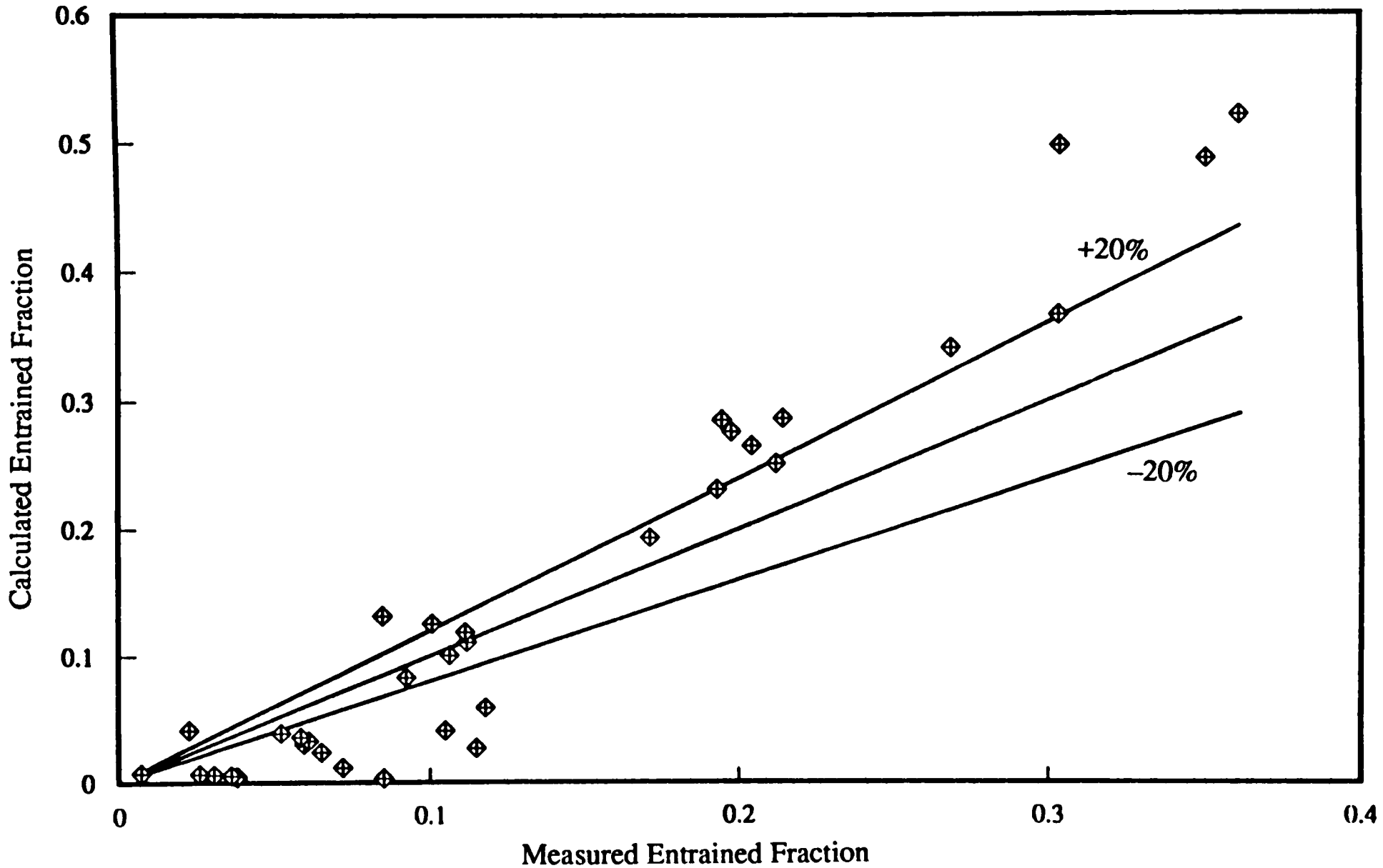

Figure 4.14 Performance of the correlation of Williams (1986) to predict the entrained fraction of the present study.

critical film flows. For this reason, it was assumed that for all liquid flow rates the liquid film would approach a critical liquid film mass flux of approximately 9 kg/m^{2}s.

Unfortunately, the correlation of Williams (1986) seems to fail to correlate the entrained liquid flow rates of the present investigation. This may be caused by the assumptions described above in which G_{LFC} is maintained constant in spite of the trends found by Dallman (1978). On the other hand, it should be recognised that the correlation of Williams (1986) was developed for annular flow. Indeed, the author has shown a very good fit with annular flow data (Figure 4.12). Data from the present study, however, was collected over a range of flow conditions which extend from stratified up to annular flows.

4.3.2. Correlations of Ishii and Mishima (1981) and Kitscha et al (1990)

Ishii and Mishima (1981) proposed an equation for predicting the fraction of entrained drops (E). Their model assumed the roll wave entrainment mechanism (Re_L>160), and was based on the onset of entrainment criterion developed by Ishii and Grolmes (1975), and discussed in section 4.1.2.

If the system is at flow conditions higher than those represented by equation (4.6) , liquid will be travelling as entrained drops. Assuming that all liquid above the critical film will be entrained in the gas, the theoretical limit of the entrained fraction is:

$$1 - E_{th} = \frac{\mu_L}{\varrho_L \, U_{SL} \, d_t} \left(11.78 \, N_\mu{}^{0.8} \, \frac{\sigma}{\mu_L \, U_{SG}} \, \sqrt{\frac{\varrho_L}{\varrho_G}} \right)^3 \qquad (4.26)$$

where the viscosity group number N_μ is given by equation (4.8), and U_{SL} is the superficial liquid velocity.

The authors also considered that for inviscid fluids the following assumption could be made:

$$N_\mu{}^{0.8} \approx 3 \, N_\mu \qquad (4.27)$$

and finally obtained the equation:

$$E_{th} = 1 - \frac{1}{\mathrm{Re}_L} \left[35 \left(\frac{\sigma \, g \, \Delta\varrho}{\varrho_G{}^2} \right)^{0.25} \frac{1}{U_{SG}} \right]^3 \qquad (4.28)$$

Equation (4.28) shows that E_{th} is dependent on the liquid Reynolds number and on a dimensionless gas velocity defined as:

$$U_{SG}^{*} \sim \frac{U_{SG}}{\left(\frac{\sigma g \Delta\varrho}{\varrho_G^2}\right)^{0.25}} \tag{4.29}$$

Ishii and Mishima compared available entrainment data with the theoretical limit E_{th}, and found that the entrained fraction was much smaller than entrainment predicted by equation (4.28), but basic trends such as dependence on dimensionless gas velocity and Re_L were correctly predicted. The authors argued that the presence of drops in the gas core changed the core inertia, and they proposed a modification in the gas density should be made:

$$U_{SG}^{*} \sim \frac{U_{SG}}{\left[\frac{\sigma g \Delta\varrho}{\varrho_G^2 \left(\frac{\Delta\varrho}{\varrho_G}\right)^n}\right]^{0.25}} \tag{4.30}$$

By plotting the results of Steen and Wallis (1964), a value of n=2/3 was found to be satisfactory.

The authors also showed that from a consideration of drop deposition, entrainment was dependent on drop concentration and hence on tube diameter. This effect was expressed in the correlation in terms of a dimensionless hydraulic diameter defined as:

$$d_t^{*} = d_t \sqrt{\frac{g\,\Delta\varrho}{\sigma}} \tag{4.31}$$

Experimental data of Cousins et al (1965) exhibit an entrance effect at positions close to the entrance, while at regions far away from the inlet, entrainment reaches a quasi-equilibrium value (E_∞). Using various experimental data in this study, Ishii and Mishima (1981) obtained that the equilibrium entrained fraction is proportional to:

$$E_\infty \sim U_{SG}^{*\,2.5}\; d_t^{*\,1.25}\; \mathrm{Re}_L^{0.25} \tag{4.32}$$

and should satisfy the following limiting conditions

$$E_\infty \ll 1 \qquad \text{for} \quad U_{SG}^{*} \le U_{SGC}^{*} \tag{4.33}$$

$$E_\infty \to 1 \qquad \text{for} \quad U_{SG}^{*} \to \infty \tag{4.34}$$

where U^*_{SGC} is the dimensionless critical gas velocity for the onset of entrainment. Finally, the authors arrived to the equation:

$$E_\infty = \tanh\ (7.25 \times 10^{-7}\ U^{*\,2.5}_{SG}\ d_t^{*\,1.25}\ \mathrm{Re}_L^{0.25}) \tag{4.35}$$

Equation (4.35) can be expressed in another form provided that U^*_{SG}, $d_t{}^*$ and Re_L are substituted by the respective definitions, becoming:

$$E_\infty = \tanh\ (7.25 \times 10^{-7}\ We'^{\,1.25}\ \mathrm{Re}_L^{0.25}) \tag{4.36}$$

where the entrainment Weber number was defined by:

$$We' = \frac{\varrho_G\ U^2_{SG}\ d_t}{\sigma}\ \left(\frac{\Delta\varrho}{\varrho_G}\right)^{\frac{1}{3}} \tag{4.37}$$

Ishii and Mishima (1981) also extended their correlation to the cases where an entrance effect on entrainment was observed, but this was only applicable to smooth injection of the liquid. They argued that for assessing the entrance effect a proper length scale should be considered, and an estimate of the entrainment rate ($\dot{E}$) was necessary. Since entrainment was caused by the shearing-off mechanism of roll wave crests, they considered that the entrainment rate should be proportional to an interfacial drag force and to the wave amplitude (expressed in terms of a power to the liquid Reynolds number). Thus

$$\dot{E} \sim U^{*\,2}_{SG}\ \mathrm{Re}_L^n \tag{4.38}$$

Using expression (4.38) for the entrainment rate, the authors achieved the equation that scales the drop entrainment:

$$\frac{E}{E_\infty} \sim \frac{\int \dot{E}\ dz}{E_\infty} \sim \frac{U^{*\,2}_{SG}\ \mathrm{Re}_L^n\ z}{U^{*\,2}_{SG}\ \mathrm{Re}_L^{0.25}\ d_t^{1.25}} \sim \frac{z}{d_t}\ \frac{\mathrm{Re}_L^{(n-0.25)}}{U^{*\,0.5}_{SG}} \tag{4.39}$$

where the small dependence on $d_t{}^*$ has not been considered. A value of $n = 0.75$ was found to correlate quite well the entrance effect on the data of Cousins et al (1965). So, the length scale (ζ) was given by:

$$\zeta = \frac{z}{d_t} \sqrt{\frac{\mathrm{Re}_L}{U^*_{SG}}} \tag{4.40}$$

and the entrained fraction at entrance locations was:

$$E = (1 - e^{-10^{-5}\zeta^2})\, E_\infty \tag{4.41}$$

The function

$$f(\zeta) = (1 - e^{-10^{-5}\zeta^2}) \tag{4.42}$$

is an exponential relaxation function that expresses the development of entrainment along the tube.

Equation (4.42) correlated well the entrance effect on the entrainment data for vertical flow of Cousins et al (1965), and indicated that the entrance region ranged for $0 < \varsigma < 600$. So, the quasi-equilibrium condition for entrainment was attained for:

$$z \geq 600\, d_t \sqrt{\frac{U^*_{SG}}{\mathrm{Re}_L}} \tag{4.43}$$

Finally, Ishii and Mishima (1981) mentioned that their correlation was tested against many experimental results for air-water systems, in the ranges of $1 < P < 4$ atm, $0.0095 < d_t < 0.032$ m, $370 < Re_L < 6400$ and $U_{SG} < 100$ m/s.

In Figure 4.15 experimental results of the present investigation are compared against the entrained fraction calculated by using the correlation of Ishii and Mishima (1981) (equation 4.36). The horizontal entrainment data obtained by Chakrabarti (1976), Dallman (1978), Laurinat (1982), Williams (1986) and Paras and Karabelas (1991) were also compared with the entrained fraction values calculated using equation (4.36). These results are shown in Figure 4.16. It should be highlighted here that the entrance effects given by equation (4.43) were developed from vertical flow data, so its application to horizontal flow may be incorrect. For this reason, it was assumed that the entrainment data for horizontal annular reached a quasi-equilibrium value, and so equation (4.36) was applied instead of equation (4.41).

From the graphs in Figures 4.15 and 4.16 it is possible to conclude that apart from some of the data presented by Dallman (1978), the correlation of Ishii and Mishima (1981) overpredicts the entrained fraction in horizontal two-phase flow. The worst fit is for the data of Williams (1986) obtained in a 0.0953 m tube, which may suggest that the correlation of Ishii

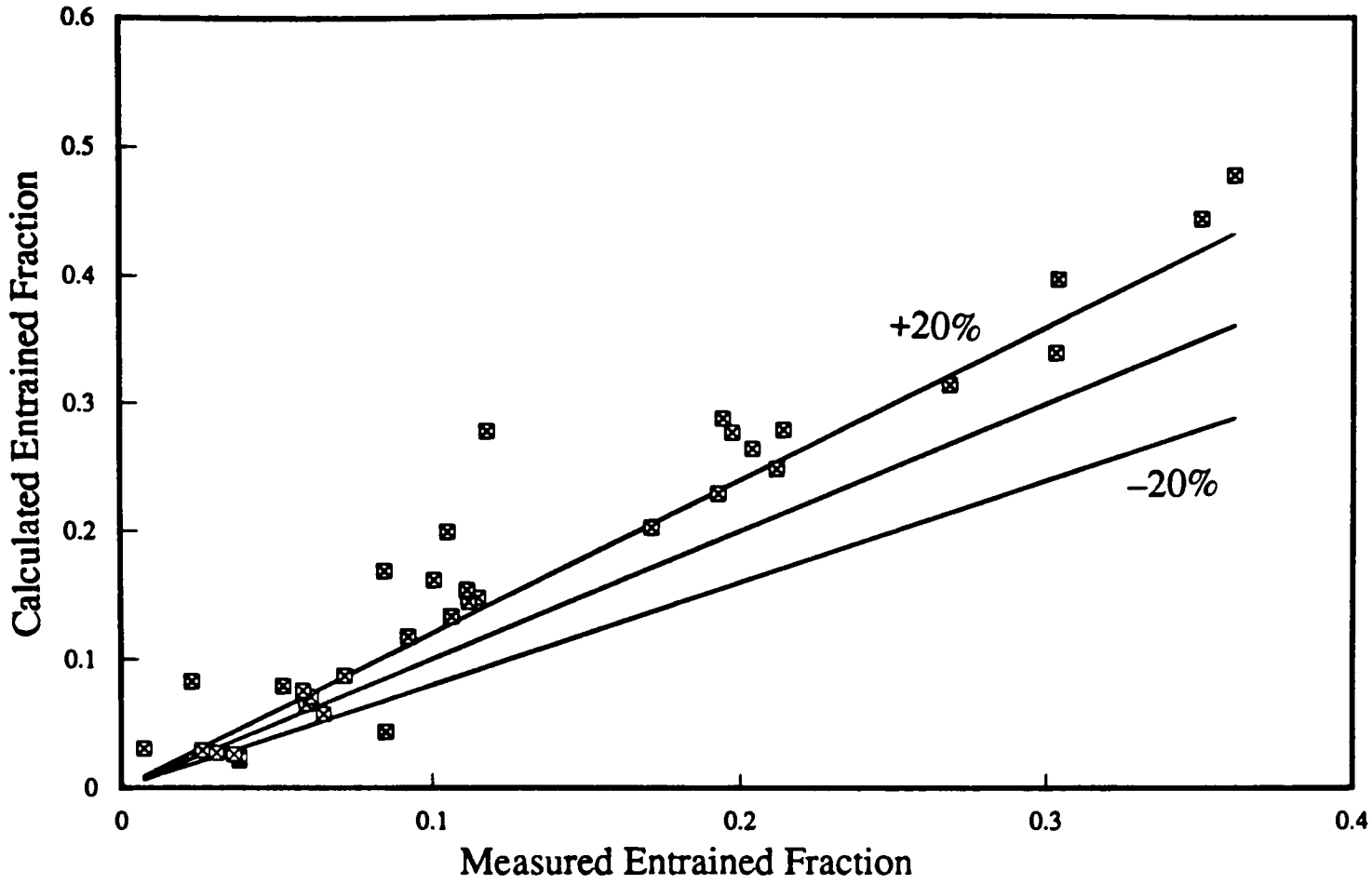

Figure 4.15 Performance of the correlation of Ishii and Mishima (1981) to predict the entrainment data of the present study.

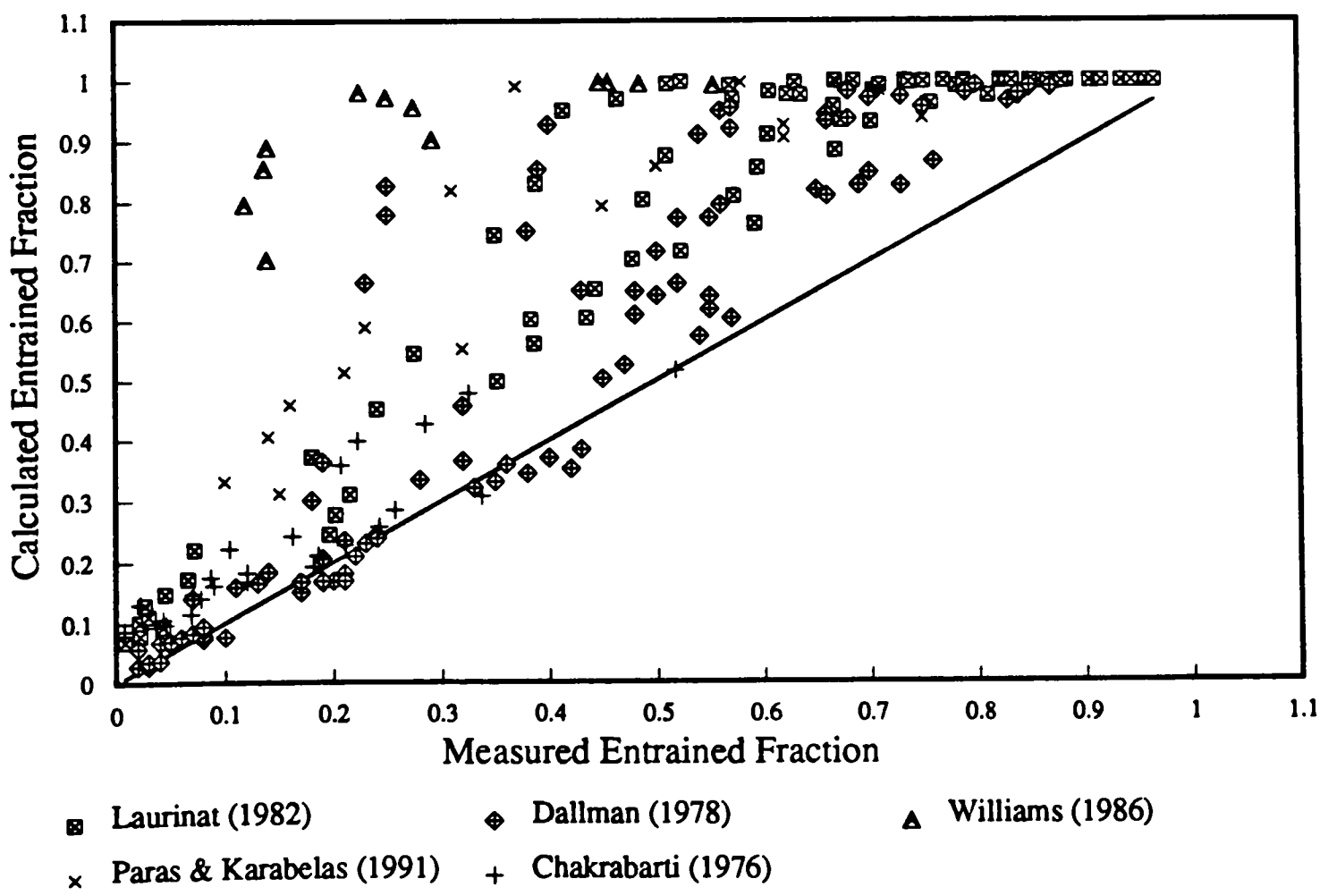

Figure 4.16 Performance of the correlation of Ishii and Mishima (1981) to predict the entrainment data of horizontal annular flow for several tube diameters.

and Mishima is not applicable at such large tube diameters. By changing the constant in equation (4.36) to 5.5 x 10^{-7} a better fit was obtained for the present set of data (Figure 4.17).

Kitscha et al (1990) presented a correlation based on the shearing off of roll wave crests mechanism. Their equation is a modification of Ishii and Mishima (1981) correlation, and has the form:

$$E = \tanh\ (4.33 \times 10^{-12}\ We'^{2.55}\ \mathrm{Re}_L^{0.26}) \qquad (4.44)$$

The authors reported that their equation correlated well their own data obtained in a 0.0503 m ID horizontal tube, and also the results of Laurinat (1982) and Butterworth (1982) as shown in Figure 4.18. However, it is important to notice that the plot of E measured against E calculated is presented on a log-log scale, which tends to mask the true trends.

The results of Laurinat (1982) were replotted in Figure 4.19, but now using a linear scale instead of log-log, and also the lines of +/-20% are indicated. It can be seen immediately that equation (4.44) does not predict the entrainment data of Laurinat correctly.

Equation (4.44) was used to correlate the results of the present investigation, as shown in Figure 4.20. Again the expression fails to correlate the data, tending to underpredict the entrained liquid fraction.

4.4. Entrainment Measurements in a Bend

Despite the liquid distribution around bends having severe implications on heat transfer and erosion/corrosion problems, studies of annular two-phase flow in bends to date are very limited.

In this section previous entrainment measurements carried out on bends are reviewed. A new set of film flow measurements taken downstream of the 90° horizontal bend for air-water are presented. The flow conditions used in these experiments match the ones used on the film flow measurements taken before the bend. Throughout these tests the pressure was maintained at 1.3 or 1.4 bar at the tapping located 0.27 m before the bend.

4.4.1. Previous Work

A literature survey reveals that little research work has been done so far, on entrainment around bends.

Anderson and Hills (1974) studied the annular flow of an air-water system in a 180° bend arranged at the top of a straight vertical tube. The drop flow in the gas core was measured using a sampling probe positioned immediately before and after the bend. Examples of these

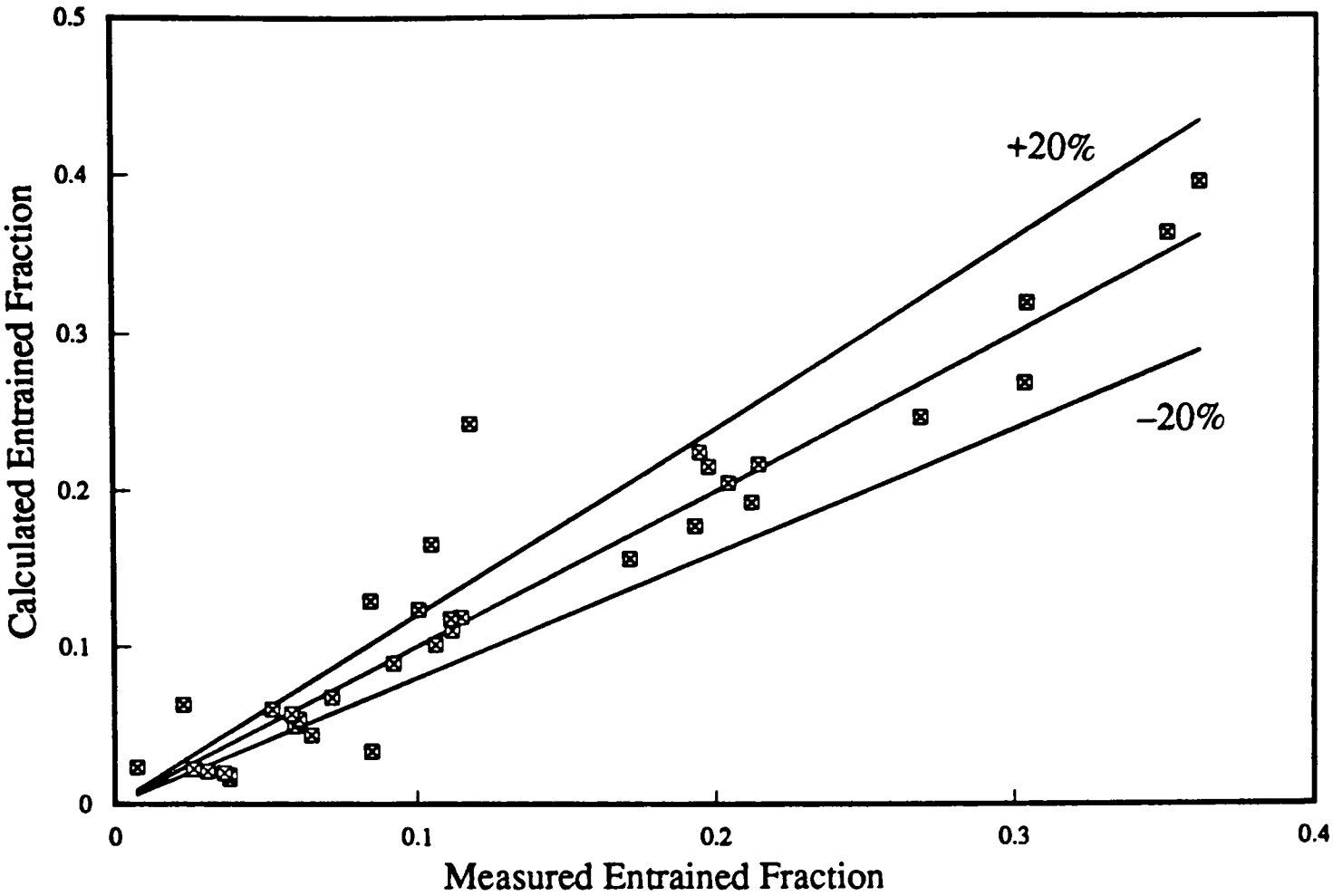

Figure 4.17 Comparison between the measured entrained fractions of this study and the entrained fractions calculated as: $E = 5.5 \times 10^{-7}\ We^{1.25}\ \mathrm{Re}_L^{0.25}$.

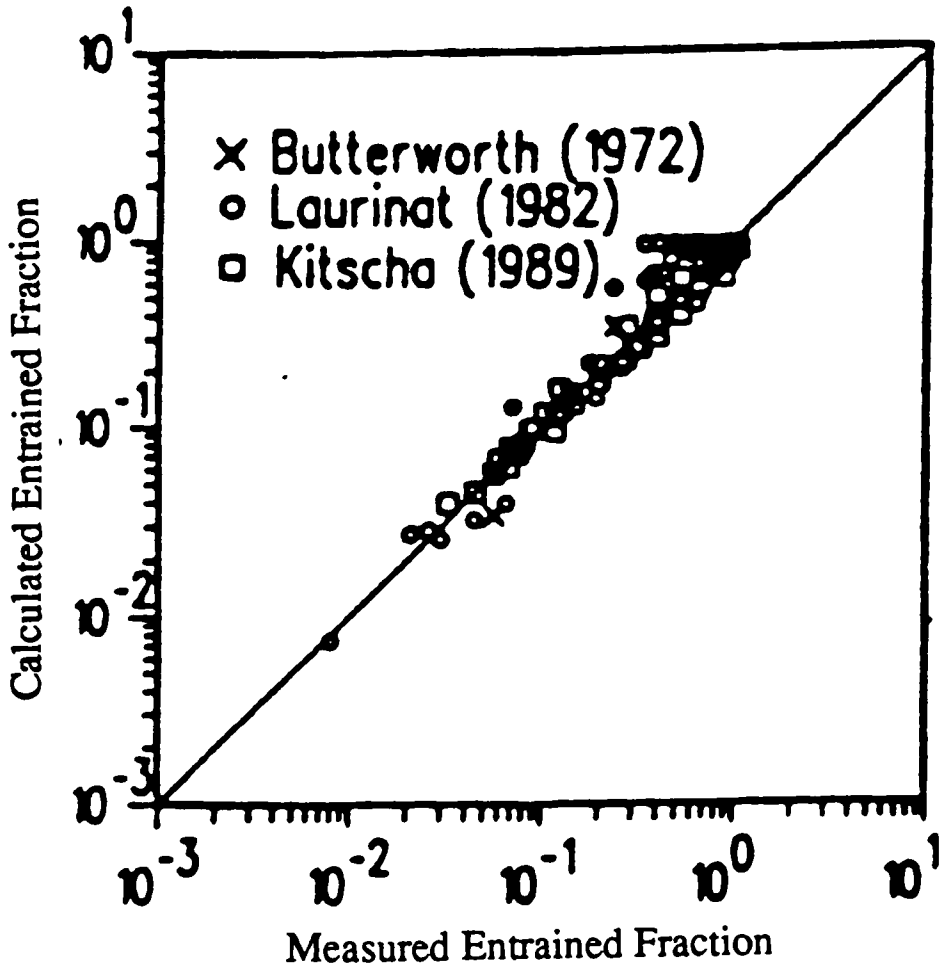

Figure 4.18 Comparison between experimental entrained fraction and predicted entrained fraction using the correlation of Kitscha et al (1991) (taken from Kitscha et al (1991)).

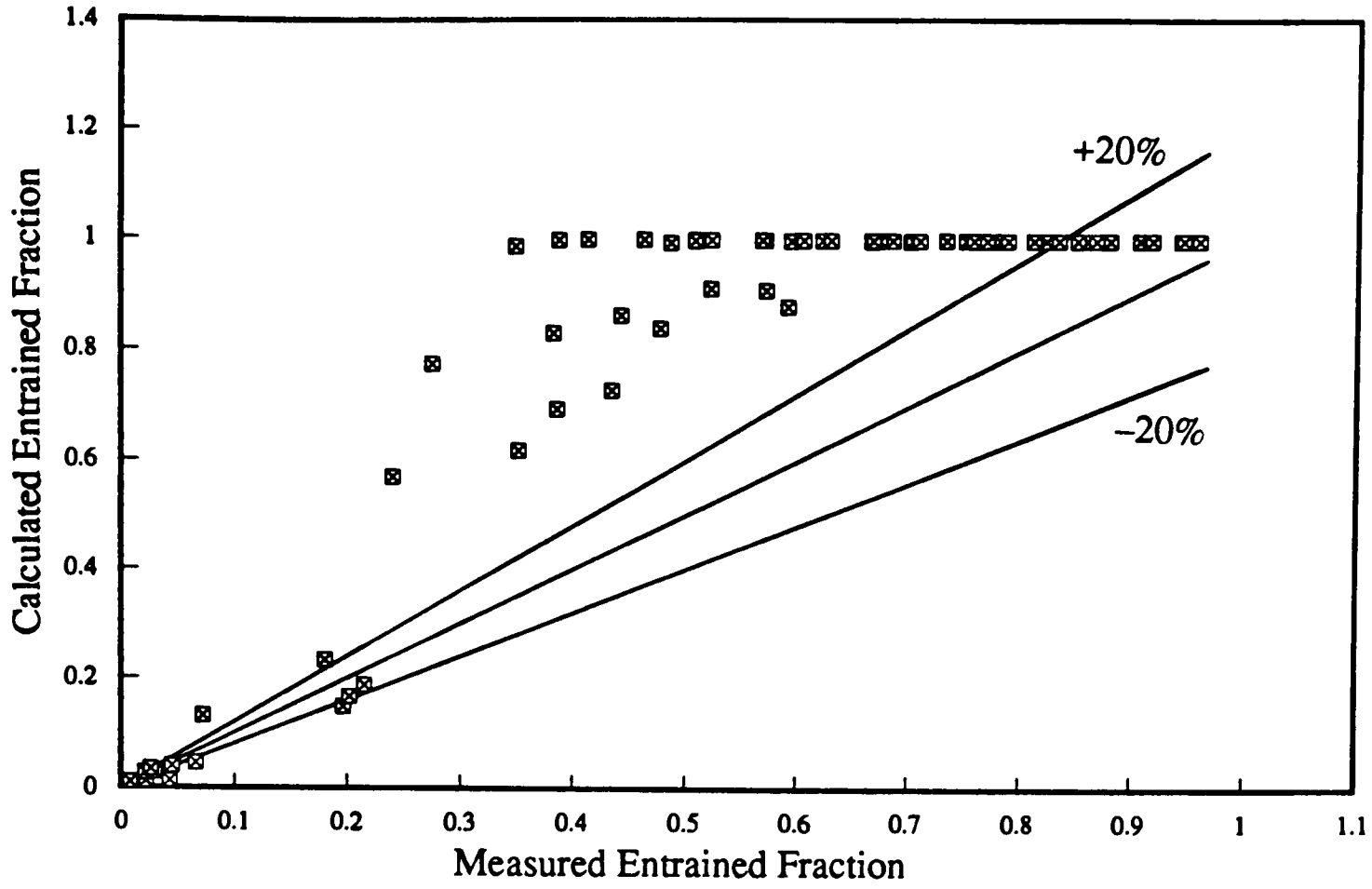

Figure 4.19 Performance of the entrainment correlation of Kitscha et al (1991) to predict the data of Laurinat (1982).

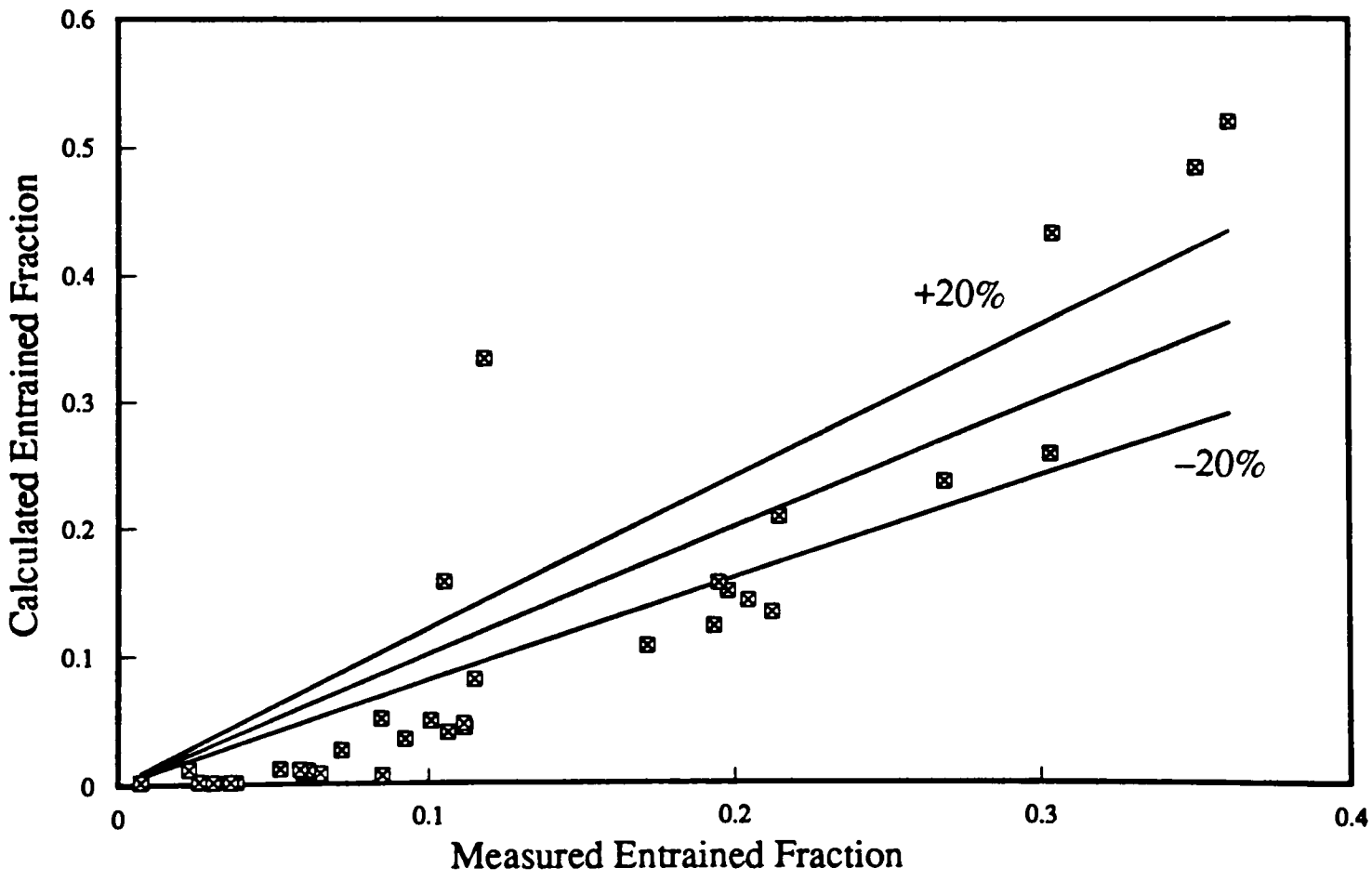

Figure 4.20 Performance of the entrainment correlation of Kitscha et al (1991) to predict the data of the present study.

measurements are shown in Figures 4.21 to 4.23. Comparison of the data indicates that the bend reduced entrainment.

Maddock et al (1974) measured among other parameters, local film flow rates using a rotatable porous wall confined to a 60° arc of the tube circumference, placed at the exit of several vertical bends. These were located at the end of a vertical straight pipe 0.0254 m in diameter. The bend radii varied from 0.0508–0.254 m and the bend angles from 30° to 90°. The authors proposed a simplified picture of the mechanisms that occur along the bend, assuming that data obtained just downstream of the bend gave a reasonable approximation to the variations occurring at corresponding points within a longer bend. In Figure 4.24, a plot of film flow rate development with respect to bend angle is shown, where film flow rates are divided into the inner and outer halves of the water surface.

Entrainment measurements around a 90° horizontal bend were reported by Chakrabarti (1976). The bend was located at the end of a 0.0254 m ID horizontal tube. Drop fluxes were measured before and after the bend using a sampling pitot tube for annular air–water flow. The author noticed that the drops on entering the bend due to their high momentum would deposit on the outer wall of the bend. This caused the liquid film thickness on the outside of the bend to increase, and entrainment to be reduced.

Balfour and Pearce (1978) reported measurements on the distribution of the liquid film and entrained drops for an air–water system in annular flow at the exit of a 180° horizontal bend. The bend was constructed from a 0.025 m bore tube with a radius of curvature of 0.485 m. A sampling probe was used to measure axial film flow rates and the mass flow rate of entrained drops at any point in the gas core.

The authors observed that the position of maximum film flow rate for a given gas flow shifts towards the inside of the bend as the quality (= $G_G/(G_G + G_L)$) increases (Figure 4.25). Another interesting feature also pointed out was the occurrence of a double peak in the film flow rate distribution for some annular flows, with maxima on both the inside and outside of the bend.

4.4.2. Present Entrainment Measurements After the Bend

In this section the influence of a 90° horizontal bend in the level of entrainment is discussed. A set of film flow measurements was carried out after the bend for stratified and annular flow conditions, using the film removal technique.

For the conditions after the bend, Figure 4.26 shows the liquid film mass flux increasing linearly with liquid mass flux. A similar trend was observed before the bend (Figure 4.7). In Figure 4.27, the liquid film mass fluxes after the bend are plotted against the superficial gas velocity. A comparison with Figure 4.8 reveals that the G_{LF} measurements immediately after the bend are less sensitive to the influence of gas velocity.

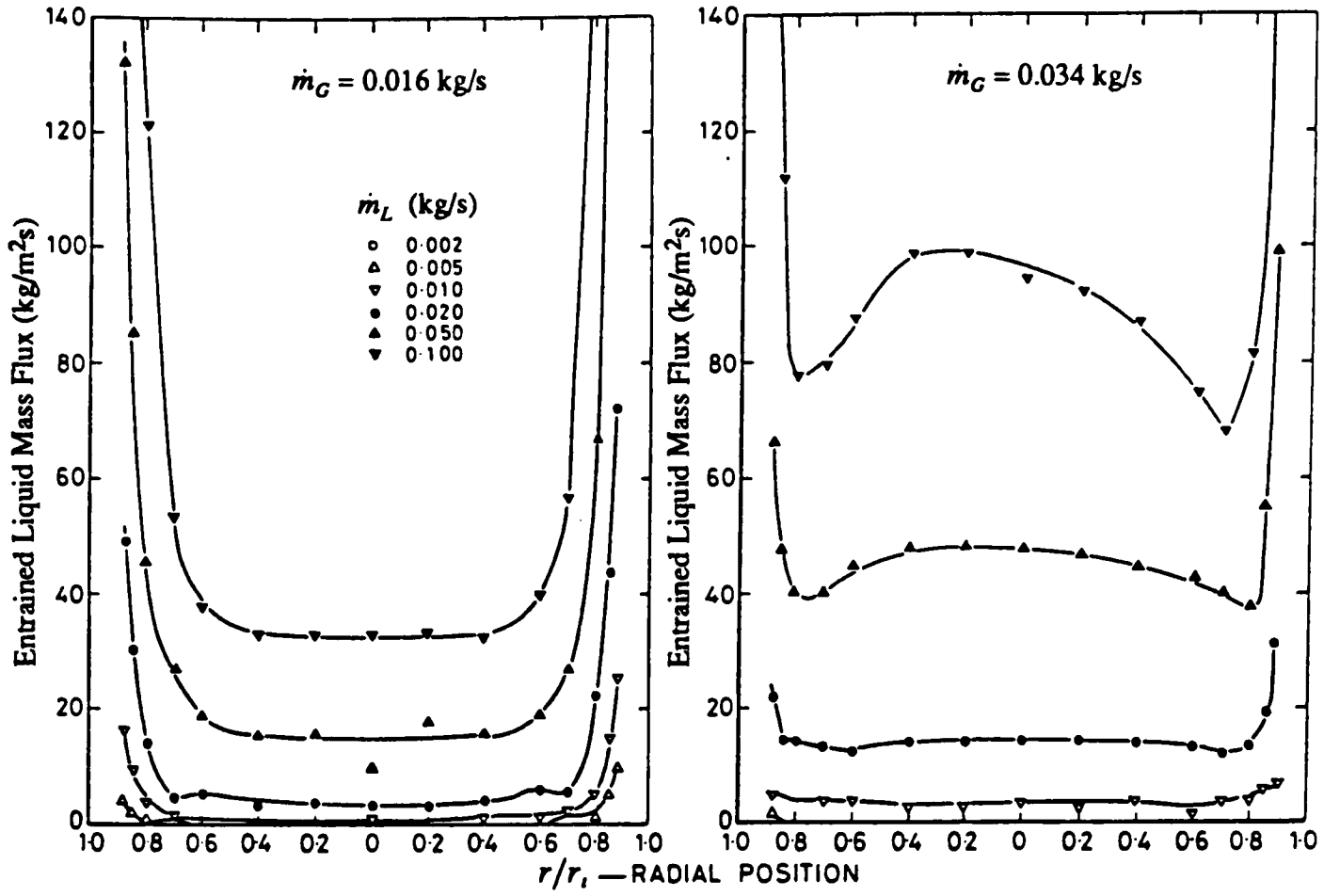

Figure 4.21 Entrained liquid mass flux profiles before the bend (Anderson and Hills (1974)).

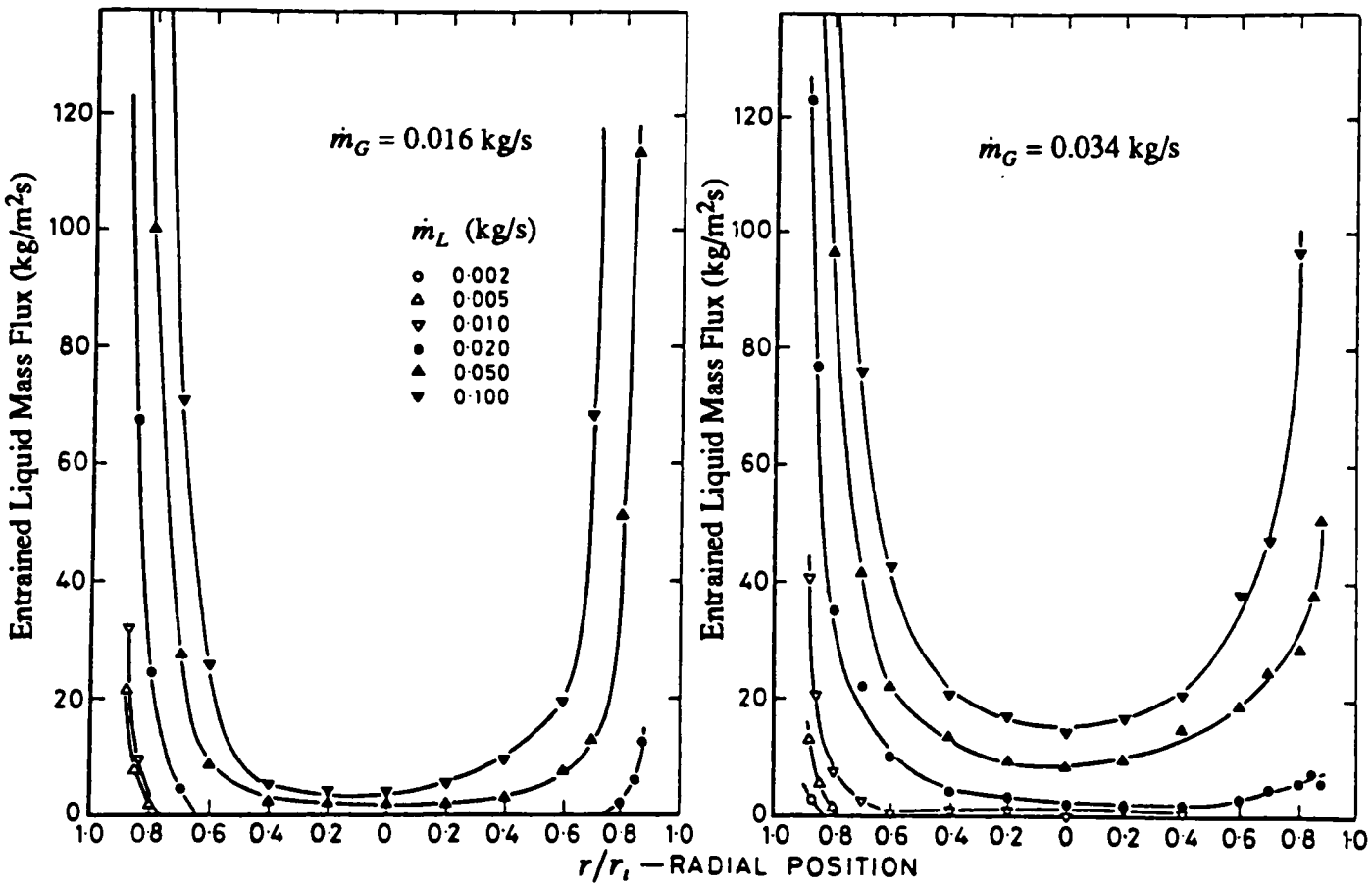

Figure 4.22 Entrained liquid mass flux profiles after the bend – transverse in plane of the bend (Anderson and Hills (1974)).

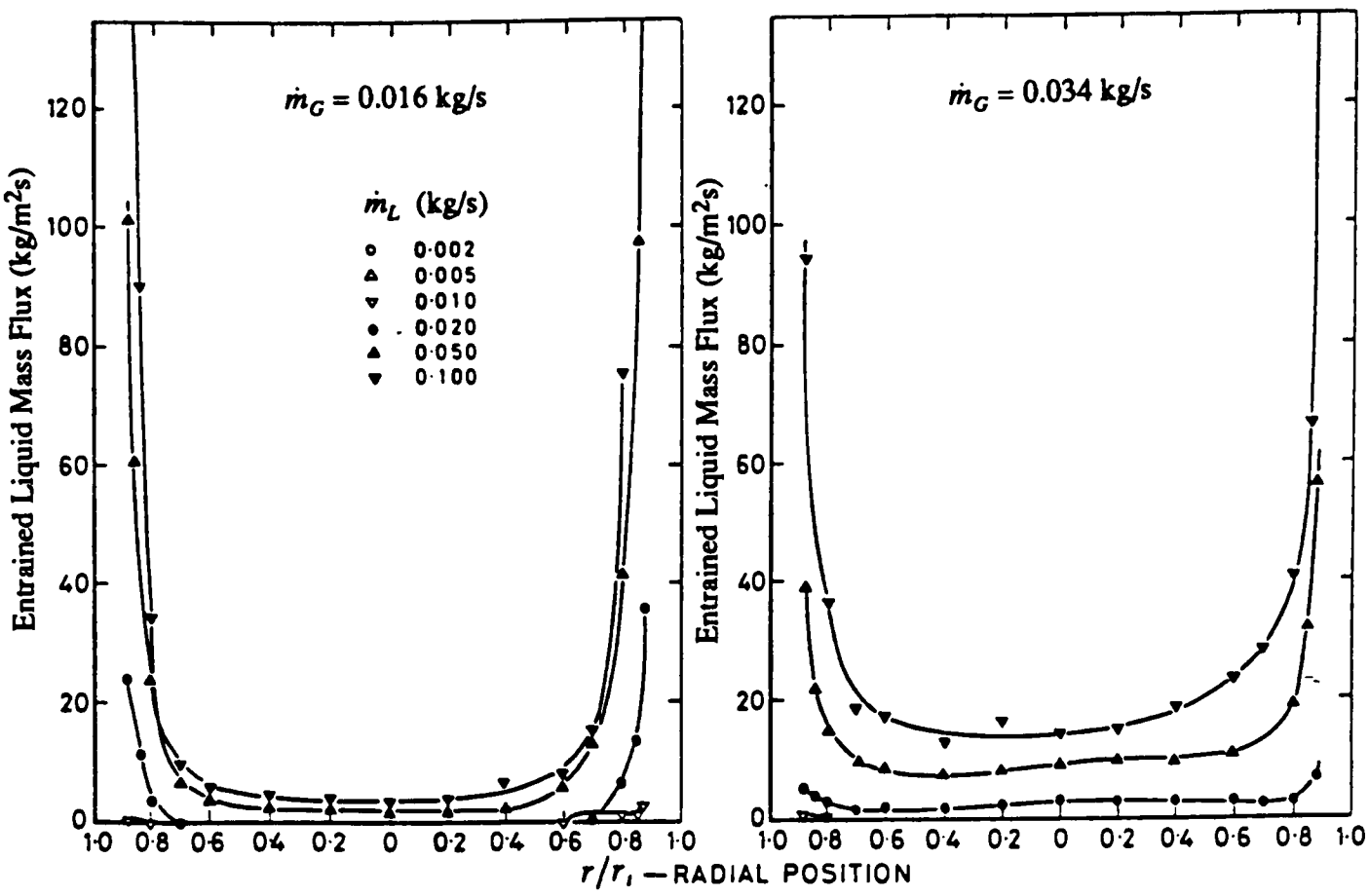

Figure 4.23 Entrained liquid mass flux profiles after the bend – transverse normal to the plane of the bend (Anderson and Hills (1974)).

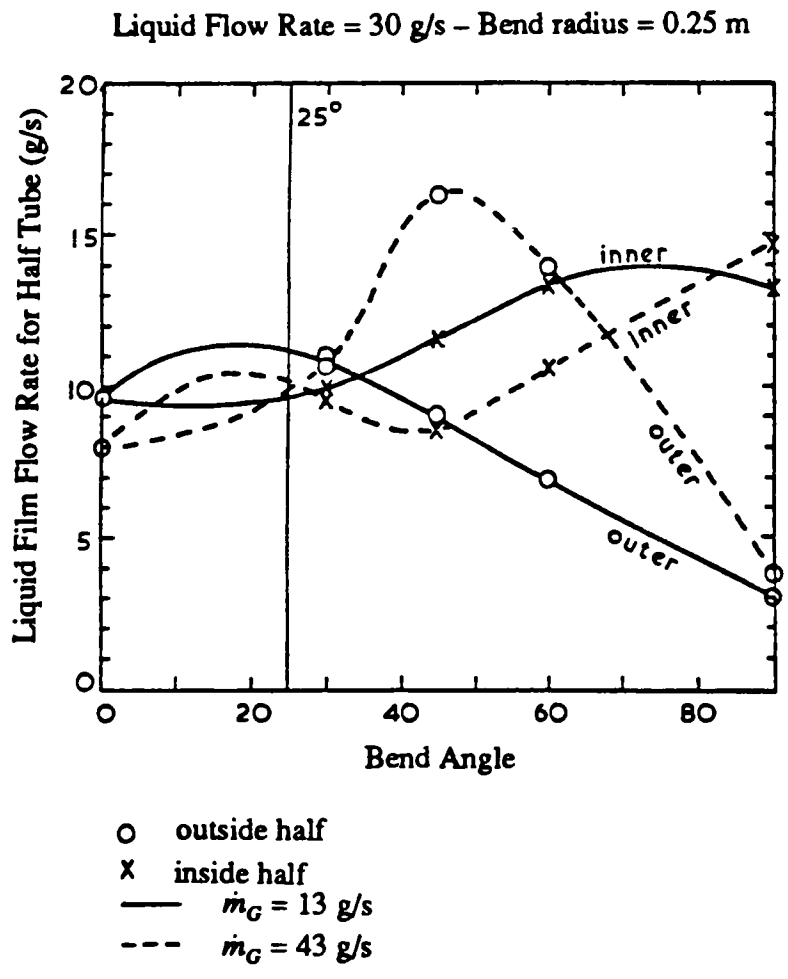

Figure 4.24 Liquid film flow rate development with respect to bend angle (Maddock et al (1974)).

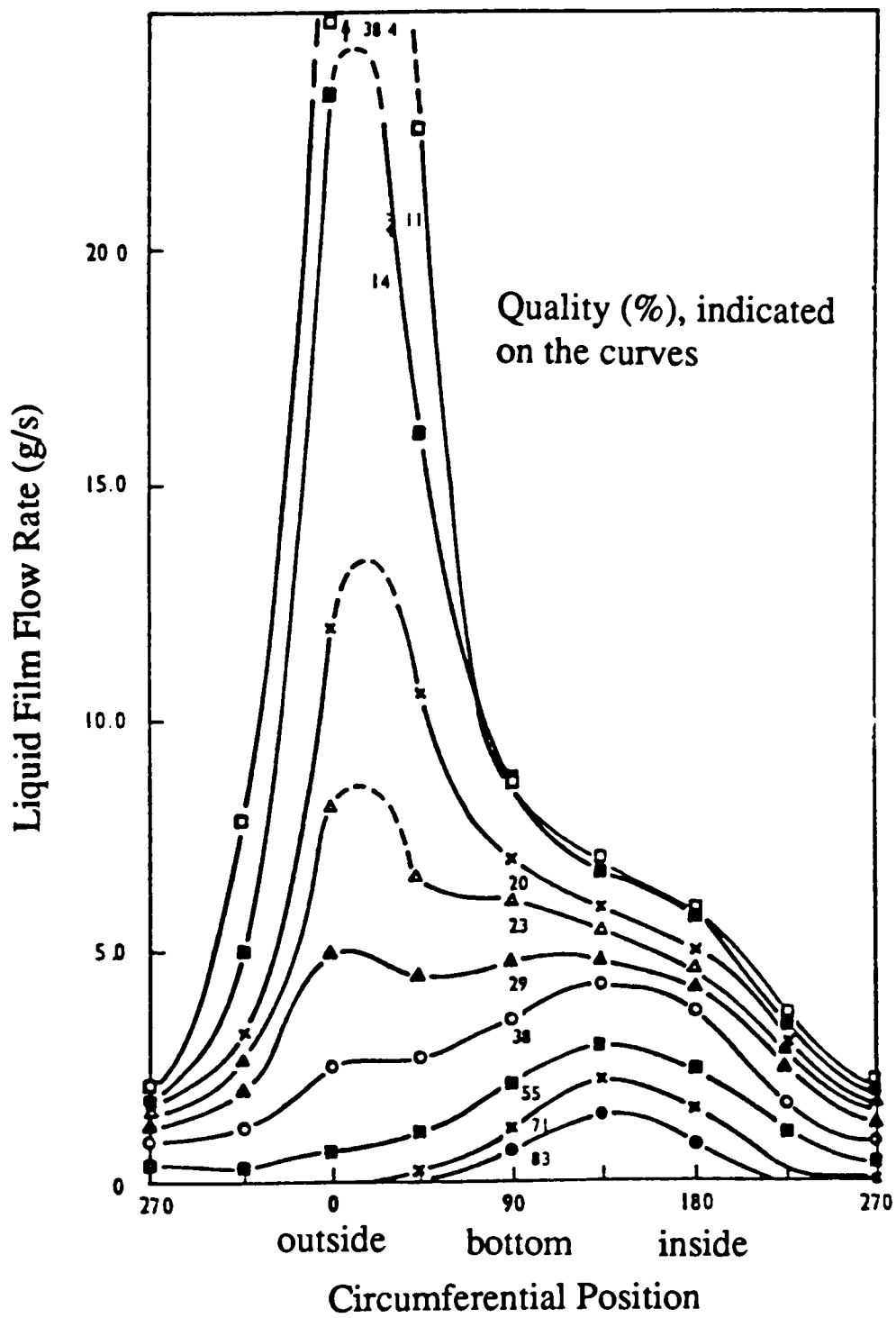

Figure 4.25 Circumferential variation of liquid film flow rate for an air flow rate of 0.024 kg/s (Balfour and Pearce (1978)).

The influence of the liquid mass flux on the measured entrained liquid mass flux (G_{LE}) after the bend is shown in Figure 4.28. This graph highlights a very interesting trend. For G_G = 20–50 kg/m^{2}s, G_{LE} first increases but than decreases, the maximum in the function occurring at around G_L = 110 kg/m^{2}s for G_G = 20 kg/m^{2}s, and at G_L = 90 kg/m^{2}s for G_G = 30–50 kg/m^{2}s. For G_G = 60 and 70 kg/m^{2}s, entrainment increases with G_L for the flow conditions analysed.

Figure 4.29 plots the entrained liquid mass flux after the bend versus the superficial gas velocity. It shows that G_{LE} increases with gas velocity (at a fixed liquid flow) for the whole range of liquid flow rates studied.

Previous studies to detect the levels of entrained liquid around different bends (section 4.4.1.) have shown a common feature: generally the presence of a bend reduces the quantity of entrainment. For the present investigation the percentage increase in the liquid film flow rate after the bend is illustrated in Figure 4.30.

Figure 4.30 shows that: (i) for G_G = 20 and 30 kg/m^{2}s, the percentage difference in the liquid film before and after the bend is very small (below 1.5 %) and does not change with increasing the liquid mass flux, and (ii) for a constant liquid flow of G_L = 10 kg/m^{2}s and increasing gas flow rate, the percentage difference between film flow before and after the bend is maintained below +/–3%. So, for these conditions of low entrainment the influence on the liquid film flow rate is not significant.

For $G_G \geq$ 40 kg/m^{2}s, and for $G_L \geq$ 30 kg/m^{2}s, the liquid film mass flux after the bend increases with gas and liquid mass fluxes. A maximum percentage difference of 35.7% occurred at G_G = 70 kg/m^{2}s and G_L = 70 kg/m^{2}s, which also corresponds to the flow conditions of the present experiments where entrainment is maximum upstream of the bend.

This increase in film flow rate after the bend (consequently a reduction in entrainment) is due to deposition of drops on the outside wall of the bend. This deposition of the drops at the bend was confirmed by visual observations described in section 3.3.

4.5. Conclusions

From the discussion in this chapter, the main conclusions can be summarized as follows, for the measurements carried out before the bend:

- The correlation of Ishii and Grolmes (1975) overpredicts the critical gas velocity for the onset of entrainment for the horizontal flow of an air–water system in a 0.032 m ID tube.
- At constant gas velocity, there is a linear relationship existing between the liquid film mass flux and and the liquid flow observed for the whole range of gas velocities studied.

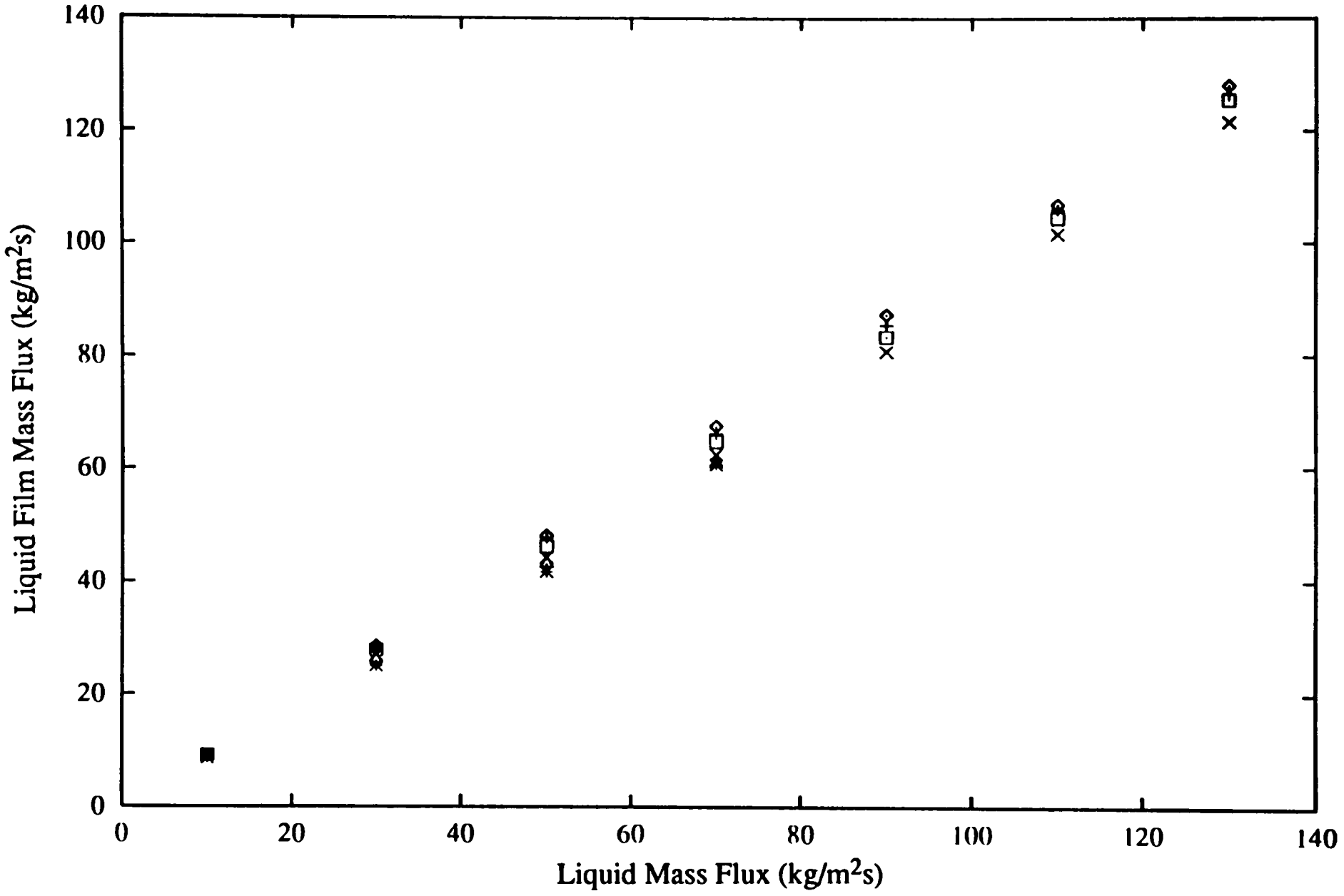

Figure 4.26 Influence of the liquid mass flow on the liquid film mass flux measurements taken after the bend.

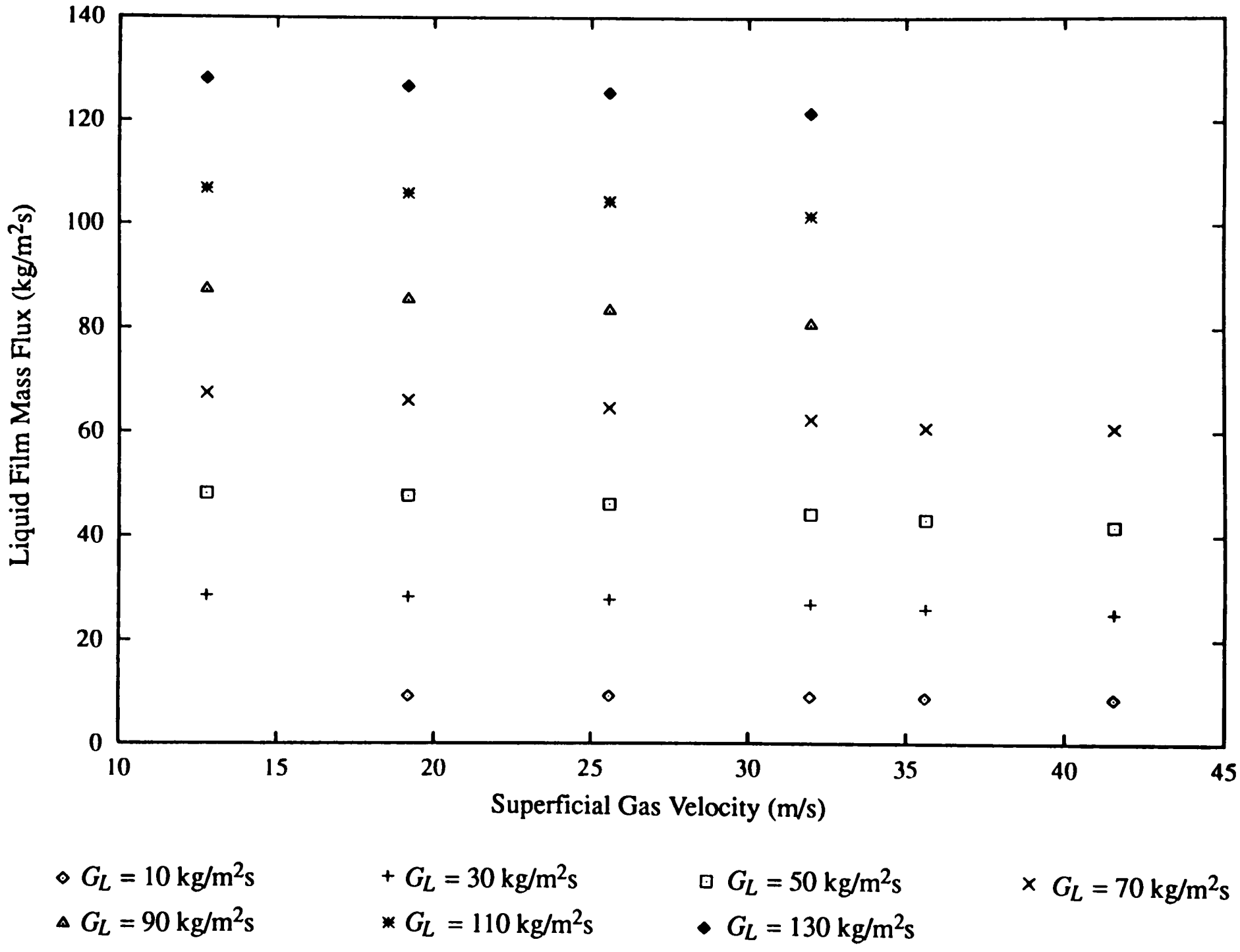

Figure 4.27 Influence of the superficial gas velocity on the liquid film mass flux measurements taken after the bend.

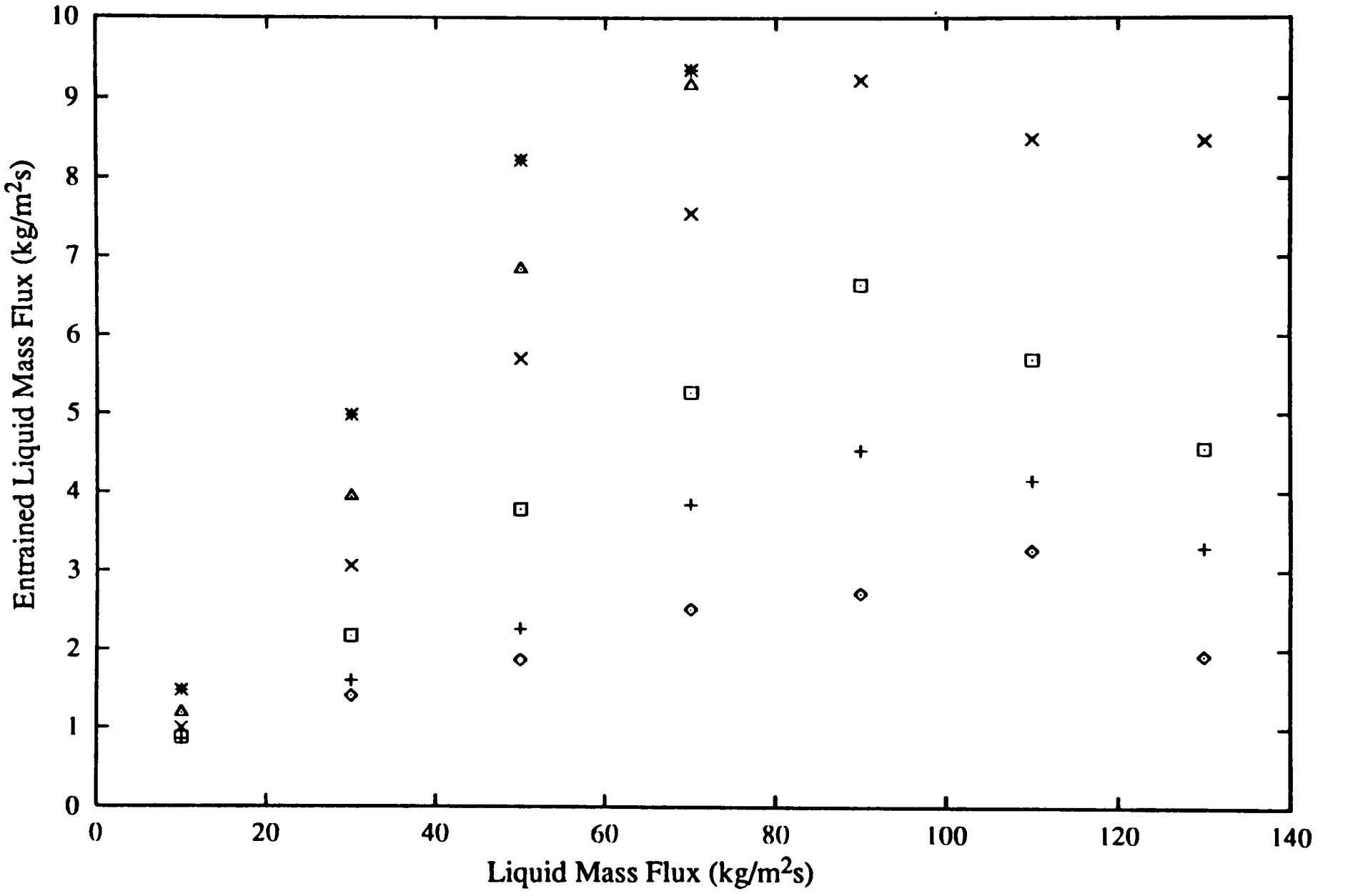

Figure 4.28 Influence of the liquid mass flux on the entrained liquid mass flux measurements taken after the bend.

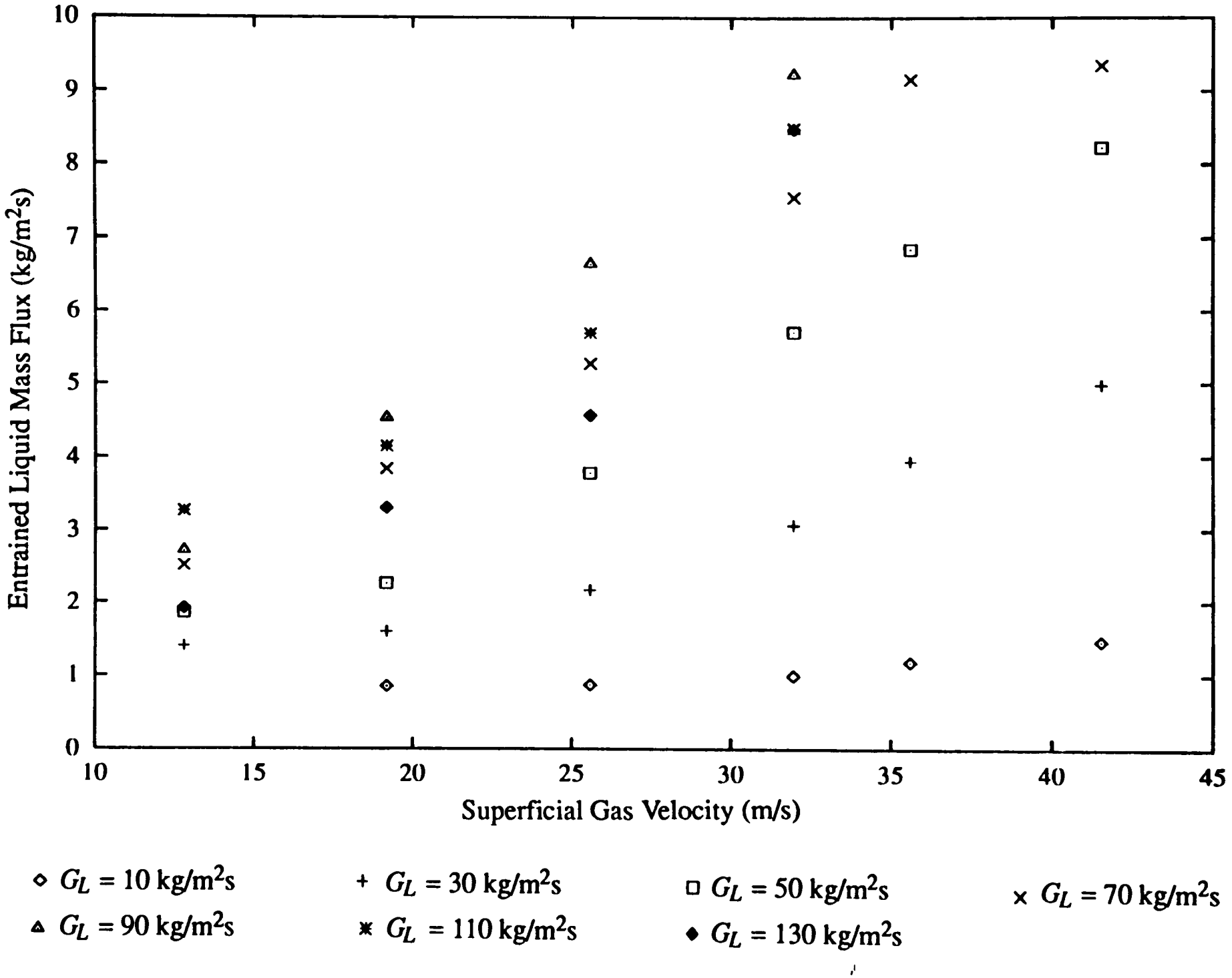

Figure 4.29 Influence of the superficial gas velocity on the entrained liquid mass flux measurements taken after the bend.

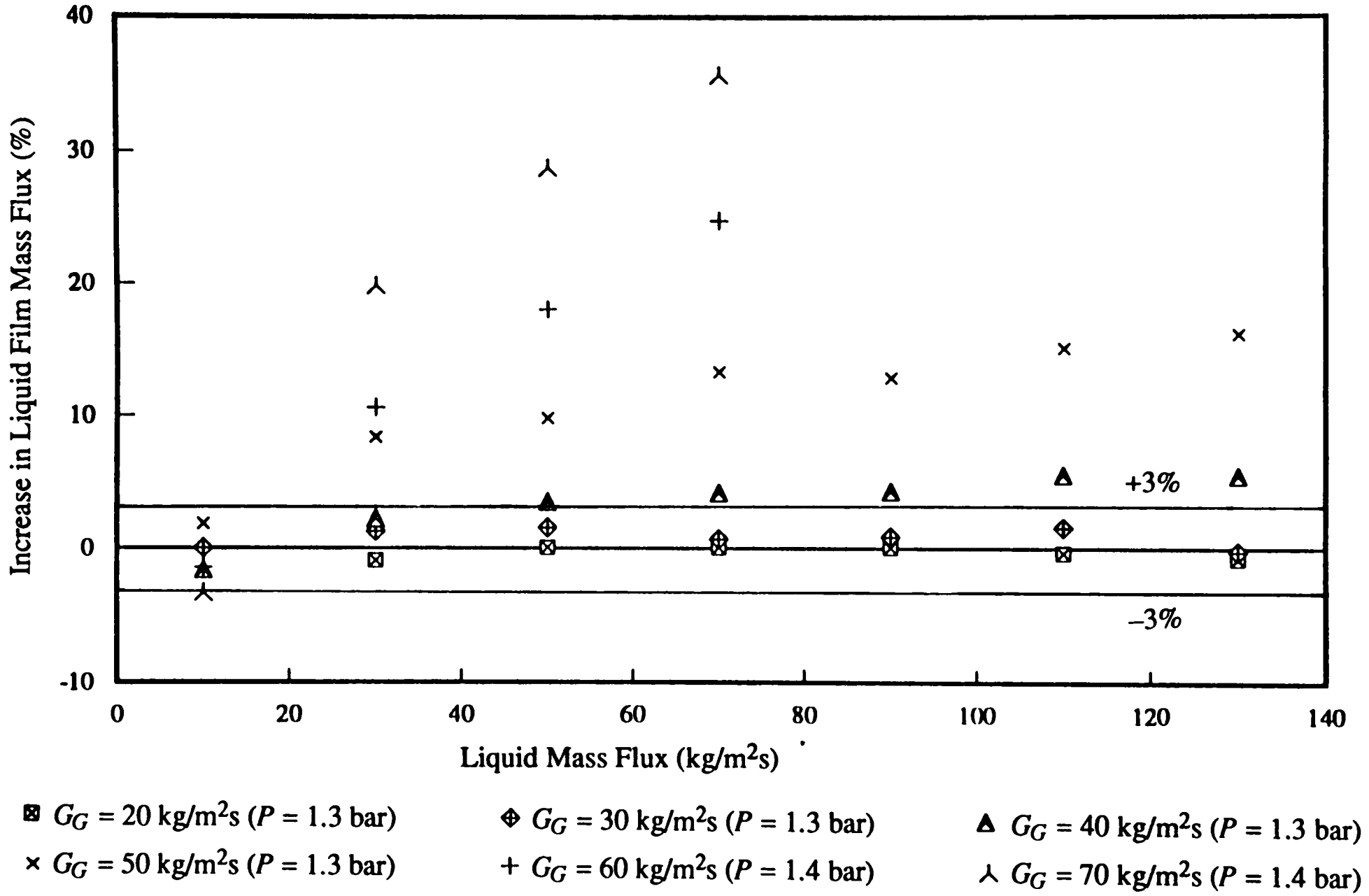

Figure 4.30 Increase in the liquid film mass flux observed after the 90° horizontal bend.

- At constant liquid flow rate, the liquid film mass flux decreases with gas velocity except for G_L =10 kg/m^{2}s, where G_{LF} is constant with increasing gas velocity.
- For the stratified/annular flows the entrained flux increased with liquid flow rate, and in some instances a plateau condition was reached. At the lowest gas mass flux conditions (G_G = 20 kg/m^{2}s and G_G = 30 kg/m^{2}s) the quantity of entrained liquid falls considerably at the highest liquid flow of 130 kg/m^{2}s. This is due to the transition to pseudo–slug flow.
- For the whole range of flow conditions covered, G_{LE} increases with gas velocity, except for G_L = 10 kg/m^{2}s where the level of entrainment is almost constant.
- The entrained liquid flow rate in horizontal annular flow was found to be lower than in vertical flow for the same flow conditions and tube diameter (0.32 m). However, as the gas velocity increases this difference is less pronounced.
- The entrainment correlation of Williams (1986) correlated well horizontal annular flow data by Dallman (1978), Laurinat (1982), Williams (1986) and Paras and Karabelas (1991). However, it does not do so for the present measurements taken across the transition from wavy–stratified to annular flow.
- The entrainment correlation of Ishii and Mishima (1981) generally overpredicts data in horizontal two–phase flow. A change in the constant of the expression seems to improve the fit with the data from this study.

The experiments taken downstream of the bend show that:

- At constant gas flow rate, liquid film flux G_{LF} increases linearly with G_L.
- At constant liquid flow rate, G_{LF} decreases with gas velocity, except for G_L = 10 kg/m^{2}s where the liquid film flow rate is almost constant.
- The curves of entrainment against liquid flow (at fixed gas mass flux) show a maximum at the low gas flow conditions. For the gas mass fluxes of G_G = 60 kg/m^{2}s and 70 kg/m^{2}s entrainment increases with G_L.
- For the flow conditions studied, G_{LE} increases with gas velocity at a constant liquid flow rate.
- Above certain flow conditions, there is an increase in film flow rate after the bend. The corresponding reduction in the amount of entrained liquid is caused by drops depositing on the outside of the bend.

5. DROP SIZE IN HORIZONTAL TWO-PHASE FLOW

The knowledge of the drop size distribution as a function of the flow conditions of the system is a very important in the study of annular two-phase flow. Drop size is known to affect heat, momentum and mass transfer problems. For example, in heated systems the formation of drops may result in the dryout of the liquid film. Processes such as erosion, are affected by the impaction of particles and drops on the surfaces of bends and fittings.

This chapter is mainly concerned with the study of the size of drops in horizontal two-phase flow. Techniques to measure drop sizes are briefly reviewed. Published work on drop size for vertical and horizontal annular two-phase flow are presented. New data on drop size for horizontal air-water flow in a 0.032 m ID tube are presented. The chapter ends with the study of the influence of a horizontal bend on drop size.

5.1. Techniques for Drop Size Measurement

A great number of drop sizing techniques have been developed. Various factors can influence the choice the drop sizing method, and ideally the diagnostic technique should give a complete size distribution. With each size technique it is vital to know its limitations with respect to the size band width, accuracy, tolerated particle densities and required optical properties of the medium and particles.

Before reviewing the most important particle sizing techniques, a distinction must be between the two approaches used to determine the drop size distribution. The first approach, spatial sampling, gives the actual size distribution of the drops contained within a volume during short periods of time, so that the contents of the volume do not change during any single observation. The second approach is temporal sampling and describes the measurement of drops passing through a fixed area during a specific time interval, indicating the mass flux of particles of different size.

5.1.1. Photography

Photography is one of the earliest non-intrusive drop sizing techniques to be used in two-phase flow. It involves the capture of drop images on a photographic plate via a single flash illumination, whose duration depends on the movement of drops within the field of view of the camera lens. The photograph must then be magnified, and the drop size distribution is obtained by counting and sizing the diameter of the particles in focus.

Illumination and the exposure duration are very important aspects to be considered when photographing moving drops. Appropriate light must be used so that the drop can be seen in

the photograph, and the time of exposure depends on the size and velocity of the drops. The grain of the photographic emulsion limits the identification of smaller drops.

The method is not without problems, especially in the analysis of the photographic images. Manual analysis is very subjective when distinguishing between in focus and out of focus drops. Also, it is very tedious and time consuming. However, recently automatic instruments have been developed, which accelerate the process and introduce a more objective approach to the analysis.

Photography can also be used for obtaining information on drop velocities and direction of movement. If two light pulses are generated in rapid succession, a double image of a single drop is obtained on the same negative. By measuring the distance travelled by the drop and knowing the time delay between the two pulses, the velocity of the drop can be determined.

5.1.2. Holography

Holography permits the user to obtain a three dimensional image of an object. In this technique, a beam of coherent light from a pulsed laser is split into two: one part is reflect by the particle field and arrives on the photographic plate on which the hologram is to be formed; the other part (reference beam) bypasses the drops unchanged in phase (Figure 5.1). The hologram is formed as a result of the interference between the scattered and unscattered light.

The recorded image can then be reconstructed by illuminating the hologram with the reference beam in the same direction as when the hologram was taken.

One advantage of this method is that it produces a recorded picture that may be analysed afterwards, and a large depth of field is permitted for all particle diameters. Holography permits measuring drop sizes as small as 2 μm (Azzopardi (1977)), but its application is restricted to diluted samples in respect of drops per unit volume.

5.1.3. Impaction Techniques

Impaction techniques use a solid surface (glass slide) which is covered with a suitable coating of fine grain structure, so that the deformations created by very small impinging drops can be examined in a microscope. When using magnesium oxide film as the coating material, measurement of drops down to 5 μm can be obtained. Correction factors relating the actual size of drops to the measured crater diameters can be obtained from a previous calibration.

The method is simple and there is a permanent retention of the craters. However, it has several disadvantages: it is intrusive, larger drops can break when impacting, smaller drops are likely to follow the gas streams around the sampling probe and without impacting the surface. The upper limit on the drop size to be measured is determined by the film thickness of the coating.

Liquid coatings can also be used to retain the captured drops. The advantage over solid coatings is that there is no need to relate the drop size to crater size.

An improvement of the coated slide technique is to collect the drops in an immersion cell where they stay suspended while they are measured. This technique offers advantages over collection on a slide: the drops remain spherical, evaporation is prevented and the real sizes of the drops are obtained (if no splitting of the drop occurs when entering the collection liquid). However, if the number of drops is too high coalescence is likely to occur, and the method is intrusive.

5.1.4. Electrical Methods

Electrical methods are based on the detection and analysis of electronic pulses produced by drop interference with an electrically operated probe.

The probe developed by Wicks and Dukler (1966) was formed by two electrically conducting needles placed exactly in line in a spray field. When a drop bridges the gap between them, an electric circuit is established and a voltage pulse may be recorded. By varying the gap size, frequency counts can be obtained in terms of the width between electrodes and then converted into drop size distributions. Drop size distributions obtained by this method might be biased towards small drops, since they follow the gas round the probe.

The charged wire technique operates on the principle that if a drop of a conducting liquid is in contact with a charged wire held by an insulated support, some charge will be transferred onto the drop. The amount of charge removed is dependent on drop size. So if the charge loss is monitored, it can be further related to drop size.

This technique, however, presents problems when dealing with sprays with high drop concentrations, as successive impingements can be superimposed on each other. Also, small drops might follow the gas stream and not hit the probe.

5.1.5. Thermal Methods

Thermal methods are mainly divided into freezing methods and evaporating methods.

Drop freezing explores the fact that if drops are solidified when they are formed, they can be treated as solids provided a low temperature is maintained. The solidified drops are then passed onto a set of standard sieves for direct analysis of its size. Alternatively, the sample can be photographed.

Rao (1978) used an isokinetic probe specially designed which was mounted with its inlet facing the drop flow. Nitrogen, coming through an annular slot located at the probe inlet, was injected into the incoming drop flow freezing the drops. These were then collected in a pre–cooled pot and analysed. This technique provides a temporal size distribution. However, the measured diameter has to be corrected for possible changes in volume occurring during the solidification process.

The evaporation method follows the behavior of a drop when it impinges on a hot surface whose temperature is above the boiling point of the liquid forming the drop. The time of complete evaporation depends on the size of the drop.

Instead of a heated surface, a thin hot wire can be exposed to the drop flow. When a drop impacts on the wire, a local cooling is observed with a corresponding decrease in the resistance of the wire. Voltage pulses from these changes can be related to drop size. The constant current energy supplied to the device consequently evaporates the drop, leaving the device ready to receive another drop. This technique gives a temporal distribution of drop sizes. However, the wire should be strong enough to withstand the impaction of drops, and smaller drops tend to by-pass the probe.

5.1.6. Optical Methods

In the previous sections various techniques for drop sizing have been reviewed. With the exception of photography and holography, these methods somehow necessitate the insertion of a probe into the flow, the reason why they are called intrusive.

However, measurements using the light scattering properties of particles to obtain information on drop size fall in the category of non-intrusive techniques. Because data acquisition is much quicker then with photography and because larger samples can be taken, the results are statistically more accurate.

Light scattering methods have been reviewed by Hewitt (1978-b). In the laser diffraction technique developed by Swithenbank et al (1976) the sample is directly illuminated by a laser beam. The particles scatter some of the light at angles which are characteristic of their size. A Fourier optical system is placed after the sample, and is used to focus the diffracted and undiffracted light onto a detector. The detector is formed by a set of semicircular photosensitive elements. Interpretation of the measured light energy distribution as a drop size distribution is carried out by a computer. This technique is commercially available from Malvern Instruments Limited, and is discussed in detail in section 2.1.5.

Laser Doppler Anemometry (LDA) can be used to obtain simultaneous information on particle sizing and velocity of the drops. A laser beam is split into two separate beams, which are focussed to intercept at the required measuring point. At this point an interference fringe pattern is produced. Drops passing the fringes scatter light with a regular modulation whose frequency is proportional to drop velocity. If the scattered light is monitored at a set angle, then the intensity of the light can be related to drop size.

Farmer (1972) was one of the first authors that investigated a method for drop sizing by relating the visibility of the Doppler burst signal to drop size. The visibility is defined as:

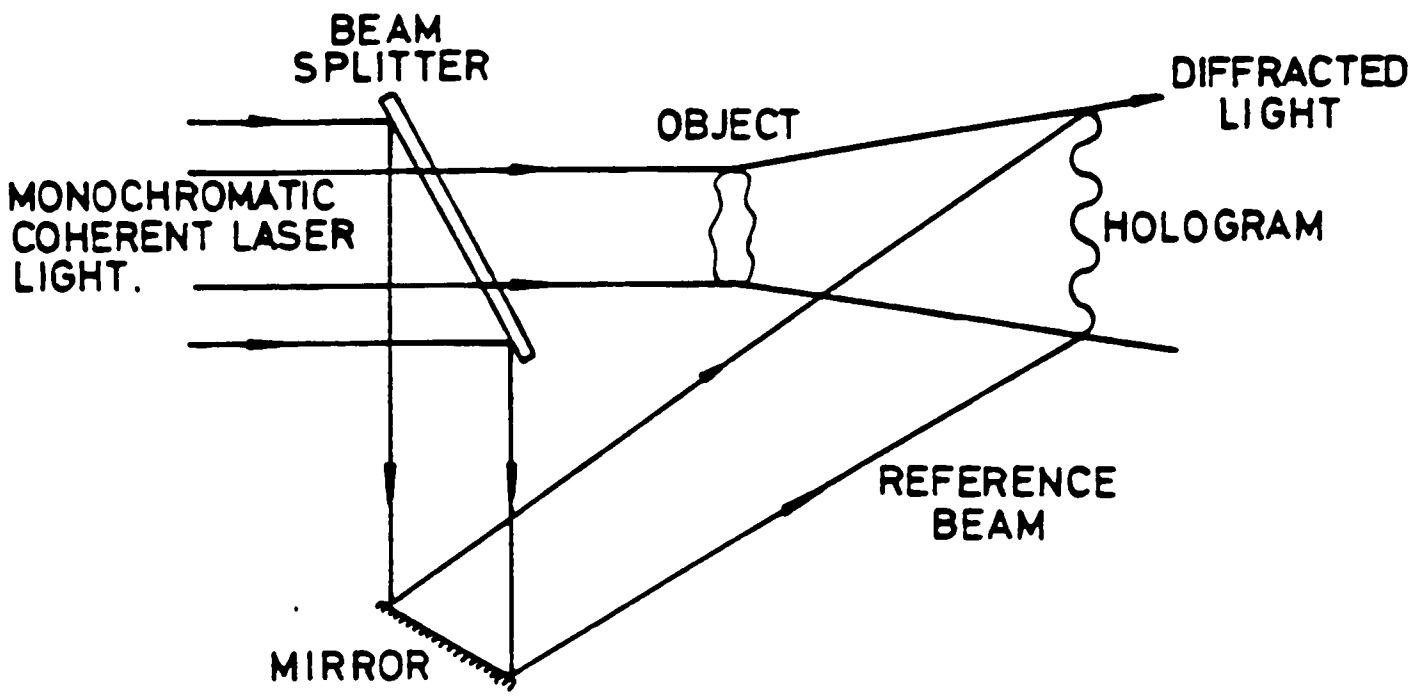

Figure 5.1 Schematic diagram for production of holograms (Azzopardi (1977)).

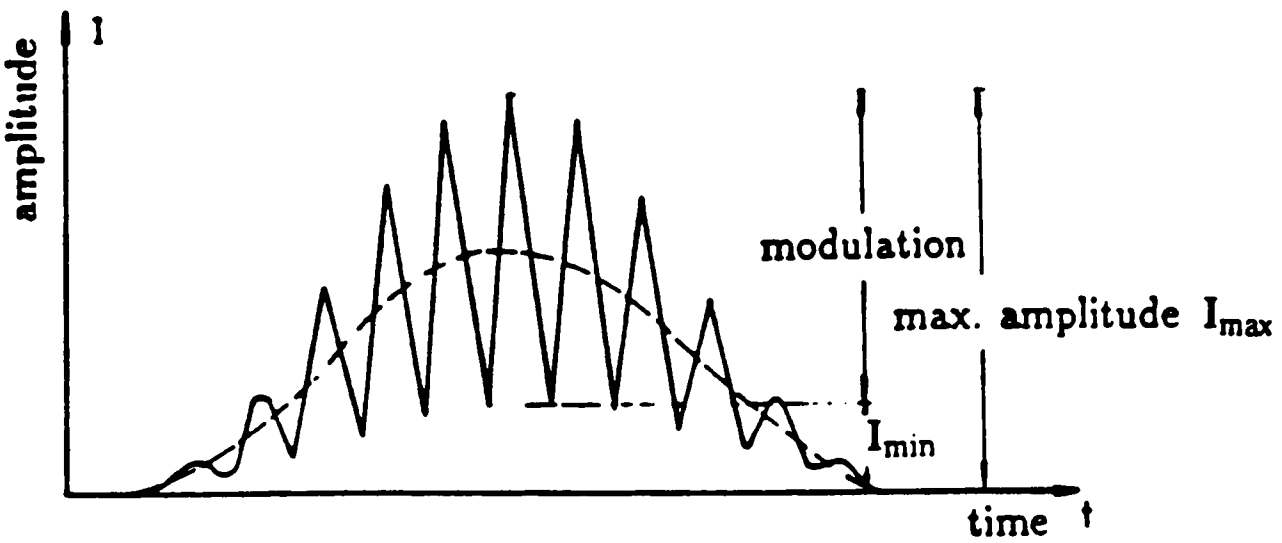

Figure 5.2 Doppler burst signal and pedestal components.

$$Visibility = \frac{I_{max} - I_{min}}{I_{max} + I_{min}} \tag{5.1}$$

where I_{max} and I_{min} are shown in Figure 5.2. However, the method proposed by Farmer was limited to a range of drop sizes which are smaller than the fringe spacing. Negus and Drain (1982) performed calculations using the Mie scattering theory which allowed to extend the relation between drop size and visibility to a wider range of drop sizes.

The LDA technique provides a temporal sampling of drop sizes. Problems can arise with this technique if the control volume is occupied with more than one drop, or if the particles do not cross the control volume at the same position.

5.2. Drop Size Measurements

5.2.1. Previous Work

The experimental techniques presented in the last section have been used to examine the effects of gas and liquid flow rates, gas density, liquid viscosity, surface tension and tube diameter on drop size. In this section, the experimental studies conducted so far on drop size in annular flow are discussed. Table 5.1 presents a summary of the research carried out for the measurement of drop size in vertical annular flow. Table 5.2 resumes the work concerning horizontal flow.

From all the parameters that influence drop size, the strongest effect is that of gas velocity. Data from several authors (Azzopardi et al (1978), Gibbons (1985), Teixeira (1988), Jepson (1992), among others) show that for vertical annular flow the Sauter mean diameter ($\overline{D}_{32}$) decreases with increasing superficial gas velocity, such that $\overline{D}_{32}$ is proportional to $U_{SG}^{-1.2}$. However, the results of Ueda (1979) follow a dependence on gas velocity to the power of -0.3.

A completely opposite trend was found in the data of Tatterson (1975), where drop size increases with gas velocity. However, his data are considered to be biased because of the measurement technique employed, as mentioned by Azzopardi (1985). Smaller drops would tend to by-pass the electric probe, and as the probe was located very close to the liquid film, it could be hit by ligaments before they broke into drops.

Figure 5.3 shows the dependence of drop size on the liquid flow rate, as obtained by Azzopardi (1983) for air-water up flow in a 0.032 m ID tube. At higher values of the liquid flow rate, drop size increases with liquid mass flux. Whilst, at lower liquid flow rates an opposite trend may be observed.

Azzopardi (1983) has linked these two opposite trends to the different mechanisms of entrainment observed, previously discussed in section 1.6.1. At low liquid flow rates the bag

TABLE 5.1 – SUMMARY OF PREVIOUS EXPERIMENTAL WORK ON DROP SIZE IN VERTICAL ANNULAR FLOW

Author	Fluids	Geometry	Flow Direction	Gas Flow	Liquid Flow	Measurement Technique
Wicks & Dukler (1966)	air–water	rect. channel 0.15 x 0.019 m	downflow	23.4–83.2 m/s	0.063 & 0.0.315 Kg/s	electric conduction probe
Cousins & Hewitt (1968)	air–water	circular tube d_t=0.0095 m	upflow	0.0050–0.0088 kg/s	0.0043–0.028 kg/s	still photography
Andreussi et al (1978)	air–water	circular tube d_t=0.024 m	downflow	0.0139–0.0438 kg/s	0.030–0.0135 kg/s	microphotography
Ueda (1979)	air–water air–alcohol/water solutions air–glycerol/water solutions	circular tube d_t=0.010 m & d_t=0.030 m	upflow	31–64 m/s & 17–40 m/s	0.017–0.133 kg/s	impaction technique
Azzopardi et al (1978)	air–water	circular tube d_t=0.032 m	upflow	43.7–79.4 kg/m^{2}s	15–96 kg/m^{2}s	laser diffraction
Azzopardi et al (1980)	air–water	circular tube d_t=0.032 m	upflow	43.7–115 kg/m^{2}s	15.9–158.8 kg/m^{2}s	laser diffraction
Gibbons (1985)	air–water air–glycerol/water solution	circular tube d_t=0.032 m & d_t=0.125 m	upflow	35.9–51.3 kg/m^{2}s	7–26 kg/m^{2}s	laser diffraction & PDA
Lopes and Dukler	air–water	d_t=0.051 m	upflow	0.037–0.069 kg/s	0.069–0.244 kg/s	PDA
Teixeira (1988)	air–water	circular tube d_t=0.032 m	upflow	43.7–91.2 kg/m^{2}s	15.9–125.3 kg/m^{2}s	laser diffraction & PDA
Jepson (1992)	air–water air–genklene helium–water CF_4–water	circular tube d_t=0.010 m & d_t=0.020 m	upflow	20–120 kg/m^{2}s & 53–105 kg/m^{2}s	20–140 kg/m^{2}s & 41–137 kg/m^{2}s	laser diffraction

TABLE 5.2 – SUMMARY OF PREVIOUS EXPERIMENTAL WORK ON DROP SIZE IN HORIZONTAL ANNULAR FLOW

Author	Fluids	Geometry	Gas Flow	Liquid Flow	Measurement Technique
Namie & Ueda (1972)	air–water	rect. channel 0.01 x 0.06 m	16–133 cm3/s	34–63 m/s	impaction technique
Russel & Rogers (1972)	air–water	rect. channel 0.025 x 0.152 m	20.4 & 25.4 m/s	0.126 kg/s	cine film
Chang (1973)	air–45%glycerine/water solution air–60%glycerine/water solution	rect. channel 0.025 x 0.152 m	20.4 m/s	0.126 kg/s	cine film
Tatterson (1975)	air–water	rect. channel 0.025 x 0.305 m	0.259–0.454 kg/s	0.030–0.135 kg/s	electric probe
Akagawa et al (1980)	air–water	rect. channel 0.05 x 0.150 m	35–60 m/s	0–0.1 kg/s	impaction technique

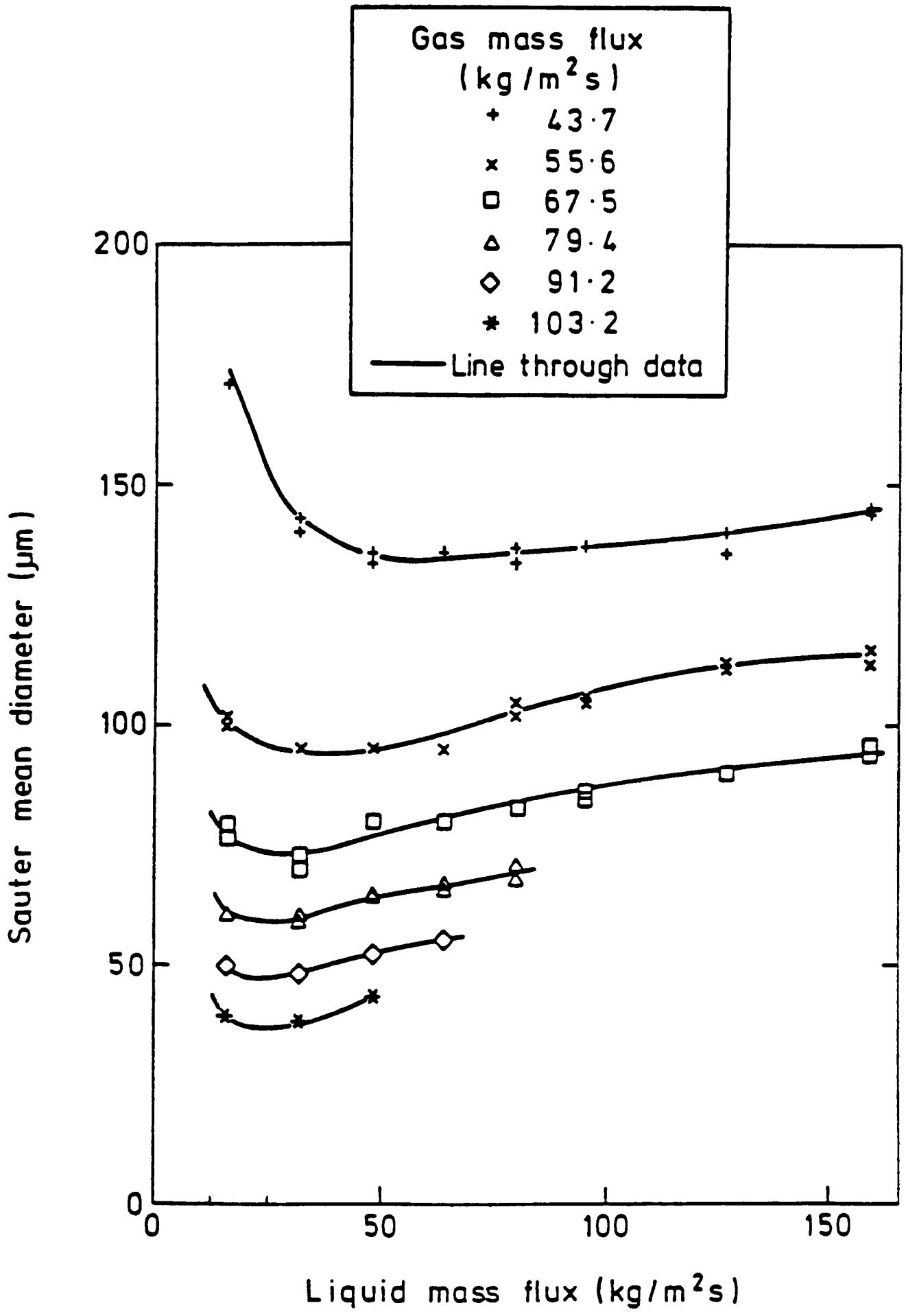

Figure 5.3 Effect of liquid flow rate on drop size for a vertical tube 0.032 m ID (Azzopardi (1983)).

break–up mechanism occurs, in which the gas undercuts a wave forming a bag. The break–up of the bag gives smaller drops from the skin and larger drops from the rim. At the higher liquid flows, the top of the waves are torn off in the form of ligaments, that are then broken into drops. It was suggested that the ligament break–up mechanism forms smaller drops than the bag break–up mechanism. If both mechanisms occur simultaneously, then with increasing liquid flow rate ligament break–up will become predominant and a decrease in drop size should be observed. However, for further increases in the liquid flow the drop size of created drops should not change, but the observed size will increase because coalescence occurs.

The effect of liquid viscosity on drop size was studied by Gibbons (1985). As shown in Figure 5.4, the results show only a small effect of liquid viscosity, with the Sauter mean diameter ($\overline{D}_{32}$) increasing with liquid viscosity. This was confirmed by the experiments of Nigmatulin et al (1986). Chang (1973) found that drop diameter passed through a maximum as viscosity was increased.

Ueda (1979) investigated the influence of surface tension on drop size using air and various aqueous alcohol solutions. Jepson et al (1990) used air–water and air–genklene. Both authors found that drop size increased with surface tension. This is an expected result because surface tension is the main factor to resist to drop break–up.

The dependence of drop size on gas density was studied by Jepson (1992). The author conducted experiments using three different gases: helium (ϱ_G = 0.27 kg/m^3), air (ϱ_G = 1.8 kg/m^3) and carbon tetrafluoride (ϱ_G = 5.0 kg/m^3) for two gas velocities. For the lower gas velocity (U_{SG} = 33.3 m/s) drop size was seen to decrease slightly with increasing gas density. For the higher gas velocity (U_{SG} = 44.4 m/s), drop size passed through a minimum. However, Jepson (1992) highlights that these trends might not be solely due to a gas density effect, and that drop break–up mechanisms and drop concentration might be contributing for these results.

The influence of tube diameter on drop size has been reported in the works of Gibbons (1985) and Jepson (1992). Gibbons found that for a given gas velocity, drop sizes measured in a 0.032 m and 0.125 m ID vertical tubes showed a very weak effect of tube diameter. However, Jepson (1992) working with tube diameters of 0.01 m and 0.02 m found drop size to decrease with tube diameter.

5.2.2. Present Work

The drop size work presented in the last section and summarised in Tables 5.1 and 5.2, indicates that most of the previous studies have been carried out for vertical annular flow. This is probably because in horizontal flow some experimental and theoretical difficulties can arise, caused by the non–axisymmetry due to gravity. The results published so far on drop size for horizontal flow are limited and have been obtained in rectangular channels.

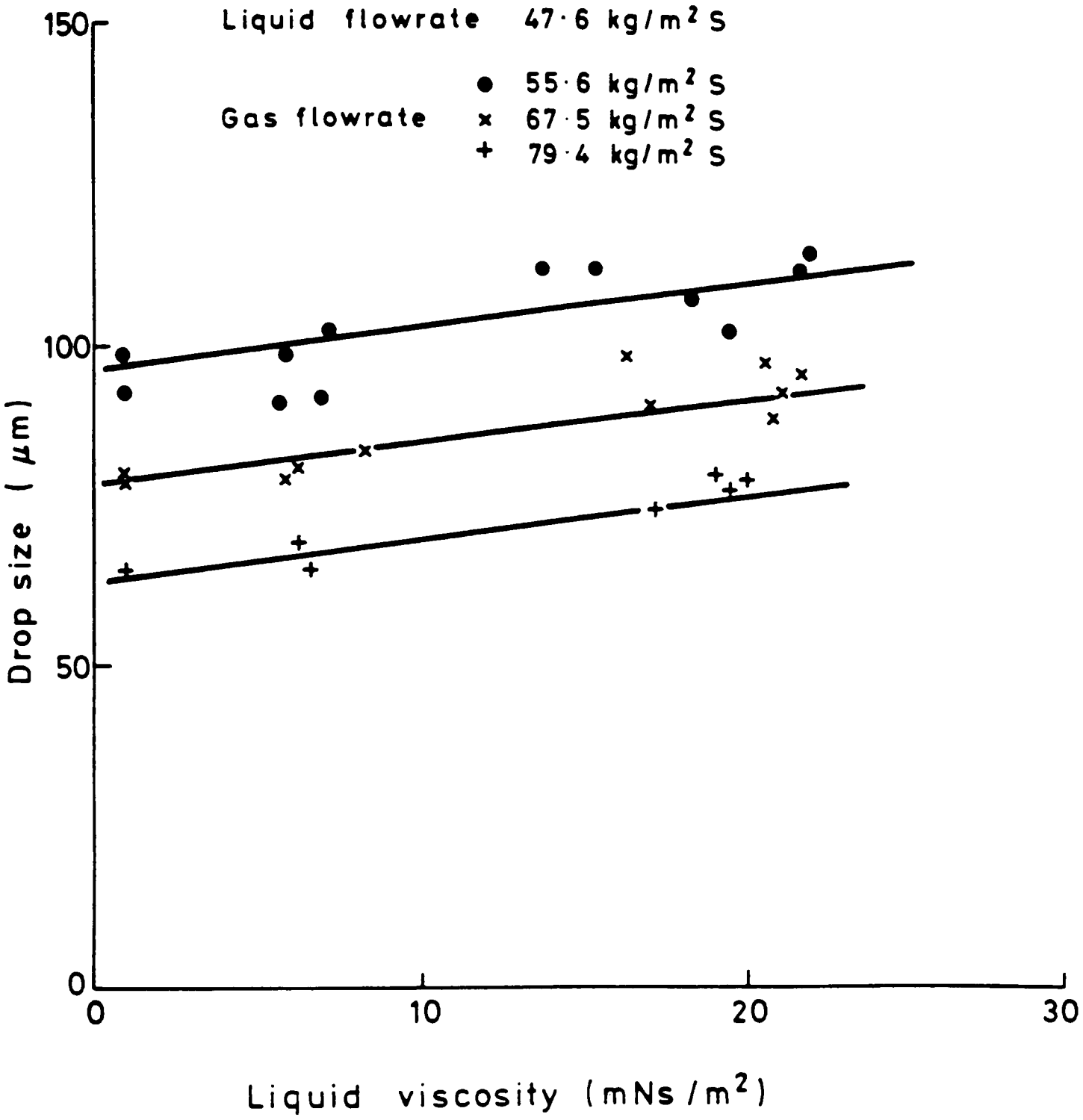

Figure 5.4 Effect of liquid viscosity on drop size (Gibbons (1985)).

The present investigation includes a new set of drop size measurements for horizontal stratified and annular two–phase flow in a tube 0.032 mm ID. The experiments were carried out at ambient temperature, and at a pressure in the test section of 1.3 bar or 1.4 bar. The measurement technique used was the laser diffraction technique developed by Swithenbank et al (1976).

The data presented in this section were obtained using a model independent analysis (see section 2.5.1.2). Various factors contributed for the choice of this type of analysis:

- The nature of the drop size histogram. For some flow conditions, the drop size histogram was represented by a multimodal curve. A typical example is shown in Figure 5.5(a), for a gas mass flux of G_G = 40 kg/m^{2}s and a liquid mass flux of G_G = 50 kg/m^{2}s.
- The log–difference parameter. When the drop size was fitted by a log–normal distribution (Figure 5.5(b)), or by a Rosin–Rammler distribution (Figure 5.5(c)), the residual difference (equation 2.3) always presented a significantly higher value than when using the model independent approach. It is known that the lower the log–difference the better the fit.

The influence of liquid mass flux on the Sauter mean diameter ($\overline{D}_{32}$) is shown in Figure 5.6 for a working pressure of 1.3 bar, and in Figure 5.7 for the results obtained at 1.4 bar. Tabulated results are presented in Tables B.16 and B.17 (Appendix B).

In Figure 5.6 and for the lower gas mass flux (G_G = 40 kg/m^{2}s), $\overline{D}_{32}$ decreases with increasing liquid flow rate. For G_G = 50 kg/m^{2}s the drop size passes through a minimum. The same sort of behaviour was found for drop size measurements in vertical annular flow. As discussed in the previous section, Azzopardi (1983) suggested that these trends can be linked to the different mechanisms responsible for drop entrainment. The cine films carried out in the present study and described in Chapter 3, have demonstrated that for the flow conditions analysed, both the bag break–up and ligament break–up mechanisms are present in horizontal flow. So, in Figure 5.6 for G_G = 40 kg/m^{2}s, the decreasing drop diameter with increasing liquid flow rate may be due to the increasing predominance of ligament break–up over bag break–up. Ligament break–up produces smaller drop sizes. For G_G = 50 kg/m^{2}s, $\overline{D}_{32}$ first decreases with liquid flow also because ligament break–up is the predominant drop entrainment mechanism. However, with further increases in the liquid flow rate, the observed drop size starts to increase probably because of drop coalescence.

For the flow conditions presented in Figure 5.7, the drop size generally increases with liquid mass flux. Under these circumstances, the concentration of drops has a predominant effect leading to drop coalescence and a consequent increase in drop size.

Figure 5.8 shows the strong influence of the superficial gas velocity on the Sauter mean diameter, $\overline{D}_{32}$ decreasing with increasing gas velocity. This is expected because the higher the gas flow, the greater shearing force imposed on the liquid gives more intense surface deformation and break–up into smaller drop sizes. For the flow conditions under study, the

(a)

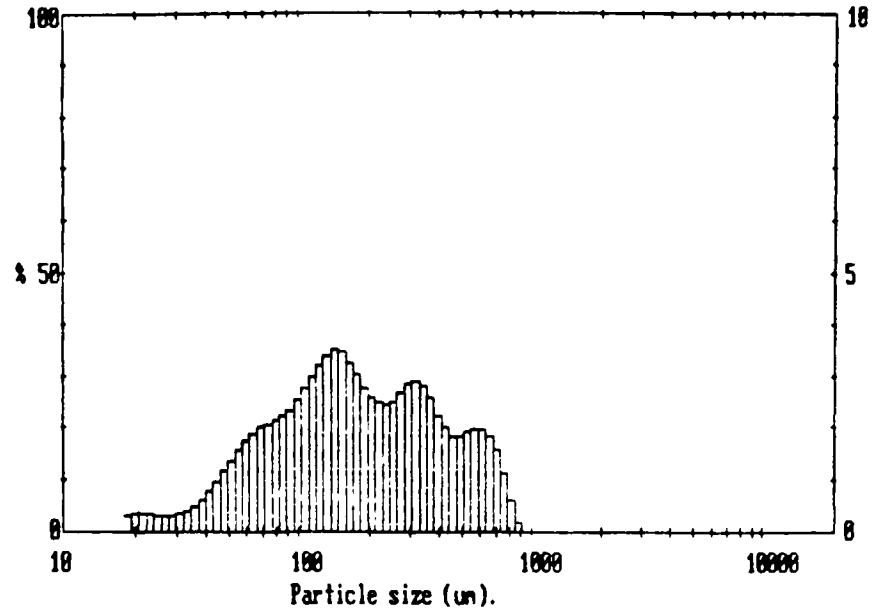

(b)

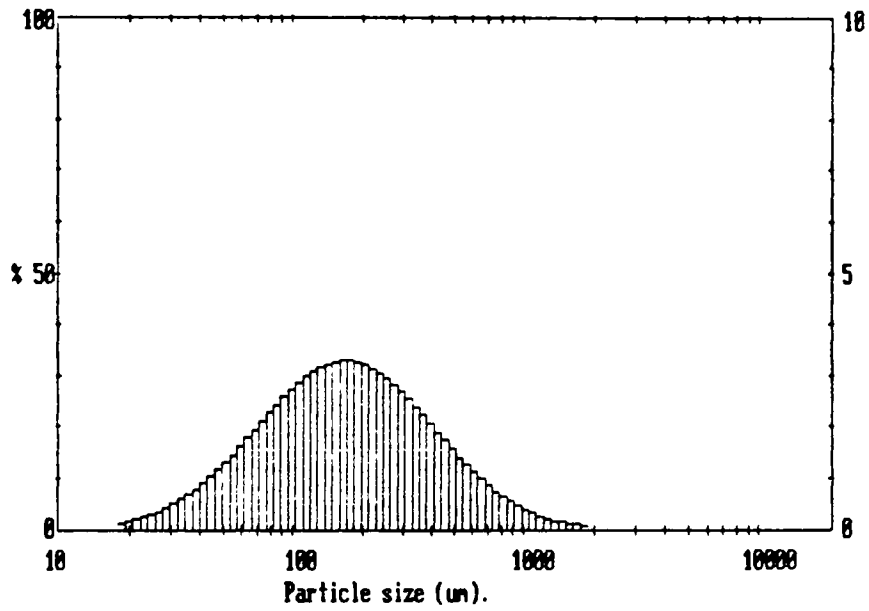

(c)

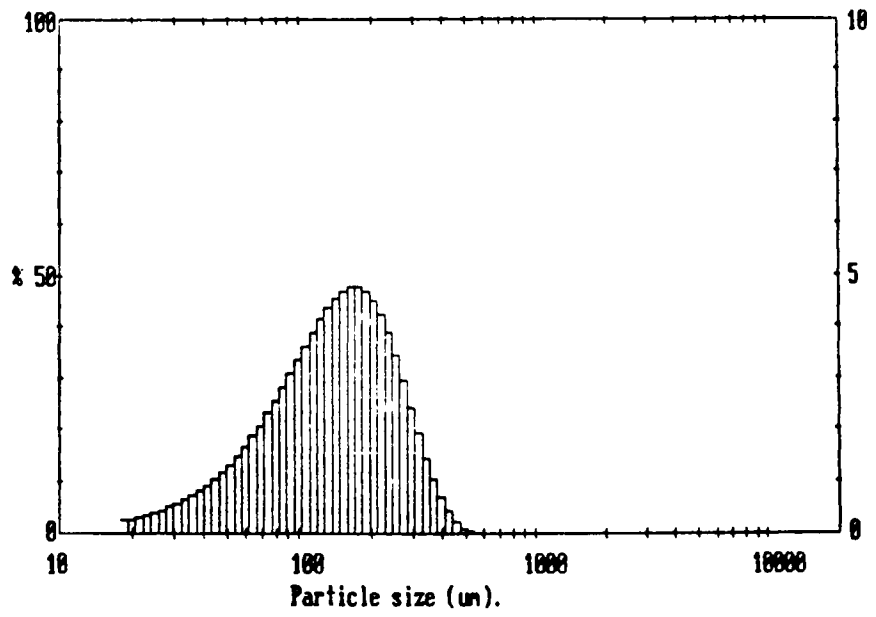

Figure 5.5 Drop size histogram for $G_G = 40$ kg/m^{2}s and $G_L = 50$ kg/m^{2}s: (a) using a model independent analysis, (b) a Log–normal model, (c) a Rosin–Rammler model

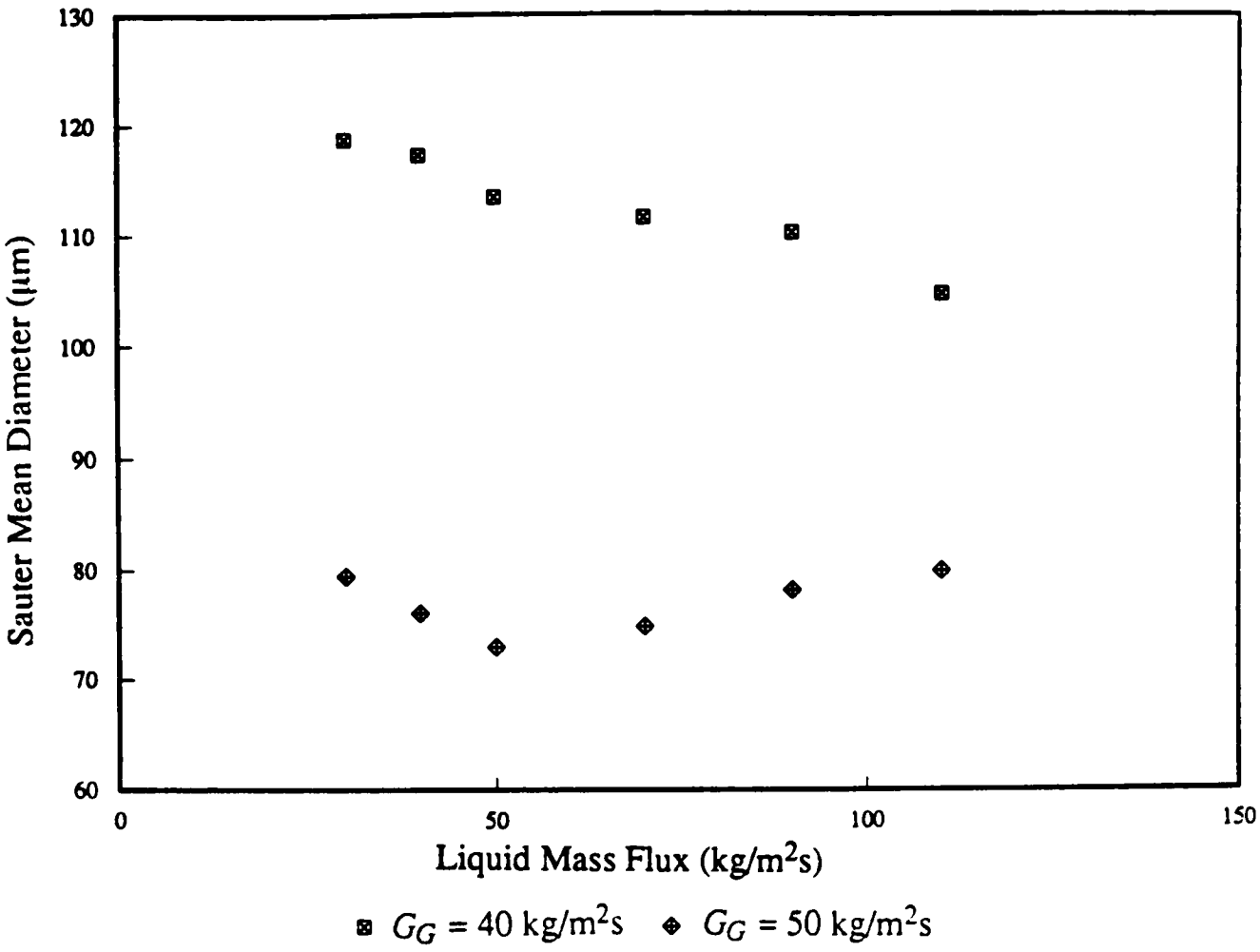

Figure 5.6 Effect of liquid mass flux on drop size for the 0.032 m ID horizontal tube, at a pressure of 1.3 bar.

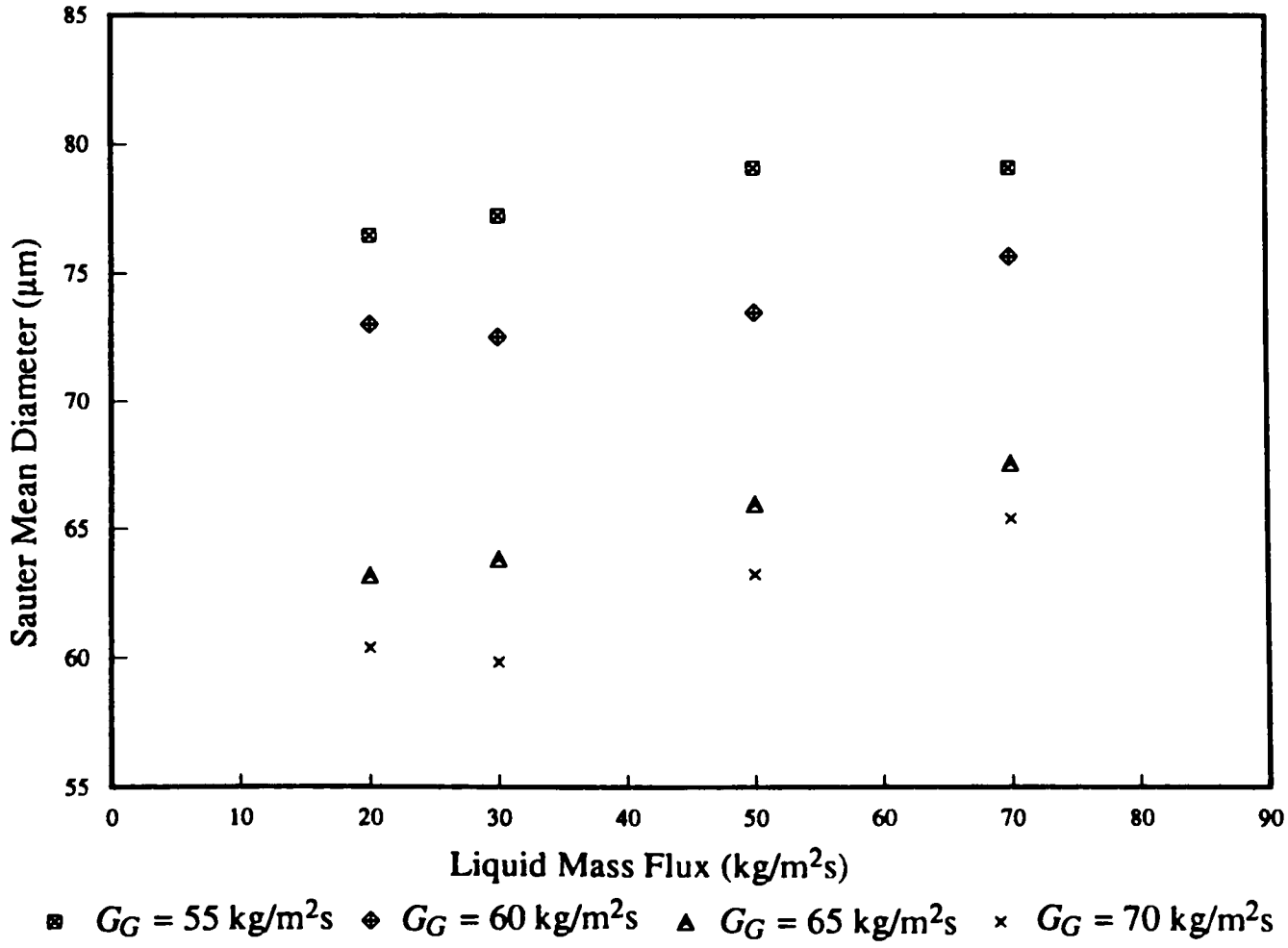

Figure 5.7 Effect of liquid mass flux on drop size for the 0.032 m ID horizontal tube, at a pressure of 1.4 bar.

Sauter mean diameter was found to be proportional to the superficial gas velocity raised to the power of –1.0. For vertical annular flow $\overline{D}_{32}$ was found to be proportional to $U_{SG}{}^{-1.2}$.

By comparing the data in Figures 5.6 and 5.7, it was decided to investigate the influence of the pressure at the measuring point on drop size. For G_G = 55 kg/m^{2}s and G_L = 30 kg/m^{2}s, drop size was measured at the pressures of 1.3 bar and 1.4 bar. An increase in the Sauter mean diameter from 71.54 μm to 77.24 μm was observed with increasing pressure. Gibbons (1985) arrived at a similar conclusion, when he measured drop size at gas densities of 1.2 kg/m^3 and 2.3 kg/m^3 but maintaining constant mass flux conditions. As the gas mass flux was maintained constant, this result can be due either to the increase in gas density or to the decrease in the gas velocity. However, it is thought that the gas velocity has probably the most dominant effect. For the present flow conditions (G_G = 55 kg/m^{2}s) the gas velocity changes from U_{SG} = 35.2 m/s at P = 1.3 bar to U_{SG} = 32.6 m/s at P = 1.4 bar. If the gas velocity has the predominant effect, the ratio $\overline{D}_{32}/U_{SG}{}^{-1}$ should be similar at both pressures. In fact, this is the case [77.24 μm /(32.6 m/s)$^{-1}$ = 71.54 μm /(35.2 m/s)$^{-1}$], which suggests that the increase in drop size observed with increasing the pressure of the system is due to the consequent reduction in gas velocity.

It is of interest to know which effect the orientation of the tube has on drop size. For this purpose, the new data from this study were compared against drop size measurements obtained under similar conditions but in a 0.032 mm ID vertical tube. The experiments published by Azzopardi et al (1980) were chosen for this comparison, where the flow conditions were expressed in mass fluxes. However, these data were taken at 1.5 bar, while the present measurements were conducted at 1.3 bar or 1.4 bar. For this reason, the comparison was made in terms of the same superficial gas velocities instead of gas mass fluxes. Also, the flow conditions of Azzopardi et al (1980) did not match the ones used in the present study, and consequently interpolation was needed. Only the drop size measurements from this study taken at a pressure of 1.4 bar, were compared against corresponding drop size data in vertical upflow (Figure 5.9(a)) for several gas velocities.

Figure 5.9(a) shows that overall the Sauter mean diameter in vertical annular flow is higher than the corresponding Sauter mean diameter in horizontal flow obtained under similar conditions. As discussed in Chapter 4, the level of the entrained mass flow rate is lower in horizontal flow than for the same velocity conditions in vertical annular flow. So, the higher drop size in vertical flow may be linked to the higher value of the entrained mass flux. Because the drop concentration is higher, drop coalescence is more likely to occur. Figure 5.9(a) also shows that as the gas velocity is increased from 32.6 m/s to 41.5 m/s the curve approches the 45° line. This means that as the gas velocity increases the difference in drop size between the two systems is reduced. At even higher gas velocities it is expected that the experimental curve will intercept the 45° line. From this point on, the drop size in both systems under the same flow conditions may be similar. The same conclusion can be taken from Figure 5.9(b), where $\overline{D}_{32}$ is plotted as function of the entrained mass flux for U_{SG} = 32.6 m/s and U_{SG} = 41.5 m/s.

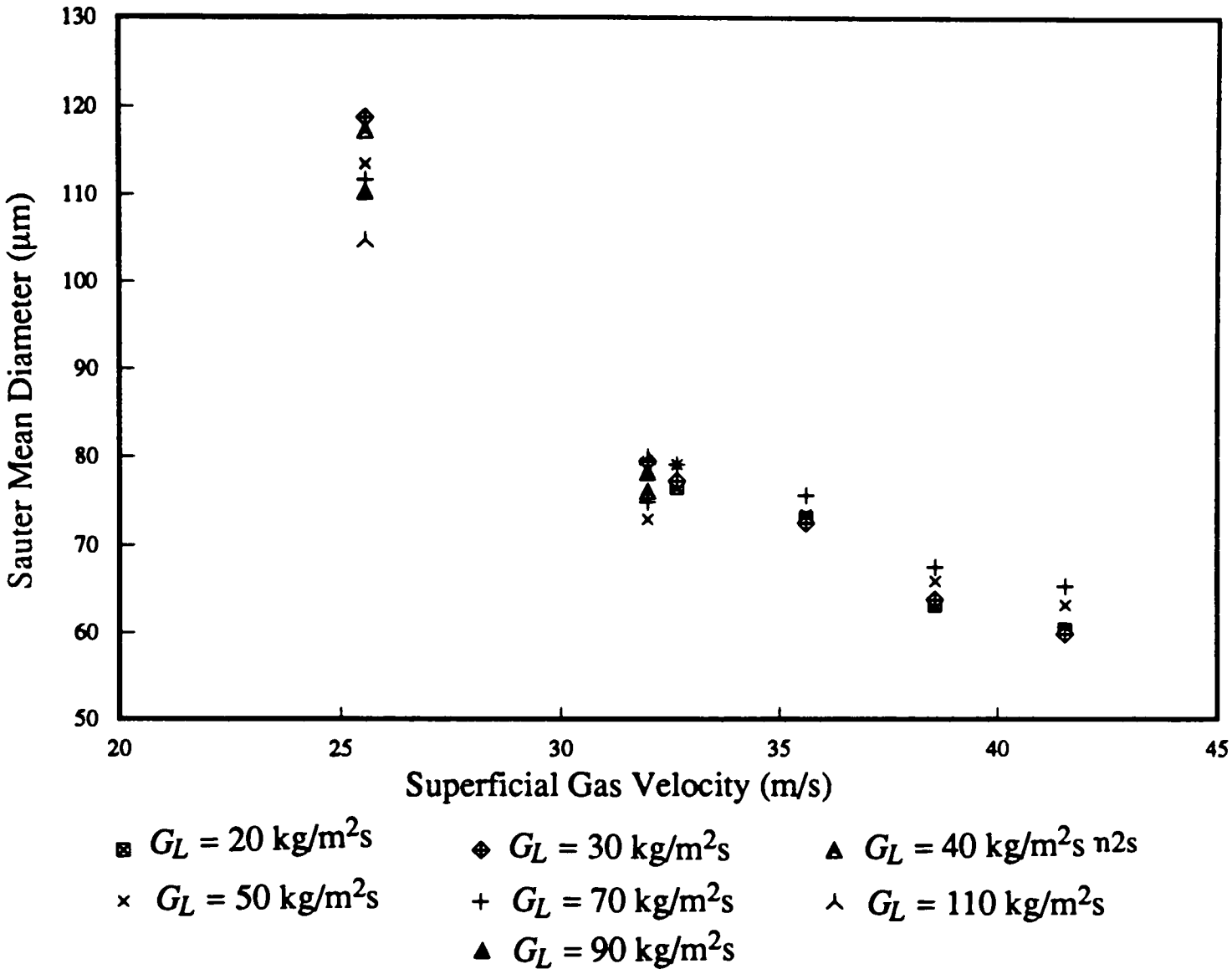

Figure 5.8 Effect of superficial gas velocity on drop size for the 0.032 m ID horizontal tube.

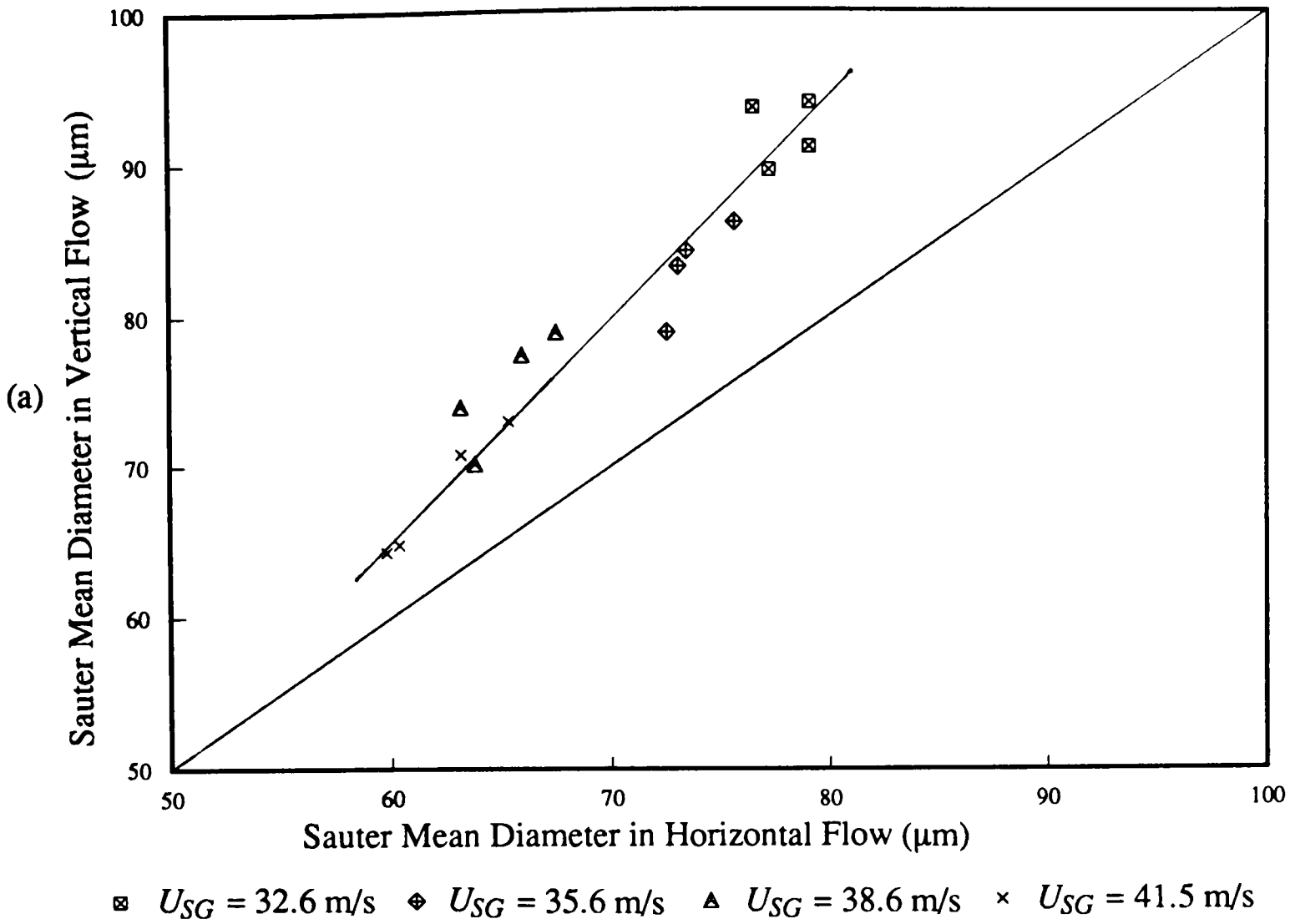

Figure 5.9 Comparison between drop size obtained in vertical and horizontal annular flow in a 0.032 m ID tube: (a) $\overline{D}_{32}$ in vertical flow versus $\overline{D}_{32}$ in horizontal flow, (b) $\overline{D}_{32}$ as a function of the entrained liquid mass flux.

It is seen that the difference between the drop size in horizontal and vertical flow is reduced, as the gas velocity is increased.

5.3. Drop Size Correlations

Section 5.2.1. summarises the experimental work carried out on drop size in horizontal and vertical flows. Drop size correlations have been developed from these studies, accounting for the several parameters that influence drop size. Most of these correlations are based on data for vertical annular flow. In the next section some of these expressions will be discussed, and tested against the drop size data obtained in the present experiments.

5.3.1 Tatterson et al (1977)

Tatterson et al (1977) assumed that the diameter of drops created in gas–liquid two–phase flow could be scaled to the size of the ligament of liquid removed from the wave. They determined the ligament size by considering a static force balance between the forces relative to the pressure variation over the wave crest and the surface tension. In addition, the authors used the friction gas velocity (instead of the gas velocity) to represent the velocity field at the gas–liquid interface. Based on these assumptions, Tatterson et al (1977) presented the following correlation for drop size, expressed in terms of the volume mean diameter:

$$\frac{\overline{D}_{v0.5}}{d_t}\left[\frac{\varrho_G\, U_{SG}^2\, f_{SG}\, d_t}{2\,\sigma}\right]^{0.5} = \frac{0.42\sqrt{6.59\;F'}}{(1\,+\,1400\;F')^{0.75}} \tag{5.2}$$

where f_{SG} is the friction factor for smooth tubes ($= 0.046\, Re_G^{-0.2}$), and F' is a flow parameter defined as:

$$F' = \frac{\gamma}{\mathrm{Re}_G^{0.9}}\,\frac{\mu_L}{\mu_G}\sqrt{\frac{\varrho_G}{\varrho_L}} \tag{5.3}$$

and

$$\gamma = \left[(0.707\;\mathrm{Re}_{LF}^{0.5})^{2.5} + (0.0379\;\mathrm{Re}_{LF}^{0.9})^{2.5}\right]^{0.4} \tag{5.4}$$

where Re_{LF} is the liquid film Reynolds number. The authors tested the data of Wicks and Dukler (1966), Cousins and Hewitt (1968) and Tatterson (1975) against equation (5.2), and found that for these conditions, the right hand side of equation (5.2) could be equaled to 0.016.

The drop size measurements of the present study are plotted in Figure 5.10 against calculated drop sizes using the correlation of Tatterson et al (1977). Conversion from volume medium diameter to Sauter mean diameter was made through the ratio $\overline{D}_{32}/\overline{D}_{v0.5} = 0.7$ (Tatterson et al (1977), which is confirmed by the present data (see Figure 5.11). Figure 5.10 shows that overall equation (5.2) performs poorly with the present drop size data.

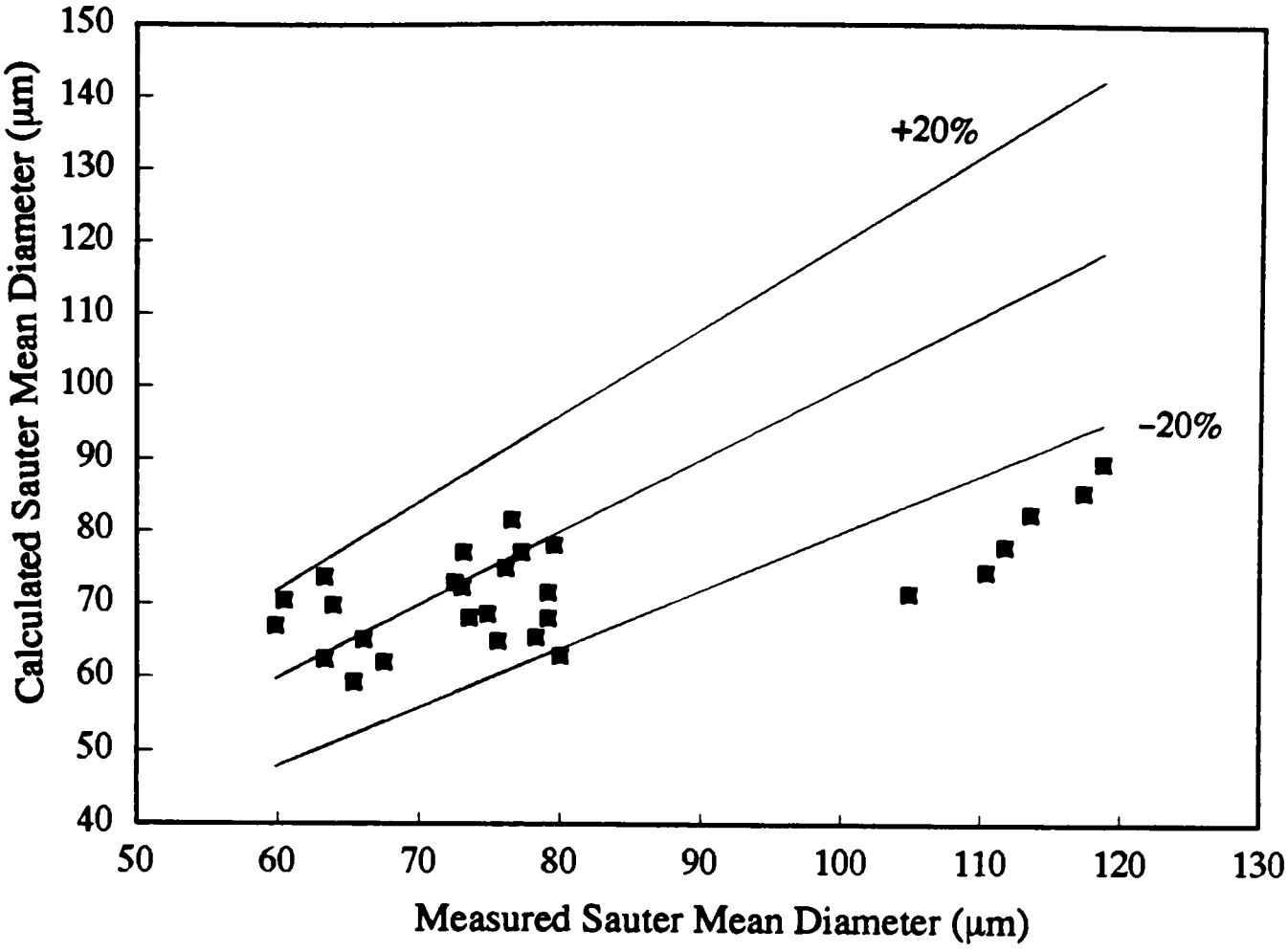

Figure 5.10 Performance of the correlation of Tatterson et al (1977) to predict the drop size data of the present study.

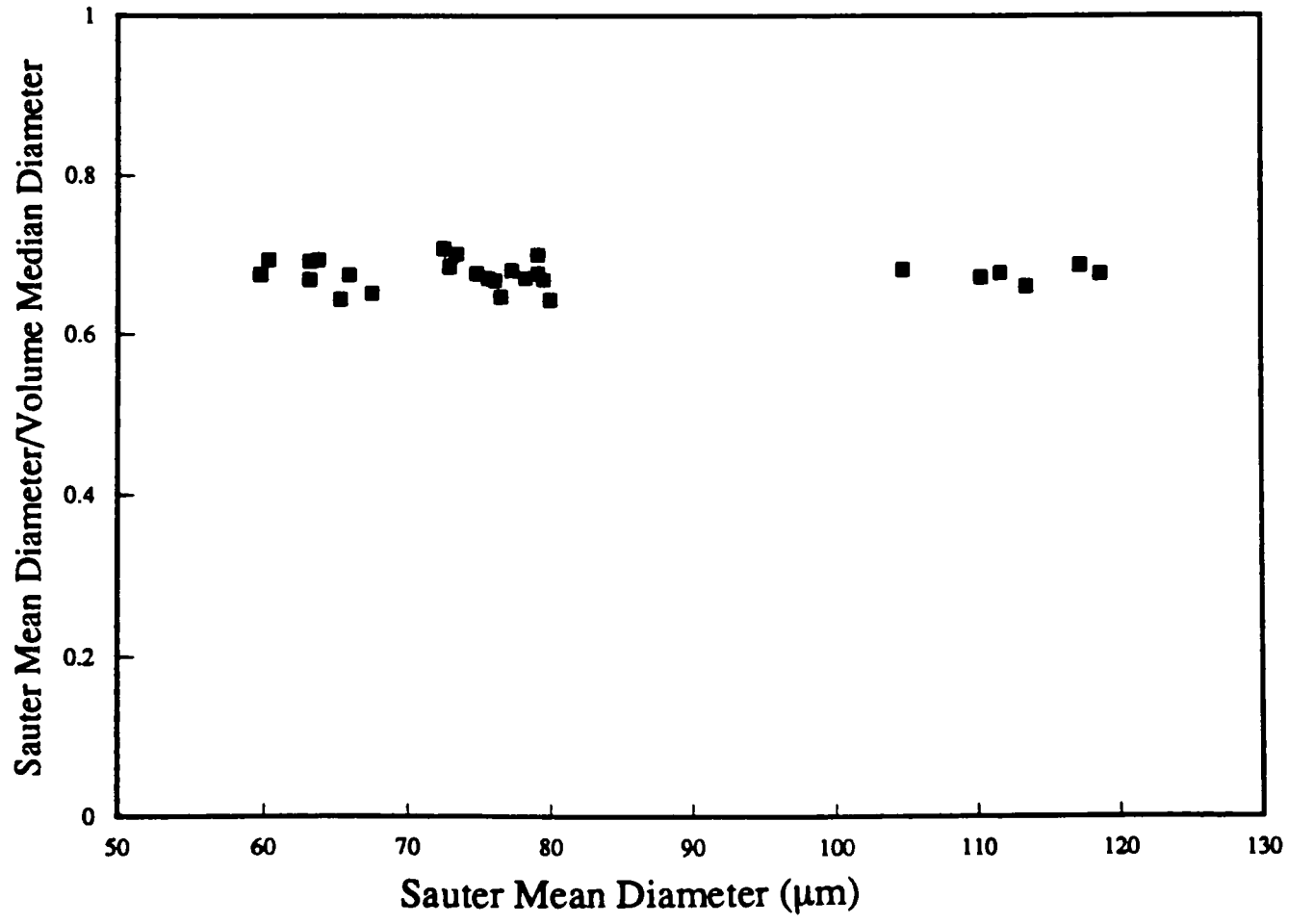

Figure 5.11 Relation between the experimental Sauter mean diameters ($\overline{D}_{32}$) and the volume median diameters ($\overline{D}_{v0.5}$)

5.3.2. Andreussi et al (1978)

Andreussi et al (1978) developed an empirical equation for drop size, including the effect of liquid flow rate expressed indirectly in terms of the film thickness m. The following equation was proposed:

$$\overline{D}_{v0.5} = \frac{4.84 \times 10^4}{\varrho_G \, U_{SG}^2} + 7.06 \times 10^2 \left(\frac{m}{d_t}\right)^{0.5} \tag{5.5}$$

The film thickness was calculated through the expression:

$$\frac{m}{d_t} = \frac{6.59 \, F'}{(1 + 1400 \, F')^{0.5}} \tag{5.6}$$

where F' was defined in equation (5.3).

In Figure 5.12 the Sauter mean diameter calculated using equation (5.5) is compared with the measured $\overline{D}_{32}$. The ratio $\overline{D}_{32}/\overline{D}_{v0.5} = 0.7$ was used to convert the volume median diameters to Sauter mean diameters. It is seen that the correlation underpredicts the present drop size data.

5.3.3. Ueda (1979)

Ueda (1979) presented a nondimensional correlation based in his experimental results, where the volume mean diameter $(\overline{D}_{31})$ is calculated as:

$$\frac{\overline{D}_{31}}{d_t} = 5.8 \times 10^{-3} \left[\frac{\sigma}{\mu_G \, U_{SG}} \left(\frac{\varrho_G}{\varrho_L}\right)^{1.25}\right]^{0.34} \tag{5.7}$$

This correlation does not account for the effect of liquid flow rate or liquid viscosity, and assumes that drop size is proportional to $U_{SG}^{-0.34}$. However, in agreement with the present experiments and most other data, drop size was found to be proportional to $U_{SG}^{-1.0}$. For this reason, the correlation of Ueda was not tested against the present drop size data.

5.3.4. Azzopardi et al (1980)

Azzopardi et al (1980) considered that the predominant mechanism for drop creation in vertical annular flow is the break-up of large packets of liquid, ejected from the liquid film into the gas core. They proposed the following equation, that was derived from turbulence break-up and coalescence analysis:

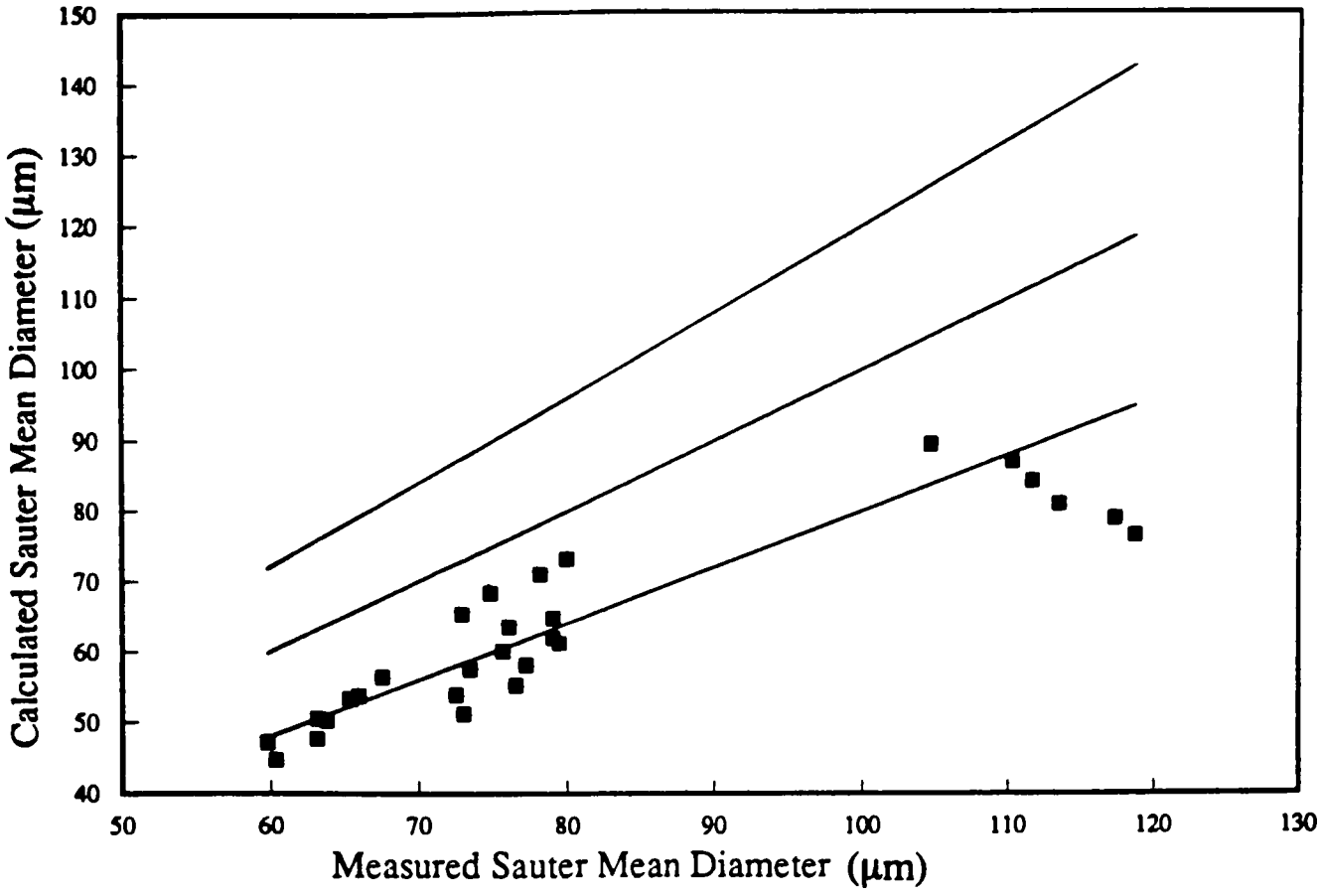

Figure 5.12 Performance of the correlation of Andreussi et al (1978) to predict the drop size data of the present study.

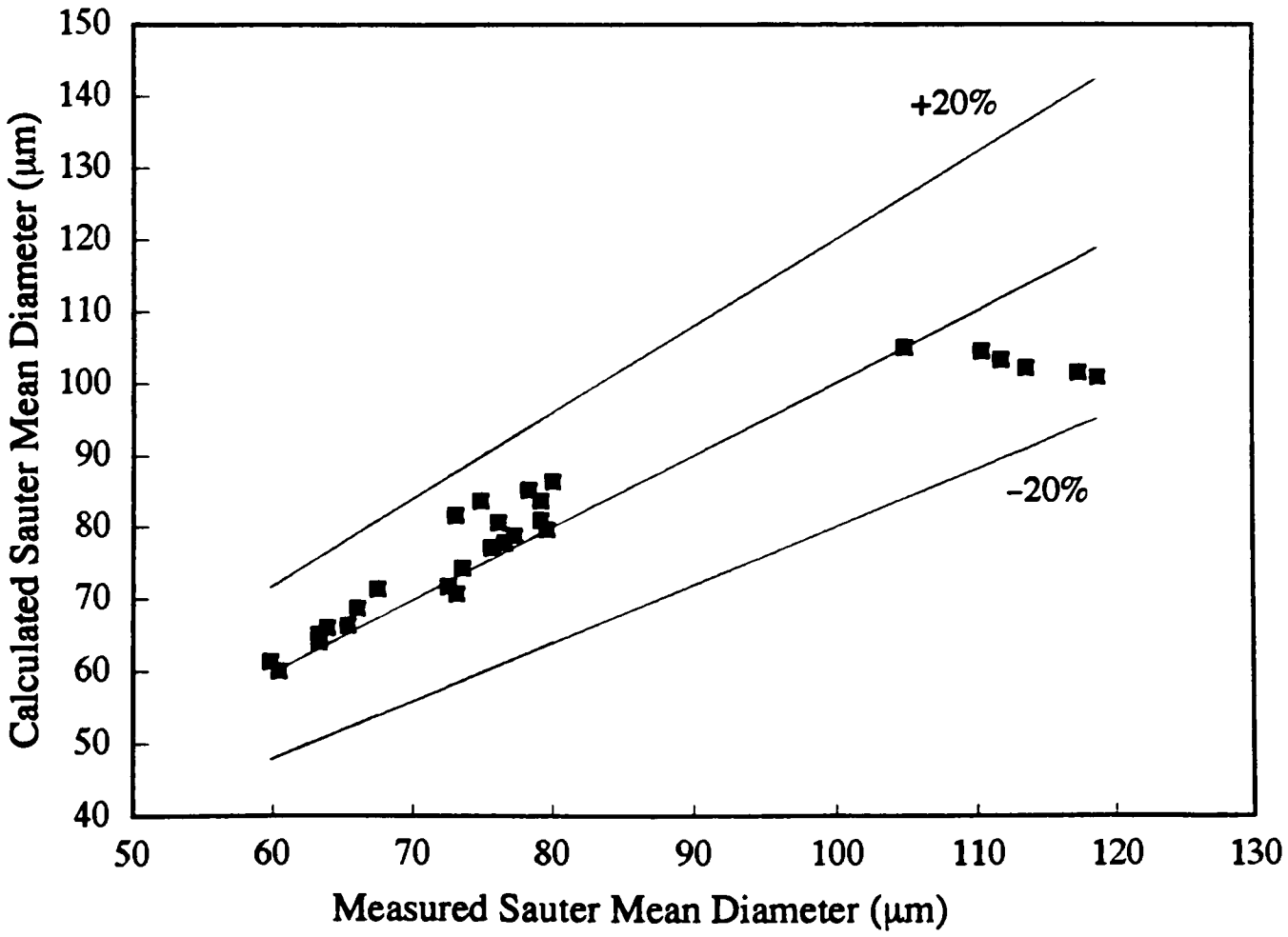

Figure 5.13 Performance of the correlation of Azzopardi et al (1980) to predict the drop size data of the present study.

$$\frac{\overline{D}_{32}}{d_t} = 1.91 \frac{\mathrm{Re}_G^{0.1}}{We^{0.6}} \left(\frac{\varrho_G}{\varrho_L}\right)^{0.6} + 0.4 \frac{G_{LE}}{\varrho_L U_{SG}} \tag{5.8}$$

where the Weber number *We* is defined by

$$We = \frac{\varrho_G \, U_{SG}^2 \, d_t}{\sigma} \tag{5.9}$$

This equation accounts for a linear increase in drop size with increasing entrained liquid flow rate. This increase in drop size shows a concentration effect due to drop coalescence. The equation predicted well the data of Azzopardi et al (1980) and of Andreussi et al (1978).

Drop size measurements for 0.032 m horizontal tube are compared in Figure 5.13 against drop sizes calculated using equation (5.8). This correlation predicts well the experimental Sauter mean diameter at high gas velocities. However, at the lowest gas mass flux ($G_G = 40$ kg/m^{2}s), where drop diameter decreases with increasing gas flow, the correlation does not perform well. This is not surprising because equation (5.8) should only be applied to conditions which show an increase in drop size with entrained liquid flow.

5.3.5. Kataoka et al (1983)

Kataoka et al (1983) proposed a correlation for drop size based on the mechanism of the shearing-off of roll wave crests. The equation was given in terms of the volume median diameter by:

$$\overline{D}_{v0.5} = 0.028 \frac{\sigma}{\varrho_G \, U_{SG}^2} \mathrm{Re}_L^{-\frac{1}{6}} \mathrm{Re}_G^{\frac{2}{3}} \left(\frac{\varrho_G}{\varrho_L}\right)^{-\frac{1}{3}} \left(\frac{\mu_G}{\mu_L}\right)^{\frac{2}{3}} \tag{5.10}$$

Experimental data by Wicks and Dukler (1966), Cousins and Hewitt (1968) and Linstead et al (1978) were correlated by equation (5.10) within $\pm$ 40% error.

The performance of equation (5.10) to represent the present drop size data can be seen in Figure 5.14, where the ratio $\overline{D}_{32}/\overline{D}_{v0.5} = 0.7$ was used to transform volume median diameters to Sauter mean diameters. This correlation badly overpredicts the present data.

5.3.6. Azzopardi (1985)

Based on drop size measurements taken in vertical tubes 0.032 m and 0.125 m ID, Azzopardi (1985) suggested that, for the same flow conditions, drop size was almost independent of tube

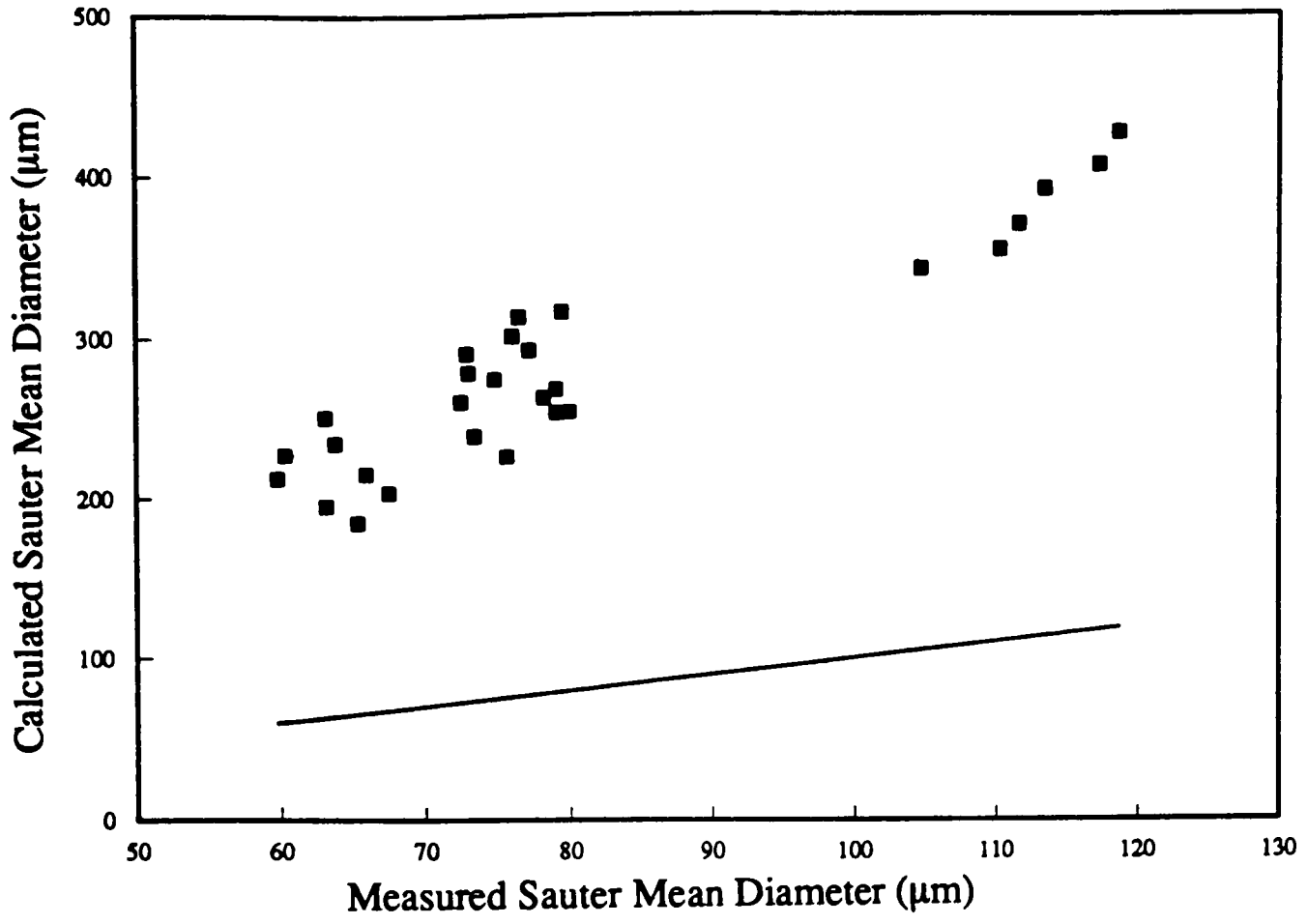

Figure 5.14 Performance of the correlation of Kataota et al (1983) to predict the drop size data of the present study.

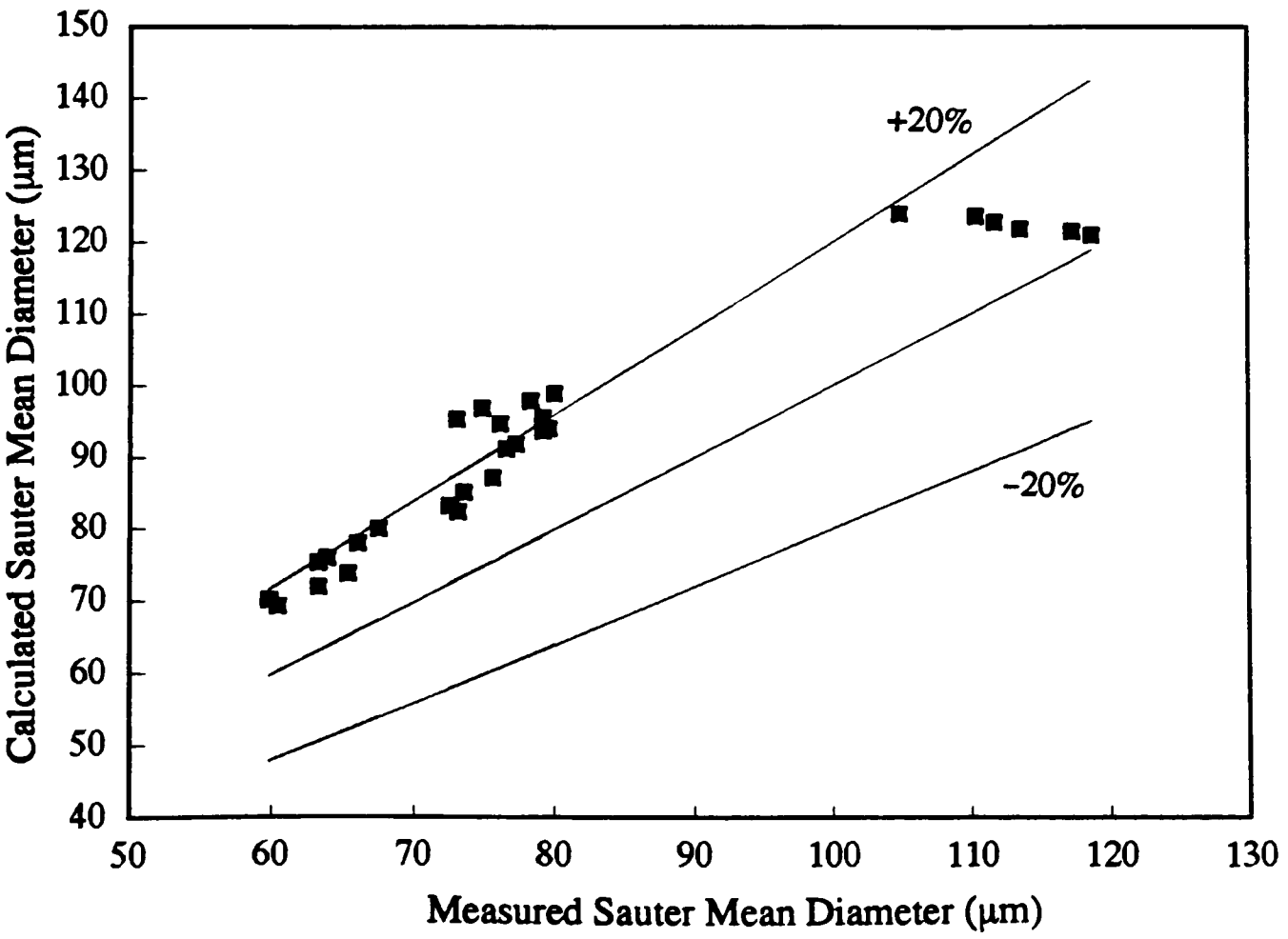

Figure 5.15 Performance of the correlation of Azzopardi (1985) to predict the drop size data of the present study.

size. The author attributed this effect to the fact that atomisation is a circumferentially localised phenomenon. He proposed an empirical correlation for drop size (modification of the equation presented by Azzopardi et al (1980)), in which the tube diameter is no longer accounted for. This correlation was:

$$\frac{\overline{D}_{32}}{\lambda_T} = \frac{15.4}{We_{\lambda_T}^{0.58}} + \frac{3.5\ G_{LE}}{\varrho_L\ U_{SG}} \tag{5.11}$$

The parameter λ_T was defined as:

$$\lambda_T = \sqrt{\frac{\sigma}{\varrho_L\ g}} \tag{5.12}$$

where We_{λ_T} is a Weber number ($= \varrho_L\ U_{SG}^2\ \lambda_T/\sigma$)

This equation accounts for the influence of gas flow on drop size and is specific to flow conditions where drop size increases with liquid flow rate.

Figure 5.15 shows the present experimental Sauter mean diameters versus the corresponding Sauter mean diameters calculated using equation (5.11). Generally, this correlation overpredicts the horizontal two-phase flow data.

5.3.7. Gibbons (1985)

Gibbons (1985) proposed a correlation for drop size, which in fact was a modification of the correlations proposed by Azzopardi et al (1980) and Azzopardi (1985). This new equation took into account the effect of liquid viscosity, gas density and tube diameter, and was represented as:

$$\overline{D}_{32} = 370\ \frac{\lambda_T}{We^{0.65}} \left(\frac{\varrho_G}{\varrho_L}\right)^{0.4} \left(\frac{\mu_L}{\mu_W}\right)^{0.05} + 0.4\ d_t\ \frac{G_{LE}}{\varrho_L\ U_{SG}} \tag{5.13}$$

where μ_W is the viscosity of the water.

The ability of equation (5.13) to predict the drop size data of this is shown in Figure 5.16. At the higher gas flow rates, this correlation generally overpredicts the data, but within a 20% error. Again, drop sizes corresponding to a gas mass flux of G_G = 40 kg/m^{2}s are not well predicted because equation (5.13) is specific to conditions where the drop size increases with entrained mass flux.

5.3.8 Lopes and Dukler (1985)

Lopes and Dukler (1985) presented a correlation for Sauter mean diameter based on the fact that the drop size distribution is mainly controlled by turbulent gas fluctuations around the

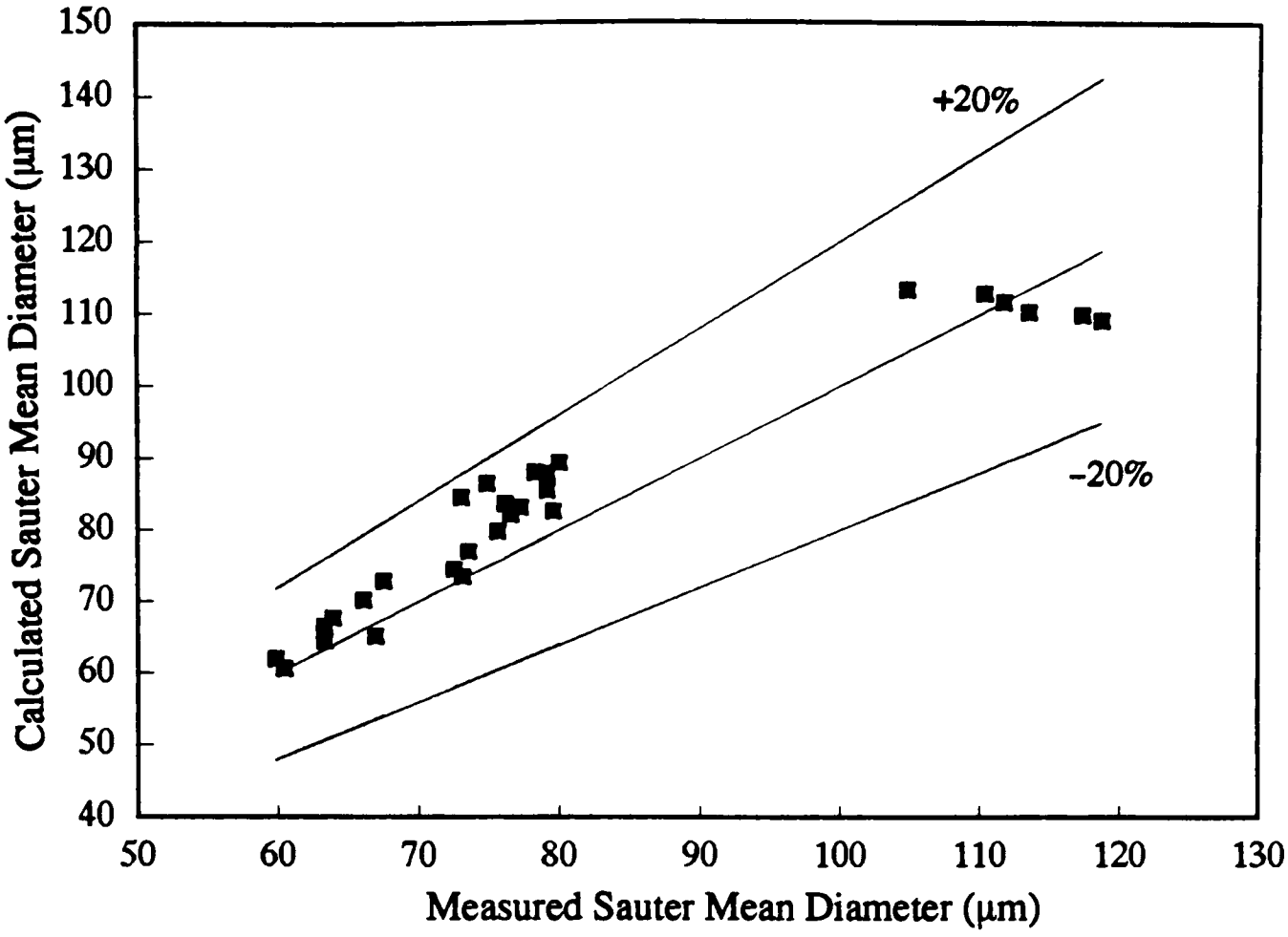

Figure 5.16 Performance of the correlation of Gibbons (1985) to predict the drop size data of the present study.

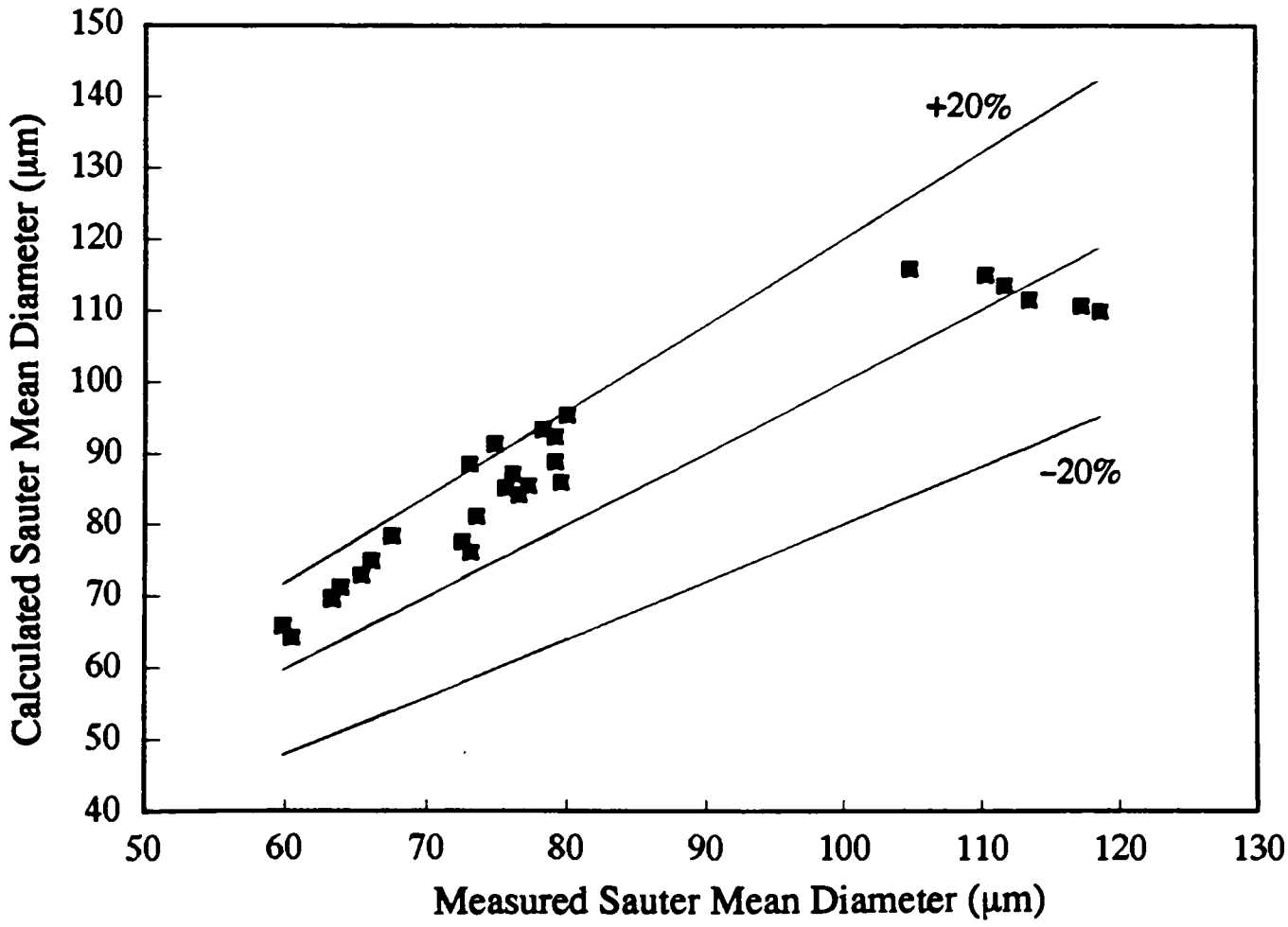

Figure 5.17 Performance of the correlation of Azzopardi et al (1989) to predict the drop size data of the present study.

drop. They suggested that the maximum stable drop size in vertical annular flow was given by:

$$D_{\max} = \left(\frac{We_c\ \sigma}{\varrho_G}\right)^{\frac{3}{5}} P_M{}^{-\frac{2}{5}} \tag{5.14}$$

where the critical Weber number (We_c) was found to be equal to 0.19, as evaluated from the experimental data. The energy dissipation per unit mass, P_M, was calculated as:

$$P_M = 2\, f_i\, \frac{U_{SG}^3}{d_t} \tag{5.15}$$

where the interfacial friction factor was given by:

$$\ln(f_i) = \frac{1.149 \times 10^{-5}}{\mathrm{Re}_G} - 5.491 \tag{5.16}$$

From their experimental results, the authors observed a constancy in the ratio $D_{max}/\overline{D}_{32} = 2.3$. Once this ratio was substituted in equation (5.14), the following expression for $\overline{D}_{32}$ was obtained:

$$\overline{D}_{32} = 0.49 \left(\frac{\sigma}{\varrho_G}\right)^{\frac{3}{5}} P_M^{-\frac{2}{5}} \tag{5.17}$$

Teixeira (1988) commented that the authors made a mistake in the empirical constant when correlating the data. The constant should be 0.078 instead of 0.49.

The correlation of Lopes and Dukler overpredicted badly the present drop size data. The work of Teixeira (1988) also confirmed that this equation did not perform well when applied to his results. This may be attributed to the region that Lopes and Dukler investigated, i.e. the churn/annular transition.

5.3.9. Azzopardi et al (1989)

Azzopardi et al (1989) examined published data on drop size for vertical annular flow where the effect of tube diameter, gas density and surface tension was accounted for. The drop size data for air–water was taken in tubes of diameters 0.01, 0.02 and 0.032 mm (Jepson et al (1989), Azzopardi et al (1991) and Teixeira (1988), respectively). Contrary to Azzopardi

(1985), who found no influence of tube diameter on drop sizes, Azzopardi et al (1989) observed a systematic effect of tube diameter. The effect of gas density was also examined in the paper by Jepson et al (1989). Finally, surface tension was also found to have an influence on drop size in Jepson et al (1990).

Based on the experimental data previously mentioned, an empirical correlation was derived:

$$\frac{\overline{D}_{32}}{d_t} = \frac{13.1}{We^{0.58}\, d_t^{0.1}} \left(\frac{\varrho_G}{\varrho_L}\right)^{0.785} \left(1 + 6.85\frac{G_{LE}}{\varrho_L}\right) \tag{5.18}$$

where the Weber number *We* was previously defined in equation (5.9).

Figure 5.17 shows the performance of this correlation to predict the drop size data of the present experiments. Generally, it overpredicts the data within 20%. Azzopardi et al recommended that equation (5.18) should only be applied to conditions where the drop size increases with liquid flow rate

5.3.10. Ambrosini et al (1991)

Ambrosini et al (1991) developed a correlation for drop size based on the model proposed by Tatterson et al (1977). Comparison with experimental data for vertical annular flow obtained by Jepson et al (1989,1990), Teixeira (1988), Andreussi et al (1978) and Azzopardi et al (1980) have shown that several factors should be accounted for in the new equation. These included the effect of the density ratio (ϱ_G/ϱ_L), the possibility of drop coalescence due to drop collision, and the considerable increase in drop size observed at low gas velocities. This last effect was taken into account through the introduction of a Weber number (We^*). The resulting equation was given by:

$$\frac{\overline{D}_{32}}{m} = 22.0 \left[\frac{\sigma}{\varrho_G\, f_i\, U_G^2\, m}\right]^{0.5} \left(\frac{\varrho_G}{\varrho_L}\right)^{0.83} \exp\left(0.60\, \frac{G_{LE}\, d_t}{\varrho_L\, U_G\, \overline{D}_{32}} + \frac{99}{We^*}\right) \tag{5.19}$$

The Weber number We^* was based on the tube diameter (d_t) and on the actual velocity of the gas core (U_G), and was defined as:

$$We^* = \frac{\varrho_G\, U_G^2\, d_t}{\sigma} \tag{5.20}$$

The values of the constants were obtained by the best fit to experimental data. Appropriate expressions to calculate the film thickness and the interfacial friction factor were also provided

by the authors. The film thickness at low values of the liquid film Reynolds number (Re_{LF}) was calculated by the following equation proposed by Asali et al (1985):

$$m_L^+ = 0.34\ \mathrm{Re}_{LF}^{0.6} \tag{5.21}$$

where $m_L{}^+$ is the dimensionless film thickness. For higher Reynolds numbers ($\mathrm{Re}_{LF} > 1000$) by the correlation of Kosky (1971)

$$m_L^+ = 0.0512\ \mathrm{Re}_{LF}^{0.875} \tag{5.22}$$

The interfacial friction factor was evaluated through the equation:

$$\frac{f_i}{f_{SG}} = 1 + 1.38\ We^{*0.2}\ \mathrm{Re}_G^{-0.6} \left(m_G^+ - 200 \sqrt{\frac{\varrho_G}{\varrho_L}} \right) \tag{5.23}$$

where f_{SG} is the friction factor for a smooth surface, and $m_G{}^+$ is given in terms of the gas friction velocity ($U_G{}^+$)

$$m_G^+ = \frac{m\ U_G^+\ \varrho_G}{\mu_G} \tag{5.24}$$

In Figure 5.18, equation (5.19) is tested against the measured drop size obtained in the present study. For the higher gas mass fluxes (G_G = 50–70 kg/m^{2}s) the data is overpredicted by the correlation within 20%. However, the correlation gives a good fit when predicting the drop size corresponding to G_G = 40 kg/m^{2}s. Previous drop size correlations (Azzopardi et al (1980), Azzopardi (1985), Gibbons (1985) and Azzopardi et al (1989)) failed to predict the trend between the drop size data and the liquid flow rate at this gas flow rate.

In summary, the equations that predict best the present drop size data are: (i) Azzopardi et al (1980) for gas mass fluxes between 50–70 kg/m^{2}s, and (ii) Ambronisi et al (1990) for drop sizes corresponding to G_G = 40 kg/m^{2}s.

It must be highlighted that both equations (5.8) and (5.19) were developed for vertical drop size data. To produce a satisfactory correlation for horizontal flow, further work is required on extending the drop size measurements to other flow conditions, tube diameters and fluid systems. Using this extended data bank, some of the existing correlations for drop size could be then modified and optimised.

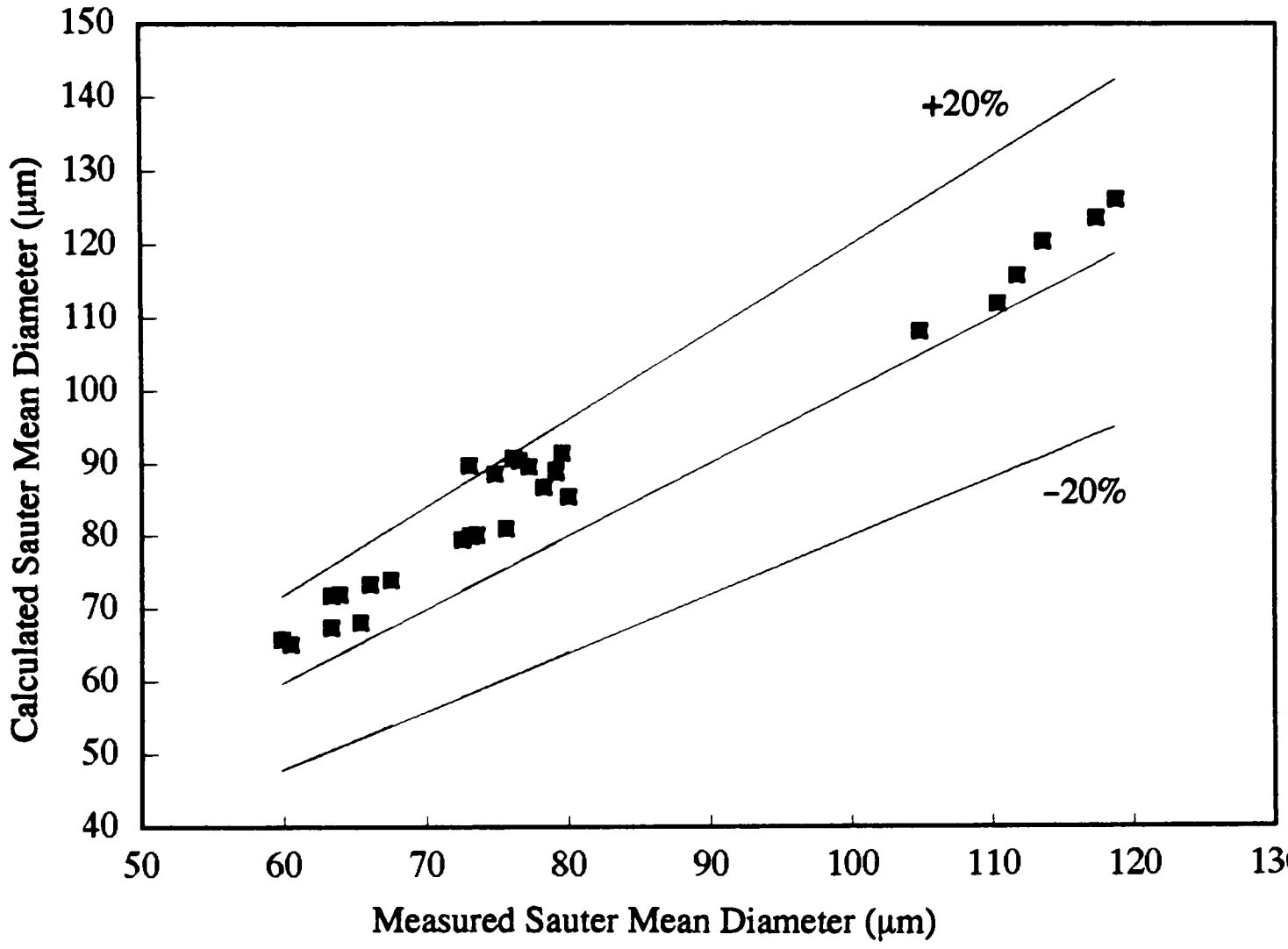

Figure 5.18 Performance of the correlation of Ambrosini et al (1991) to predict the drop size data of the present study.

5.4 Drop Size Measurements After the Bend

In this section the influence of a 90° horizontal bend on the drop size characteristics of horizontal annular two–phase flow is discussed. A set of drop size measurements was carried out after the bend for flow conditions that cover annular two–phase flow. The measurements were collected at ambient temperature and the pressure at the test section was maintained at 1.3 bar or 1.4 bar. The data were obtained with the laser diffraction technique, and was treated using the model independent analysis. Results are presented in Table B.18 and B.19 (Appendix B).

For all the flow conditions studied, the drop size histograms were represented by a multimodal curve. A typical drop size histogram is presented in Figure 5.19, for a gas mass flux of G_G = 40 kg/m^{2}s and a liquid mass flux of G_L = 50 kg/m^{2}s.

In Figure 5.20 the Sauter mean diameter is plotted against liquid mass flux. For the lower gas mass fluxes (G_G = 40 kg/m^{2}s and G_G = 50 Kg/m^{2}s) drop size is almost independent of the liquid flow rate. For G_G = 60 Kg/m^{2}s and G_G = 70 kg/m^{2}s, there is a tendency for the drop size to decrease with increasing liquid flow rate.

The effect of gas velocity is represented in the graph shown in Figure 5.21. Like the data before the bend, the drop size after the bend decreases with increasing gas flow. For the flow conditions analysed, the Sauter mean diameter is proportional to the superficial velocity raised to the power of –1.5.

A comparison between the drop size data before and after the bend, shows that generally the Sauter mean diameter increases after the bend. High speed still photography carried out downstream of the bend, confirmed that drops with diameters within the size ranges obtained using the diffraction technique, were present. The drops were photographed after removing the liquid film. This has already been discussed in section 3.4.

Several phenomena may contribute to the coarsening in drop size at the bend. It is believed that an important factor is the coalescence of drops. This study has captured photographic evidence which showed the coalescence and subsequence separation of two drops (see Figure 3.13(b)). Had conditions been more favorable, permanent coalescence could have equally arisen.

The secondary flow pattern (see Figure 1.13) existing in the gas phase at the bend may also contribute to enhance this increase in drop size. During the present experiments it was observed that in the upper half of the tube, the liquid film was dragged from the outer wall of the bend to the top of the tube in an anti–clockwise , cork–screwing fashion. On the lower half, the liquid film was dragged from the outer wall towards the bottom of the tube, in a clockwise motion. This movement of the liquid film, which was caused by the secondary flow in the gas phase, causes an accumulation of liquid on the inner wall of the bend. From this thick film, drops may be re–entrained into the gas. These are expected to be large, because

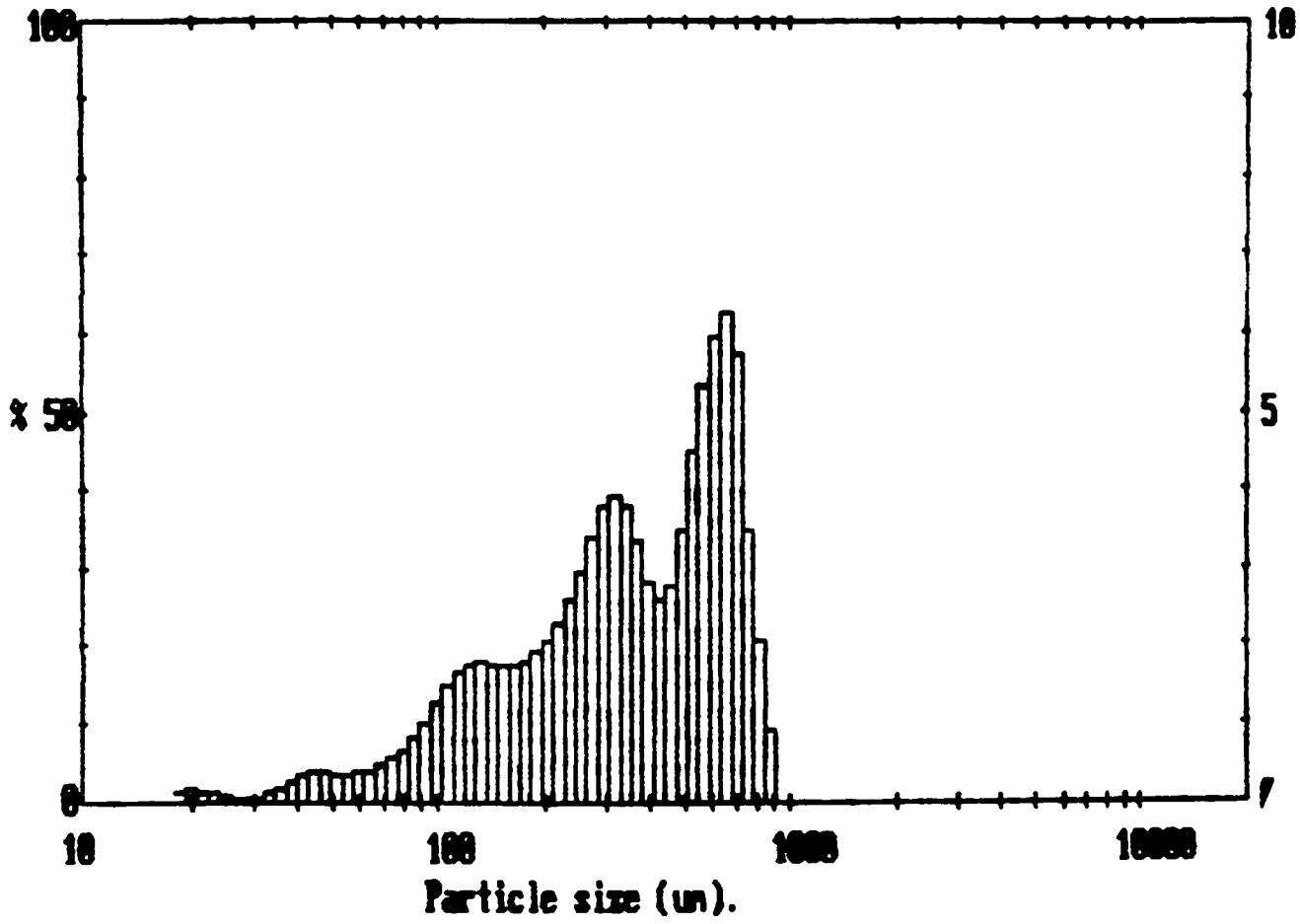

Figure 5.19 Typical drop size histogram for G_G = 40 kg/m^{2}s and G_L =50 kg/m^{2}s (after the bend).

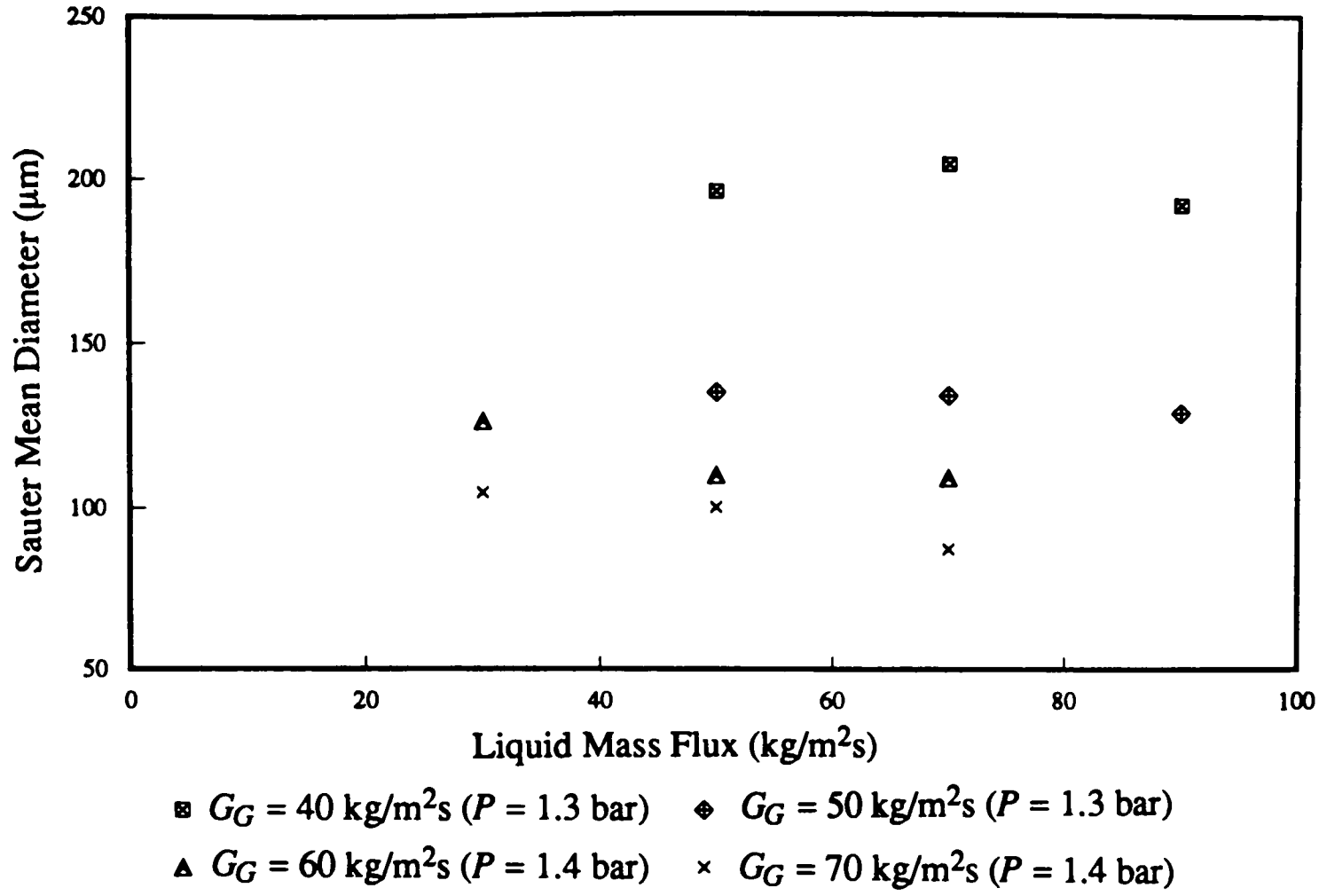

Figure 5.20 Influence of the liquid mass flux on drop size for the data obtained in the 0.032 m horizontal tube, after the bend.

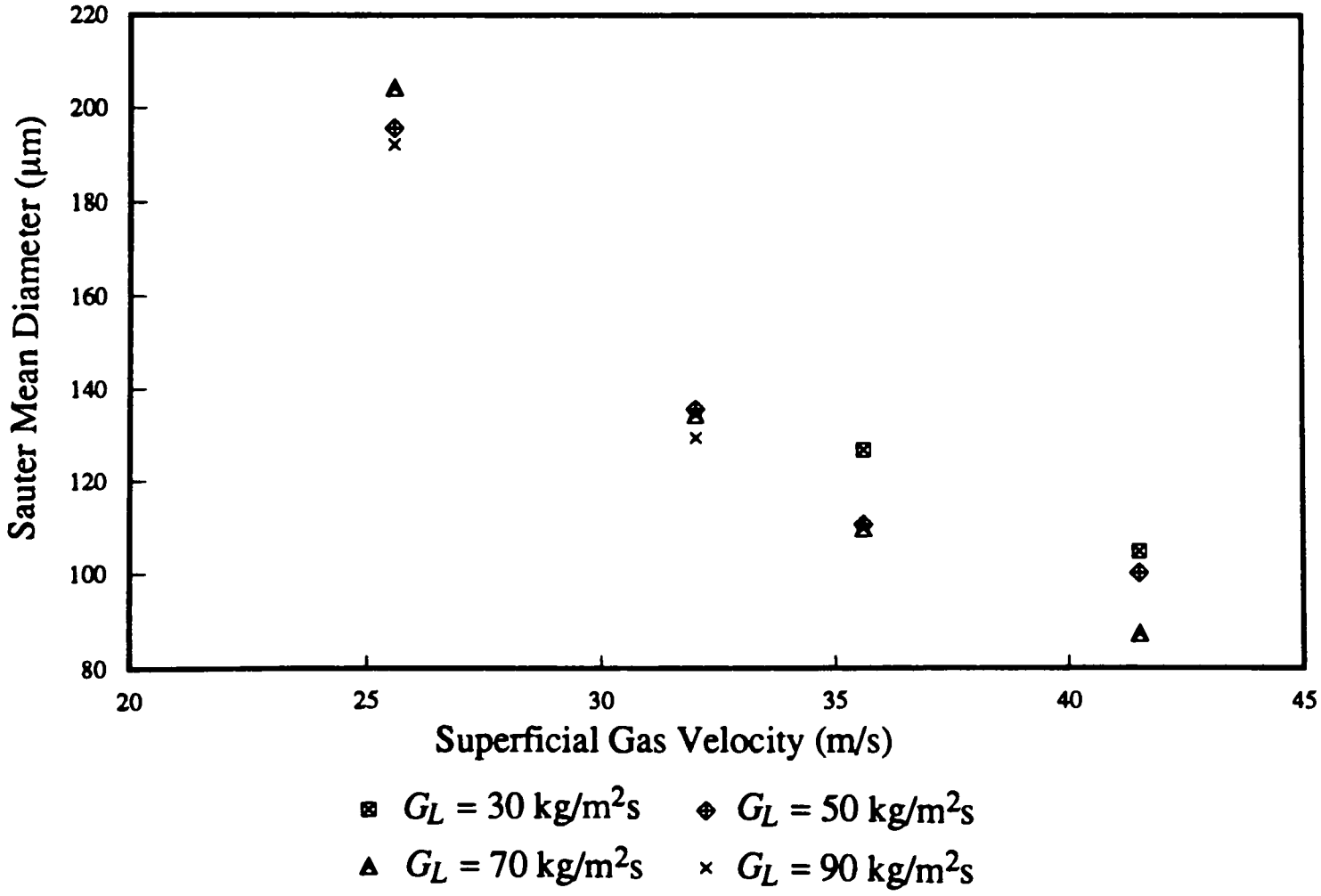

Figure 5.21 Influence of the superficial gas velocity on drop size for the data obtained in the 0.032 m horizontal tube, after the bend.

the local gas velocity has a minimum value towards the inside of the bend. Previous studies of the gas velocity at the exit of a bend (Anderson and Hills (1974) and Chakrabarti (1976)) showed that the velocity profile was distorted, with the maximum towards the outside of the bend.

At high gas velocities and low liquid loadings film inversion may occur at the bend, as discussed in section 1.7.2. This can also cause a thickning of the liquid film on the inside of the bend, and consequent appearance of large drops created by re–entrainment. Film inversion could explain why in Figure 5.20 for the higher gas velocities (G_G = 60 Kg/m^{2}s and G_G = 70 kg/m^{2}s) the drop size decreases with increasing liquid flow rate.

The previous paragraphs discussed several phenomena that may take place at a bend. It is possible that some of these occur simultaneously but it is difficult to say which of them has the dominant effect.

An increase in drop size after a bend was also reported by Farwagi (1983). This author investigated the coalescence and deposition of water drops suspended in a turbulent air stream, and used a photographic technique to determine drop size distributions. In spite of considering his results not statiscally representative, Farwagi stated that they were qualitatively valid. For comparison purposes, no other publications were found in the open literature concerning the study of the effect of a bend on drop size distribution.

5.5. Conclusions

From the above discussion, the following conclusions can be drawn concerning drop size measurements conducted in horizontal two–phase flow before the bend:

- Previous work on the measurement of drop sizes in annular two–phase flow was mostly carried out in vertical flow. The limited data published on horizontal flow was obtained in rectangular channels.
- For the present experiments, the drop size data were analysed using a model independent approach. The model independent fit to the multimodal drop size distributions was always significantly better than the Rosin–Rammler and Log–normal fits.
- For the conditions of this study, the Sauter mean diameter ($\overline{D}_{32}$) varied between 60–119 μm.
- The gas velocity has a strong effect on drop size. The present data showed that the Sauter mean diameter is proportional to the superficial gas velocity raised to the power of –1.0.
- The influence of liquid flow rate is somewhat more complex. For the lower gas mass flux (G_G = 40 kg/m^{2}s), $\overline{D}_{32}$ decreased with increasing liquid flow rate. For

G_G = 50 Kg/m^{2}s, the curve passed through a minimum. For the higher gas flows (G_G = 55–70 kg/m^{2}s) drop diameter increased with liquid flow rate. These trends are linked to different mechanisms of entrainment.

At low liquid flow rates the bag break–up mechanism, which produces larger drops, is thought to be dominant over the ligament break–up. As liquid flow rate increases, the entrainment mechanism changes predominantly to ligament break–up and the drop size decreases. At sufficiently high drop concentrations, the observed drop size increases with liquid flow rate due to the presence of coalescence.

- The influence of the pressure of the system on drop size was studied for G_G = 55 kg/m^{2}s and G_L = 30 kg/m^{2}s. An increase in $\overline{D}_{32}$ from 71.54 μm to 77.24 μm was observed by increasing the pressure from 1.3 bar to 1.4 bar. It is considered that this result is due to differences in gas velocity rather than changes in gas density.

- Drop size in horizontal annular flow was found to be lower than in vertical flow, for the same flow conditions and tube diameter (0.032 m). However, as the gas velocity increases this difference becomes less pronounced.

- Several existing drop size correlations were tested against the present measurements. The equations of Tatterson et al (1977) and Ishii and Kataoka (1982) performed badly against the present data. The correlation of Andreussi et al (1978) generally underpredicted the drop size.

  - For gas mass fluxes of 50–70 kg/m^{2}s, the drop size correlation of Azzopardi et al (1980) gave the best fit. However, as this equation accounts for an increase in drop size with entrained liquid flow, it predicted the wrong trend for the drop sizes corresponding to G_G = 40 kg/m^{2}s.

  - The correlations of Azzopardi (1985), Gibbons (1985) and Azzopardi et al (1989) overpredicted the present results within 20%, for G_G = 50–70 kg/m^{2}s. They also predicted the wrong trend for drop sizes corresponding to G_G = 40 kg/m^{2}s.

  - For the higher gas flow rates (G_G = 50–70 kg/m^{2}s) the correlation of Ambrosini et al (1990) overpredicts the present data within 20%. However, this is the only equation that predicted the correct trend for the drop sizes obtained at a gas mass flux of 40 kg/m^{2}s.

The drop size measurements carried out after the bend can be summarised as follows:

- For all flow conditions studied, the drop size histograms were represented by a multimodal curve.

- Measured Sauter mean diameters ranged between 87–204 μm.

- For the lower gas mass fluxes (G_G = 40 kg/m^{2}s and G_G = 50 kg/m^{2}s), the drop size was almost independent of liquid flow rate. For G_G = 40 kg/m^{2}s and G_G = 50 kg/m^{2}s the drop size decreased slightly with increasing liquid flow.
- The drop size decreased with increasing gas velocity. The Sauter mean diameter was found to be proportional to the superficial gas velocity raised to the power of –1.5.
- The effect of the 90° horizontal bend on the drop size distribution was to increase the diameter of drops. Several processes taking place at the bend, such as drop coalescence may be responsible for the coarsening of the distribution. The secondary flow pattern existing in the gas phase at the bend and film inversion are thought to have also some contribution.

6. DROP VELOCITY IN HORIZONTAL TWO-PHASE FLOW

6.1. Introduction

In horizontal two-phase flow atomisation begins under stratified conditions, as discussed before in Chapter 4. Drops are torn from the crests of roll waves present in the liquid film. These drops then interact with the turbulent gas stream.

The initial aim of the work reported in this chapter was to track the velocity of drops from the moment of their creation, to obtain information on their velocity history. For this purpose, a high speed cine film was used with the camera positioned sideways, facing the test tube (see section 2.1.3.3.). However, when analysing the films it proved very difficult to track these new drops. Instead, the analysis was redirected to track drops in the free gas stream, in a band restricted to the centre of the tube. The majority of these drops were seen to travel at almost constant velocity within the time frame of analysis.

For this reason, this chapter revises previous studies on drop velocity in horizontal and vertical annular flow, and presents new data on axial drop velocity for air-water flow in a horizontal tube 0.032 m ID. However, it should be emphasised, that due to the sample size and measurement technique employed, these results should be regarded only from a qualitative point of view.

6.2. Previous Work

Most of the earlier studies on the measurement of drop velocity were obtained from the analysis of high speed cine films. The main problem with these techniques is the considerable time involved in analysing the records. The results were usually averaged over the tube cross section and over several diameters in the axial direction. Drop velocity can also be obtained using double pulse photography, as mentioned in section 5.1.1.

A photographic technique that allows measurement of the radial drop velocity in annular two-phase flow, uses a parallel beam of light shining along the axis of the tube and was reported by Whalley et al (1979). This optical arrangement is illustrated in Figure 6.1. A parallel beam of laser light having the same diameter as the tube passes through the glass windows. Any protuberances on the liquid film or drops obstructing the beam appear as shadows in the focal plane of a cine film camera. The radial movement of drops in the section of the tube can be followed but without knowledge of their axial position. Using this method drops with diameters higher than 0.25 mm can be followed on a frame by frame analysis.

With the laser Doppler anemometry technique already described in section 5.1.6, simultaneous information on drop size and drop velocity can be obtained. As this technique

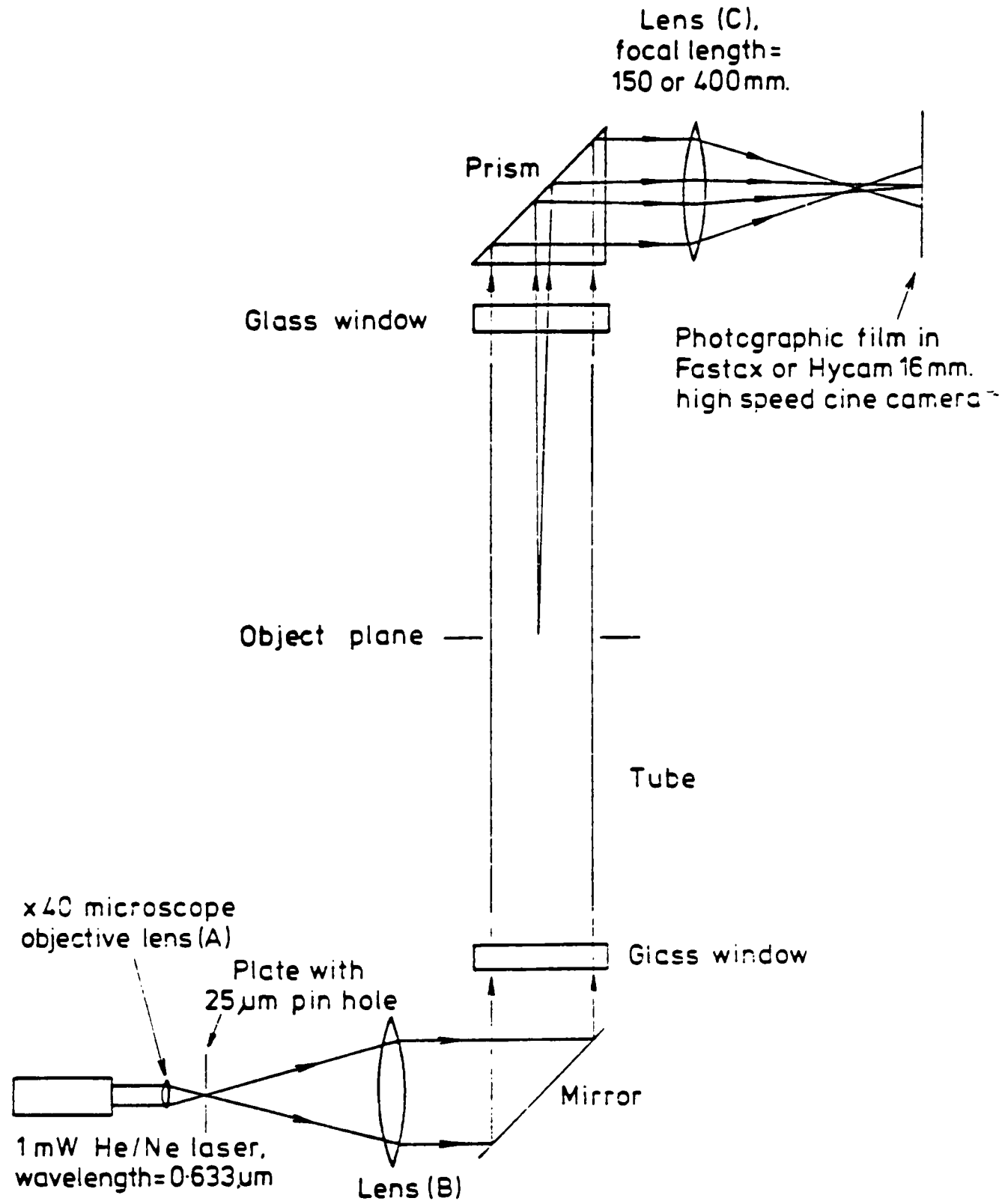

Figure 6.1 Optical arrangement of the parallel light technique used by Whalley et al (1979).

uses temporal sampling of drops, it provides local drop size/velocity measurements. Depending on the complexity of the apparatus up to three components of the velocity v_{Dz}, v_{Dy} and v_{Dx} can be measured. These components are related to the frame of reference shown in Figure 6.2.

The measurement techniques mentioned above were used by several authors to study drop velocity in gas–liquid flow. Table 6.1 summarises their work and makes reference to the direction of flow, and velocity components under investigation. It shows that with the exception of Chang (1973), all the experiments were conducted for air–water mostly flowing in vertical tubes.

Several parameters affect the drop velocity components. The next sections discuss how gas velocity and liquid flow rates were seen to influence the drop axial velocity and radial drop velocities. The relation between drop size and drop velocity is also pointed out.

6.2.1. Axial Drop Velocity

It is clear from previous experimental results that there is a considerable dependence of the axial drop velocity on the gas velocity. In general, the mean drop velocity increases with gas velocity. This was seen with the work of Gibbons (1985), Lopes and Dukler (1985) and Teixeira (1988) for vertical annular flow, and by Russel and Rogers (1972) for horizontal flow. The axial drop velocity usually lagged behind the gas velocity, as observed in Figure 6.3 taken from Teixeira (1988).

Liquid flow rate had only a small effect on the axial drop velocity, as illustrated by the graph in Figure 6.4 (Teixeira (1988)). This graph also shows the change in the axial drop velocity with the radial position, the maximum occurring at the centre of the tube. Teixeira (1988) suggested that this could be explained because: (i) in vertical annular flow the gas velocity is higher at the centre of the tube, and so there is a greater drag force experienced by the drops travelling at the centre, (ii) these are likely to have spent a longer time in the flow, being accelerated to higher velocities. Gibbons (1985) and Lopes and Dukler (1985) arrived at similar conclusions.

6.2.2. Radial Drop Velocities

The effect of gas velocity, liquid flow rate and system pressure on the radial components of drop velocity was studied by Andreussi and Azzopardi (1982) using axial view photography. Based on their experimental results, the authors proposed that the average drop transverse velocity v_{Dt} (resultant of the radial velocities v_{Dx} and v_{Dy}) was well correlated by:

$$v_{Dt} = 11.1\ U_G^+ \left(\frac{\varrho_G}{\varrho_L}\right)^{\frac{1}{2}} \qquad (6.1)$$

(a)

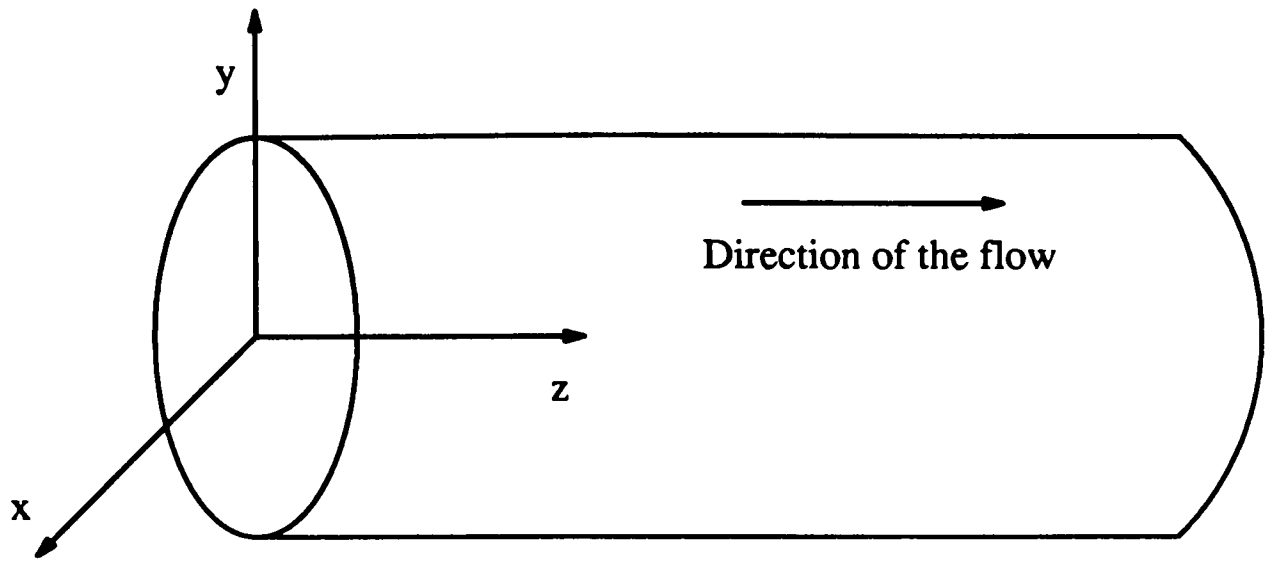

(b)

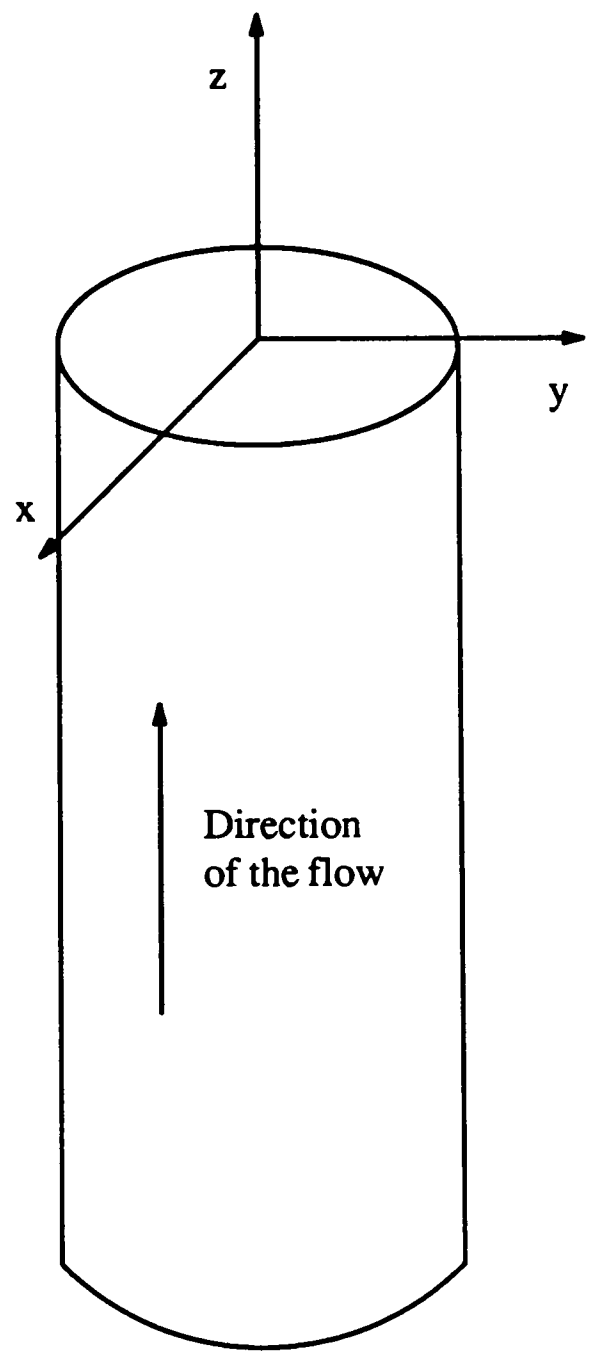

Figure 6.2 Frame of reference for drop velocites in: (a) horizontal flow, (b) vertical upflow

TABLE 6.1 SUMMARY OF PREVIOUS EXPERIMENTAL WORK ON DROP VELOCITY IN TWO-PHASE FLOW

Author	Fluids	Geometry	Flow Direction	Velocity Component Measured	Gas Flow	Liquid Flow	Measurement Technique
Cousins & Hewitt (1968)	air–water	circular tube d_t = 0.0095 m	vertical upflow	axial (v_{Dz})	28.5 & 49.7 m/s	0.0043–0.028 kg/s	cine film
Russel & Rogers (1972)	air–water	rect. channel 0.025 x 0.152 m	horizontal	axial (v_{Dz}) & radial (v_{Dy})	20.4 & 25.3 m/s	0.126 kg/s	cine film
Chang (1973)	air–45% glycerine/water solution air–60% glycerine/water solution	rect. channel 0.025 x 0.152 m	horizontal	axial (v_{Dz}) & radial (v_{Dy})	20.4 m/s	0.126 kg/s	cine film
Whalley et al (1979)	air–water	circular tube d_t = 0.032 m	vertical upflow	radial (v_{Dy}) & radial (v_{Dx})	24 m/s	16 kg/m^{2}s	axial view photography
James et al (1980)	air–water	circular tube d_t = 0.032 m	vertical upflow	radial (v_{Dy}) & radial (v_{Dx})	24 m/s	16 kg/m^{2}s	axial view photography
Andreussi and Azzopardi (1982)	air–water	circular tube d_t = 0.032 m	vertical upflow	radial (v_{Dy}) & radial (v_{Dx})	12.5–71.5 kg/m^{2}s	16–32 kg/m^{2}s	axial view photography
Wilkes et al (1982)	air–water	circular tube d_t = 0.01 m	vertical upflow	radial (v_{Dy}) & radial (v_{Dx})	–	–	axial view photography
Gibbons (1985)	air–water	circular tube d_t = 0.032 m	vertical upflow	axial (v_{Dz})	24–43.5 m/s	31.7 kg/m^{2}s	LDA
Lopes and Dukler (1985)	air–water	circular tube d_t = 0.051 m	vertical upflow	axial (v_{Dz}) & radial (v_{Dy})	14–24.7 m/s	0.034–0.121 m/s	LDA
Azzopardi (1987)	air–water	circular tube d_t = 0.032 m	horizontal	radial (v_{Dy}) & radial (v_{Dx})	20.8 & 32 kg/m^{2}s	32–89.6 kg/m^{2}s	axial view photography
Teixeira (1988)	air–water	circular tube d_t = 0.032 m	vertical upflow	axial (v_{Dz})	13.6–30.9 m/s	15.9–47.6 kg/m^{2}s	LDA

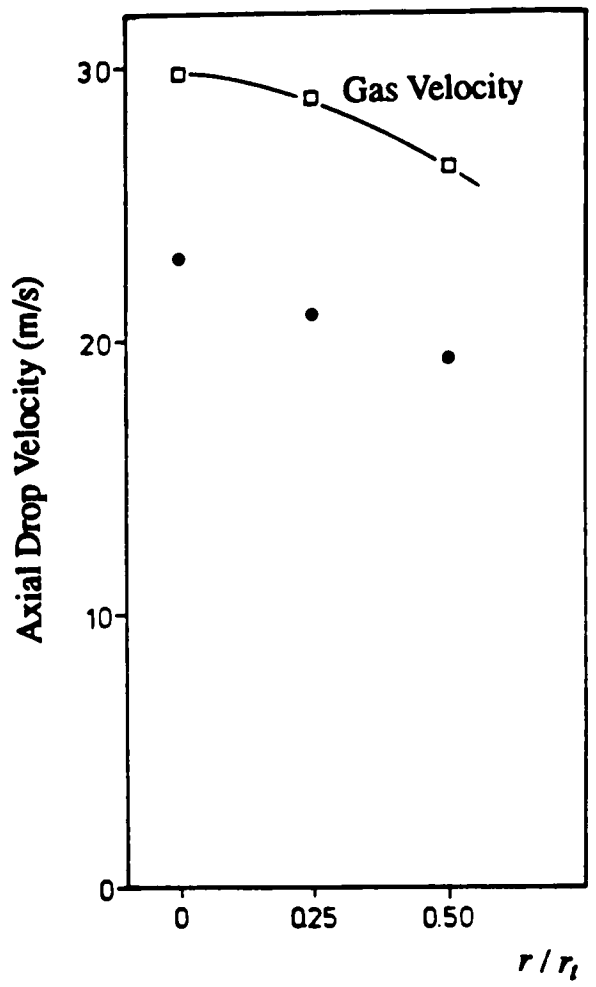

Figure 6.3 Radial variation of axial drop velocity and comparison with the gas velocity profile, for G_G = 43.7 kg/m^{2}s and G_L = 15.9 kg/m^{2}s (Teixeira (1988)).

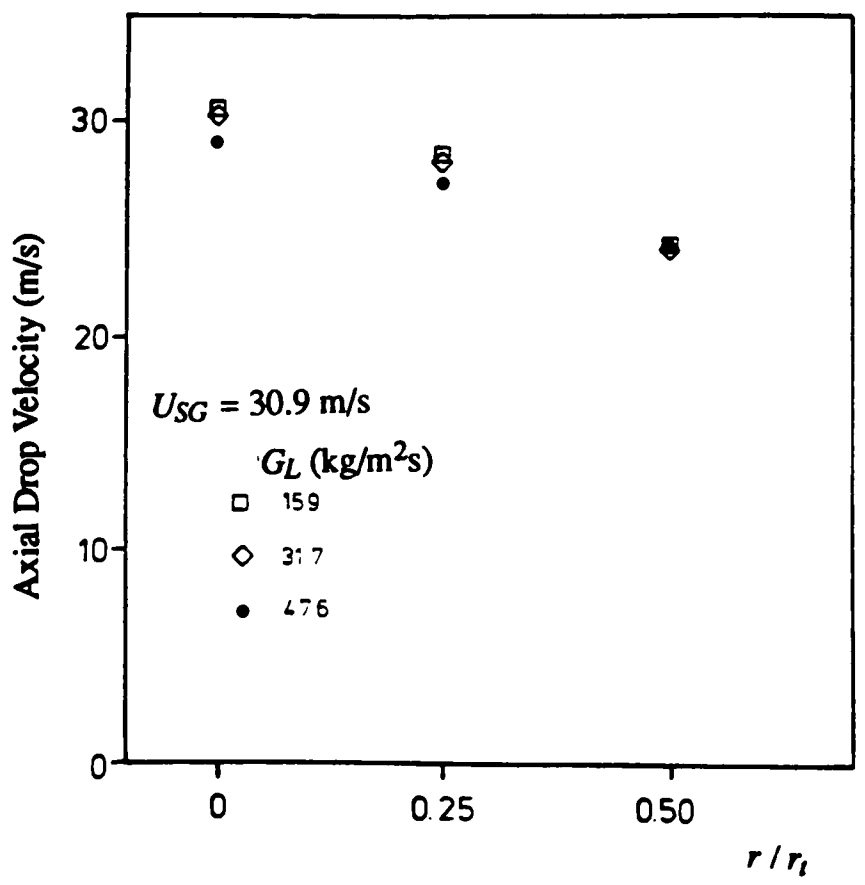

Figure 6.4 Effect of liquid mass flux on the radial distribution of mean axial velocity (Teixeira (1988)).

where U_G^+ is the gas friction velocity, and ϱ_G and ϱ_L are the gas and the liquid densities, respectively. No influence of liquid flow rate was seen in these experiments.

Wilkes et al (1983) extended the work of Andreussi and Azzopardi (1982) to a tube 0.01 m ID, and reported data that showed the radial drop velocities to be affected by the tube diameter. For the range of flow conditions studied, the values of the drop transverse velocity were higher for the tube with greater diameter.

Figure 6.5 shows the radial drop velocity (v_{Dy}) plotted against gas Reynolds number obtained by Lopes and Dukler (1985) using a LDA technique. This graph indicates that for the flow conditions analysed the radial drop velocity was independent of gas and liquid flow rates, being constant along the tube radius.

For horizontal annular flow, the only work on the study of drop radial velocities was reported by Azzopardi (1987). The results of that investigation are present in Table 6.2, and showed no trends of the transverse drop velocity with gas or liquid flow rate. However, the author pointed out the need for carrying out further work over a wider range of flow conditions.

TABLE 6.2 TRANSVERSE DROP VELOCITIES (FROM AZZOPARDI (1987))

Run	G_G	G_L	Pressure	v_{Dt}
	(kg/m^2s)		(bar)	(m/s)
A	20.8	70.8	1.25	1.80
B	20.8	89.6	1.25	1.57
C	32.0	32.0	1.25	1.43
D	32.0	70.4	1.25	1.53
E	32.0	89.6	1.25	2.10

6.2.3. Dependence of Drop Velocities on Their Sizes

Several of the studies listed in Table 6.1 attempted to relate drop size to the corresponding drop velocity. In this section the dependence of the axial drop velocity and drop radial velocities on drop size will be analysed.

By plotting individual measurements of drop size against transverse drop velocity, Andreussi and Azzopardi (1982) found no dependence between these two variables. The authors suggested that this finding could be influenced by the limited range of drop sizes covered by their experimental technique, where drops smaller than 0.25 mm could not be measured.

In order to relate drop size to drop velocity, Lopes and Dukler (1985) used a conditional sampling analysis to treat their data. The measured drops were classified into classes

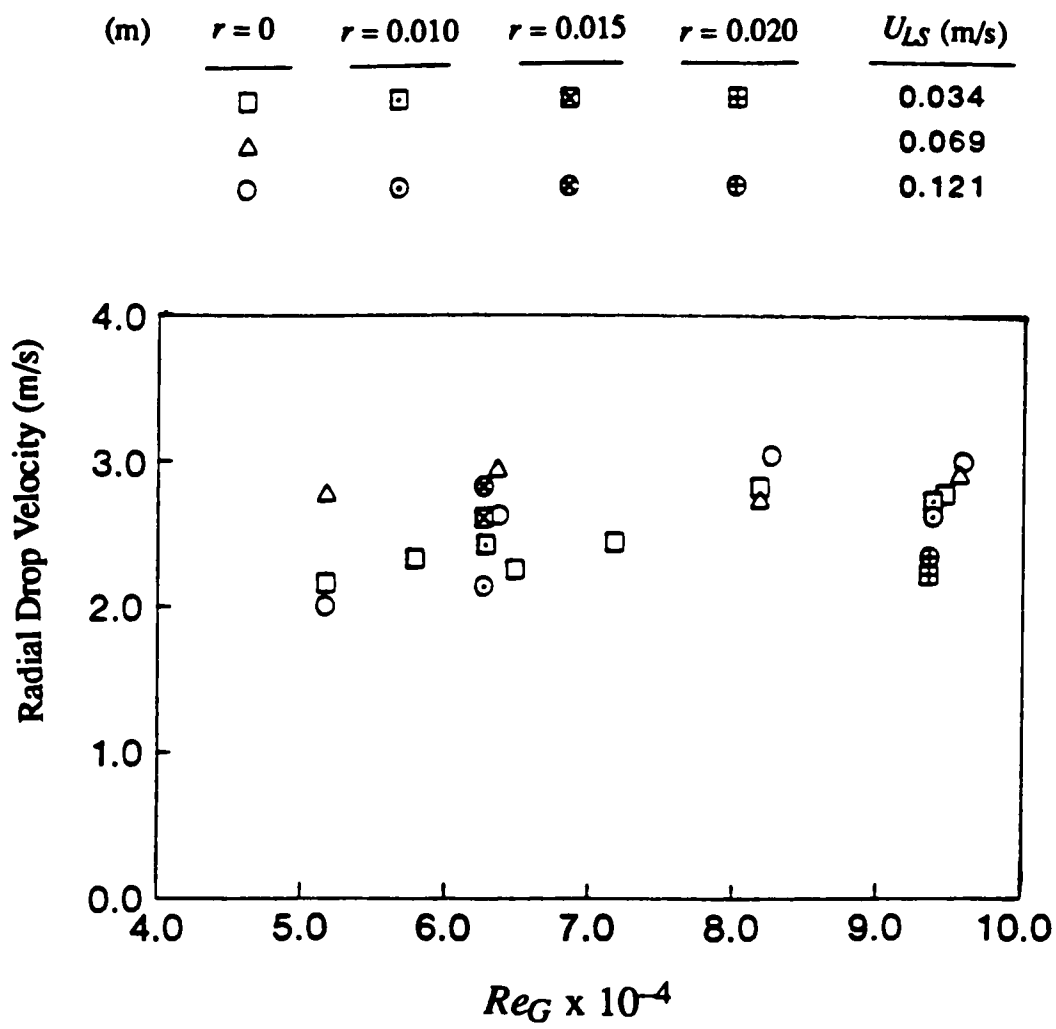

Figure 6.5 Dependence of the average radial velocity on the liquid velocity and radial position (Lopes and Dukler (1985)).

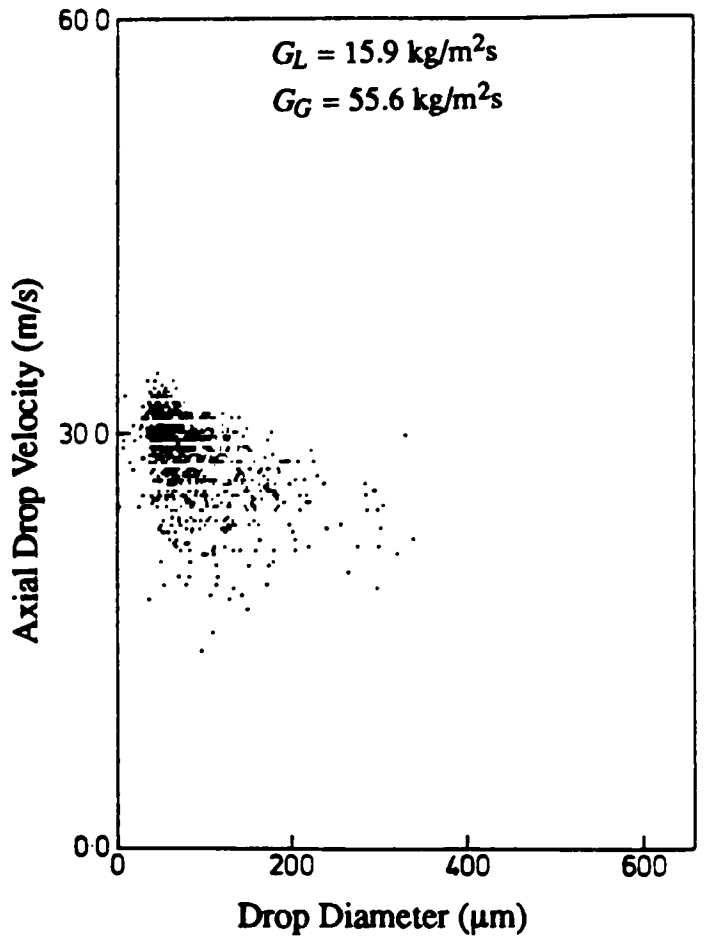

Figure 6.6 Relationship between drop size and axial drop velocity (Teixeira (1988)).

according to their size. For each class size they calculated an average drop diameter and the corresponding averages of radial drop velocity and axial drop velocity. The authors found the average axial drop velocity increased with average drop diameter. On the other hand, the average radial velocities were seen to have an almost constant value for all the average diameters considered.

Teixeira (1988) investigated the possibility of an existing correlation between drop size and axial drop velocity, by analysing his data in terms of a correlation coefficient proposed by Green and Margerison (1978). The author claimed that such a correlation existed, and axial drop velocity was seen to decrease with increasing drop size. Teixeira also argued that the same conclusion could be deduced from the scatter plot of drop size against axial drop velocity shown in Figure 6.6.

From the above discussion it can be concluded that most of the experimental work on the measurement of drop velocities has been carried out for vertical annular flow. For horizontal flow in tubes, the only study was reported by Azzopardi (1987). However, this was restricted to the measurement of radial velocities over a limited range of flow conditions. Also, at the moment there are contradictory results with respect to the relationship between drop size and drop velocity. Further work is required in this area, especially for horizontal flow.

6.3. Present Work

It was mentioned earlier that the initial objective of this work was to follow the velocity of drops from the moment of their creation. High speed cine film was used to track the movement of the drops on a frame by frame basis. However, it proved very difficult to follow these newly created drops. Instead, the analysis was redirected to track drops in the free gas stream, in a band restricted to the centre of the tube. The majority of these drops were seen to travel at almost constant velocity within the time frame of analysis.

It must be stressed before hand, that the data that will be presented in this section should be regarded only in qualitative terms. Firstly, the photographic technique has limitations with regard to the minimum drop size that could be measured. Secondly, the number of drops analysed per set of flow conditions (around 60 drops) is too small to be considered as statistically representative.

The results were gathered from cine films taken at a gas mass flux of G_G = 20 kg/m^{2}s and liquid mass fluxes of G_L = 70 and 90 kg/m^{2}s (wavy-stratified flow), G_G = 20 kg/m^{2}s and G_L = 130 kg/m^{2}s (pseudo-slug flow), and at G_G = 30 kg/m^{2}s and G_L = 70 kg/m^{2}s (wavy-stratified flow), at ambient temperature. The pressure at the test section varied between 1.2-1.3 bar.

The films were analysed using a Vanguard film analyser. With this apparatus and after calibration against the tube diameter, it is possible to measure the coordinates (z,y) (see Figure

6.2(a)) of a drop on each frame. By knowing the film speed (2000 frames per second), the velocity of the drop between frames may be calculated. Each drop was followed for at least five consecutive frames.

The equivalent drop diameter and average axial drop velocity for each drop are presented in Tables B.7 to B.10 (Appendix B). For each drop, the drop diameters in the z–direction (D_z) and in the y–direction (D_y) were averaged over several frames. As some drops appeared not to be spherical, but instead had an ellipsoid form, an equivalent diameter (D_{eq}) was considered. This was already discussed in section 3.2.4. The axial drop velocity was also averaged over several frames, and it was almost constant from frame to frame.

Measurements of the radial drop velocity (v_{Dy}) indicated that this component was negligible when compared to the axial drop velocity. Figures 6.7, 6.8, 6.9 and 6.10 represent scatter plots of the equivalent drop size against the respective axial drop velocities for G_G = 20 kg/m^{2}s and G_L = 70 kg/m^{2}s, G_G = 20 kg/m^{2}s and G_L = 90 kg/m^{2}s, G_G = 20 kg/m^{2}s and G_L = 130 kg/m^{2}s, and G_G = 30 kg/m^{2}s and G_L = 70 kg/m^{2}s, respectively. These graphs indicate no trend between drop size and the axial drop velocity. According to Gibbons (1985), the existence of drops of different 'ages' flowing in the gas stream can explain the spread in the drop axial velocity at a given drop size. A drop that has just been released will not have sufficient time to approach the gas velocity.

In the present study, the drops analysed showed an almost constant axial velocity over the time frame of analysis (~ 0.0025 s). However, this time frame is several orders of magnitude smaller than the time taken by a drop to accelerate to near the gas velocity (~ 0.67 s for a drop with a diameter of 0.5 mm travelling in a gas stream of U_{SG} = 13.9 m/s to reach an axial velocity of 12.5 m/s (= 0.9 U_{SG})). To calculate an estimate of the time necessary for a drop to reach a given velocity, a simplified method described in Appendix F was used. So, at the measurement section, both 'old' and 'new' drops were observed.

The influence of the superficial gas velocity on the axial drop velocity can be seen by comparing Figures 6.7 and 6.10. In general, drop velocity increases with gas velocity, as was found by previous investigators. This is expected because the higher the gas velocity, the greater the accelerating force exerted by the flow on the drops.

By comparing the graphs in Figures 6.6 and 6.7 it appears that liquid flow rate has no effect on the axial drop velocity. However, for G_G = 20 kg/m^{2}s and G_L = 130 kg/m^{2}s (Figure 6.9) the spread in the axial drop velocities has increased towards higher values. This may be due to the fact that this flow condition lies in a different flow regime, the pseudo–slug flow.

As stated earlier, the results in this section should only be considered from a qualitative point of view. The influence of gas and liquid flow rates on the axial velocity has confirmed the conclusions of previous investigators. However, to establish the true relationship between

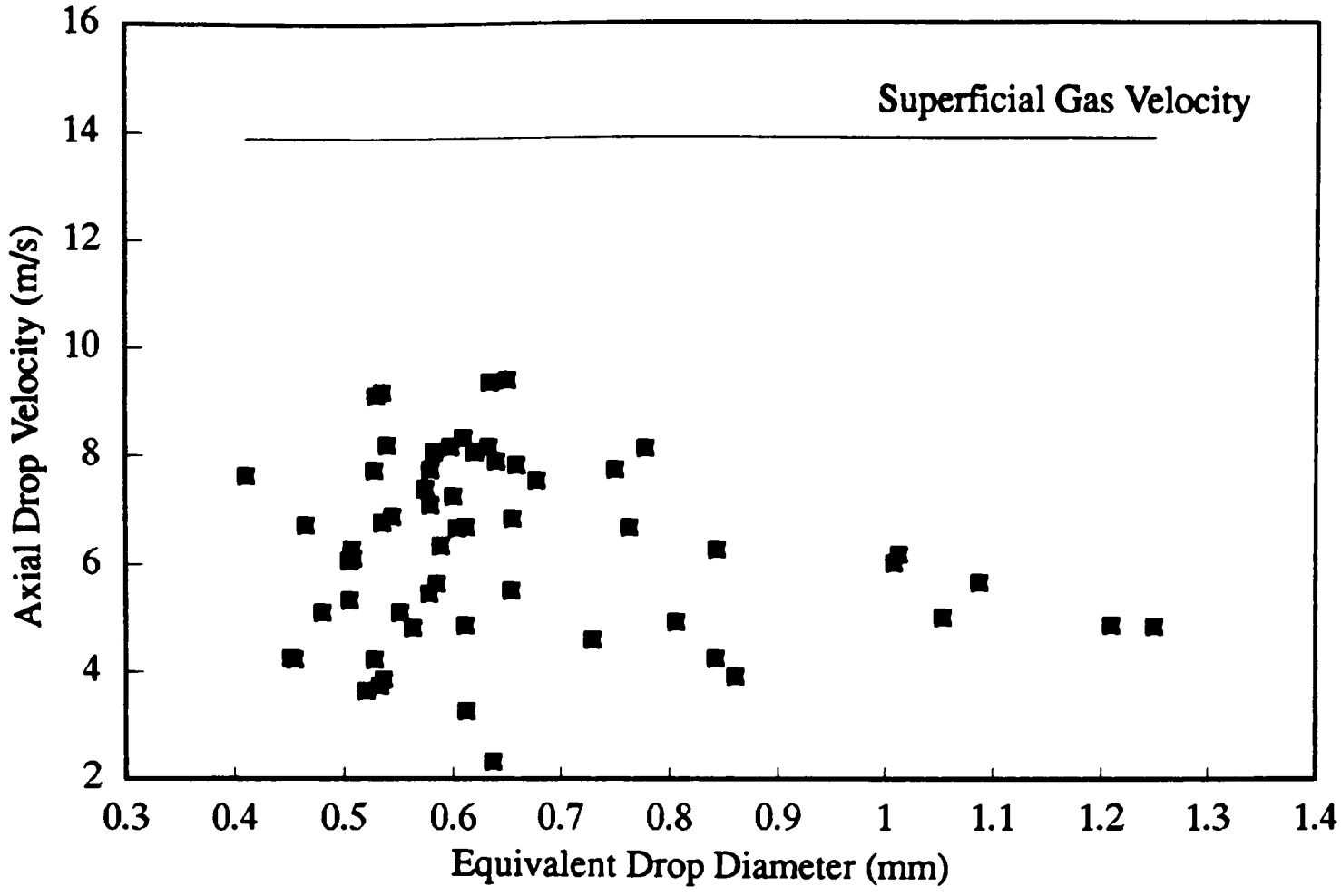

Figure 6.7 Correlation between axial drop velocity and drop size for G_G = 20 kg/m^{2}s and G_L = 70 kg/m^{2}s (present data).

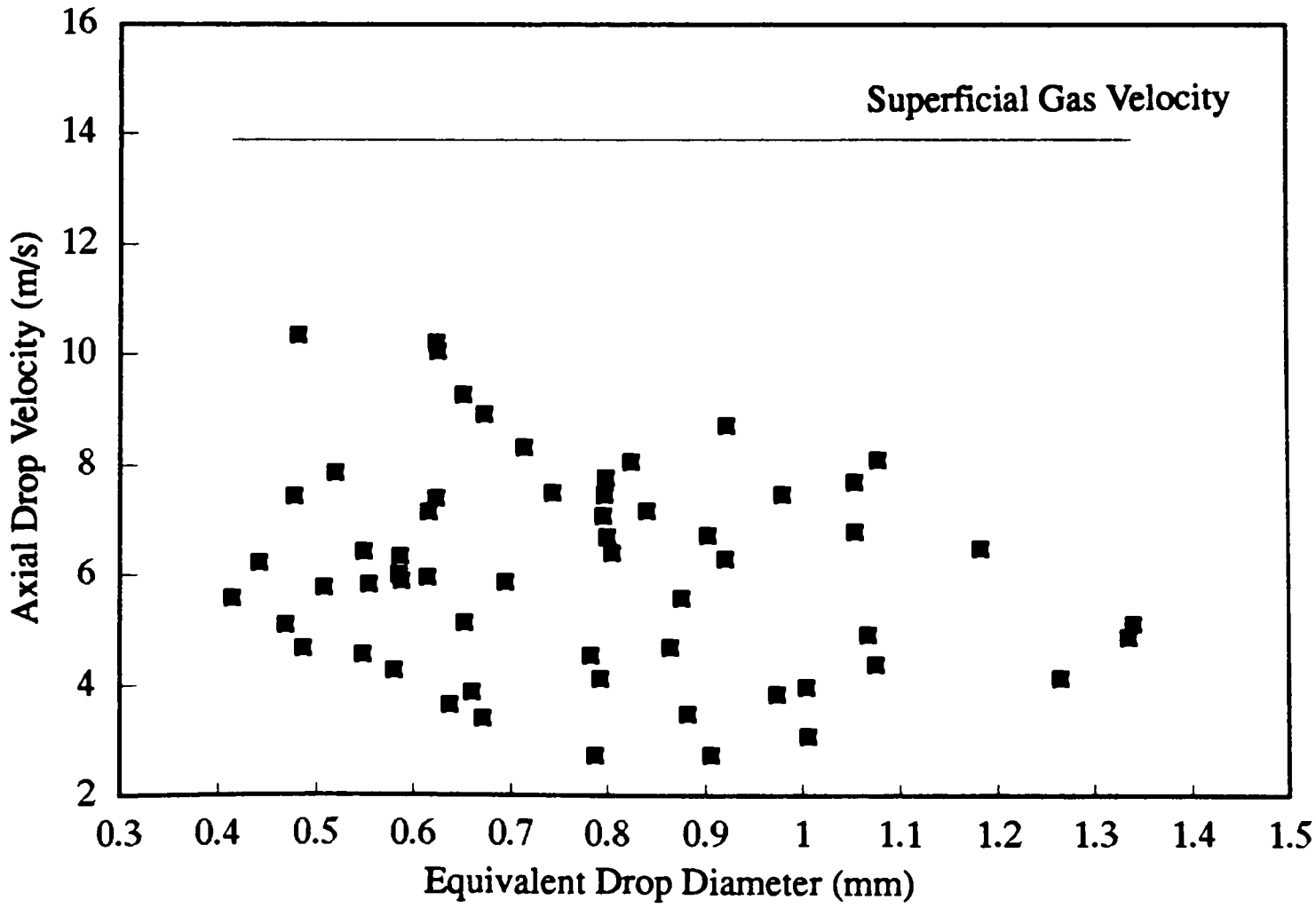

Figure 6.8 Correlation between axial drop velocity and drop size for G_G = 20 kg/m^{2}s and G_L = 90 kg/m^{2}s (present data).

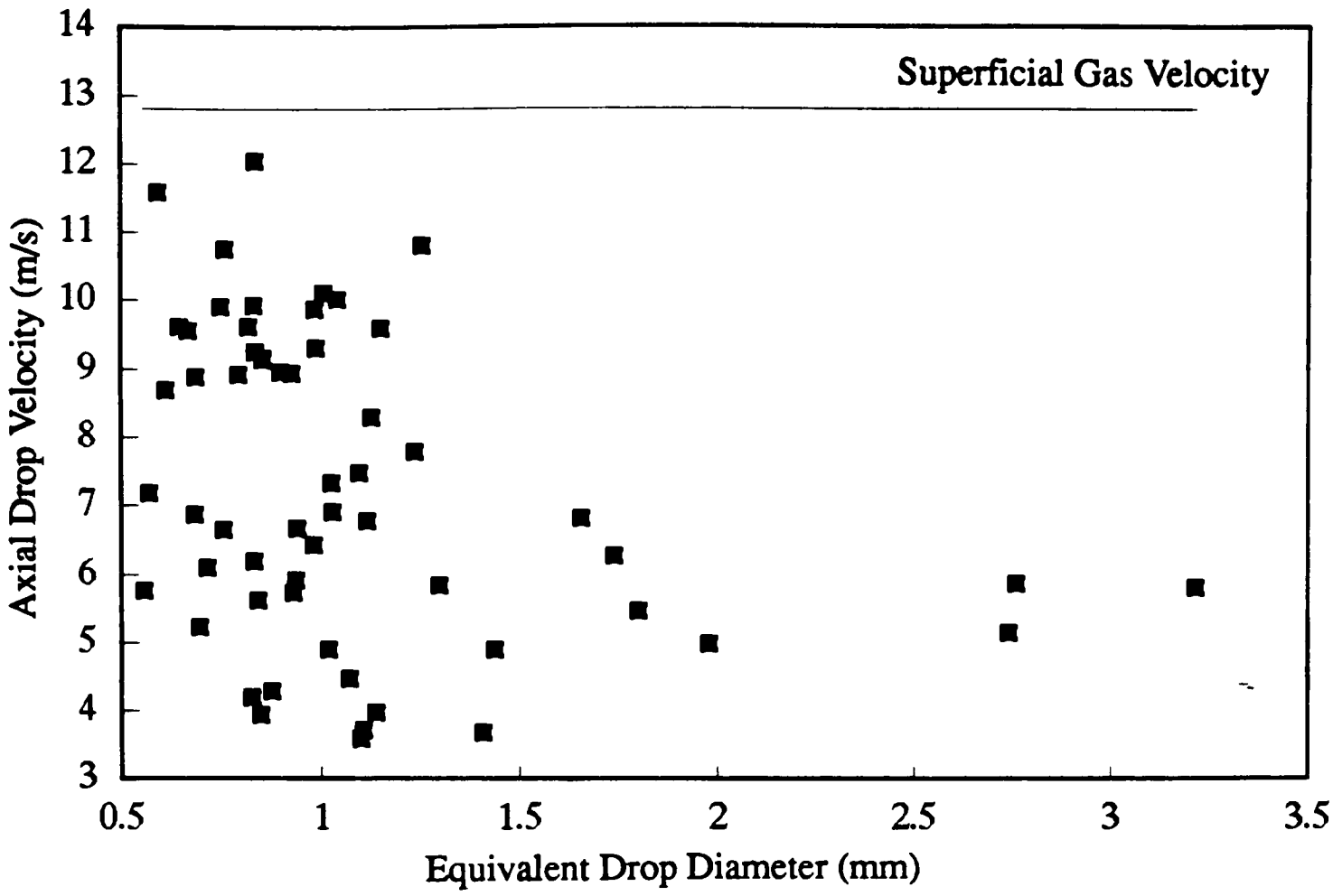

Figure 6.9 Correlation between axial drop velocity and drop size for G_G = 20 kg/m^{2}s and G_L = 130 kg/m^{2}s (present data).

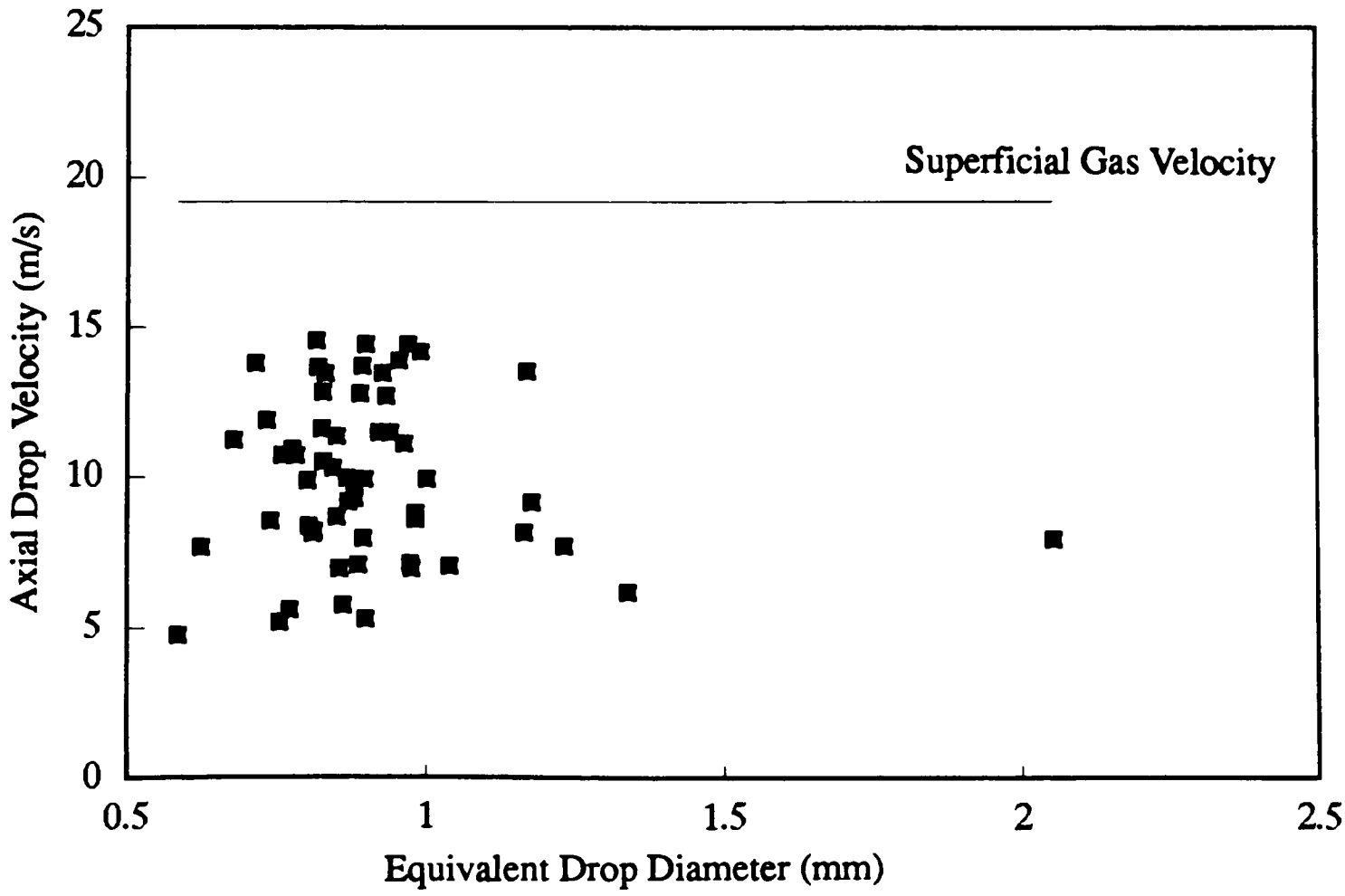

Figure 6.10 Correlation between axial drop velocity and drop size for G_G = 30 kg/m^{2}s and G_L = 70 kg/m^{2}s (present data).

drop size and axial drop velocity in horizontal flow, a more sophisticated method such as a LDA based technique should be used.

6.4. Conclusions

The discussion carried out in this chapter can be summarised as follows:

- With the cine film technique used in the present work it was not possible to follow the velocity of drops from their point of creation.
- Because of the method of measurement employed and the sample size, the present results should only be regarded from a qualitative point of view.
- The radial drop velocity component measured was negligible in comparison with the axial drop velocity.
- For the flow conditions analysed, no significant correlation was found between drop size and axial drop velocity.
- Axial drop velocity increased with superficial gas velocity.
- For G_G = 20 kg/m^{2}s and liquid mass fluxes of 70 kg/m^{2}s and 90 kg/m^{2}s, no influence of the liquid flow rate on the axial drop velocity was seen. However, the increase in the spread of drop velocity towards higher values observed for G_G = 20 kg/m^{2}s and G_L = 130 kg/m^{2}s, may be due to a change in the flow regime to pseudo–slug flow.

7. ENTRAINMENT AND DROP SIZE IN VERTICAL ANNULAR FLOW

7.1. Introduction

Annular flow is an important flow regime in gas–liquid upflow. As mentioned in section 1.5. this regime is characterised by the gas occupying the centre of the tube, while the liquid flows as a thin film along the wall. Beyond critical gas and liquid flow rates, the gas–liquid interface becomes highly agitated and large waves appear. These waves are torn by the fast moving gas flow giving rise to drop entrainment in the gas core. At the same time, drops are also deposited on the liquid film.

Drops play an important role in transport phenomena occurring in annular flow. The work presented in this chapter deals with measurements of the entrained mass flux and drop size for air–water annular flow in a vertical tube 0.01026 m ID. It extends the investigation of Jepson (1992) who measured the effect of gas density on the film flow rate, drop size and deposition mass transfer coefficient. Modifications performed in the rig described by Jepson (1992) (the gas came directly from the main air supply rather than from a compressor) allowed an extension of the measurements to higher flow conditions.

7.2. Entrainment Measurements

Liquid film flow measurements were performed for air–water upflow in a vertical tube 0.01026 m ID using the film removal technique. The entrained mass fluxes were calculated from the liquid film flow rates. The experimental conditions were established at ambient temperature and at a pressure of 1.5 bar in the measuring section. The range of gas mass fluxes analysed cover $G_G = 60–120$ kg/m^{2}s, and liquid mass fluxes of 40–120 kg/m^{2}s. The results are shown in Table G.1 (Appendix G).

Figure 7.1 illustrates the linear relation existing between the entrained liquid fraction and the total liquid mass flux, for a constant gas mass flow rate. Liquid film mass fluxes are presented in Figure 7.2 against gas mass flux, for a constant liquid flow. From Figure 7.1 it can be concluded that both gas and liquid mass flow rates have a strong influence on the entrained liquid flow rate. The increase in the level of entrainment with gas velocity can be explained by an increase in the shear force acting on the liquid layer, as the gas velocity is increased. The graph in Figure 7.2 shows that, as the liquid flow rate decreases, the decrease in G_{LF} with gas flow rate is less pronounced.

Data on the liquid film mass flux from the present experiments is compared in Figure 7.3 with the results obtained by Jepson (1992) under the same flow conditions for a gas mass flux of 80 kg/m^{2}s. There is a maximum difference of 5% existing between both sets of data, as can be observed from the values tabulated in Table G.1 (Appendix G).

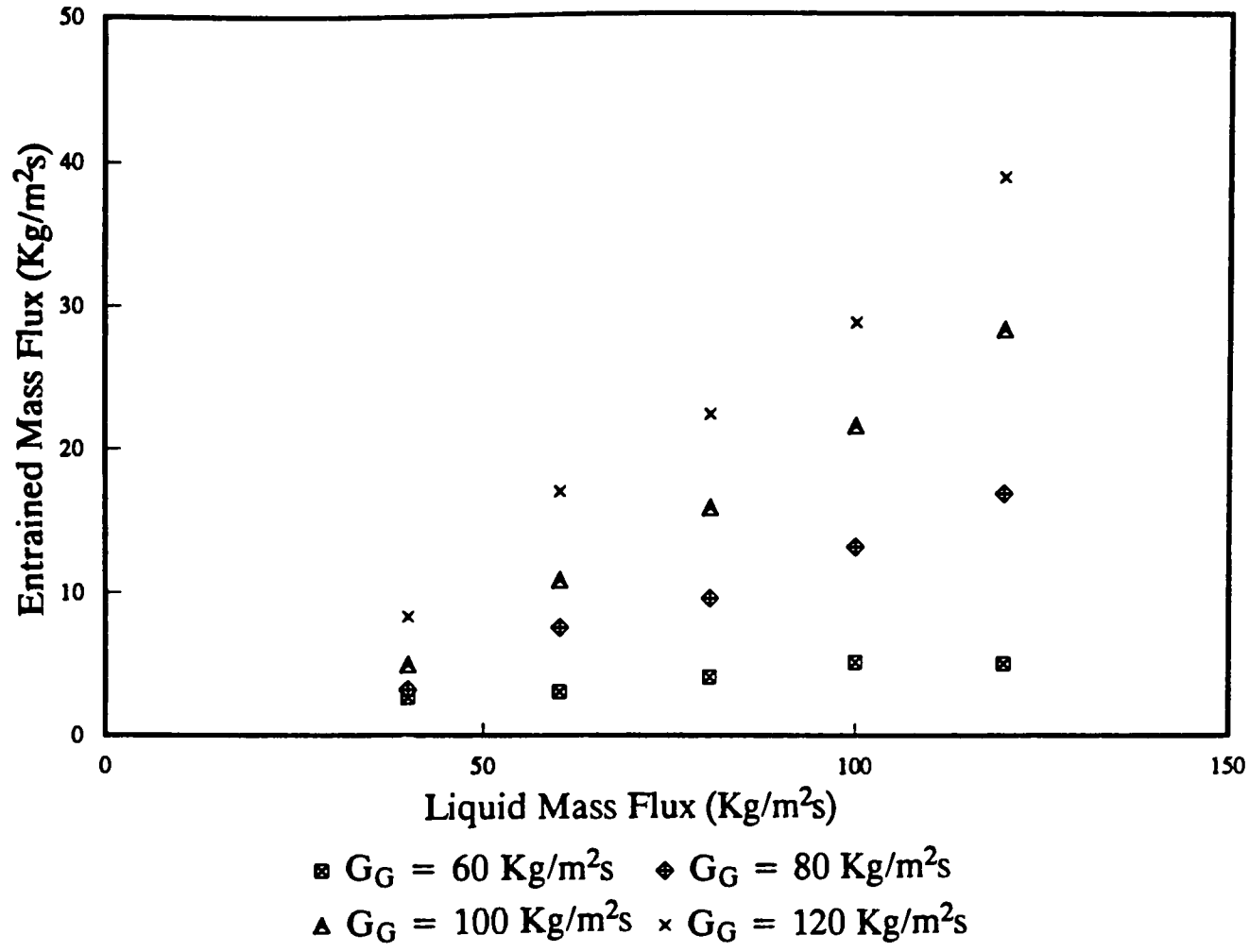

Figure 7.1 Influence of liquid mass flux on the entrained mass flux.

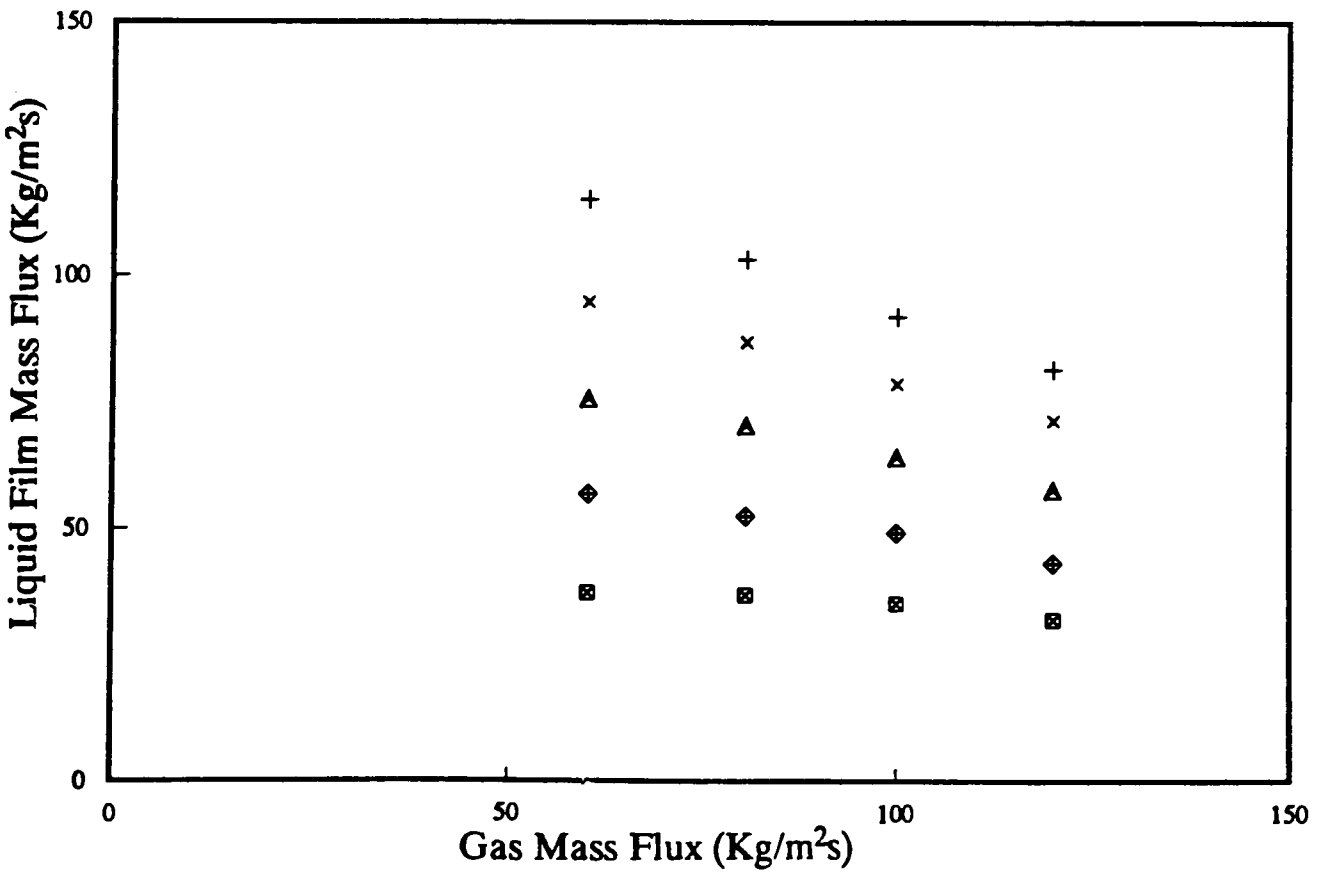

Figure 7.2 Influence of the gas mass flux on the liquid film flow measurements.

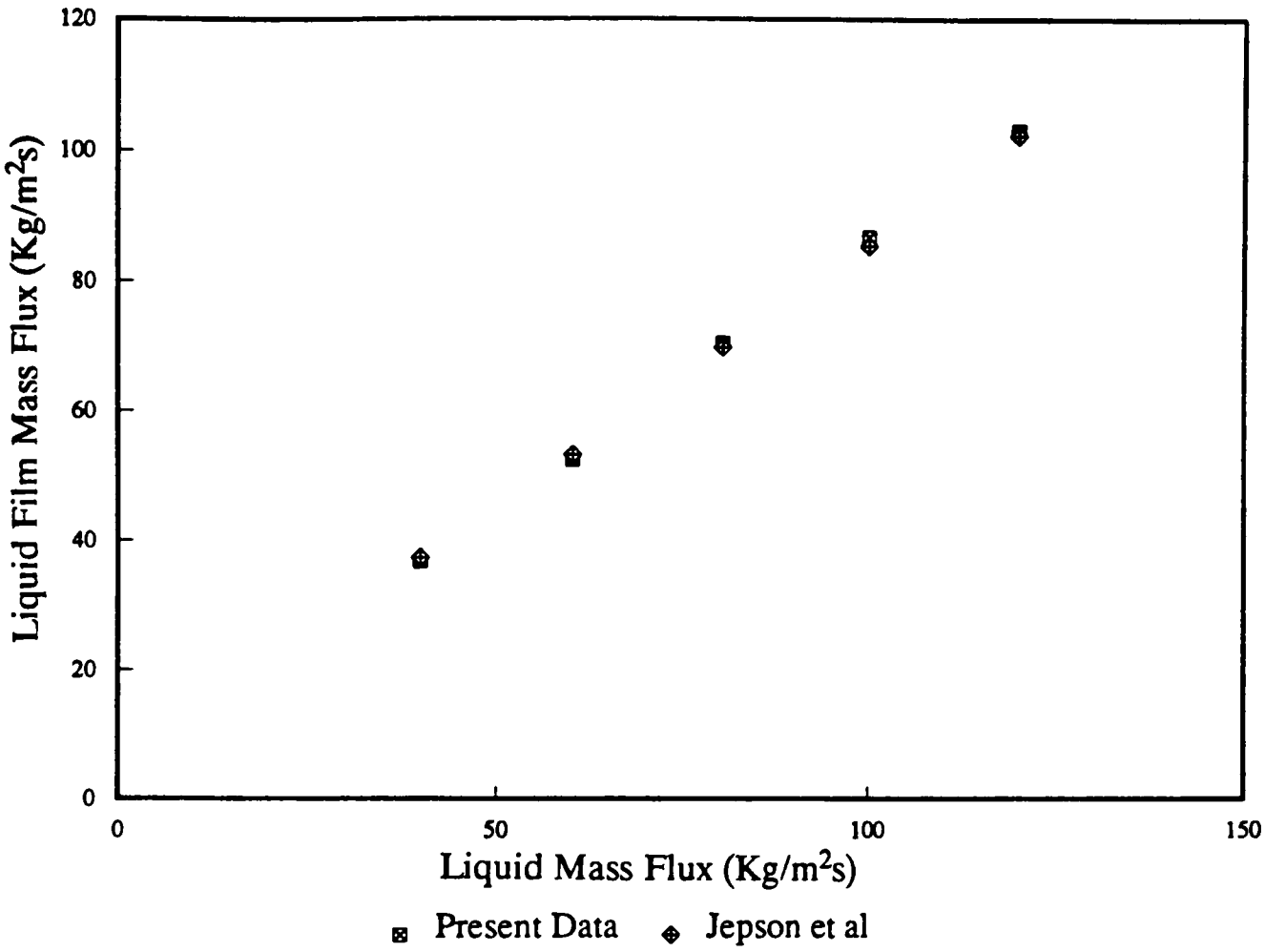

Figure 7.3 Liquid film flow measurements of the present study and the data of Jepson (1992), for G_G = 80 kg/m^{2}s.

7.3. Entrainment Correlations

A number of equations have been proposed to predict the amount of liquid that flows as drops. In this section, the present entrainment data is compared against correlations developed for vertical annular flow.

Govan (1990) deduced an entrainment rate correlation and a deposition rate correlation based on a data bank for vertical annular flow, covering many fluid systems, tube diameters and operating conditions. The deposition rate, given by the best fit to the experimental results (Figure 7.4), was:

$$k_D \sqrt{\frac{\varrho_G \, d_t}{\sigma}} = 0.18 \qquad \text{if } \frac{C}{\varrho_G} < 0.3 \tag{7.1}$$

$$k_D \sqrt{\frac{\varrho_G \, d_t}{\sigma}} = 0.083 \left(\frac{C}{\varrho_G} \right)^{-0.65} \qquad \text{if } \frac{C}{\varrho_G} > 0.3 \tag{7.2}$$

The entrainment rate equation ($\dot{E}$) was developed from equilibrium data, and taking into account the critical film flow rate for the onset of atomisation (G_{LFC}), the author obtained:

$$\frac{\dot{E}}{G_G} = 5.75 \times 10^{-5} \left[(G_{LF} - G_{LFC})^2 \, \frac{d_t \, \varrho_L}{\sigma \, \varrho_G^2} \right]^{0.316} \tag{7.3}$$

This is illustrated in Figure 7.5. To calculate the critical liquid film flow rates, Govan used the expression proposed by Owen and Hewitt (1986):

$$\mathrm{Re}_{LFC} = \exp\left(5.8405 + 0.4249 \, \frac{\mu_G}{\mu_L} \sqrt{\frac{\varrho_L}{\varrho_G}} \right) \tag{7.4}$$

where Re_{LFC} is the critical liquid film Reynolds number. Equations (7.1), (7.2) and (7.3) can be used to correlate equilibrium entrainment data, by assuming that at equilibrium $\dot{E} = \dot{D}$. As the entrainment rate $\dot{E}$ depends on the liquid film flow rate, it is necessary to apply an iterative procedure.

Figure 7.6 compares the data of this study against the entrained mass fluxes calculated using the correlation of Govan (1990), where the critical liquid film flow rates were estimated from equation 7.4. The graph shows that the data are quite scattered. Also, the correlation of Owen

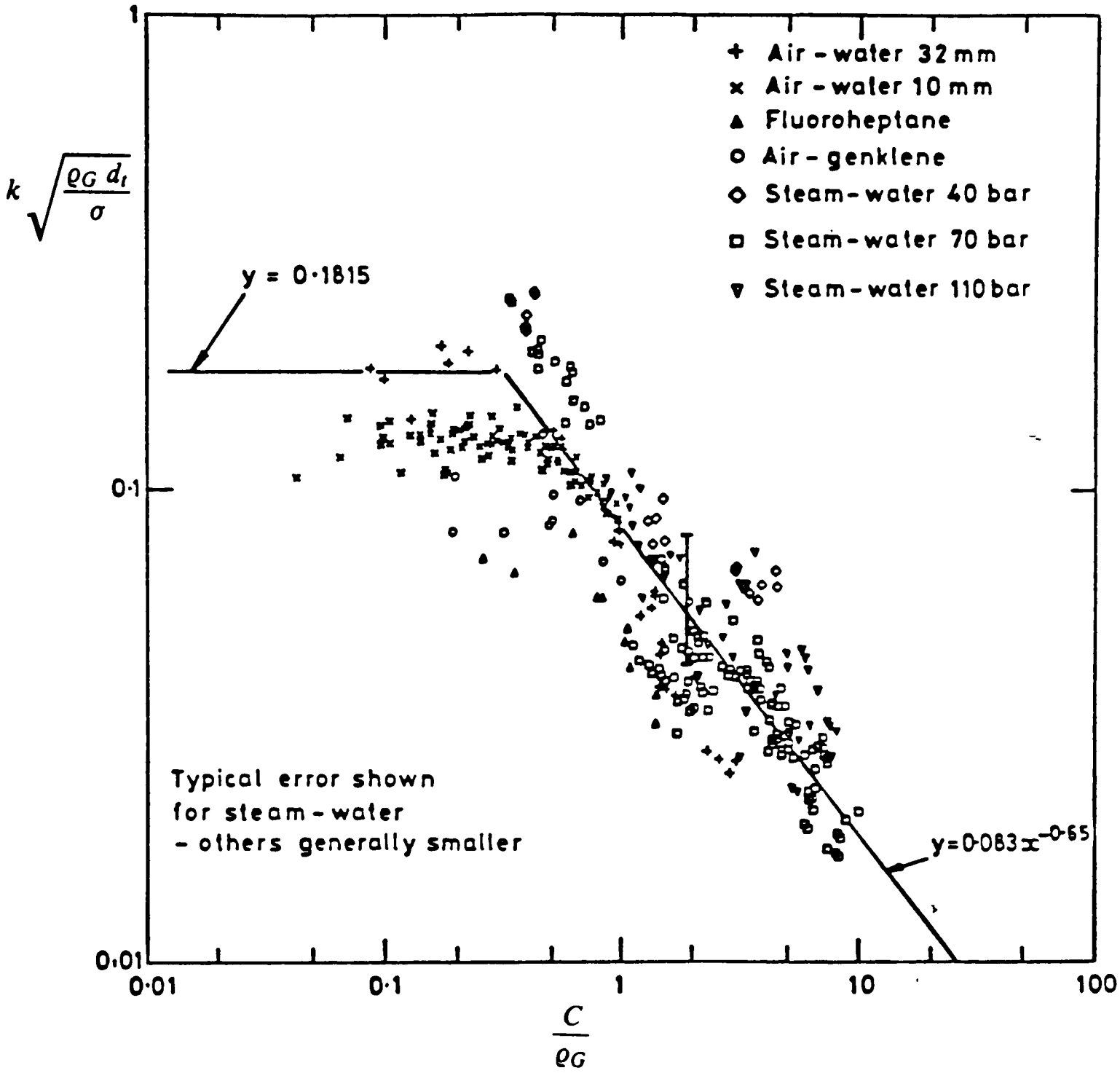

Figure 7.4 Deposition correlation (Govan (1990)).

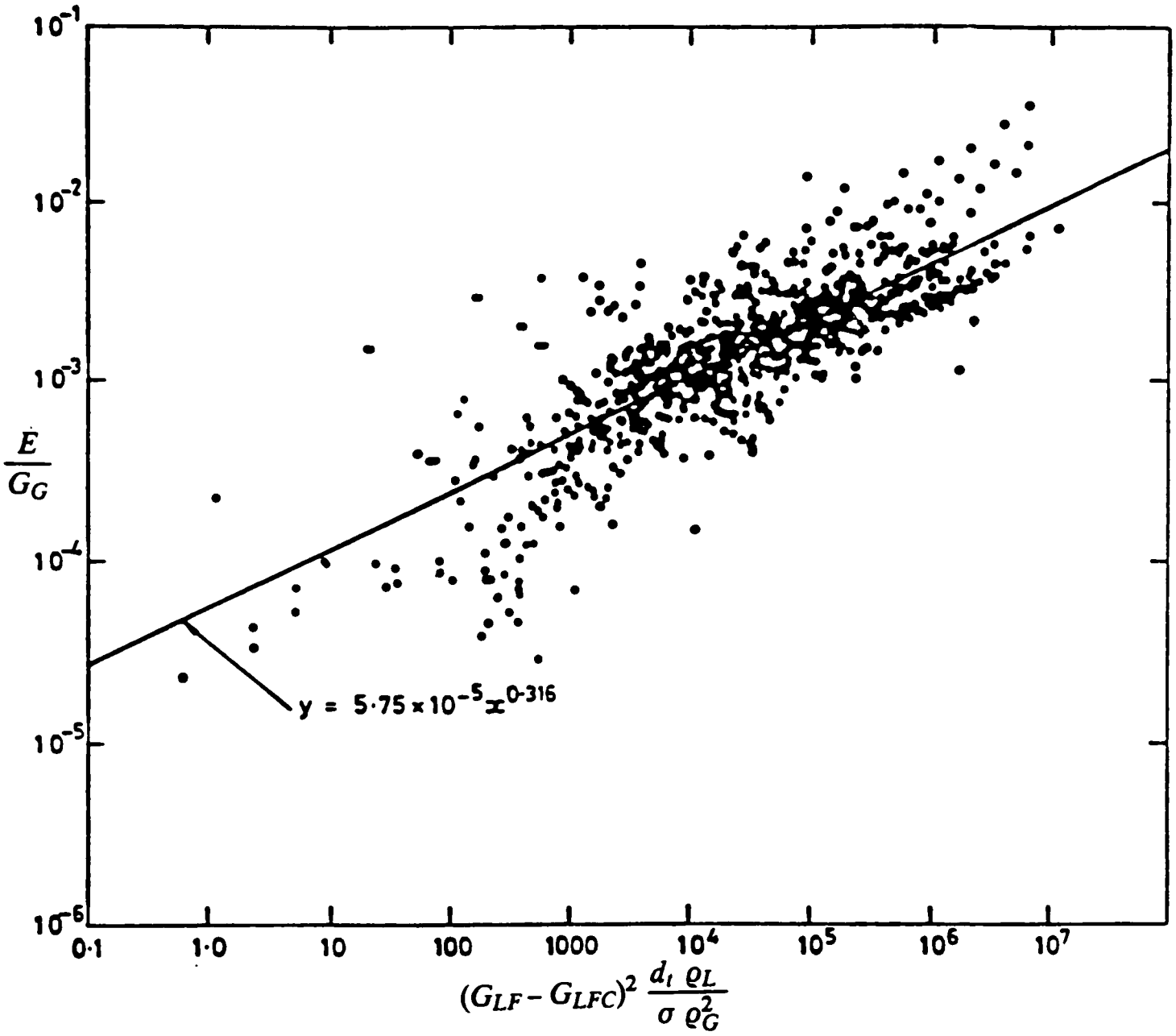

Figure 7.5 Entrainment rate correlation (Govan (1990)).

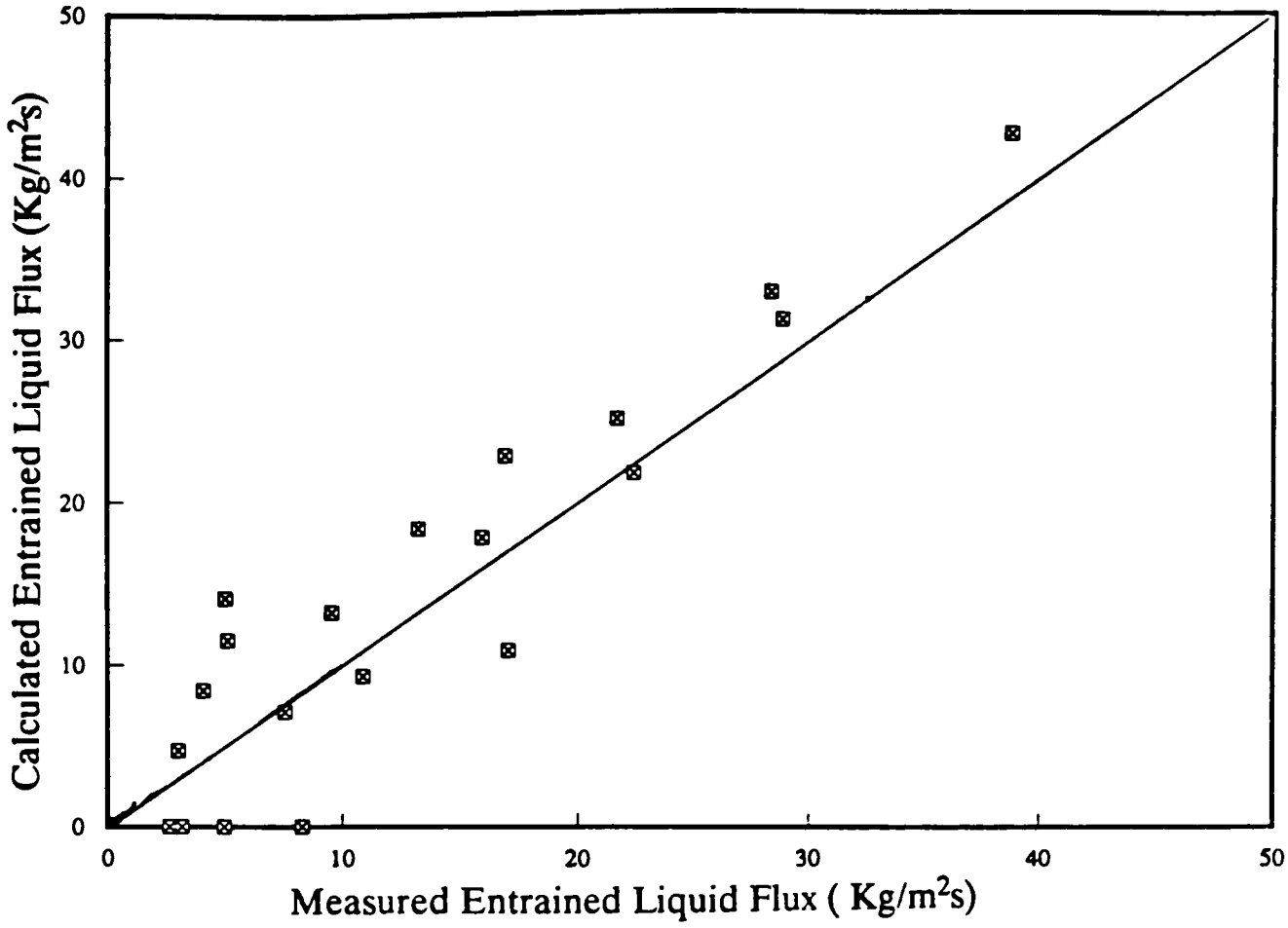

Figure 7.6 Comparison of present entrained liquid mass fluxes with the correlation of Govan (1990).

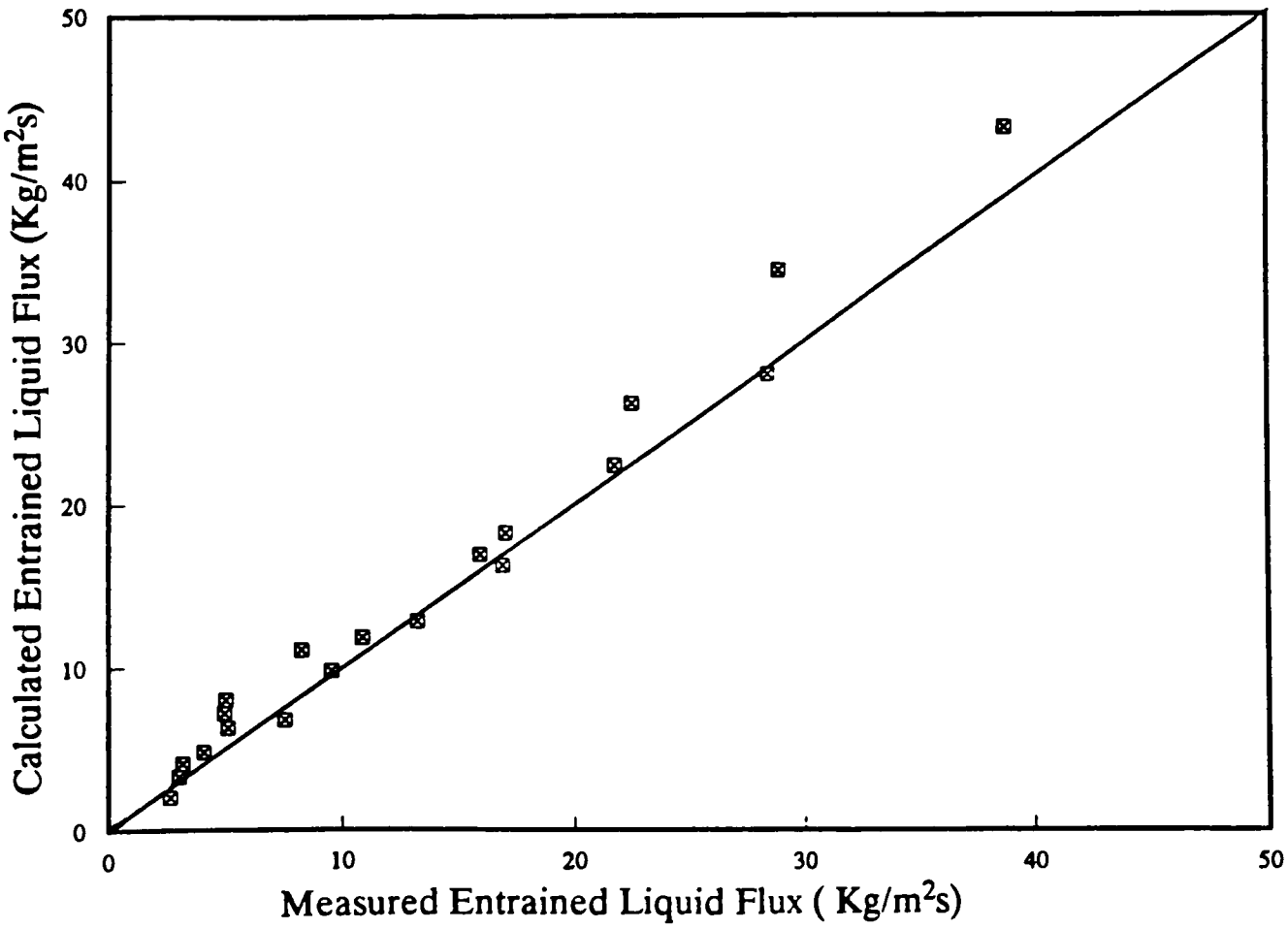

Figure 7.7 Comparison of present entrained liquid mass fluxes with the correlation of Ishii and Mishima (1981)

and Hewitt (1986) predicts a critical liquid film flux of 44.7 kg/m^{2}s for the present conditions, which is not in agreement with the experimental results obtained. For a liquid mass flux of G_L = 40 kg/m^{2}s, entrainment was measured for the whole range of gas mass fluxes studied (G_G = 60–120 kg/m^{2}s). Willets (1987) and Jepson (1992) also reported the occurrence of entrainment at G_G = 40 kg/m^{2}s. These data indicate that equation (7.4) overpredicts the critical film flow rate for the conditions of the present experiments. Jepson (1992) tested the sensitivity of the correlation of Govan (1990) to predictions in the critical liquid film. The author found that the performance of the entrainment correlation was not improved.

In chapter 4, entrainment correlations directly related to horizontal flow have been discussed. In particular, the equation of Ishii and Mishima (1981) presented in section 4.3.2., is also valid for the prediction of entrained liquid mass fluxes in vertical upflow. This correlation (equation (4.41)) was tested against the results of the present study. The comparison between measured and calculated entrained liquid mass fluxes is shown in Figure 7.7. In general, this correlation represents well the entrainment data, and gives a better performance than the correlation of Govan (1990).

7.4. Drop Size Measurements

Drop size measurements were carried out using the laser diffraction technique for air mass fluxes varying between 80–120 kg/m^{2}s, and water mass fluxes of 40–120 kg/m^{2}s. The results are tabulated in Table G.2 (Appendix G), and shown in Figure 7.8 as Sauter mean diameter versus liquid mass flux.

It is observed that the gas velocity has a strong influence on drop size, i.e., drop size decreases with increasing gas flow rate. The effect of liquid flow rate is more complex. For the lowest gas flow rate, drop size decreases slightly with increasing liquid flow. For G_G = 100 kg/m^{2}s no influence on drop size is seen. For the higher gas mass flux (G_G = 120 kg/m^{2}s) drop size increases with liquid flow rate. These trends can be linked to the different mechanisms of drop entrainment, as suggested by Azzopardi (1983), and already discussed in section 5.2.1. The decrease in drop size with increasing liquid flow is due to the predominance of ligament break-up over bag break- up. For further increases in the liquid flow rate, the size of the created drops does not change, but the observed drop size increases because coalescence occurs.

In Figure 7.9 the data reported by Jepson (1992) is compared with the results obtained in the present work. The maximum difference existing between drop sizes taken under similar conditions is 8% (see Table G.2 – Appendix G), representing a good agreement between both sets of data.

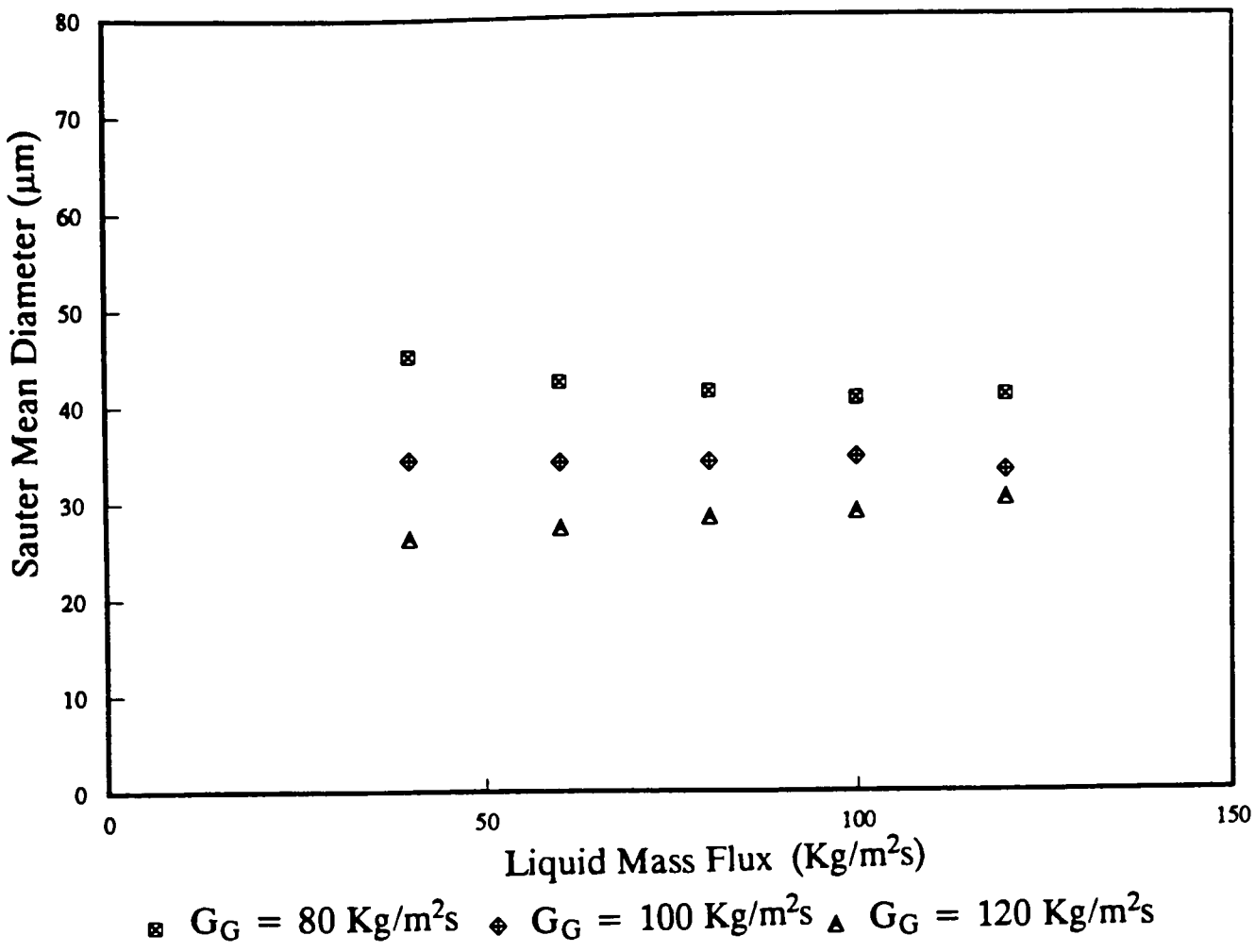

Figure 7.8 Influence of liquid mass flux on drop size.

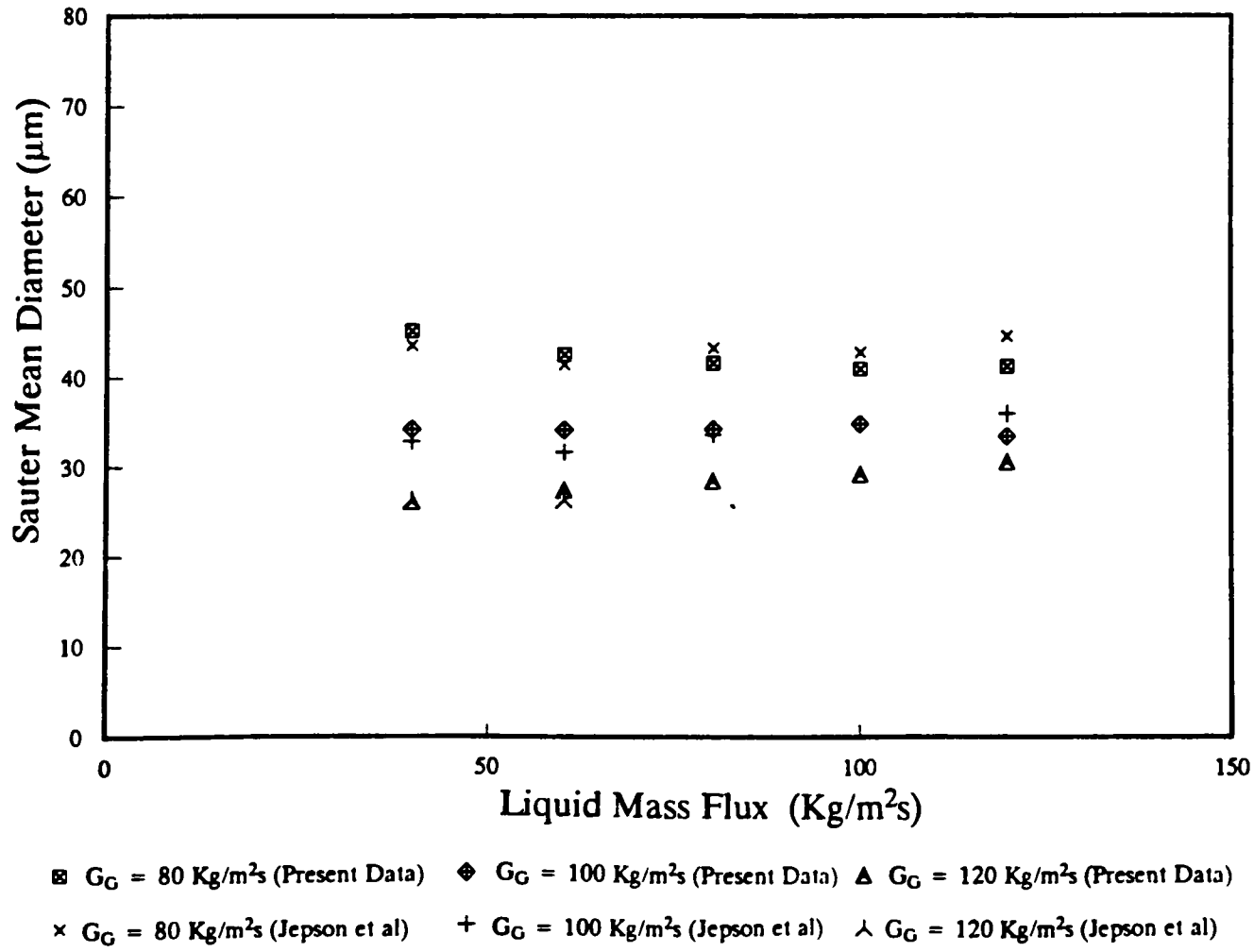

Figure 7.9 Comparison of present data with the results of Jepson (1992).

7.5. Drop Size Correlations

The experimental drop size measurements of this study were tested against some correlations already discussed in section 5.3: Azzopardi et al (1980), Azzopardi (1985), Gibbons (1985), Azzopardi et al (1989) and Ambrosini et al (1991). These correlations were chosen because they predict the Sauter mean diameter directly, and take into account various factors that can affect the drop size.

Figures 7.10 to 7.14 show the performance of the previous equations to represent the present data, as calculated mean diameter against measured mean diameter. The best correlation of the results is given by the expressions proposed by Azzopardi et al (1989) (equation (5.18)) and Ambrosini et al (1991) (equation (5.19)).

The equation of Azzopardi et al (1980) (equation (5.8)) underpredicts the results. This correlation was developed based on drop size data taken in a 0.032 m ID tube, and accounts for an increase in drop size with liquid flow rate. However, the present data only exhibit this trend for G_G = 120 kg/m^{2}s.

The correlations by Gibbons (1985) (equation (5.13)) and Azzopardi (1985) (equation (5.11)) both overpredict the measured drop sizes. Azzopardi (1985) substituted the tube diameter in the correlation by Azzopardi et al (1980), by a new parameter λ_T. The expression of Gibbons (1985) is more sensitive to tube diameter, and it can be seen that the calculated values of drop size using equation (5.13) are closer to the measured drop sizes, than the ones given by equation (5.11). Again, both equations (5.11) and (5.13) account for an increase in drop size with liquid flow rate.

As mentioned previously, the equations by Azzopardi et al (1989) and Ambrosini et al (1991) are the best to correlate the experimental results. Equation (5.18) by Azzopardi et al (1989) was based on experimental results taken in tube diameters ranging from 0.010–0.032 m for different fluid systems. It accounts for an influence of tube diameter on drop size and should be applied for flow conditions where drop size increases with liquid flow rate.

Equation (5.19) by Ambrosini et al (1991) was developed using data covering a wide range of gas and liquid flow rates, physical properties and pipe diameters. A comparison between the performance of the two equations to represent the measured drop sizes, reveals that for a gas mass flux of 120 kg/m^{2}s drop diameters are much better predicted by the expression of Azzopardi et al (1989), as seen in Figure 7.15. On the other hand, the correlation of Ambrosini et al gives a better fit when predicting the drop sizes corresponding to G_G = 80 kg/m^{2}s.

7.6. Conclusions

In this work, the laser diffraction technique has been used to obtain drop size data in vertical annular flow. These data are complemented with film flow measurements. The main conclusions can be summarized as follows:

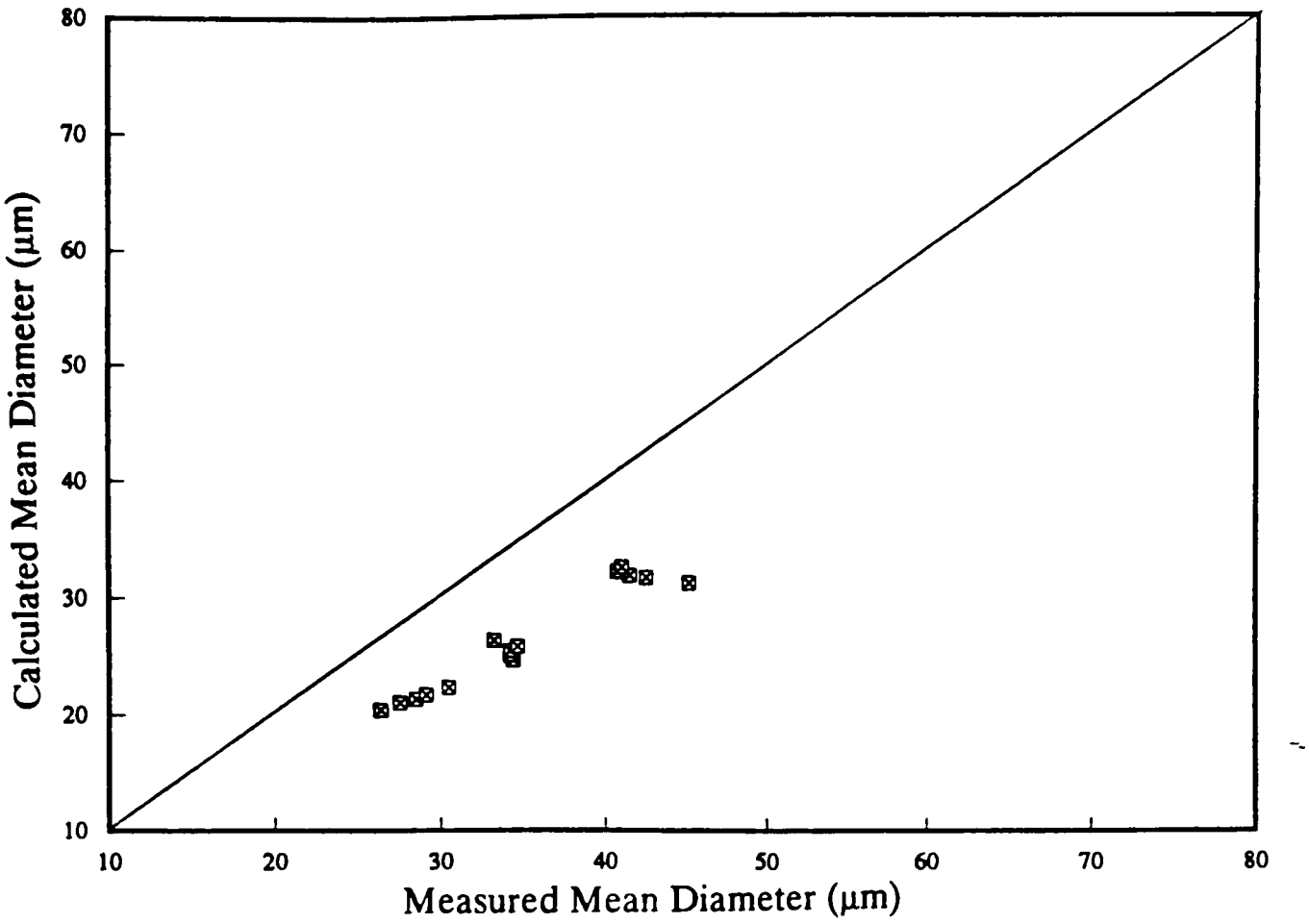

Figure 7.10 Performance of the correlation of Azzopardi (1980) to predict the drop size data of the present study.

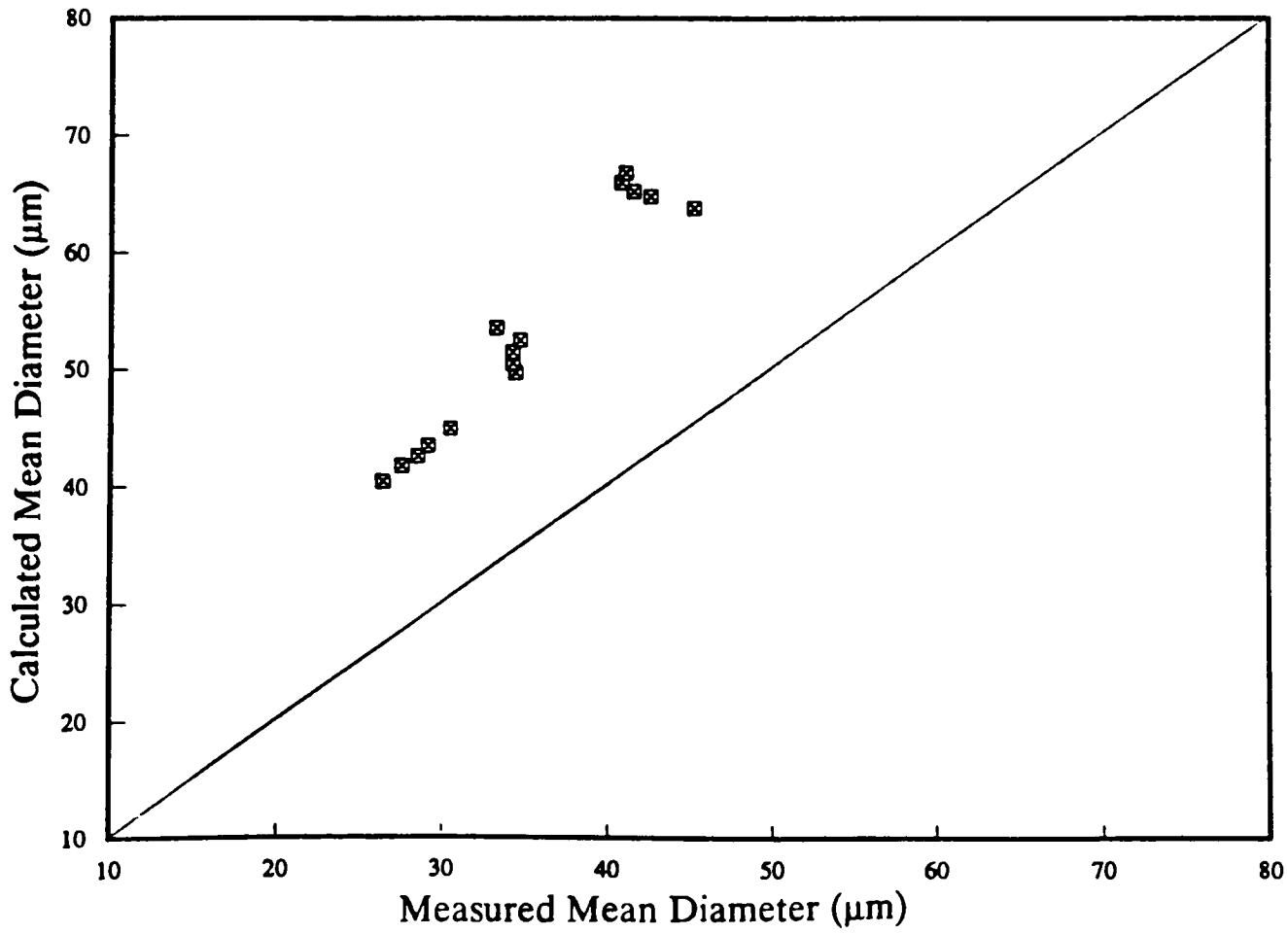

Figure 7.11 Performance of the correlation of Azzopardi (1985) to predict the drop size data of the present study.

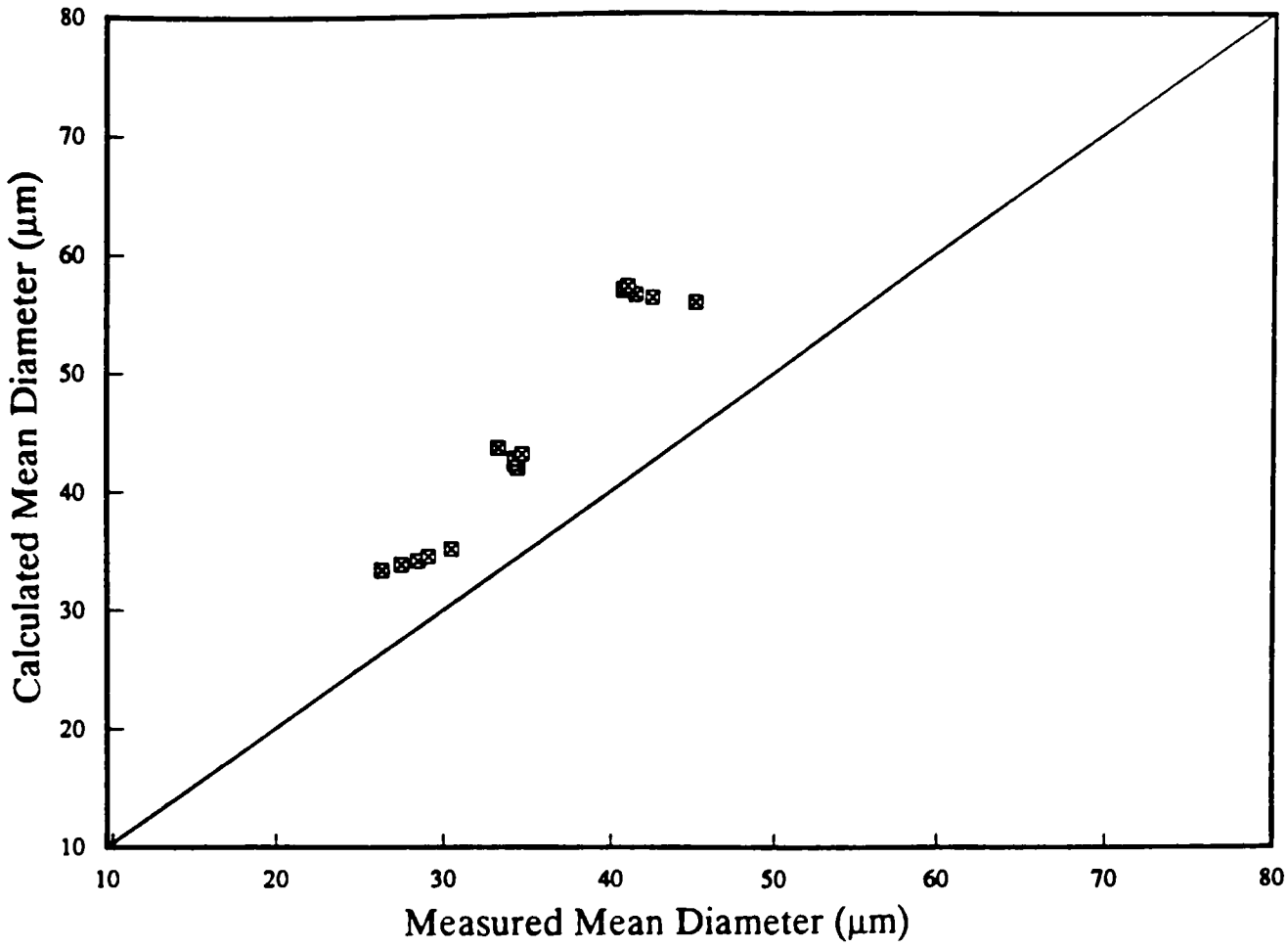

Figure 7.12 Performance of the correlation of Gibbons (1985) to predict the drop size data of the present study.

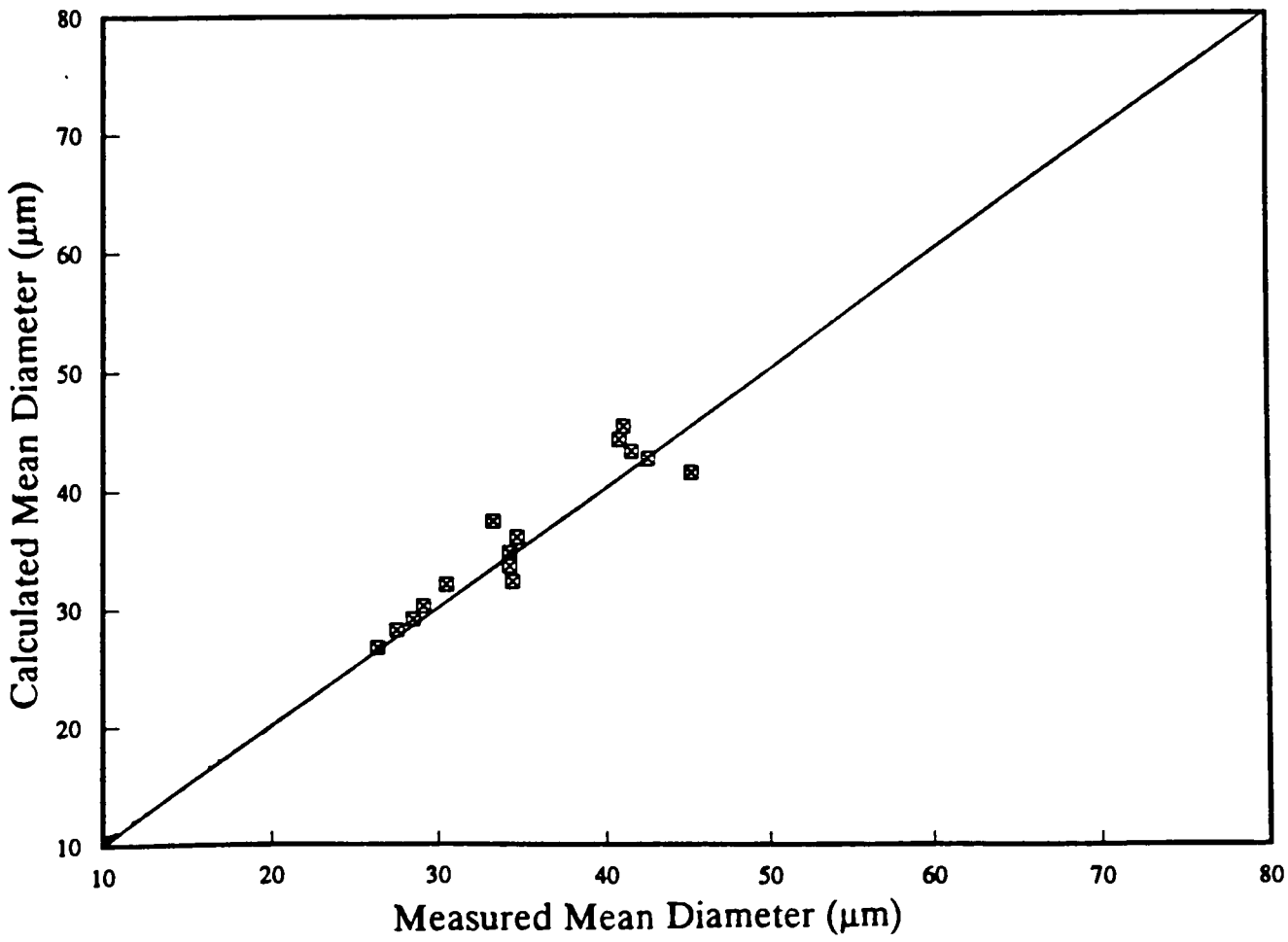

Figure 7.13 Performance of the correlation of Azzopardi et al (1989) to predict the drop size data of the present study.

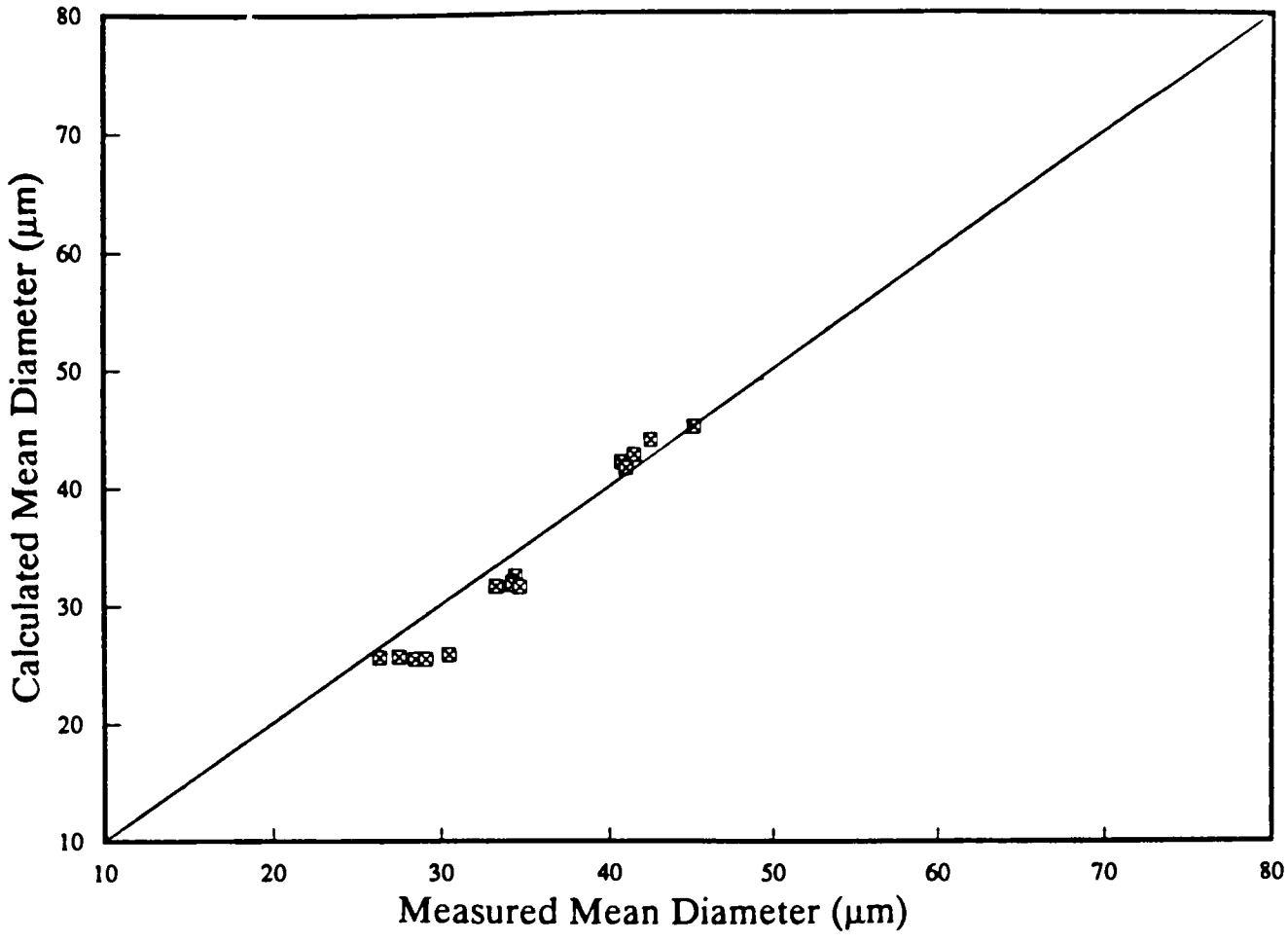

Figure 7.14 Performance of the correlation of Ambrosini et al (1991) to predict the drop size data of the present study.

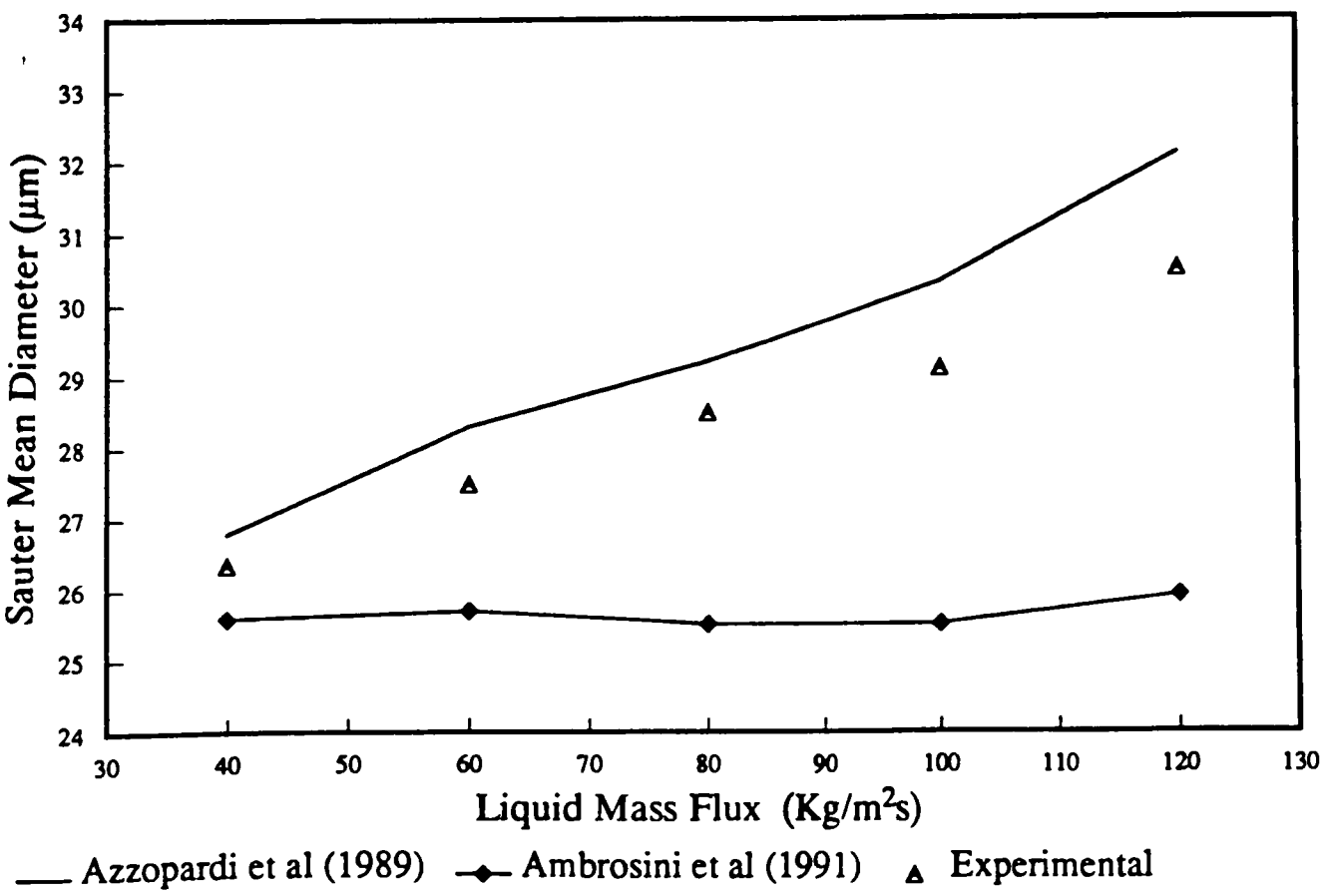

Figure 7.15 Comparative performance of drop size correlations to predict the drop size data of the present study for G_G = 120 kg/m^{2}s.

- Both gas and liquid mass flow rates have a strong influence on the entrained liquid flow rate. Above the critical film flow rate, the entrained flow rate increases directly with gas velocity. An increase in liquid flow rate increases the amount of liquid available for entrainment.
- A linear function is observed between entrained liquid flux and total liquid flux.
- The present entrainment data are well correlated by the equation of Ishii and Mishima (1981).
- For the flow conditions studied, the drop size varied between 26–45 μm.
- Drop size decreases with increasing gas mass flow rate. This can be explained because a higher gas flow increases the shearing force on the liquid surface, and so more surface deformation occurs which releases smaller drops.
- The liquid flow rate has a small influence on drop size. For the lowest gas flow rate, the drop size decreases with increasing liquid flow. For G_G = 100 kg/m^{2}s no influence on drop size is observed. For G_G = 120 kg/m^{2}s the drop size increases with increasing liquid flow. These trends can be linked to the different mechanisms of drop entrainment, as suggested by Azzopardi (1983). The decrease in drop size with increasing liquid flow is due to the predominance of ligament break-up over bag break-up. For further increases in the liquid flow rate, the size of the created drops does not change, but the observed drop size increases because coalescence occurs.
- The correlations of Azzopardi et al (1989) and Ambrosini et al (1990) perform best in fitting the drop size data of this study.
- Comparison of present drop size measurements shows good agreement with the experiments of Jepson (1992) taken under similar conditions.

8. CONCLUSIONS AND FUTURE WORK

The present investigation was concerned primarily with the study of air–water flow in a horizontal 0.032 m ID tube, and the influence of a 90° horizontal bend on the flow characteristics. Visualisation, entrainment and drop size tests were carried out in a new horizontal two–phase flow facility, before and after the 90° bend.

In the visualisation studies high speed still photography and cine films were used. The entrained mass fluxes were determined from the liquid film flow rates measured using the film removal technique, while the drop size distributions were obtained with a laser diffraction technique. Drop velocity data were extracted from the analysis of the cine films. Prior to the horizontal flow study, drop size and film flow rates were measured for air–water flow in a vertical tube 0.01026 m, employing the same techniques as in horizontal flow.

This chapter summarises the major conclusions of the present work, and points out areas where further investigation is needed.

8.1. Conclusions

8.1.1. Visualisation Studies in Horizontal Two–Phase Flow

- For the range of air–water flow rates studied, the flow patterns observed were wavy–stratified with and without atomisation, annular and pseudo–slug flow.
- During wavy–stratified flow, the fraction of wetted perimeter increased with both gas and liquid flow rates. The present experimental data are closer to the correlation of Hamersma and Hart (1987) compared to the data presented by Fukano and Ousaka (1988).
- Photographs taken before the bend showed interesting features, such as the presence of air bubbles entrained in the liquid film, and the creation of liquid drops at the crest of roll waves.
- The size of entrained air bubbles was measured from the cine film taken at G_G = 20 kg/m^{2}s and G_L = 150 kg/m^{2}s. The larger bubbles had an ellipsoid shape, while the smaller ones were almost spherical. The larger bubbles observed had an equivalent diameter of 2.47 mm.
- For the flow conditions of G_G = 10–25 kg/m^{2}s and G_L = 6.2–50 kg/m^{2}s, it was possible to identify the conditions for the onset of the entrainment of air bubbles in the liquid film.
- The present cine films showed that both mechanisms of drop entrainment (bag break–up and ligament break–up) occur in horizontal air–water flow.

- The phenomenon of film inversion reported by Banerjee et al (1967) was observed at the 90° horizontal bend.
- At the horizontal 90° bend, the liquid film was seen to have a swirl movement, in which at the upper part of the tube the liquid was pulled across from the outer wall of the bend to the top of the tube in an anti–clockwise, cork screwing fashion. In the lower half, the liquid film was drawn from the outer wall towards the bottom of the tube, in a clockwise motion. It is thought that a secondary flow existing in the gas phase can be responsible for this swirl movement of the liquid film at the bend.
- The still photographs of the drop flow taken after the bend, confirm that drop size decreased with increasing gas flow rate. These photographs also support the drop size measurements obtained with the laser diffraction technique (Chapter 5).
- The photographic work after the bend has captured evidence of drop coalescence and the subsequent separation of two drops.

8.1.2. Entrainment in Horizontal Two–Phase Flow

The experiments carried out before the bend are summarised as:

- The correlation of Ishii and Grolmes (1975) overpredicts the critical gas velocity for the onset of entrainment for the horizontal flow of an air–water system in a 0.032 m ID tube.
- At constant gas velocity, there is a linear relationship existing between the liquid film mass flux and and the liquid flow observed for the whole range of gas velocities studied.
- At constant liquid flow rate, the liquid film mass flux decreases with gas velocity except for G_L =10 kg/m^{2}s, where G_{LF} is constant with increasing gas velocity.
- For the stratified/annular flows the entrained flux increased with liquid flow rate, and in some instances a plateau condition was reached. At the lowest gas mass flux conditions (G_G = 20 kg/m^{2}s and G_G = 30 kg/m^{2}s) the quantity of entrained liquid falls considerably at the highest liquid flow of 130 kg/m^{2}s. This is due to the transition to pseudo–slug flow.
- For the whole range of flow conditions covered, G_{LE} increases with gas velocity, except for G_L = 10 kg/m^{2}s where the level of entrainment is almost constant.
- The entrained liquid flow rate in horizontal annular flow was found to be lower than in vertical flow for the same flow conditions and tube diameter (0.32 m). However, as the gas velocity increases this difference is less pronounced.

- The entrainment correlation of Williams (1986) correlated well horizontal annular flow data by Dallman (1978), Laurinat (1982), Williams (1986) and Paras and Karabelas (1991). However, it does not do so for the present measurements taken across the transition from wavy–stratified to annular flow.
- The entrainment correlation of Ishii and Mishima (1981) generally overpredicts data in horizontal two–phase flow. A change in the constant of the expression seems to improve the fit with the data from this study.

The experiments taken downstream of the bend show that:

- At constant gas flow rate, liquid film flux G_{LF} increases linearly with G_L.
- At constant liquid flow rate, G_{LF} decreases with gas velocity except for G_L = 10 kg/m^{2}s where the liquid film flow rate is almost constant.
- The curves of entrainment against liquid flow (at fixed gas mass flux) show a maximum at the low gas flow conditions. For the gas mass fluxes of G_G = 60 kg/m^{2}s and 70 kg/m^{2}s entrainment increases with G_L.
- For the flow conditions studied, G_{LE} increases with gas velocity at a constant liquid flow rate.
- Above certain flow conditions, there is an increase in film flow rate after the bend. The corresponding reduction in the amount of entrained liquid is caused by drops depositing on the outside of the bend.

8.1.3. Drop Size in Horizontal Two–Phase Flow

The following conclusions can be drawn from the measurements conducted before the bend:

- Previous work on the measurement of drop sizes in annular two–phase flow was mostly carried out in vertical flow. The limited data published on horizontal flow were obtained in rectangular channels.
- For the present experiments, the drop size data were analysed using a model independent approach. The model independent fit to the multimodal drop size distributions was always significantly better than the Rosin–Rammler and Log–normal fits.
- For the conditions of this study, the Sauter mean diameter ($\overline{D}_{32}$) varied between 60–119 μm.
- The gas velocity has a strong effect on drop size. The present data showed that the Sauter mean diameter is proportional to the superficial gas velocity raised to the power of –1.0.
- The influence of liquid flow rate is somewhat more complex. For the lower gas mass flux (G_G = 40 kg/m^{2}s), $\overline{D}_{32}$ decreased with increasing liquid flow rate. For

G_G = 50 kg/m^{2}s, the curve passed through a minimum. For the higher gas flows (G_G = 55–70 kg/m^{2}s) drop diameter increased with liquid flow rate. These trends are linked to different mechanisms of entrainment.

At low liquid flow rates the bag break–up mechanism, which produces larger drops, is thought to be dominant over the ligament break–up. As liquid flow rate increases, the entrainment mechanism changes predominantly to ligament break–up and the drop size decreases. At sufficiently high drop concentrations, the observed drop size increases with liquid flow rate due to the presence of coalescence.

- The influence of the pressure of the system on drop size was studied for G_G = 55 kg/m^{2}s and G_L = 30 kg/m^{2}s. An increase in $\overline{D}_{32}$ from 71.54 μm to 77.24 μm was observed by increasing the pressure from 1.3 bar to 1.4 bar. It is considered that this result is due to differences in gas velocity rather than changes in gas density.
- Drop size in horizontal annular flow was found to be lower than in vertical flow, for the same flow conditions and tube diameter (0.032 m). However, as the gas velocity increases this difference becomes less pronounced.
- Several existing drop size correlations were tested against the present measurements. The equations of Tatterson et al (1977) and Ishii and Kataota (1982) performed badly against the present data. The correlation of Andreussi et al (1978) generally underpredicted the drop size.
  - For gas mass fluxes of 50–70 kg/m^{2}s, the drop size correlation of Azzopardi et al (1980) gave the best fit. However, as this equation accounts for an increase in drop size with entrained liquid flow, it predicted the wrong trend for the drop sizes corresponding to G_G = 40 kg/m^{2}s.
  - The correlations of Azzopardi (1985), Gibbons (1985) and Azzopardi et al (1989) overpredicted the present results within 20%, for G_G = 50–70 kg/m^{2}s. They also predicted the wrong trend for drop sizes corresponding to G_G = 40 kg/m^{2}s.
  - For the higher gas flow rates (G_G = 50–70 kg/m^{2}s) the correlation of Ambrosini et al (1990) overpredicts the present data within 20%. However, this is the only equation that predicted the correct trend for the drop sizes obtained at a gas mass flux of 40 kg/m^{2}s.

The drop size measurements carried out after the bend can be summarised as follows:

- For all flow conditions studied, the drop size histograms were represented by a multimodal curve.
- Measured Sauter mean diameters ranged between 87–204 μm.

- For the lower gas mass fluxes (G_G = 40 kg/m^{2}s and G_G = 50 kg/m^{2}s), the drop size was almost independent of liquid flow rate. For G_G = 40 kg/m^{2}s and G_G = 50 kg/m^{2}s the drop size decreased slightly with increasing liquid flow.
- The drop size decreased with increasing gas velocity. The Sauter mean diameter was found to be proportional to the superficial gas velocity raised to the power of –1.5.
- The effect of the 90° horizontal bend on the drop size distribution was to increase the diameter of drops. Several processes taking place at the bend, such as drop coalescence may be responsible for the coarsening of the distribution. The secondary flow pattern existing in the gas phase at the bend and film inversion are thought to have also some contribution.

8.1.4. Drop Velocity in Horizontal Two–Phase Flow

- With the cine film technique used in the present work it was not possible to follow the velocity of drops from their point of creation.
- Because of the method of measurement employed and the sample size, the present results should only be regarded from a qualitative point of view.
- The radial drop velocity component measured was negligible in comparison with the axial drop velocity.
- For the flow conditions analysed, no significant correlation was found between drop size and axial drop velocity.
- Axial drop velocity increased with superficial gas velocity.
- For G_G = 20 kg/m^{2}s and liquid mass fluxes of 70 kg/m^{2}s and 90 kg/m^{2}s, no influence of the liquid flow rate on the axial drop velocity was seen. However, the increase in the spread of drop velocity towards higher values observed for G_G = 20 kg/m^{2}s and G_L = 130 kg/m^{2}s, may be due to a change in the flow regime to pseudo–slug flow.

8.1.5. Entrainment and Drop Size Measurements in Vertical Annular Flow

- Both gas and liquid mass flow rates have a strong influence on the entrained liquid flow rate. Above the critical film flow rate, the entrained flow rate increases directly with gas velocity. An increase in liquid flow rate, increases the amount of liquid available for entrainment.
- A linear function is observed between entrained liquid flux and total liquid flux.
- The present entrainment data are well correlated by the equation of Ishii and Mishima (1981).

- For the flow conditions studied, the drop size varied between 26–45 μm.
- Drop size decreases with increasing gas mass flow rate. This can be explained because a higher gas flow increases the shearing force on the liquid surface, and so more surface deformation occurs which releases smaller drops.
- The liquid flow rate has a small influence on drop size. For the lowest gas flow rate, the drop size decreases with increasing liquid flow. For G_G = 100 kg/m^{2}s no influence on drop size is observed. For G_G = 120 kg/m^{2}s the drop size increases with increasing liquid flow. These trends can be linked to the different mechanisms of drop entrainment, as suggested by Azzopardi (1983). The decrease in drop size with increasing liquid flow is due to the predominance of ligament break–up over bag break–up. For further increases in the liquid flow rate, the size of the created drops does not change, but the observed drop size increases because coalescence occurs.
- The correlations of Azzopardi et al (1989) and Ambrosini et al (1990) perform best in fitting the drop size data of this study.
- Comparison of present drop size measurements shows good agreement with the experiments of Jepson (1992) taken under similar circumstances.

8.2 Future Work

The experiments conducted in this investigation have highlighted some new features of air–water flow in a horizontal 0.032 m tube, and how it is affected by the 90° horizontal bend. Nonetheless, the picture is far from complete, and future work is required in the following areas:

- Extend the present entrainment and drop size measurements in horizontal flow to higher flow conditions, and to other fluid systems and tube diameters. Using this extended data bank, existing correlations for drop size and entrainment could then be modified and optimised.
- Use of a LDA based technique to obtain simultaneous information on drop size/velocity, and establishment of possible relationship between these two variables.
- Study of the gas phase turbulence for horizontal stratified/annular flow, and how it is affected by the presence of a bend.
- Measurement of the drop deposition at the bend, and identification of which drop sizes are preferentially deposited.
- Other points of interest include the study of local distributions of the liquid film around the bend, changing the orientation of the bend, and the use of other bends with different radii.

LIST OF SYMBOLS

B_{eq}	equivalent bubble diameter defined by equation (3.3)
B_z	bubble diameter in the z–direction
B_y	bubble diameter in the y–direction
C	drop concentration in the gas core
C'	constant in equation (4.18)
C''	constant in equation (4.25)
C_e	equilibrium concentration of drops in the gas core defined by equation (1.11)
C_D	drag coefficient given by equation (F.2)
C_X, C_N	corrections to the Rosin–Rammler parameters
C_G	gas percentage by volume defined by equation (1.4)
$\dot{D}$	deposition rate
D	drop diameter
D_b	beam diameter
D_d	detector diameter
D_{eq}	equivalent drop diameter defined by equation (3.4)
D_l	lens diameter
D_{max}	maximum drop diameter
D_{min}	minimum drop diameter
D_z	average drop diameter in the z–direction
D_y	average drop diameter in the y–direction
$\overline{D}_{mn}$	mean droplet diameter defined by equation (2.7)
$\overline{D}_{v0.5}$	volume median diameter (defined as the diameter at which 50% by volume of the material is smaller)

$\overline{D}_{v0.1}$	volume median diameter (defined as the diameter at which 10% by volume of the material is smaller)
$\overline{D}_{32}$	Sauter mean diameter (= mean diameter when m=3 and n=2)
$\overline{D}_{31}$	volume mean diameter (=mean diameter when m=3 and n=1)
d_t	hydraulic diameter
d_t^*	dimensionless hydraulic diameter defined by equation (4.31)
E	entrained liquid fraction defined by equation (4.1)
E'	energy falling on the particle
$\dot{E}$	entrainment rate
E_M	maximum entrained fraction defined by equation (4.2)
E_{th}	theoretical upper limit of the entrained fraction
E_∞	equilibrium value of the entrained fraction
F	fraction of wetted perimeter
F'	flow parameter defined by equation (5.3)
F_H	horizontal flow parameter defined by equation (E.2)
Fr	Froude number defined by equation (1.7)
Fr_L	Froude number for the liquid phase $\left(= (\varrho_L/\Delta\varrho)\left(U_{SL}^2/(\varepsilon_L^2\ g\ d_t)\right)\right)$
F_v	cumulative undersize distribution
f	lens focal length
f_i	interfacial friction factor
f_{SG}	friction factor for a smooth tube $(= 0.046\,\mathrm{Re}_G^{-0.2})$
f_v	distribution function
Ga	Galileo number $\left(= d_t^3\ \varrho_L\ (\varrho_L - \varrho_G)\ g/\mu_L^2\right)$
G_G	gas mass flux
G_L	liquid mass flux

G_{LE}	entrained liquid mass flux
G_{LF}	liquid film mass flux
G_{LFC}	critical film mass flux for the onset of entrainment
g	gravitational acceleration
h	liquid height of the stratified layer
J_1	Bessel function of first kind of order 1
J_0	Bessel function of first kind of order 0
K	parameter defined by equation (1.8)
k_A	drop atomization coefficient
k_D	deposition mass transfer coefficient
L	light energy falling on the detector
La	Laplace number $\left(= \mu_L^2/(\varrho_L\ \sigma\ d_t)\right)$
m	film thickness
$\dot{m}_G$	gas mass flow rate
$\dot{m}_L$	liquid mass flow rate
$\dot{m}_{LE}$	entrained liquid mass flow rate
$\dot{m}_{LF}$	liquid film mass flow rate
$\dot{m}_{LFC}$	critical liquid film mass flow rate
m_G^+	dimensionless film thickness defined by equation (5.24)
m_L^+	dimensionless film thickness $(= m\ U_L^+\ \varrho_L/\mu_L)$
N_μ	viscosity number defined by equation (4.8)
$\overline{N}$	distribution parameter
OB	obscuration
P	system pressure

P_M	energy dissipation per unit mass defined by equation (5.15)
PD	percentage difference between present liquid film flow rate and liquid film results of Jepson et al (1989) [= (G_{LF} - Datum)/G_{LF}]
PD'	percentage difference between the present Sauter mean diameter and drop diameter results of Jepson et al (1989) [= ($\overline{D}_{32}$ - Datum)/D_{32}]
$(dp/dz)_G$	pressure drop if the gas flows alone
$(dp/dz)_L$	pressure drop if the liquid flows alone
R	radius of curvature of the coil in equation (1.14)
Re_G	gas Reynolds number (= $G_G\ d_t/\mu_G$)
Re_L	liquid Reynolds number (= $G_L\ d_t/\mu_L$)
Re_{LF}	liquid film Reynolds number (= $G_{LF}\ d_t/\mu_L$)
Re_{LFC}	critical liquid film Reynolds number
Rep	particle Reynolds number defined by equation (F.3)
r	distance along the radius
r_p	particle radius
r_t	internal radius of the tube
S	dimensionless parameter (= $U_{SGC}\ \mu_L/\sigma$)
s_1 , s_2	radial displacement in the detector plane
T	parameter defined by equation (1.6)
T_0	time flight of a drop
T'	Malvern matrix of coefficients
U_G	actual gas velocity defined by equation (4.14)
U_G^+	gas friction velocity
U_{LE}	velocity of the entrained liquid
U_{LF}	velocity of the liquid film

U_L^+	liquid friction velocity
U_M	velocity of a gas–liquid mixture defined by equation (1.3)
U_{SG}	superficial gas velocity
U_{SGC}	critical superficial gas velocity
U_{SG}^*	dimensionless gas velocity defined by equation (4.29)
U_{SL}	superficial liquid velocity
v_{Dt}	average drop transverse velocity
v_{Dx}	radial drop velocity component in the x–direction
v_{Dy}	radial drop velocity component in the y–direction
v_{Dz}	axial drop velocity component
x	maximum distance between the sample and the lens, defined by equation (2.6)
X	Martinelli parameter defined by equation (1.5)
$\overline{X}$	distribution parameter
y^+	dimensionless distance from the wall
W	drop size distribution in equation (2.2)
We	Weber number defined by equation (5.9)
We'	Weber number defined by equation (4.37)
We_{λ_T}	Weber number defined as $(= \varrho_G \, U_{SG}^2 \, \lambda_T/\sigma)$
We^*	Weber number defined by equation (5.20)
We_c	critical Weber number
z	axial distance from the inlet

GREEK SYMBOLS

α_M	maximum scattering angle
$\Delta\varrho$	density difference $(= \varrho_L - \varrho_G)$
ε_L	liquid holdup $\left(= \left(1 + 3.57 \, (U_{SG}/U_{SL})^{0.64} \, (\varrho_G/\varrho_L)^{0.28} \, (\mu_G/\mu_L)^{0.07}\right)^{-1}\right)$

ζ	dimensionless distance defined by equation (4.40)
γ	variable defined by equation (5.4)
γ_H	variable defined by equation (E.3)
λ	parameter defined by equation (1.1)
λ'	wavelength of the incident beam
λ_T	parameter defined by equation (5.12)
μ_G	gas viscosity
μ_L	liquid viscosity
μ_W	water viscosity
ϱ_A	air density
ϱ_G	gas density
ϱ_L	liquid density
ϱ_w	water density
θ	displacement angle in equation (1.14)
σ	surface tension
σ_w	surface tension of air–water
ψ	parameter defined by equation (1.2)

SUBSCRIPTS

G	gas
L	liquid
LE	entrained liquid
LF	liquid film
LFC	critical liquid film
max	maximum value

min	minimum value

REFERENCES

AKAGAWA, K., SAKAGUCHI, T., FUJII, T., NAKATANI, T., NAKASEKO, K. and ITO, J. (1980), 'Horizontal Liquid Film-Mist Two-Phase Flow (1st Report, Concentration Distribution and Diffusivity of Entrained Liquid Droplets)', Bull. JSME, Vol.23, No. 180, pp 910-917.

AKAI, M., INOUE, A. and AOKI, S. (1977), 'Structure of a Co-Current Stratified Two-Phase Flow with Wavy Interface', Theoretical Applied Mechanics', Vol. 25, pp 445-456.

AMBROSINI, W., ANDREUSSI, P. and AZZOPARDI, B. J. (1991), 'A Physical Based Correlation for Drop Size in Annular Flow', Int. J. Multiphase Flow, Vol. 17, No. 4, pp 497-507.

ANDERSON, G. H. and HILLS, P. D. (1974), 'Two-Phase Annular Flow in Tube Bends', Symp. Multiphase Flow Systems, U. Strathclyde, 2-4 April 1974, paper No. J1, published in I. Chem. E. Symp. Series No. 38, 21 pp.

ANDREUSSI, P. and AZZOPARDI, B. J. (1982), 'Liquid Entrainment in Annular Two-Phase Flow', The 2nd Int. Conf. on Liquid Atomisation and Spray Syst., Madison, WI, USA, 20-24 Jun. 1982, Paper 8-1, pp 209-214.

ANDREUSSI, P., ROMANO G. and ZANELLI, S. (1978), 'Drop Size Distribution in Annular Flows', 1st Int. Conf. Liquid Atomisation Spray Systems Tokyo, 27-31 Aug. 1978, 8 pp.

ANDRITSOS, N. and HANRATTY, T . J. (1987), 'Interfacial Instabilities for Horizontal Gas-Liquid Flows in Pipelines', Int. J. Multiphase Flow, Vol. 13, No. 5, pp 583-603.

ARRUDA, P. J. (1970), 'Stratified-Wavy Transitions in Horizontal Two Phase Flow', M. Ch. E. Thesis, University of Delaware.

ASALI, J. C., HANRATTY, T. J. and ANDREUSSI, P. (1985), 'Interfacial Drag and Film Height for Vertical Annular Flow', AIChE J., Vol. 31, pp 895-902.

AZZOPARDI, B. J., PIEARCEY, A. and JEPSON, D. M. (1991), 'Drop Size Measurements for Annular Two-Phase Flow in a 20 mm Diameter Vertical Tube', Experiments in Fluids, Vol. 11, pp 191-197.

AZZOPARDI, B. J., TEIXEIRA, J. C. F. and JEPSON, D. M. (1989), 'Drop Sizes and Velocities in Vertical Annular Two-Phase Flow', Proc. of Int. Conf. on Mechanics of Two-Phase Flows, National Taiwan University, Taipei, Taiwan, ROC, 12-15 June 1989, National Science Foundation, USA et al (spons), R. S. Lhee, F. Durst (Ed), pp 261-266.

AZZOPARDI, B. J. (1987), 'Observations of the Drop Motion in Horizontal Annular Flow', Chemical Engineering Science, Vol. 42, No. 8, pp 2059-2062.

AZZOPARDI, B. J. (1985), 'Drop Sizes in Annular Two-Phase Flow', Experiments in Fluids, Vol. 3, pp 53-59.

AZZOPARDI, B. J. and RUSSELL, C. M. B. (1984), 'Two-Phase Flow Patterns in Horizontal Tubes at High Qualities', 14th HTFS Res. Symp., Univ. Warwick, 25 Sep 1984, paper RS538, pp 185-192.

AZZOPARDI, B. J. (1983), 'Mechanisms of Entrainment in Annular Two-Phase Flow', U.K.A.E.A. report AERE R-11068, Harwell.

AZZOPARDI, B. J., FREEMAN, G. and KING, D. J. (1980), 'Drop Sizes and Deposition in Annular Two Phase Flow', U.K.A.E.A. report AERE R-9634, Harwell.

AZZOPARDI, B. J., FREEMAN, G. and WHALLEY, P. B. (1978), 'Drop Sizes in Annular Two-Phase Flow', ASME Mtg., San Francisco, California, 10-15 Dec. 1978, 8 pp.

AZZOPARDI, B. J (1977), 'Measurement of Drop Sizes', U.K.A.E.A. report AERE R-8667, Harwell.

BAKER, O. (1954), 'Simultaneous Flow of Oil and Gas', Oil Gas J., Vol. 53, pp 185-195.

BALFOUR, J. D. and PEARCE, D. L. (1978), 'Annular Flows in Horizontal 180° Bends: Measurements of Water Flow Rate Distributions in the Film and Vapour Core', CEGB report No. CERL/RD/L/N96/78, 26 pp.

BANERJEE, S., RHODES, E. and SCOTT, D. S. (1967), 'Film Inversion of Cocurrent Two-Phase Flow in Helical Coils', AIChE Journal, Vol. 13, No. 1, pp 189-191.

BROWN, D. J. (1978), 'Disequilibrium in Annular Two-Phase Flow', Ph.D. Thesis, University of Oxford.

BUTTERWORTH, D. and PULLING, D. J. (1973), 'Film Flow and Film Thickness Measurements for Horizontal, Annular, Air-Water Flow, U.K.A.E.A. report AERE RS95, Harwell.

BUTTERWORTH, D. (1972),'Air-Water Annular Flow in a Horizontal Tubes', in Progress in Heat and Mass Transfer (ed. G. Hetsroni), Vol. 6, pp 235-251.

BUTTERWORTH, D. and PULLING, D. J. (1972), A Visual Study of Mechanisms in Horizontal, Annular, Air-Water Flow, U.K.A.E.A. report AERE M2556, Harwell.

CHAKRABARTI, P. (1976), ' Some Aspects of Annular Two-Phase Flow in a Horizontal Tube', Ph.D. Thesis, Univ. of London.

CHANG, D. R. C. (1973), 'The Generation, Movement and Deposition of Droplets in Annular Two-phase Flow', Ph.D. Thesis, University of Delaware, U.S.

CHARRON, Y. (1990), 'Liquid Film Flow Rate Experiments', AEA Technology, report AEA-APS-0047.

CONEY, M. W. E. and FISHER, S. A. (1976),'Instrumentation for Two-Phase Flow in Use on Under Developement at the Central Electricity Research Laboratories', European Two-Phase Flow Group Meeting, Paper B2.

COUSINS, L. B. and HEWITT, G. F. (1968), 'Liquid Phase Mass Transfer in Annular Two-Phase Flow: Droplet Deposition and Liquid Entrainment', U.K.A.E.A. report AERE R-5657, Harwell.

COUSINS, L. B., DENTON, W. H. and HEWITT, G.F. (1965), 'Liquid Mass Transfer in Annular Two-Phase Flow', U.K.A.E.A. report AERE R-4926, Harwell.

DALLMAN, J. C. (1978), 'Investigation of the Separated Flow Model in Annular Gas-Liquid Two-Phase Flows', Ph.D. Thesis, University of Illinois, Urbana-Champaign, USA.

DARLING, R. S. and McMANUS, H. N. (1968), 'Flow Patterns in Circular Ducts with Circumferential Variation of Roughness: a Two-Phase Flow Analogy', Dev. Mech., Vol. 5, pp 153-163.

DEAN, W. R. (1928), 'Stream-Line Motion of a Fluid in a Curved Pipe', Phil. Mag., Vol. 5, No. 30, pp 673-695.

DEAN, W. R. (1927), 'Note on the Motion of a Fluid in a Curved Pipe', Phil. Mag., Vol. 4, pp 208-223.

DEWHURST, S. J., MARTIN, S. R., JAYANTI, S. and COSTIGAN, G. (1990), 'Flow Measurements Using a 3-D LDA System in a Square Section 90° Bend, report AEA-InTec-0078.

DODGE, L. G. (1984), 'Calibration of the Malvern Particle Sizer', Applied Optics, Vol. 23, No. 14, pp 2415–2419.

EUSTICE, J. (1911), 'Experiments on Stream–Line Motion in Curved Pipes', Proc. R. Soc. (London), Ser. A, Vol. 85, pp 119–131.

FARMER, W. M. (1972), 'Measurement of Particle Size, Number Density and Velocity Using a Laser Interferometer', Appl. Opt., Vol. 11, No. 11, pp 2603–2612.

FARWAGI, S. (1983), 'Coagulation and Deposition in Dispersed Gas Liquid Flow', Ph.D. Thesis, Imperial College, London.

FELTON, P. G., HAMIDI, A. A. and AGIGAL, A. K. (1985), 'Measurement of Drop Size Distribution in Dense Sprays by Laser Diffraction', ICLASS 85, Imperial College of London, UK.

FOGWELL, T. W. and HOPE, C. B. (1987), 'Photochromic Dye Tracing Technique Applied to Stratified and Slug Flow in a Horizontal Pipe', U.K.A.E.A. report AERE R 12657, Harwell, presented at the 17th Res. Symp., City Univ., London, 22 Sept., paper RS 718, pp 345–360.

FUKANO, T. and OUSAKA, A. (1988), 'Air–Water Two–Phase Annular Flow in Near–Horizontal Tubes (Effect of Pipe Inclination on the Fundamental Parameters), JSME Int. J. Series II, Vol. 31, No. 3, pp 477–485.

GARDNER, G. C. and NELLER, P. H. (1969), 'Phase Distributions in Flow of an Air–Water Mixture Round Bends and Past Obstructions at the Wall of a 76 mm Bore Tube', Proc. Inst. Mech. Engrs., Vol. 184, PT.3C, pp 93–101.

GARNER, F. J., ELLIS, S. R. M. and LACEY, J. A. (1954), 'The Size Distribution and Entrainment of Drops', Trans. Inst. Chem. Engrs., Vol. 32, pp 222–235.

GEORGE, K. K. (1971), 'Two–Phase Flow in 180° Return Bends – High Speed Cine Film', U.K.A.E.A. report AERE M–2459, Harwell.

GIBBONS, D. B. (1985), 'Drop Formation in Annular Two–Phase Flow', Ph.D. Thesis, University of Birmingham.

GOVAN, A. H. (1990), 'Modelling of Vertical Annular and Dispersed Two–Phase Flow', Ph.D. Thesis, Imperial College, University of London.

GOVIER, G. W. and OMER, M. M. (1962), 'The Horizontal Pipeline Flow of Air–Water Mixtures, Can. J. Chem. Eng., Vol. 40, No. 93, pp 93–104.

GREEN, J. R. and MARGERISON, D. (1978), 'Statistical Treatement of Experimental Data', Elsevier Scientific Publishing Company, Amsterdam.

GRIFFITH, P. and SNYDER, G. A. (1964), 'The Bubble–Slug Transition in a High Velocity Two–Phase Flow', Mass Int. Technol. report No. 5003–29, 20 pp.

GUEVARA, E. and GOTHAM, D. H. T. (1983), 'Entrainment in Condensing Annular Flow', Int. J. Multiphase Flow, Vol. 9, No. 4, pp 411–419.

HAMERSMA, P. J. and HART, J. (1987), 'A Pressure Drop Correlation for Gas/Liquid Pipe Flow with a Small Liquid Holdup', Chemical Engineering Science, Vol. 42, No. 5, pp 1187–1196.

HANRATTY, T. J. and ENGEN, J. M. (1957), 'Interaction Between a Turbulent Air Stream and a Moving Water Surface', AIChE J., Vol. 3, No. 3, pp 299–304.

HEWITT, G. F. (1982), 'Flow Regimes', in Handbook of Multiphase Systems (ed. G. Hetsroni), pp 2–3/2–43, McGraw–Hill, New York.

HEWITT, G. F. (1978–a), 'Liquid Mass Transport in Annular Two–Phase Flow', Int. Seminar Momentum Heat and Mass Transfer in Two–Phase Energy and Chemical Systems, Dubrovnik, Yugoslavia, 4–9 Sept. 1978, Spons. ICHMT, 30 pp.

HEWITT, G.F. (1978–b), 'Measurement of Two Phase Flow Parameters', Academic Press, London.

HEWITT, G. F. and LOVEGROVE, P. C. (1976), 'Experimental Methods in Two–Phase Flow Studies', AERE report to EPRI, January, 244 pp.

HEWITT, G. F. and HALL–TAYLOR, N. S. (1970), 'Annular Two–Phase Flow', Pergamon Press, Oxford.

HEWITT, G. F. and ROBERTS, D. N. (1969), 'Studies of Two–Phase Flow Patterns by Simultaneous X–Ray and Flash Photography', U.K.A.E.A. report AERE M 2159, Harwell.

HOOGENDOORN, C. J. (1959), 'Gas–Liquid Flow in Horizontal Pipes', Chem. Eng. Sci., Vol. 8, pp 205–217.

HSU, Y. Y., SIMONEAU, R. J., SIMON, F. F. and GRAHAM, R. W. (1969), 'Photographic and Other Optical Techniques for Studying Two–Phase Flow', 11th National ASME/AICHE Heat Transfer Conf., Minneapolis, Minnesota, 3–6 August 1969, pp 1–23.

HUTCHINSON, P. and WHALLEY, P. B. (1972), 'A Possible Characterization of Entrainment in Annular Flow', U.K.A.E.A. report AERE R–7126, Harwell.

ISHII, M. and MISHIMA, K. (1981), 'Correlation for Liquid Entrainment in Annular Two–Phase Flow of Low Viscous Fluid', K. Argonne Nat. Lab., Il., USA, Rep. ANL/RAS/LWR 81–2, 39 pp.

ISHII, M. and GROLMES, M. A. (1975),'Inception Criteria for Droplet Entrainment in Two-Phase Concurrent Gas-Liquid Flow', AIChE J., Vol. 21, No. 2, pp 308-318.

JAMES, P. W., HEWITT, G. F. and WHALLEY, P. B. (1980), 'Droplet Motion in Two-Phase Flow', U.K.A.E.A. report AERE R-9711, Harwell.

JAYANTI, S. (1990), 'Contribution to the Study of Non-Axisymmetric Flows', Ph.D. Thesis, Imperial College, University of London.

JEPSON, D. M. (1992), 'Vertical Annular Flow, the Effects of Physical Properties', D.Phil. Thesis, University of Oxford.

JEPSON, D. M., AZZOPARDI, B. J. and WHALLEY, P. B. (1990), 'The Effect of Physical Properties on Drop Size in Annular Flow', 9th Int. Heat Transfer Conf., Jerusalem, Vol. 6, pp 95-100.

JEPSON, D. M., AZZOPARDI, B. J. and WHALLEY, P. B. (1989), 'The Effect of Gas Properties on Drops in Annular Flow', Int. J. Multiphase Flow', Vol. 15, No. 3, pp 327-339.

KATAOKA, I., ISHII, M. and MISHIMA, K. (1983), 'Generation and Size Distribution of Droplet in Annular Two-Phase Flow', J. Fluids Eng., Vol. 105, No. 2, pp 230-238.

KINNEY, G. R., ABRAMSON, G. R. and SLOP, J. L. (1952), 'Internal-Liquid-Film-Cooling Experiments with Air-Stream Temperatures to 2000°F in a 2 and 4-Inch-Diameter Horizontal Tubes', Nat. Advisory Committee for Aeronautics, report No. 1087, 20 pp.

KITSCHA, J., CHANG, C. T. and KOCAMUSTAFAOGULLARI, G. (1990), 'Characteristics of Horizontal Annular Two-Phase Flow Determined by Experimental Techniques', Proc. 9th Int. Heat Transfer Conf., Jerusalem, Israel, 19-24 Aug. 1990, G. Hetsroni et al (Ed.), Hemisphere Pub. Corp., Vol. 6, pp 15-21.

KOSKY, P. G. (1971), 'Thin Liquid Films Under Simultaneous Shear and Gravity Forces', Int. J. Heat Mass Transfer, Vol. 14, pp 1120-1224.

LAPPLE, C. E. and SHEPHERD, C. B. (1940), 'Calculation of Particles Trajectories', Industrial and Engineering Chemistry, Vol. 32, pp 605-617.

LAURINAT, J. E., HANRATTY, T. J. and DALLMAN, J. C. (1984), 'Pressure Drop and Film Height Measurements for Annular Gas-Liquid Flow', Int. J. Multiphase Flow, Vol. 10, No. 3, pp 341-356.

LAURINAT, J. E. (1982), 'Studies of the Effects of Pipe Size on Horizontal Annular Two-Phase Flows', Ph.D. Thesis, University of Illinois, Urbana.

LIN, P. Y. and HANRATTY, T. J. (1987), 'Effect of Pipe Diameter on Flow Patterns for Air-Water Flow in Horizontal Pipes', Int. J. Multiphase Flow, Vol. 13, No. 4, pp 549-563.

LINÉ, A., MASBERNAT, L., MIRÉ, A. and SOUALMIA, A. (1991), 'Analysis of the Local Structure of Co-Current Stratified Two-Phase Flow, European Two-Phase Flow Group Meeting, Rome, Italy, 27-29 May, Paper K2, 14 pp.

LINDSTED, R. D., EVANS, D. L., GASS, J. and SMITH, R. V. (1978), Droplet and Flow Pattern Data, Vertical Two-Phase (Air-water) Flow Using Axial Photography', Whicita State University, Department of Mechanical Engineering.

LOPES, J. C. B. and DUKLER, A. E. (1985), 'Droplet Sizes, Dynamics and Deposition in Vertical Annular Flow', U. S. Nuclear Regulatory Commission Washington D. C., Usa, Report NUREG/CR-4424.

MANDHANE, J. M., GREGORY, G. A. and AZIZ, K. (1974), 'A Flow Pattern Map for Gas-Liquid Flow in Horizontal Pipes', Int. J. Multiphase Flow, Vol. 1, No. 4, pp 537-551.

MADDOCK, C., LACEY, P. M. C. and PATRICK, M. A. (1974), 'The Structure of Two-Phase Flow in a Curved Pipe', Symp. Multiphase Flow Systems, U. Strathclyde, 2-4 April 1974, Paper No. J2, Published in I. Chem. E. Symp. Series No. 38, 22 pp.

McCOY, D. D. and HANRATTY, T. J. (1977), 'Rate of Deposition of Droplets in Annular Two-Phase Flow', Int. J. Multiphase Flow, Vol. 3, No. 4, pp 319-331.

MISHIMA, K. and MICHIYOSHI, I. (1987), 'Boundary of Two-Phase Annular Flow in a Horizontal Duct', Annu. Rep. Res. Reactor Inst. Kyoto Univ., Vol. 20, pp 58-65.

MOECK, E. O. (1969), 'Measurement of Liquid Film Flow and Wall Shear Stress in Two-Phase Flow, 11th Heat Transfer Conference, 3-6 Aug. 1969, Minneapolis, Minnesota, pp 36-46.

MUGELE, R. A. and EVANS, H. D. (1951), 'Droplet Size Distribution in Sprays', Industrial and Engineering Chemistry, Vol. 43, No. 6, pp 1317-1324.

NAMIE, S. and UEDA, T. (1972), 'Droplet Transfer in Two-Phase Annular Mist Flow (Part 1, Experiment of Droplet Transfer Rate and Distributions of Droplet Concentration and Velocity), Bulletin of the JSME, Vol. 15, No. 90, pp 1568-1580.

NEGUS, C. R. and DRAIN, L. E. (1982), 'Mie Calculations of the Scattered Light from a Spherical Particle Transversing a Fringe Pattern Produced by Two Intersecting Laser Beams', J. Phys. D. Appl. Phys., Vol.15, pp 375–402.

NEWITT, D. M., DOMBROWSKI, N. and KNELMAN, F. H. (1954), 'Liquid Entrainment, 1. The Mechanism of Drop Formation from Gas or Vapour Bubbles', Trans. Inst. Chem. Engrs., Vol. 32, pp 244–261.

NIGMATUILIN, B. I., MARKOVICH, E. E., GUGUCHKIN, V. V. and VASILIEV, N. I. (1986), 'Investigation of Droplet–Liquid Interaction in Annular–Dispersed Flow', Heat Transfer 1986 (Proc. 8th Heat Transfer Conf., San Francisco, CA, USA, 17–22 Aug. 1986), C.L. et al (Ed), Hemisphere Pub. Corp., Vol. 5, pp 2295–2299.

NIGMATUILIN, B. I. (1984), 'Post Burntout Dispersed Steam–Droplet Flow in Heated Channels', Int. Symp. on Two Phase Annular and Dispersed Flows, University of Pisa, Italy, June (1984).

OWEN, D. G. (1986), 'An Experimental and Theoretical Analysis of Equilibrium Annular Flows', Ph.D. Thesis, University of Birmingham.

OWEN, D. G. and HEWITT, G. F. (1986), 'A Proposed Entrainment Correlation', U.K.A.E.A., report AERE R–12279, Harwell, presented at 16th HTFS Res. Symp., Heriot–Walt Univ., 16 Sep. 1986, Paper RS 648, pp 239–250.

PALEEV, I. I. and FILIPPOVICH, B. S. (1966), 'Phenomena of Liquid Transfer in Two–Phase Dispersed Annular Flow', Int. J. Heat and Mass Transfer, Vol. 9, pp 1089–1093.

PARAS, S. V. and KARABELAS, A. J. (1991), 'Droplet Entrainment and Deposition in Horizontal Annular flow', Int. J. Multiphase Flow, Vol. 17, No. 4, pp 455–468.

PARAS, S. V. and KARABELAS, A. J. (1990–a), 'Wave Characteristics of the Liquid Layer in Horizontal Annular Flow', Phase Interface Phenomena in Multiphase Flow, ICHMT Seminar, Dubrovnik, Yugoslavia, 14–18 May 1990, Paper B8, 10 pp.

PARAS, S. V. and KARABELAS, A. J. (1990–b), 'Droplet Concentration Distribution in Horizontal Annular Flow', European Two–Phase Flow Group Mtg., Varese, Italy, 21–23 May 1990, Paper C3, 15 pp.

RAO, K.V. L. (1978), 'Liquid Nitrogen Cooled Sampling Probe for the Measurement of Spray Drop Size Distribution In Moving Liquid–Air Sprays', Proceedings of the 1st Int. Conf. on Liquid Atomisation and Sprays Systems, Tokyo, 1978, pp 293–300.

ROSIN, P. and RAMMLER, E. (1933), 'The Laws Governing the Finess of Powdered Coal', Inst. of Fuel, Vol. 7, 29 pp.

ROSSON, H. F. and MEYERS, J. A. (1965), 'Point Values of Condensing Film Coefficients inside a Horizontal Pipe', Chem. Eng. prog. Symp. Series, Vol. 61, No. 59, pp 190-199.

RUSSELL, D. W. F. and ROGERS, R. W. (1972), 'Droplet Behaviour in Horizontal Gas-Liquid Flow', AIChE Meeting, Multiphase Flow in Pipes, Dallas, Texas, Feb. 1972.

SCOTT, D. S. (1963), 'Properties of Co-Current Gas-Liquid Flow', In Advances in Chemical Engineering, Vol. 4, pp 199-277.

SEKOGUCHI, K., OUSAKA, A., FUKANO, T. and MORIMOTO, T. (1982), 'Air-Water Annular Two-Phase Flow in a Horizontal Tube (1st Report, Circumferencial Distribution of Film Thickness)', Bull. JSME, Vol. 25, No. 208, pp 1559-1566.

SEKOGUCHI, K., SATO, Y. and KARIYASAKI, A. (1968), 'The Influences of Mixers, Bends, and Exit Sections on Horizontal Two-Phase Flow', Int. Symposium on Research in Cocurrent Gas-Liquid Flow, University of Waterloo, Canada, Sept. 1968.

STEEN, D. A. and WALLIS, G. B. (1964), 'The Transition from Annular to Annular-Mist Concurrent Two-Phase Downflow', AEC report NYO-3114-2.

STUIVER, W. (1955), 'Two-Phase Fluid Flow, Flow through Bends and Preliminary Study of Pressure Drop along Pipes', DPL New Zealand, Report R.257, 32 pp.

SWITHENBANK, J., BEER, J. M., TAYLOR, D. S., ABBOT, D. and McCREATH, G. C. (1976), 'A Laser Diagnostic for the Measurement of Droplet and Particle Size Distribution', Department of Chemical Engineering and Fuel Technology, Sheffield University, report No. AD AO21/30.

TAITEL, Y. and DUKLER, A. E. (1976), 'A Model for Predicting Flow Regime Transitions in Horizontal and Near Horizontal Gas-Liquid Flow', AIChE J., Vol. 22, No. 1, pp 47-55.

TATTERSON, D. F., DALLMAN, J. C. and HANRATTY, T. J. (1977), 'Drop Size in Annular Gas-Liquid Flow', AIChE J., Vol. 23, pp 69-75.

TATTERSON, D. F. (1975), 'Rates of Atomization and Drop Size in Annular Two-Phase Flow', Ph.D. Thesis, University of Illinois, Urbana, Illinois.

TEIXEIRA, J. C. F. (1988), 'Turbulence in Annular Two-Phase Flow', Ph.D. Thesis, University of Birmingham.

UEDA, T. (1979), 'Entrainment Rate and Size of Entrained Droplets in Annular Two-Phase Flow', Bulletin of the JSME, Vol. 22, No. 171, pp 1258-1265.

VAN ROSSUM, J. J. (1959), 'Experimental Investigation of Horizontal Liquid Films, Wave Formation, Atomisation, Film Thickness', Chem. Engng. Sci., Vol. 11, pp 35-52.

WEISMAN, J. (1979), 'Flow Pattern Identification in Concurrent Vapour-Liquid Flow', Proc. Japan-US Seminar Two Phase Flow Dynamics, Inter-University Seminar House, Kansai, Japan.

WHALLEY, P. B. (1987), 'Boiling, Condensation and Gas-Liquid Flow', Oxford Engineering Science Series 21, Oxford Science Publications.

WHALLEY, P. B. (1980), 'Air-Water Flow in a Helically Coiled Tube', Int. J. Multiphase Flow, Vol. 6, No. 4, pp 345-356.

WHALLEY, P .B., HEWITT, G. F. and TERRY, J. W. (1979), 'Photographic Studies of Two-Phase Flow Using a Parallel Light Technique', U.K.A.E.A. report AERE R-9389, Harwell.

WHALLEY, P. B., AZZOPARDI, B. J., PSHYK, L. and HEWITT, G. F. (1977), 'Axial View Photography of Waves in Annular Two-Phase Flow', European Two-Phase Flow Group Mtg., Grenoble, Paper No. A5, 6-9 June 1977, 26 pp.

WHALLEY, P. B., HEWITT, G. F. and HUTCHINSON, P. (1973), 'Experimental Wave and Entrainment Measurements in Vertical Annular Two-Phase Flow', U.K.A.E.A. report AERE R-7521, Harwell.

WICKS, M. and DUKLER, A. E. (1966), 'In Situ Measurements of Drop Size Distribution in Two-Phase Flow: a New Method for Electrically Conducting Liquids', Paper presented at the Int. Heat and Mass Transfer Conference, Chicago, Ill.

WICKS, W. and DUKLER, A. E. (1960), 'Entrainment and Pressure Drop in Concurrent Gas-Liquid Flow: I. Air-Water in Horizontal Flow', AIChE J., Vol. 6, No. 3, pp 463-468.

WILKES, N. S., AZZOPARDI, B. J. and WILLETTS, I. (1982), 'Drop Motion and Deposition in Annular Two-Phase Flow', U.K.A.E.A. report AERE R-10571, Harwell,

presented at 12th HTFS Res. Symp., Univ. Warwick, 14 Sep. 1982, Paper RS 425, pp 252-263.

WILLETTS, I. P. (1987), 'Non-Aqueous Annular Two-Phase Flow', D.Phil. Thesis, Jesus College, Univ. Oxford.

WILLIAMS, L. R. (1986), 'Entrainment Measurements in a 4-inch Horizontal Pipe', M.Sc. Thesis, University of Illinois, Urbana-Champaign, USA.

WOODMANSEE, D. E. and HANRATTY, T. J. (1969), 'Mechanism for the Removal of Droplets from a Liquid Surface by a Parallel Air Flow', Chem. Engng. Sci., Vol. 24, pp 299-307.

Appendix A

CALIBRATIONS

CONTENTS

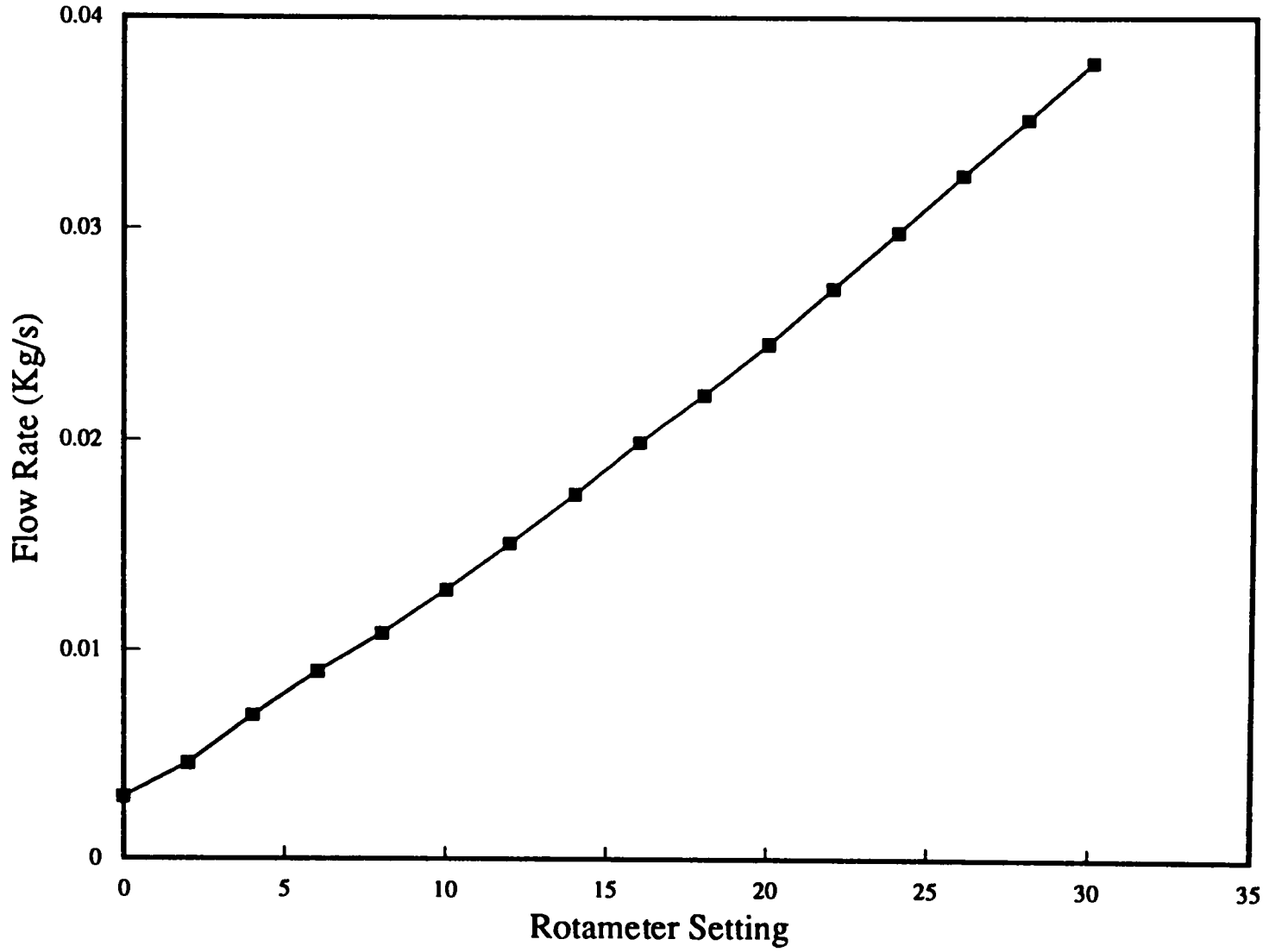

Figure A.1 Calibration curve of rotameter FI1

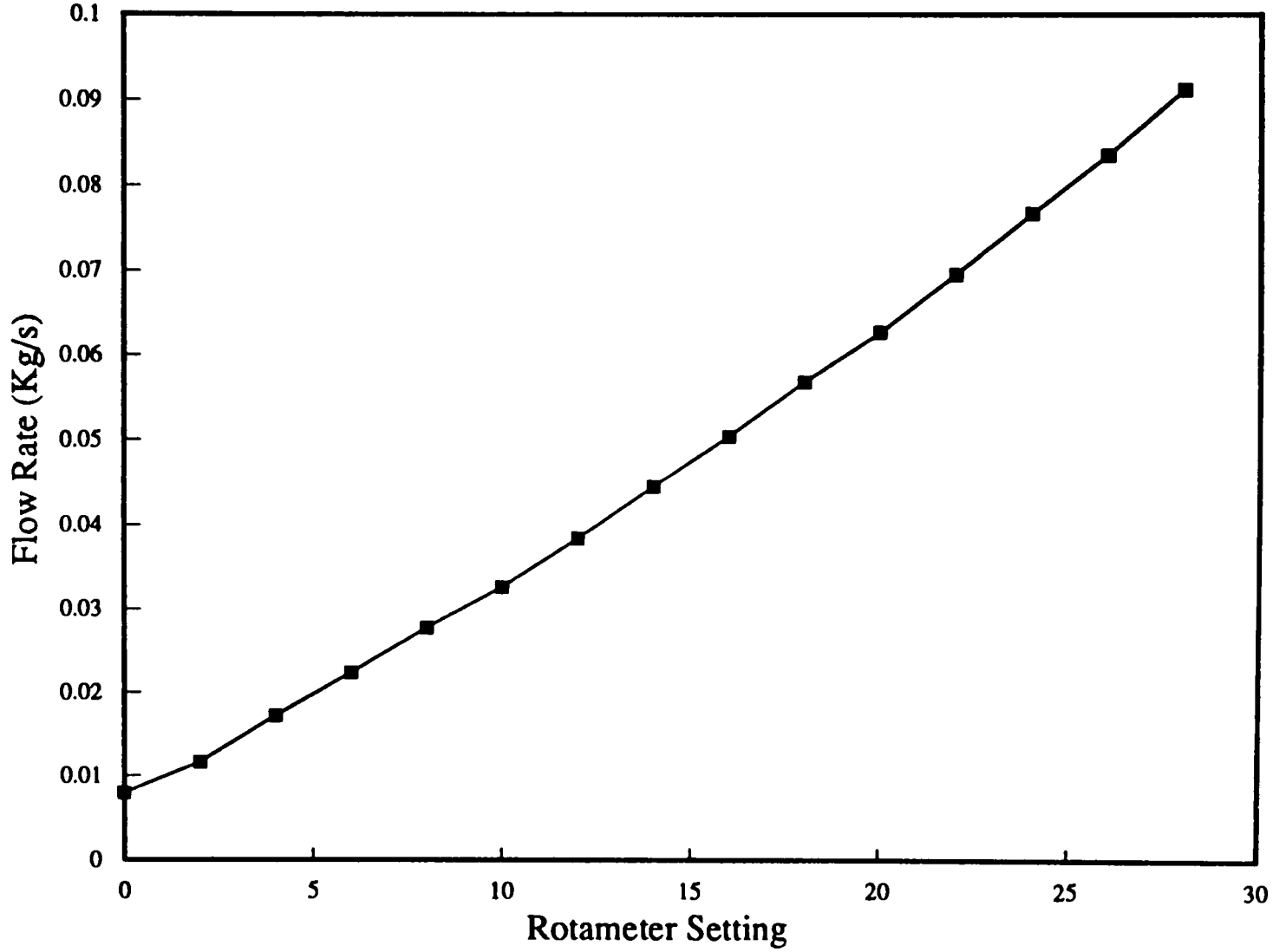

Figure A.2 Calibration curve of rotameter FI2

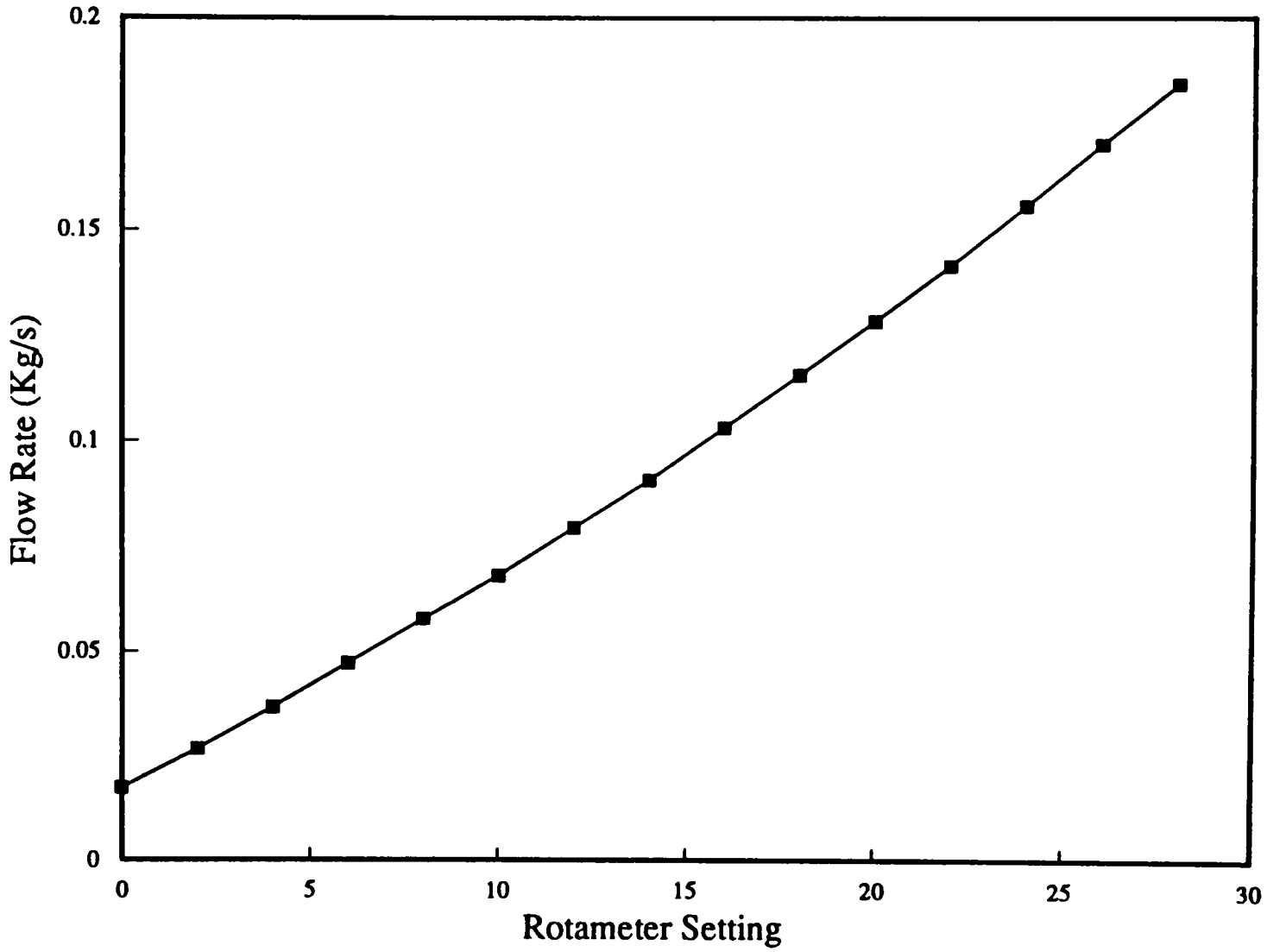

Figure A.3 Calibration curve of rotameter FI3

Appendix B

EXPERIMENTAL RESULTS FOR HORIZONTAL TWO-PHASE FLOW

CONTENTS

Table B.18 Drop size measurements after the bend

Table B.19 Raw data referring to drop sizes after the bend

TABLE B.1 PRESSURE DROP MEASUREMENTS IN SINGLE PHASE (test tube near the bend and tappings located at 45° from the top of the tube to the inside of the bend).

Tappings	G_G (kg/m²s)	Δz (m)	Distance from the Bend (m)	dP/dz (N/m²/m)
1-3	10	0.10	0.105	33.8
3-5		0.10	0.205	26.3
5-7		0.10	0.305	30.0
7-9		0.10	0.405	30.0
9-11		0.10	0.505	30.0
11-13		0.10	0.605	31.9
13-16		0.15	0.730	30.0
16-18		0.10	0.855	30.0
1-3	20	0.10	0.105	113.1
3-5		0.10	0.205	86.3
5-7		0.10	0.305	101.3
7-9		0.10	0.405	102.5
9-11		0.10	0.505	106.3
11-13		0.10	0.605	113.1
13-16		0.15	0.730	101.7
16-18		0.10	0.855	99.4
1-3	30	0.10	0.105	217.5
3-5		0.10	0.205	158.8
5-7		0.10	0.305	190.0
7-9		0.10	0.405	191.9
9-11		0.10	0.505	199.4
11-13		0.10	0.605	212.5
13-16		0.15	0.730	190.4
16-18		0.10	0.855	185.0
1-3	40	0.10	0.105	341.9
3-5		0.10	0.205	246.3
5-7		0.10	0.305	295.0
7-9		0.10	0.405	299.4
9-11		0.10	0.505	308.1
11-13		0.10	0.605	333.8
13-16		0.15	0.730	291.3
16-18		0.10	0.855	288.8
1-3	50	0.1	0.105	480.6
3-5		0.1	0.205	341.9
5-7		0.1	0.305	411.3
7-9		0.1	0.405	418.8
9-11		0.1	0.505	428.1
11-13		0.1	0.605	466.9
13-16		0.15	0.730	401.3
16-18		0.1	0.855	405.0

TABLE B.2 PRESSURE DROP MEASUREMENTS IN SINGLE PHASE (test tube near the bend and tappings located at 45°from the top of the tube to the outside of the bend).

Tappings	G_G (Kg/m²s)	Δz (m)	Distance from the Bend (m)	dP/dz (N/m²/m)
1-3	10	0.10	0.105	33.5
3-5		0.10	0.205	25.0
5-7		0.10	0.305	30.0
7-9		0.10	0.405	30.6
9-11		0.10	0.505	31.3
11-13		0.10	0.605	33.1
13-16		0.15	0.730	30.0
16-18		0.10	0.855	30.0
1-3	20	0.10	0.105	115.0
3-5		0.10	0.205	86.3
5-7		0.10	0.305	101.3
7-9		0.10	0.405	101.3
9-11		0.10	0.505	107.5
11-13		0.10	0.605	115.0
13-16		0.15	0.730	103.3
16-18		0.10	0.855	100.0
1-3	30	0.10	0.105	222.5
3-5		0.10	0.205	160.0
5-7		0.10	0.305	193.8
7-9		0.10	0.405	193.1
9-11		0.10	0.505	203.8
11-13		0.10	0.605	220.0
13-16		0.15	0.730	196.7
16-18		0.10	0.855	190.0
1-3	40	0.10	0.105	347.5
3-5		0.10	0.205	248.1
5-7		0.10	0.305	300.0
7-9		0.10	0.405	302.5
9-11		0.10	0.505	312.5
11-13		0.10	0.605	342.5
13-16		0.15	0.730	300.4
16-18		0.10	0.855	295.0
1-3	50	0.10	0.105	488.8
3-5		0.10	0.205	345.0
5-7		0.10	0.305	417.5
7-9		0.10	0.405	420.0
9-11		0.10	0.505	428.8
11-13		0.10	0.605	477.5
13-16		0.15	0.730	415.8
16-18		0.10	0.855	414.4

TABLE B.3 PRESSURE DROP MEASUREMENTS IN SINGLE PHASE (test tube at 0.3 m from the bend and tappings located at the top of the tube).

Tappings	G_G (kg/m²s)	Δz (m)	Distance from the Bend (m)	dP/dz (N/m²/m)
1-3	10	0.10	0.405	33.1
3-5		0.10	0.505	25.6
5-7		0.10	0.605	31.9
7-9		0.10	0.705	30.6
9-11		0.10	0.805	31.3
11-13		0.10	0.905	32.5
13-16		0.15	1.030	30.0
16-18		0.10	1.155	30.0
1-3	20	0.10	0.405	116.3
3-5		0.10	0.505	87.5
5-7		0.10	0.605	105.0
7-9		0.10	0.705	103.1
9-11		0.10	0.805	109.4
11-13		0.10	0.905	113.8
13-16		0.15	1.030	103.3
16-18		0.10	1.155	97.5
1-3	30	0.10	0.405	222.5
3-5		0.10	0.505	164.4
5-7		0.10	0.605	199.4
7-9		0.10	0.705	197.5
9-11		0.10	0.805	209.4
11-13		0.10	0.905	220.6
13-16		0.15	1.030	196.3
16-18		0.10	1.155	188.8
1-3	40	0.10	0.405	347.5
3-5		0.10	0.505	255.0
5-7		0.10	0.605	308.8
7-9		0.10	0.705	308.1
9-11		0.10	0.805	324.4
11-13		0.10	0.905	341.3
13-16		0.15	1.030	300.0
16-18		0.10	1.155	293.8
1-3	50	0.1	0.405	490.0
3-5		0.1	0.505	353.0
5-7		0.1	0.605	426.9
7-9		0.1	0.705	432.5
9-11		0.1	0.805	450.6
11-13		0.1	0.905	475.6
13-16		0.15	1.030	415.8
16-18		0.1	1.155	410.0

TABLE B.4 PRESSURE DROP MEASUREMENTS IN TWO-PHASE FLOW (test tube near the bend, and tappings located at 45°from the top of the tube to the inside of the bend).

Tappings	G_G (kg/m^{2}s)	G_L (kg/m^{2}s)	Δz (m)	Distance from the Bend (m)	dP/dz (N/m^2/m)
1–3	10	10	0.10	0.105	35.8
3–5			0.10	0.205	30.8
5–7			0.10	0.305	33.3
7–9			0.10	0.405	35.8
9–11			0.10	0.505	33.3
11–13			0.10	0.605	36.7
13–16			0.15	0.730	33.3
16–18			0.10	0.855	33.3
1–3	40	10	0.10	0.105	500.0
3–5			0.10	0.205	440.0
5–7			0.10	0.305	460.0
7–9			0.10	0.405	446.7
9–11			0.10	0.505	480.0
11–13			0.10	0.605	506.7
13–16			0.15	0.730	497.8
16–18			0.10	0.855	453.3
1–3	40	70	0.10	0.105	1030.0
3–5			0.10	0.205	996.7
5–7			0.10	0.305	1040.0
7–9			0.10	0.405	1073.3
9–11			0.10	0.505	1073.3
11–13			0.10	0.605	1060.0
13–16			0.15	0.730	1044.4
16–18			0.10	0.855	980.0

TABLE B.5 PRESSURE DROP MEASUREMENTS IN TWO-PHASE FLOW (test tube near the bend, and tappings located at 45° from the top of the tube to the outside of the bend).

Tappings	G_G (kg/m^{2}s)	G_L (kg/m^{2}s)	Δz (m)	Distance from the Bend (m)	dP/dz (N/m^2/m)
1–3	10	10	0.10	0.105	39.2
3–5			0.10	0.205	30.0
5–7			0.10	0.305	31.7
7–9			0.10	0.405	31.7
9–11			0.10	0.505	35.8
11–13			0.10	0.605	37.5
13–16			0.15	0.730	33.9
16–18			0.10	0.855	35.0
1–3	40	10	0.10	0.105	513.3
3–5			0.10	0.205	460.0
5–7			0.10	0.305	470.0
7–9			0.10	0.405	460.0
9–11			0.10	0.505	473.3
11–13			0.10	0.605	563.3
13–16			0.15	0.730	493.3
16–18			0.10	0.855	446.7
1–3	40	70	0.10	0.105	1063.3
3–5			0.10	0.205	953.3
5–7			0.10	0.305	1040.0
7–9			0.10	0.405	1046.7
9–11			0.10	0.505	1026.7
11–13			0.10	0.605	1026.7
13–16			0.15	0.730	1035.6
16–18			0.10	0.855	980.0

TABLE B.6 PRESSURE DROP MEASUREMENTS IN TWO-PHASE FLOW (test tube at 0.3 m from the bend, and tappings located at the top of the tube).

Tappings	G_G (Kg/m^{2}s)	G_L (Kg/m^{2}s)	Δz (m)	Distance from the Bend (m)	dP/dz (N/m^2/m)
1-3	10	10	0.10	0.405	35.0
3-5			0.10	0.505	25.8
5-7			0.10	0.605	30.8
7-9			0.10	0.705	30.8
9-11			0.10	0.805	30.8
11-13			0.10	0.905	35.0
13-16			0.15	1.030	31.7
16-18			0.10	1.155	35.0
1-3	40	10	0.10	0.405	526.7
3-5			0.10	0.505	426.7
5-7			0.10	0.605	480.0
7-9			0.10	0.705	480.0
9-11			0.10	0.805	495.0
11-13			0.10	0.905	506.7
13-16			0.15	1.030	466.7
16-18			0.10	1.155	445.8
1-3	40	70	0.10	0.405	1026.7
3-5			0.10	0.505	953.3
5-7			0.10	0.605	993.3
7-9			0.10	0.705	1053.3
9-11			0.10	0.805	1100.0
11-13			0.10	0.905	1026.7
13-16			0.15	1.030	1033.3
16-18			0.10	1.155	940.0

TABLE B.7 DATA TAKEN FROM THE ANALYSIS OF THE CINE FILM

(G_G = 20 kg/m^{2}s and G_L = 70 kg/m^{2}s)

Drop No.	D_z (mm)	std(D_z) (mm)	D_y (mm)	std(D_y) (mm)	D_{eq} (mm)	esu(D_{eq}) (mm)	v_{Dz} (m/s)	std(v_{Dz}) (m/s)
1	0.88	0.17	0.81	0.24	0.84	0.21	6.30	0.12
2	0.61	0.11	0.54	0.07	0.58	0.09	7.41	0.15
3	1.06	0.27	0.96	0.08	1.01	0.17	6.03	0.29
4	0.79	0.17	0.68	0.17	0.73	0.17	4.61	0.23
5	0.58	0.05	0.60	0.13	0.59	0.09	5.64	0.15
6	0.64	0.14	0.59	0.09	0.61	0.12	4.86	0.18
7	0.98	0.18	1.13	0.18	1.05	0.18	5.04	0.27
8	1.25	0.17	1.17	0.14	1.21	0.16	4.89	0.25
9	0.41	0.06	0.42	0.09	0.41	0.07	7.63	0.15
10	0.61	0.11	0.59	0.10	0.60	0.11	7.27	0.21
11	0.67	0.10	0.64	0.15	0.66	0.13	6.86	0.10
12	0.71	0.16	0.82	0.12	0.76	0.14	6.69	0.17
13	0.67	0.08	0.54	0.08	0.60	0.08	7.76	0.20
14	0.67	0.06	0.56	0.07	0.61	0.06	6.70	0.15
15	0.63	0.06	0.59	0.07	0.61	0.07	8.33	0.27
16	0.54	0.14	0.50	0.16	0.52	0.15	3.66	0.36
17	0.65	0.10	0.52	0.03	0.58	0.06	8.09	0.28
18	0.71	0.09	0.60	0.18	0.65	0.14	9.41	0.22
19	0.65	0.11	0.59	0.08	0.62	0.09	8.09	0.18
20	0.80	0.05	0.70	0.17	0.75	0.11	7.78	0.52
21	0.43	0.03	0.48	0.05	0.46	0.04	4.23	0.31
22	0.49	0.05	0.59	0.11	0.54	0.08	3.86	0.19
23	0.71	0.10	0.65	0.06	0.68	0.08	7.56	0.15
24	0.66	0.11	0.61	0.10	0.63	0.11	9.36	0.14
25	0.71	0.10	0.61	0.13	0.66	0.12	7.85	0.13
26	0.69	0.07	0.58	0.06	0.63	0.06	8.18	0.24
27	0.83	0.19	0.89	0.18	0.86	0.19	3.93	0.33
28	0.77	0.02	0.78	0.12	0.78	0.07	8.17	0.36
29	0.60	0.09	0.49	0.10	0.54	0.10	8.20	0.18
30	0.64	0.06	0.56	0.08	0.60	0.07	8.17	0.13
31	0.65	0.12	0.63	0.12	0.64	0.12	7.92	0.24
32	0.55	0.08	0.52	0.06	0.53	0.07	6.78	0.16
33	0.60	0.07	0.58	0.10	0.59	0.08	6.35	0.24
34	0.63	0.07	0.58	0.05	0.60	0.06	6.68	0.19
35	0.61	0.10	0.49	0.10	0.54	0.10	6.89	0.12
36	1.17	0.09	1.01	0.12	1.09	0.10	5.68	0.11
37	0.54	0.08	0.52	0.07	0.53	0.08	7.72	0.23
38	0.63	0.04	0.53	0.07	0.58	0.06	5.46	0.11
39	0.54	0.11	0.48	0.07	0.50	0.09	6.07	0.11
40	0.64	0.07	0.53	0.08	0.58	0.08	7.10	0.18
41	0.85	0.09	0.84	0.15	0.84	0.12	4.26	0.32
42	0.65	0.08	0.58	0.14	0.61	0.11	3.27	0.69
43	0.61	0.06	0.66	0.10	0.64	0.08	2.34	0.71
44	0.60	0.10	0.48	0.08	0.54	0.09	9.18	0.09
45	0.55	0.07	0.51	0.07	0.53	0.07	9.12	0.15
46	0.50	0.08	0.43	0.04	0.47	0.06	6.71	0.13
47	0.50	0.01	0.51	0.12	0.51	0.07	6.11	0.16
48	0.60	0.09	0.51	0.06	0.55	0.07	5.11	0.26
49	0.71	0.08	0.60	0.06	0.65	0.07	5.52	0.17
50	0.57	0.10	0.45	0.08	0.51	0.09	6.28	0.24
51	0.72	0.06	1.43	0.20	1.01	0.11	6.20	0.17
52	0.52	0.05	0.39	0.06	0.45	0.06	4.27	0.25
53	0.57	0.08	0.50	0.10	0.53	0.09	3.75	0.14
54	0.53	0.10	0.44	0.06	0.48	0.08	5.09	0.24
55	0.61	0.06	0.52	0.05	0.56	0.05	4.83	0.19
56	0.56	0.08	0.50	0.09	0.53	0.08	4.24	0.23
57	0.53	0.08	0.48	0.08	0.50	0.08	5.33	0.07
58	1.31	0.19	1.20	0.14	1.25	0.16	4.88	0.11
59	0.73	0.11	0.90	0.08	0.81	0.09	4.94	0.09

std – standard deviation

esu – estimated uncertainty

TABLE B.8 DATA TAKEN FROM THE ANALYSIS OF THE CINE FILM
(G_G = 20 kg/m^{2}s and G_L = 90 kg/m^{2}s)

Drop No.	D_z (mm)	std(D_z) (mm)	D_y (mm)	std(D_y) (mm)	D_{eq} (mm)	esu(D_{eq}) (mm)	v_{Dz} (m/s)	std(v_{Dz}) (m/s)
1	0.75	0.12	0.85	0.15	0.80	0.14	7.78	0.24
2	0.69	0.12	0.70	0.10	0.69	0.11	5.89	0.12
3	0.56	0.06	0.54	0.08	0.55	0.07	6.45	0.45
4	0.56	0.07	0.55	0.09	0.55	0.08	5.84	0.25
5	0.55	0.05	0.47	0.08	0.51	0.07	5.80	0.60
6	0.44	0.07	0.39	0.04	0.41	0.05	5.60	0.07
7	0.59	0.07	0.40	0.08	0.48	0.08	10.36	0.07
8	0.61	0.10	0.74	0.24	0.67	0.16	3.41	0.19
9	0.88	0.13	0.88	0.09	0.88	0.11	3.49	0.16
10	0.90	0.11	0.92	0.13	0.90	0.12	2.74	0.17
11	0.87	0.07	0.89	0.04	0.87	0.06	5.57	0.19
12	0.84	0.10	0.89	0.34	0.86	0.22	4.68	0.37
13	0.91	0.14	0.90	0.12	0.90	0.13	6.73	0.25
14	0.66	0.05	0.66	0.20	0.66	0.13	3.88	0.29
15	0.99	0.07	1.02	0.05	1.00	0.06	3.08	0.16
16	0.51	0.08	0.46	0.07	0.49	0.08	4.68	0.30
17	0.92	0.20	1.10	0.21	1.00	0.21	3.97	0.39
18	0.58	0.08	0.52	0.10	0.55	0.09	4.58	0.27
19	0.56	0.04	0.39	0.04	0.47	0.04	5.12	0.30
20	0.76	0.20	1.25	0.18	0.97	0.20	3.84	0.38
21	0.69	0.10	0.49	0.08	0.58	0.09	4.29	0.18
22	0.76	0.05	0.81	0.09	0.78	0.07	4.55	0.24
23	1.05	0.14	1.53	0.19	1.26	0.17	4.13	0.23
24	0.61	0.06	0.56	0.07	0.59	0.07	6.37	0.13
25	0.79	0.14	0.79	0.14	0.79	0.14	4.12	0.20
26	0.76	0.07	0.73	0.24	0.74	0.16	7.51	0.22
27	0.89	0.07	0.72	0.11	0.80	0.09	6.71	0.14
28	1.04	0.18	1.07	0.16	1.05	0.17	6.78	0.35
29	0.64	0.12	0.67	0.13	0.65	0.13	5.16	0.18
30	1.29	0.15	1.39	0.14	1.34	0.14	5.11	0.18
31	1.16	0.03	1.54	0.10	1.33	0.06	4.87	0.20
32	1.34	0.19	1.04	0.06	1.18	0.12	6.47	0.28
33	0.58	0.07	0.60	0.09	0.59	0.08	5.92	0.21
34	1.02	0.12	1.12	0.10	1.07	0.11	4.92	0.17
35	1.08	0.12	1.07	0.07	1.07	0.09	4.37	0.09
36	0.63	0.10	0.43	0.06	0.52	0.08	7.89	0.23
37	0.96	0.13	1.00	0.18	0.98	0.16	7.45	0.45
38	0.50	0.06	0.46	0.08	0.48	0.07	7.46	0.25
39	0.66	0.04	0.57	0.07	0.61	0.06	5.99	0.24
40	0.96	0.16	0.88	0.11	0.92	0.14	8.72	0.33
41	0.79	0.07	0.82	0.11	0.80	0.09	6.41	0.20
42	0.79	0.12	0.65	0.06	0.71	0.09	8.32	0.21
43	0.65	0.08	0.59	0.08	0.62	0.08	7.42	0.14
44	0.84	0.08	0.76	0.06	0.79	0.07	7.07	0.08
45	0.78	0.13	0.80	0.09	0.79	0.11	2.75	0.41
46	0.63	0.09	0.54	0.06	0.58	0.07	6.02	0.19
47	1.12	0.20	0.99	0.25	1.05	0.23	7.68	0.12
48	0.73	0.08	0.52	0.07	0.61	0.08	7.16	0.23
49	0.80	0.13	0.84	0.13	0.82	0.13	8.06	0.45
50	0.47	0.09	0.41	0.12	0.44	0.10	6.25	0.17
51	0.72	0.15	0.54	0.17	0.62	0.17	10.23	0.48
52	0.64	0.10	0.61	0.12	0.62	0.11	10.07	0.19
53	0.69	0.09	0.65	0.17	0.67	0.13	8.94	0.10
54	0.76	0.13	0.56	0.06	0.65	0.09	9.29	0.22
55	1.08	0.21	1.08	0.27	1.08	0.24	8.08	0.20
56	0.63	0.09	0.64	0.11	0.64	0.10	3.67	0.11
57	0.84	0.12	1.01	0.19	0.92	0.15	6.30	0.22
58	0.87	0.16	0.81	0.06	0.84	0.11	7.18	0.28
59	0.80	0.12	0.79	0.10	0.80	0.11	7.46	0.19

std – standard deviation

esu – estimated uncertainty

TABLE B.9 DATA TAKEN FROM THE ANALYSIS OF THE CINE FILM
(G_G = 20 kg/m^{2}s and G_L = 130 kg/m^{2}s)

Drop No.	D_z (mm)	std(D_z) (mm)	D_y (mm)	std(D_y) (mm)	D_{eq} (mm)	esu(D_{eq}) (mm)	v_{Dz} (m/s)	std(v_{Dz}) (m/s)
1	0.80	0.08	0.85	0.20	0.83	0.13	4.20	0.27
2	1.05	0.13	0.97	0.18	1.01	0.16	10.12	0.22
3	1.08	0.08	1.18	0.17	1.13	0.12	8.30	0.21
4	1.20	0.14	1.27	0.19	1.24	0.16	7.80	0.09
5	1.08	0.18	0.99	0.16	1.03	0.17	6.91	0.10
6	0.90	0.09	1.45	0.14	1.14	0.11	3.98	0.14
7	3.39	0.15	3.04	0.19	3.21	0.17	5.82	0.21
8	0.56	0.11	0.56	0.10	0.56	0.11	5.77	0.51
9	0.83	0.02	0.85	0.06	0.84	0.04	5.62	0.04
10	1.02	0.16	1.04	0.15	1.03	0.16	7.33	0.44
11	1.01	0.13	1.19	0.11	1.10	0.12	7.48	0.17
12	1.01	0.25	0.97	0.18	0.99	0.22	9.31	0.19
13	0.95	0.11	1.10	0.17	1.02	0.14	4.91	0.16
14	2.35	0.29	3.20	0.18	2.74	0.25	5.17	0.34
15	0.85	0.19	0.95	0.11	0.90	0.15	8.95	0.18
16	0.88	0.11	1.00	0.16	0.94	0.13	6.68	0.09
17	1.26	0.13	2.57	0.19	1.80	0.16	5.47	0.29
18	0.97	0.11	0.90	0.16	0.93	0.14	5.73	0.71
19	0.80	0.28	0.86	0.20	0.83	0.24	6.20	0.30
20	0.88	0.14	1.00	0.32	0.94	0.23	5.92	0.50
21	0.68	0.11	0.68	0.10	0.68	0.10	6.87	0.45
22	0.72	0.04	0.79	0.08	0.75	0.06	9.91	0.23
23	0.66	0.11	0.63	0.08	0.64	0.09	9.63	0.26
24	0.83	0.14	0.70	0.08	0.76	0.11	10.77	0.43
25	0.80	0.11	0.88	0.04	0.84	0.07	12.04	0.20
26	0.91	0.23	0.95	0.15	0.93	0.19	8.93	0.26
27	0.83	0.07	0.76	0.06	0.79	0.07	8.93	0.39
28	0.83	0.07	0.83	0.08	0.83	0.07	9.92	0.13
29	0.60	0.04	0.58	0.09	0.59	0.07	11.59	0.16
30	1.39	0.33	1.49	0.21	1.44	0.27	4.91	0.32
31	0.65	0.08	0.58	0.08	0.61	0.08	8.69	0.45
32	1.08	0.17	1.13	0.18	1.10	0.17	3.60	0.42
33	1.49	0.34	1.33	0.08	1.41	0.20	3.69	0.56
34	0.89	0.14	1.09	0.15	0.98	0.15	6.43	0.14
35	0.64	0.08	0.76	0.12	0.70	0.10	5.24	0.22
36	0.80	0.08	0.91	0.09	0.85	0.08	9.14	0.27
37	1.13	0.19	1.02	0.09	1.07	0.14	4.48	0.24
38	1.06	0.08	1.49	0.15	1.26	0.11	10.81	0.27
39	1.49	0.09	2.03	0.37	1.74	0.22	6.29	0.11
40	1.08	0.14	1.01	0.15	1.04	0.15	10.03	0.18
41	0.92	0.05	0.80	0.07	0.86	0.06	9.15	0.15
42	1.10	0.13	1.54	0.23	1.30	0.18	5.85	0.24
43	1.95	0.27	2.00	0.18	1.98	0.23	4.99	0.10
44	0.71	0.13	0.80	0.18	0.75	0.15	6.65	0.26
45	0.95	0.15	1.03	0.07	0.99	0.11	9.87	0.19
46	2.58	0.16	2.95	0.15	2.76	0.16	5.87	0.12
47	0.96	0.35	1.28	0.30	1.11	0.33	3.72	0.30
48	0.79	0.12	0.98	0.04	0.88	0.09	4.29	0.10
49	0.80	0.12	0.85	0.08	0.82	0.10	9.63	0.26
50	0.78	0.14	0.92	0.12	0.85	0.13	3.95	0.04
51	0.60	0.14	0.54	0.44	0.57	0.29	7.19	0.39
52	1.54	0.30	1.79	0.09	1.66	0.20	6.84	0.12
53	0.67	0.13	0.67	0.15	0.67	0.14	9.57	0.22
54	1.16	0.14	1.15	0.13	1.15	0.14	9.61	0.30
55	1.14	0.25	1.10	0.18	1.12	0.21	6.78	0.46
56	0.64	0.10	0.74	0.07	0.69	0.09	8.89	0.33
57	0.89	0.11	0.79	0.05	0.84	0.08	9.26	0.17
58	0.69	0.12	0.74	0.08	0.71	0.10	6.11	0.24

std – standard desviation

esu – estimated uncertainty

TABLE B.10 DATA TAKEN FROM THE ANALYSIS OF THE CINE FILM

(G_G = 30 kg/m^{2}s and G_L = 70 kg/m^{2}s)

Drop No.	D_z (mm)	std(D_z) (mm)	D_y (mm)	std(D_y) (mm)	D_{eq} (mm)	esu(D_{eq}) (mm)	v_{Dz} (m/s)	std(v_{Dz}) (m/s)
1	0.93	0.14	1.16	0.22	1.04	0.18	7.08	0.18
2	0.73	0.11	0.89	0.30	0.80	0.20	8.42	0.30
3	0.95	0.12	0.79	0.16	0.87	0.14	9.23	0.37
4	1.14	0.25	1.21	0.21	1.18	0.23	9.17	0.41
5	0.84	0.31	0.78	0.26	0.81	0.28	8.18	0.33
6	1.04	0.22	0.91	0.19	0.97	0.20	7.00	0.33
7	1.17	0.34	1.30	0.32	1.23	0.33	7.72	0.49
8	0.84	0.09	0.80	0.15	0.82	0.12	13.72	0.19
9	0.99	0.11	0.97	0.21	0.98	0.16	8.66	0.13
10	0.91	0.08	1.05	0.14	0.98	0.11	8.86	0.15
11	0.80	0.06	0.75	0.07	0.77	0.06	10.96	0.21
12	0.71	0.10	0.81	0.10	0.76	0.10	10.77	0.18
13	0.82	0.02	0.80	0.10	0.81	0.06	8.27	0.23
14	1.11	0.16	1.23	0.19	1.17	0.17	13.54	0.40
15	0.86	0.06	0.84	0.16	0.85	0.11	8.72	0.26
16	0.93	0.08	0.98	0.16	0.95	0.12	13.90	0.32
17	0.56	0.07	0.60	0.05	0.58	0.06	4.77	0.15
18	0.70	0.13	0.78	0.06	0.74	0.10	8.61	0.27
19	0.73	0.08	0.84	0.16	0.78	0.12	10.79	0.59
20	0.81	0.12	0.85	0.16	0.83	0.14	13.51	0.16
21	1.06	0.21	0.92	0.17	0.99	0.19	14.21	0.69
22	0.79	0.13	0.90	0.22	0.84	0.17	10.35	0.22
23	0.68	0.06	0.68	0.09	0.68	0.08	11.26	0.38
24	0.86	0.14	0.84	0.06	0.85	0.10	11.38	0.28
25	0.94	0.08	0.99	0.11	0.97	0.09	14.47	0.18
26	0.95	0.15	0.84	0.13	0.89	0.14	13.73	0.35
27	0.75	0.15	1.04	0.25	0.88	0.20	9.71	0.23
28	0.81	0.08	0.74	0.08	0.77	0.08	5.64	0.32
29	0.79	0.12	0.94	0.27	0.86	0.19	5.80	0.37
30	1.68	0.62	2.51	0.34	2.05	0.52	7.93	0.50
31	0.88	0.32	0.92	0.14	0.90	0.23	5.32	0.20
32	0.83	0.35	0.83	0.07	0.83	0.21	10.55	0.41
33	0.85	0.34	0.80	0.17	0.82	0.25	11.66	0.38
34	0.92	0.35	0.81	0.13	0.87	0.23	10.04	0.23
35	0.61	0.22	0.63	0.06	0.62	0.14	7.70	0.26
36	1.30	0.49	1.37	0.17	1.34	0.33	6.16	0.27
37	0.71	0.27	0.80	0.12	0.75	0.20	5.22	0.27
38	0.92	0.37	0.94	0.22	0.93	0.29	12.74	0.29
39	0.77	0.29	0.70	0.05	0.73	0.17	11.96	0.23
40	0.99	0.46	0.89	0.23	0.94	0.34	11.52	0.23
41	1.09	0.39	1.24	0.31	1.16	0.35	8.20	0.29
42	0.95	0.34	0.85	0.16	0.89	0.25	7.99	0.38
43	0.85	0.32	0.93	0.12	0.89	0.23	7.15	0.17
44	0.94	0.34	0.89	0.13	0.92	0.23	11.53	0.27
45	0.95	0.34	0.90	0.07	0.93	0.20	13.48	0.07
46	0.97	0.40	0.96	0.10	0.96	0.25	11.16	0.48
47	0.91	0.38	0.89	0.06	0.90	0.22	14.44	0.36
48	0.85	0.32	0.81	0.08	0.82	0.20	12.85	0.19
49	0.80	0.30	1.00	0.09	0.90	0.21	9.99	0.24
50	0.89	0.37	0.87	0.15	0.88	0.26	9.33	0.27
51	0.84	0.36	0.87	0.27	0.85	0.31	6.99	0.08
52	0.91	0.34	0.87	0.07	0.89	0.20	12.82	0.18
53	0.82	0.30	0.78	0.15	0.80	0.22	9.96	0.30
54	0.98	0.17	1.02	0.14	1.00	0.15	9.99	0.19
55	0.86	0.13	1.11	0.11	0.97	0.12	7.18	0.70
56	0.84	0.08	0.79	0.07	0.82	0.08	14.60	0.33
57	0.77	0.25	0.66	0.12	0.71	0.18	13.82	0.42

std – standard desviation

esu – estimated uncertainty

TABLE B.11 ENTRAINMENT MEASUREMENTS BEFORE THE BEND

G_G (kg/m²s)	G_L (kg/m²s)	P (bar)	ϱ_G (kg/m3)	U_{SG} (m/s)	G_{LF} (kg/m²s)	std (G_{LF}) (kg/m²s)	G_{LE} (kg/m²s)
20	30	1.3	1.56	12.8	28.86	-	1.14
	50				48.11	0.25	1.89
	70				67.47	0.38	2.53
	90				87.24	0.82	2.76
	110				107.15	-	2.85
	130				129.06	1.71	0.94
30	10	1.3	1.56	19.2	9.15	0.14	0.85
	30				28.05	0.25	1.95
	50				47.02	0.31	2.98
	70				65.73	0.79	4.27
	90				84.74	0.77	5.26
	110				104.27	0.78	5.73
	130				127.04	1.60	2.96
40	10	1.3	1.56	25.6	9.28	0.15	0.72
	30				27.23	-	2.77
	50				44.68	0.10	5.32
	70				62.17	-	7.83
	90				79.97	0.09	10.03
	110				98.90	1.20	11.10
	130				118.98	2.34	11.02
50	10	1.3	1.56	32.0	8.85	0.25	1.15
	30				24.86	0.53	5.14
	50				40.34	0.58	9.66
	70				55.16	0.98	14.84
	90				71.61	0.89	18.39
	110				88.25	0.41	21.75
	130				104.69	0.54	25.31
60	10	1.3	1.56	38.4	8.80	0.14	1.20
	30				22.91	0.69	7.09
60	10	1.4	1.69	35.6	8.95	0.11	1.05
	30				23.57	0.38	6.43
	50				36.57	0.42	13.43
	70				48.76	0.70	21.24
70	10	1.4	1.69	41.5	8.82	0.11	1.18
	30				20.88	0.21	9.12
	50				32.46	0.74	17.54
	70				44.70	0.42	25.30

TABLE B.12 RAW DATA REFERRING TO FILM FLOW MEASUREMENTS BEFORE THE BEND

G_G (kg/m^{2}s)	G_L (kg/m^{2}s)	P (bar)	ϱ_G (kg/m^3)	G_{LF} (kg/m^{2}s)
20	30	1.3	1.56	plateau graph *
20	50	1.3	1.56	47.92 47.88 48.13 48.51
20	70	1.3	1.56	68.00 67.48 67.25 66.88 67.71
20	90	1.3	1.56	86.86 86.39 86.26 86.50 87.47 88.72 87.84 87.85
20	110	1.3	1.56	plateau graph *
20	130	1.3	1.56	128.13 125.80 128.96 130.45 130.55 130.47
30	10	1.3	1.56	9.08 9.16 9.45 9.20 9.13 8.93 9.16 9.08
30	30	1.3	1.56	27.76 28.53 28.02 28.17 27.74 28.15 27.99
30	50	1.3	1.56	46.94 47.48 46.88 47.14 46.69 46.63 46.89 47.53
30	70	1.3	1.56	64.10 65.93 66.55 65.80 66.34 65.66

* see Table B.13

TABLE B.12 RAW DATA REFERRING TO FILM FLOW MEASUREMENTS BEFORE THE BEND (cont.)

G_G (kg/m^{2}s)	G_L (kg/m^{2}s)	P (bar)	ϱ_G (kg/m^3)	G_{LF} (kg/m^{2}s)
30	90	1.3	1.56	85.45 84.95 84.93 85.45 83.03 84.61 85.33 84.19
30	110	1.3	1.56	105.12 105.17 105.14 104.58 103.39 103.89 103.74 103.16
30	130	1.3	1.56	128.87 126.28 128.15 125.97 124.97 129.89 126.10 126.13
40	10	1.3	1.56	9.10 9.35 9.10 9.42 9.53 9.12 9.41 9.21
40	30	1.3	1.56	plateau graph *
40	50	1.3	1.56	44.61 44.56 44.75 44.82
40	70	1.3	1.56	plateau graph *
40	90	1.3	1.56	79.88 79.88 80.04 80.08
40	110	1.3	1.56	97.76 99.24 100.93 97.28 100.08 98.77 98.23

* see Table B.13

TABLE B.12 RAW DATA REFERRING TO FILM FLOW MEASUREMENTS BEFORE THE BEND (cont.)

G_G (kg/m^{2}s)	G_L (kg/m^{2}s)	P (bar)	ϱ_G (kg/m3)	G_{LF} (kg/m^{2}s)
40	130	1.3	1.56	115.64 122.23 122.01 115.76 118.08 122.27 118.14 117.88 118.80 118.97
50	10	1.3	1.56	8.76 9.10 9.23 8.42 8.71 8.78 8.93
50	30	1.3	1.56	24.30 25.23 25.90 24.30 24.94 24.54 24.77
50	50	1.3	1.56	39.43 40.21 41.45 40.51 40.36 40.16 39.81 40.83
50	70	1.3	1.56	54.40 56.00 54.23 54.61 55.46 56.66 56.33 56.21 53.51 54.54 54.83
50	90	1.3	1.56	70.69 69.85 72.85 72.46 71.69 72.11 71.34 71.23 72.23
50	110	1.3	1.56	88.87 88.15 88.27 87.73
50	130	1.3	1.56	104.91 103.76 105.15 104.94

TABLE B.12 RAW DATA REFERRING TO FILM FLOW MEASUREMENTS BEFORE THE BEND (cont.)

G_G (kg/m²s)	G_L (kg/m²s)	P (bar)	ϱ_G (kg/m³)	G_{LF} (kg/m²s)
60	10	1.3	1.56	8.56 8.62 8.78 8.89 8.86 8.98 8.87
60	30	1.3	1.56	22.74 22.81 24.39 22.81 22.33 22.35
60	10	1.4	1.69	9.20 9.01 8.96 8.86 8.94 8.86 8.91 8.81 8.99
60	30	1.4	1.69	23.57 23.81 24.38 23.66 22.99 23.48 23.32 23.35
60	50	1.4	1.69	37.39 36.62 36.11 36.22 36.93 36.04 36.72 36.54
60	70	1.4	1.69	49.11 48.54 48.88 48.91 47.33 48.41 50.00 48.91
70	10	1.4	1.69	8.92 9.01 8.78 8.80 8.73 8.69
70	30	1.4	1.69	20.51 20.97 21.13 20.97 20.80

TABLE B.12 RAW DATA REFERRING TO FILM FLOW MEASUREMENTS BEFORE THE BEND (cont.)

G_G (kg/m^{2}s)	G_L (kg/m^{2}s)	P (bar)	ϱ_G (kg/m^3)	G_{LF} (kg/m^{2}s)
70	50	1.4	1.69	31.53 32.04 31.79 31.98 33.39 33.03 33.42
70	70	1.4	1.69	44.49 45.57 44.68 44.94 44.35 44.63 44.21

TABLE B.13 INFLUENCE OF GAS TAKE-OFF RATE IN THE LIQUID FILM FLOW RATE EXTRACTION (FILM REMOVAL TECHNIQUE)

G_G (kg/m²s)	G_L (kg/m²s)	Gas Take-off (%)	Liquid Take-off (%)
20	30	0	96.0
		1.9	96.1
		3.8	98.3
		5.7	95.6
		6.7	97.0
		8.9	97.5
		10.1	96.1
		10.3	98.6
20	110	0	49.8
		1.0	92.9
		1.3	93.4
		2.3	95.0
		4.5	97.2
		5.0	97.5
		7.2	97.2
		8.6	97.8
		9.0	97.3
40	30	0	90.9
		0.3	91.0
		0.4	90.8
		0.5	90.4
		0.8	90.7
		1.6	91.1
		2.5	91.5
		3.2	91.1
		4.0	90.5
		4.6	91.8
		6.6	91.3
40	70	0	86.9
		1.0	88.4
		1.7	88.6
		2.2	88.6
		3.2	89.4
		3.8	88.9
		4.2	88.4
		4.7	88.0
		5.1	88.1

TABLE B.14 ENTRAINMENT MEASUREMENTS AFTER THE BEND

G_G (kg/m²s)	G_L (kg/m²s)	P (bar)	ϱ_G (kg/m³)	U_{SG} (m/s)	G_{LF} (kg/m²s)	std (G_{LF}) (kg/m²s)	G_{LE} (Kg/m²s)
20	30	1.3	1.56	12.8	28.40	0.08	1.40
	50				48.14	0.30	1.86
	70				67.49	0.73	2.51
	90				87.29	1.47	2.71
	110				106.74	0.41	3.26
	130				128.08	1.27	1.92
30	10	1.3	1.56	19.2	9.15	0.11	0.85
	30				28.40	0.18	1.60
	50				47.74	0.53	2.26
	70				66.16	0.62	3.84
	90				85.47	0.88	4.53
	110				105.85	0.86	4.15
	130				126.70	1.12	3.30
40	10	1.3	1.56	25.6	9.13	0.18	0.87
	30				27.83	0.14	2.17
	50				46.22	0.54	3.78
	70				64.73	0.32	5.27
	90				83.36	1.40	6.64
	110				104.31	0.56	5.69
	130				125.44	0.63	4.56
50	10	1.3	1.56	32.0	9.01	0.14	0.99
	30				26.94	0.30	3.06
	50				44.30	0.25	5.70
	70				62.46	0.24	7.54
	90				80.78	2.33	9.22
	110				101.52	1.54	8.48
	130				121.54	1.21	8.46
60	10	1.3	1.56	38.4	8.83	0.07	1.17
	30				26.14	0.13	3.86
60	10	1.4	1.69	35.6	8.82	0.19	1.18
	30				26.06	0.28	3.94
	50				43.16	0.29	6.84
	70				60.84	0.13	9.16
70	10	1.4	1.69	41.5	8.53	0.29	1.47
	30				25.02	0.18	4.98
	50				41.78	0.58	8.22
	70				60.65	0.63	9.35

TABLE B.15 RAW DATA REFERRING TO FILM FLOW MEASUREMENTS AFTER THE BEND

G_G (kg/m^{2}s)	G_L (kg/m^{2}s)	P (bar)	ϱ_G (kg/m^3)	G_{LF} (kg/m^{2}s)
20	30	1.3	1.56	28.49 28.65 28.56 28.70
20	50	1.3	1.56	48.18 48.50 47.66 48.24
20	70	1.3	1.56	68.44 66.19 67.56 67.66 67.58
20	90	1.3	1.56	85.82 89.75 86.87 87.10 89.61 85.67 87.06 86.45
20	110	1.3	1.56	106.52 106.80 107.38 106.26
20	130	1.3	1.56	128.35 127.61 129.68 128.82 126.33 128.46 125.98 129.42
30	10	1.3	1.56	8.99 9.21 9.11 9.30
30	30	1.3	1.56	28.57 28.26 28.57 28.19
30	50	1.3	1.56	47.17 48.59 47.48 47.72
30	70	1.3	1.56	65.23 65.61 66.47 65.92 65.68 66.76 67.17 66.47
30	90	1.3	1.56	84.89 84.75 85.28 86.95

TABLE B.15 RAW DATA REFERRING TO FILM FLOW MEASUREMENTS AFTER THE BEND (cont.)

G_G (kg/m²s)	G_L (kg/m²s)	P (bar)	ϱ_G (kg/m³)	G_{LF} (kg/m²s)
30	110	1.3	1.56	104.79 107.96 105.90 105.55 105.68 105.60 105.90 105.45
30	130	1.3	1.56	124.55 128.22 127.06 125.73 126.93 127.04 127.94 126.14
40	10	1.3	1.56	8.89 9.34 9.16
40	30	1.3	1.56	27.70 27.81 27.75 28.06
40	50	1.3	1.56	45.73 47.12 45.92 46.12
40	70	1.3	1.56	65.25 64.41 64.69 64.55
40	90	1.3	1.56	84.39 82.52 83.76 80.26 85.25 84.05 83.32 83.34
40	110	1.3	1.56	103.15 104.88 104.37 104.71 104.83 103.99 104.25
40	130	1.3	1.56	125.43 126.75 125.32 124.74 125.34 125.98 124.53 125.77 125.08

TABLE B.15 RAW DATA REFERRING TO FILM FLOW MEASUREMENTS AFTER THE BEND (cont.)

G_G (kg/m^{2}s)	G_L (kg/m^{2}s)	P (bar)	ϱ_G (kg/m^3)	G_{LF} (kg/m^{2}s)
50	10	1.3	1.56	9.11 8.86 9.35 8.99 8.96 8.91 8.98 8.98 8.99
50	30	1.3	1.56	27.54 26.64 26.68 26.69 27.04 27.08 27.18 26.69
50	50	1.3	1.56	44.72 44.09 44.17 44.24
50	70	1.3	1.56	62.50 62.08 62.73 62.55
50	90	1.3	1.56	81.66 75.21 84.10 80.85 81.41 80.93 81.03 81.03
50	110	1.3	1.56	98.09 101.82 101.86 103.79 102.78 101.07 101.40 101.34
50	130	1.3	1.56	119.04 122.55 121.54 122.73 121.69 121.71
60	10	1.3	1.56	8.78 8.90 8.73 8.90
60	30	1.3	1.56	26.10 26.32 26.19 25.97

TABLE B.15 RAW DATA REFERRING TO FILM FLOW MEASUREMENTS AFTER THE BEND (cont.)

G_G (kg/m^{2}s)	G_L (kg/m^{2}s)	P (bar)	ϱ_G (kg/m^3)	G_{LF} (kg/m^{2}s)
60	10	1.4	1.69	8.89 8.75 8.50 9.06 8.93
60	30	1.4	1.69	25.86 25.80 26.07 26.51
60	50	1.4	1.69	43.04 42.76 43.52 43.33
60	70	1.4	1.69	60.89 60.98 60.63 60.87
70	10	1.4	1.69	8.26 8.24 8.94 8.67
70	30	1.4	1.69	24.99 24.74 25.16 25.18
70	50	1.4	1.69	42.72 41.16 41.71 41.55
70	70	1.4	1.69	60.94 61.72 60.37 59.49 60.82 60.41 60.77

TABLE B.16 DROP SIZE MEASUREMENTS BEFORE THE BEND

G_G (kg/m^{2}s)	G_L (kg/m^{2}s)	P (bar)	ϱ_G (kg/m^3)	U_{SG} (m/s)	$\overline{D}_{32}$ (μm)	std($\overline{D}_{32}$) (μm)	$\overline{D}_{v0.5}$ (μm)	std($\overline{D}_{v0.5}$) (μm)
40	30	1.3	1.56	25.6	118.73	4.31	175.62	7.98
40	40	1.3	1.56	25.6	117.33	3.10	170.81	5.32
40	50	1.3	1.56	25.6	113.51	3.51	172.01	5.16
40	70	1.3	1.56	25.6	111.67	2.91	165.06	5.89
40	90	1.3	1.56	25.6	110.33	3.48	164.44	5.71
40	110	1.3	1.56	25.6	104.77	1.31	153.71	2.02
50	30	1.3	1.56	32.0	79.48	1.42	118.73	1.48
50	40	1.3	1.56	32.0	76.08	0.36	113.86	0.77
50	50	1.3	1.56	32.0	72.96	0.52	106.37	1.02
50	70	1.3	1.56	32.0	74.84	1.99	110.38	2.33
50	90	1.3	1.56	32.0	78.22	0.58	116.45	0.98
50	110	1.3	1.56	32.0	79.96	1.49	124.07	0.67
55	20	1.4	1.69	32.6	76.51	1.29	118.08	1.30
55	30	1.4	1.69	32.6	77.24	0.82	113.45	1.30
55	50	1.4	1.69	32.6	79.08	0.72	112.72	0.47
55	70	1.4	1.69	32.6	79.09	0.21	116.67	1.04
60	20	1.4	1.69	35.6	73.06	1.23	104.53	2.98
60	30	1.4	1.69	35.6	72.55	0.58	102.33	0.99
60	50	1.4	1.69	35.6	73.46	0.27	104.61	0.73
60	70	1.4	1.69	35.6	75.64	0.51	112.60	0.35
65	20	1.4	1.69	38.6	63.19	1.43	91.21	1.29
65	30	1.4	1.69	38.6	63.83	0.62	91.89	1.02
65	50	1.4	1.69	38.6	65.96	0.25	97.61	0.58
65	70	1.4	1.69	38.6	67.54	0.67	103.57	0.34
70	20	1.4	1.69	41.5	60.38	0.35	86.90	0.67
70	30	1.4	1.69	41.5	59.82	0.31	88.50	0.17
70	50	1.4	1.69	41.5	63.19	0.81	94.39	1.37
70	70	1.4	1.69	41.5	65.35	0.52	101.31	0.31

TABLE B.17 RAW DATA REFERRING TO DROP SIZES BEFORE THE BEND

G_G (kg/m²s)	G_L (kg/m²s)	P (bar)	ϱ_G (kg/m³)	Lens Focal Length (mm)	Log. Diff.	$\overline{D}_{32}$ (μm)	$\overline{D}_{v0.5}$ (μm)
40	30	1.3	1.56	1000	3.842	123.29	183.52
				1000	3.768	120.59	178.78
				1000	3.748	122.85	184.80
				1000	3.081	112.72	165.21
				1000	3.100	112.53	165.77
				1000	3.233	113.21	164.20
				1000	2.806	119.69	174.85
				1000	2.729	121.22	179.98
				1000	3.043	122.46	183.45
40	40	1.3	1.56	1000	2.375	123.98	181.14
				1000	2.303	115.88	167.46
				1000	2.187	114.07	163.76
				1000	2.514	116.48	169.74
				1000	2.613	118.24	171.69
				1000	2.719	115.00	165.54
				1000	2.719	118.28	170.83
				1000	2.526	121.36	178.68
				1000	2.773	116.40	172.87
				1000	2.666	113.57	166.35
40	50	1.3	1.56	1000	3.719	119.81	181.65
				1000	2.885	113.49	168.09
				1000	2.911	115.09	170.70
				1000	3.022	110.34	167.56
				1000	2.696	113.46	175.88
				1000	2.877	108.87	168.15
40	70	1.3	1.56	300	3.960	110.40	162.09
				1000	2.185	113.02	167.69
				1000	2.420	113.40	167.61
				1000	2.629	117.11	175.89
				1000	2.040	108.28	157.86
				1000	2.351	108.25	158.00
				1000	2.224	111.25	166.27
40	90	1.3	1.56	1000	2.420	112.74	170.47
				1000	2.309	114.01	171.32
				1000	1.669	112.64	166.11
				1000	2.044	111.24	164.25
				1000	2.119	114.08	170.34
				1000	2.446	106.51	158.81
				1000	2.559	105.63	157.44
				1000	2.517	105.80	156.78
40	110	1.3	1.56	1000	2.566	103.82	151.24
				1000	2.809	105.68	155.77
				1000	2.326	104.77	152.47
				1000	2.442	105.91	154.90
				1000	2.497	104.30	151.24
				1000	2.731	102.40	153.61
				1000	2.485	106.52	156.73
50	30	1.3	1.56	300	3.120	79.39	119.82
				300	3.075	79.94	119.46
				300	2.961	80.37	117.93
				300	2.764	78.42	117.10
				300	3.204	78.15	117.19
				300	2.711	80.01	118.14
				300	2.832	80.80	119.54
				1000	3.616	82.54	117.98
				1000	2.714	77.55	118.40
				1000	2.605	77.68	117.93
				1000	2.408	79.39	122.54
50	40	1.3	1.56	1000	2.706	75.96	113.35
				1000	2.724	76.71	115.18
				1000	2.537	76.17	114.03
				1000	2.552	76.15	113.66
				1000	2.483	75.99	114.23
				1000	2.698	75.50	112.70

TABLE B.17 RAW DATA REFERRING TO DROP SIZES BEFORE THE BEND (cont.)

G_G (kg/m²s)	G_L (kg/m²s)	P (bar)	ϱ_G (kg/m³)	Lens Focal Length (mm)	Log. Diff.	$\bar{D}_{32}$ (μm)	$\bar{D}_{v0.5}$ (μm)
50	50	1.3	1.56	1000	1.866	72.63	107.44
				1000	1.463	72.34	106.77
				1000	1.321	72.66	107.58
				1000	2.098	73.92	106.28
				1000	2.231	73.30	105.28
				1000	2.029	72.92	104.86
50	70	1.3	1.56	1000	2.003	74.39	108.64
				1000	1.949	74.04	108.41
				1000	1.919	74.75	109.00
				1000	2.246	78.27	114.49
				1000	2.242	77.82	113.75
				1000	2.384	73.04	109.59
				1000	2.343	72.31	108.07
				1000	2.160	74.12	111.06
50	90	1.3	1.56	1000	2.453	78.85	116.99
				1000	2.080	77.61	116.75
				1000	2.253	79.11	117.95
				1000	2.566	77.56	114.74
				1000	2.607	78.18	115.97
				1000	2.362	77.99	116.28
50	110	1.3	1.56	300	3.532	81.39	124.70
				300	3.550	81.65	125.00
				300	3.572	81.17	123.70
				300	3.547	77.85	122.98
				300	3.566	79.09	124.25
				300	3.556	78.61	123.79
55	20	1.4	1.69	300	3.646	75.54	119.47
				300	3.584	76.28	119.11
				300	3.617	74.74	116.53
				300	3.117	76.10	116.07
				300	2.997	78.20	118.65
				300	2.966	78.18	118.67
55	30	1.4	1.56	300	3.173	72.16	98.84
				300	3.231	72.29	99.34
				300	3.213	72.60	99.48
				300	3.743	71.29	101.35
				300	3.951	70.19	99.74
				300	3.739	70.73	100.07
55	30	1.4	1.69	300	3.067	76.70	112.56
				300	3.233	78.90	116.12
				300	3.095	76.77	113.12
				300	3.328	77.22	113.07
				300	3.339	77.47	113.72
				300	3.436	76.39	112.10
55	50	1.4	1.69	300	3.655	79.72	113.12
				300	3.641	79.61	112.66
				300	3.623	79.99	113.16
				300	2.919	78.67	113.17
				300	3.057	78.24	112.13
				300	2.933	78.22	112.09
55	70	1.4	1.69	300	2.938	79.03	117.61
				300	2.838	79.05	117.74
				300	2.959	78.75	117.61
				300	3.015	79.14	115.19
				300	2.954	79.45	116.26
				300	2.957	79.09	115.59

TABLE B.17 RAW DATA REFERRING TO DROP SIZES BEFORE THE BEND (cont.)

G_G (kg/m²s)	G_L (kg/m²s)	P (bar)	ϱ_G (kg/m³)	Lens Focal Length (mm)	Log. Diff.	$\overline{D}_{32}$ (μm)	$\overline{D}_{v0.5}$ (μm)
60	20	1.4	1.69	300	3.736	75.61	109.92
				300	3.748	73.03	106.45
				300	3.715	74.59	109.00
				300	3.777	73.47	103.09
				300	3.828	72.53	101.15
				300	3.827	72.53	101.83
				300	3.423	71.76	102.69
				300	3.285	72.12	103.51
				300	3.193	71.88	103.14
60	30	1.4	1.69	300	3.829	72.14	102.86
				300	3.893	72.74	103.80
				300	3.902	71.81	102.46
				300	2.986	72.34	100.81
				300	2.853	73.65	102.72
				300	2.797	72.62	101.35
60	50	1.4	1.69	300	3.268	73.87	105.51
				300	3.392	73.18	104.28
				300	3.562	73.71	105.55
				300	3.389	73.41	104.33
				300	3.292	73.49	104.49
				300	3.211	73.12	103.47
60	70	1.4	1.69	300	3.130	75.45	112.35
				300	3.005	75.73	113.03
				300	3.143	75.20	112.29
				300	3.107	74.93	112.24
				300	3.176	76.18	112.56
				300	3.150	76.35	113.12
65	20	1.4	1.69	300	3.334	61.91	90.27
				300	3.297	61.33	89.26
				300	3.295	62.30	91.23
				300	3.290	63.88	91.02
				300	3.299	65.22	93.30
				300	3.237	64.50	92.17
65	30	1.4	1.69	300	3.155	63.28	90.72
				300	3.135	63.52	91.73
				300	3.155	64.69	93.21
65	50	1.4	1.69	300	3.023	66.04	98.02
				300	3.046	66.01	97.85
				300	2.992	66.42	98.56
				300	3.005	65.80	97.07
				300	3.038	65.64	96.92
				300	3.022	65.85	97.25
65	70	1.4	1.69	300	2.918	67.65	103.45
				300	2.973	68.30	104.04
				300	2.703	66.68	103.23
70	20	1.4	1.69	300	3.380	60.39	87.01
				300	3.412	60.43	87.66
				300	3.356	60.27	86.98
				300	3.068	61.09	87.65
				300	3.098	60.01	85.79
				300	3.177	60.09	86.33
70	30	1.4	1.69	300	2.795	59.78	88.47
				300	2.783	60.09	88.72
				300	2.798	60.04	88.44
				300	2.730	60.14	88.71
				300	2.715	59.61	88.43
				300	2.821	59.27	88.22

TABLE B.17 RAW DATA REFERRING TO DROP SIZES BEFORE THE BEND (cont.)

G_G (kg/m²s)	G_L (kg/m²s)	P (bar)	ϱ_G (kg/m³)	Lens Focal Length (mm)	Log. Diff.	$\overline{D}_{32}$ (μm)	$\overline{D}_{v0.5}$ (μm)
70	50	1.4	1.69	300	3.029	63.94	95.59
				300	2.969	63.99	95.74
				300	2.996	64.36	96.23
				300	4.370	63.10	95.22
				300	4.642	62.45	94.54
				300	4.969	61.53	94.36
				300	3.417	63.03	92.52
				300	3.443	63.04	92.51
				300	3.381	63.28	92.80
70	70	1.4	1.69	300	2.780	65.06	101.45
				300	2.946	64.76	101.57
				300	2.724	64.72	101.75
				300	3.540	65.88	101.15
				300	3.518	65.77	100.84
				300	3.551	65.91	101.11

TABLE B.18 DROP SIZE MEASUREMENTS AFTER THE BEND

G_G (kg/m²s)	G_L (kg/m²s)	P (bar)	ϱ_G (kg/m³)	U_{SG} (kg/m³)	$\overline{D}_{32}$ (μm)	std($\overline{D}_{32}$) (μm)
40	50	1.3	1.56	25.6	195.80	8.96
40	70	1.3	1.56	25.6	204.42	5.60
40	90	1.3	1.56	25.6	192.21	5.27
50	50	1.3	1.56	32.0	135.54	2.04
50	70	1.3	1.56	32.0	134.53	1.99
50	90	1.3	1.56	32.0	129.40	1.23
60	30	1.4	1.69	35.6	126.73	0.98
60	50	1.4	1.69	35.6	110.46	5.64
60	70	1.4	1.69	35.6	109.65	1.82
70	30	1.4	1.69	41.5	104.62	5.39
70	50	1.4	1.69	41.5	100.06	5.11
70	70	1.4	1.69	41.5	87.25	1.40

TABLE B.19 RAW DATA REFERRING TO DROP SIZES AFTER THE BEND

G_G (kg/m²s)	G_L (kg/m²s)	P (bar)	ϱ_G (kg/m³)	$\overline{D}_{32}$ (μm)
40	50	1.3	1.56	195.7 186.71 185.27 203.02 208.29
40	70	1.3	1.56	199.59 212.26 201.4
40	90	1.3	1.56	188.55 199.67 188.42
50	50	1.3	1.56	132.76 137.6 136.26
50	70	1.3	1.56	131.69 134.27 133.61 135.35 137.73
50	90	1.3	1.56	127.66 130.36 130.18
60	30	1.4	1.69	125.1 125.88 127.27 126.6 127.78 127.73
60	50	1.4	1.69	117.44 117.16 104.46 106.47 106.76
60	70	1.4	1.69	108.16 108.59 112.21
70	30	1.4	1.69	110.73 109.24 99.07 99.44
70	50	1.4	1.69	96.32 94.37 94.28 105.3 104.81 105.26
70	70	1.4	1.69	86.71 85.87 89.17

Appendix C

USE OF A CLASS IIIA LASER IN THE HORIZONTAL TWO-PHASE FLOW RIG

CONTENTS

C.1. Scope

This document is concerned with the laser safety precautions that should be undertaken when using the Malvern 2600 Particle Sizer to measure drop sizes in the Two-Phase Flow Rig.

C.2. Laser Characteristics

The Malvern 2600 Particle Sizer uses a 2 mW Helium/Neon laser, with output wavelength of 633 nM, having a 9mm beam expansion, collimation and spatial filtering for TEM 00 mode. This laser is considered of Class IIIA according to BS 4803.

For the Long Bed Option the beam expansion is 18 mm, so the output power of the laser is reduced.

C.3. Location

The Malvern instrument will be operated with the Two-Phase Flow Rig, situated at the balcony of Building 392. The laser instrument does not affect the rig performance or operating instructions.

C.4. Laser Responsible Officer

The Malvern 2600 Particle Sizer is under the responsibility of Dr. P. Birchenough.

C.5. Laser Operator

The apparatus will be operated by Ms. Albina Ribeiro. The proposed laser operator has received previous training which includes:

- Watching a video about laser safety.
- Previous operation of a Malvern Particle Sizer in the Double Closed Loop Rig, Building 10.4-Bay D (rig no longer in operation).

C.6. Laser Safety

This section deals with the safety precautions required when operating the Particle Sizer (a Class IIIA laser).

C.6.1. Designated Laser Area (DLA)

Operation of the laser must be inside a complete cubicle, whose walls define the designated laser area. All the walls and the door were checked to ensure that they are opaque to laser radiation.

Warning signs carrying the laser classification are displayed at access points of the DLA, and and the access of unauthorised persons is prohibited while the laser is in operation.

Also, warning lights are installed at the entrance of the area. An amber warning light will operate with the laser power supply, and a red warning light will indicate when the laser is emitting or has the potential to emit.

C.6.2. Interlocked Access to DLA

The entrance of the DLA is interlocked such that it is not possible for anyone to enter the area without preventing the laser from emitting light by activating a shutter. If the DLA door is opened by an unauthorised person while the laser is in operation, a shutter which blocks the laser beam is automatically released. The shutter system is preferable to an interlock on the laser power switch since it is not recommended the laser should be switched on and off.

C.6.3. Safety Features of Malvern 2600 Particle Sizer

C.6.3.1. Labelling

The laser system is labelled according to BS 5378 and the SAFETY CODE CLM-SC17.

The following labels (Figure C.1) are displayed on the laser unit:

i) A hazard label and a supplementary yellow label bearing the following words in black letters:

'LASER RADIATION
CLASS 3A LASER PRODUCT
Max. output 5mW CW
He-Ne 632.8 nM'

ii) A prohibition label and a red supplementary label bearing the following inscription in white letters:

'DO NOT STARE INTO BEAM'

iii) A mandatory label and a blue supplementary label bearing the following words in white letters:

'OBTAIN SAFETY OFFICERS APPROVAL FOR USE OF OPTICAL INSTRUMENTS'

iv) The protective housings have a warning label affixed with the following inscription:

'CAUTION
Laser radiation when panels open and interlocks overridden'

Figure C.1 Labels on the laser unit.

C.6.3.2. Key Control

The Malvern Drop Sizer is provided with a keyswitch for authorised control of power input.

C.6.4. Training

The operation of the laser system must be made only by persons who have received training to an appropriate level.

C.6.5. Laser Goggles

The use of appropriate laser goggles is not mandatory with Class IIIA lasers. However, laser goggles are optionally provided which filter out the light of wavelengths related to the laser light.

C.7 References

BS 4803, Guide on Protection of Personnel against hazards from Laser Radiation, 1972.

CLM-SC17 SAFETY CODE, Safety in the Use of Lasers in the Laboratory, 1982, UKAEA.

Instruction Manual-System 2600, Issue 2.1, 1991, Malvern Instruments Ltd.

Appendix D

STILL PHOTOGRAPHS OF THE HORIZONTAL TWO-PHASE FLOW

CONTENTS

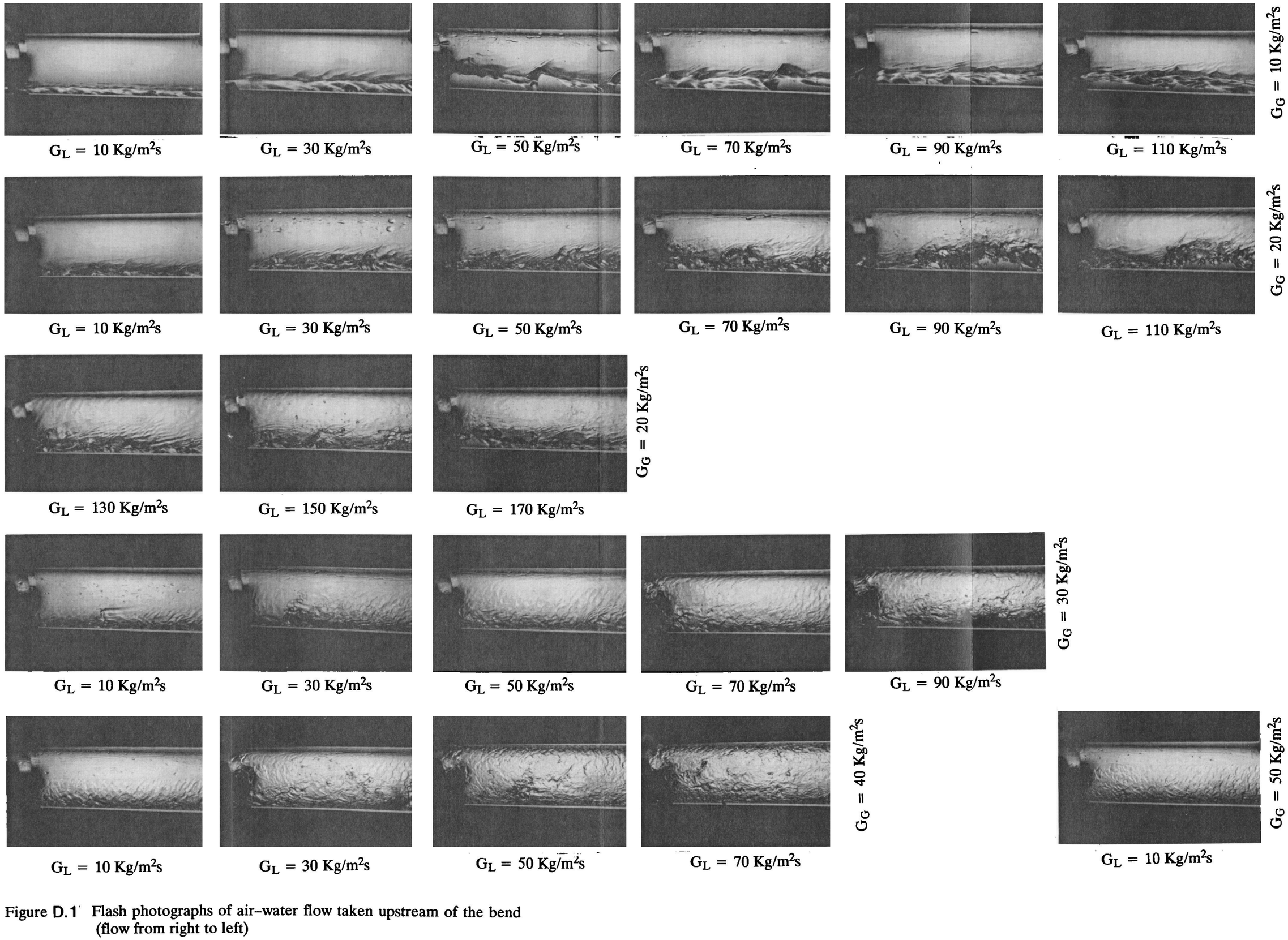

Figure D.1 Flash photographs of air–water flow taken upstream of the bend (flow from right to left)

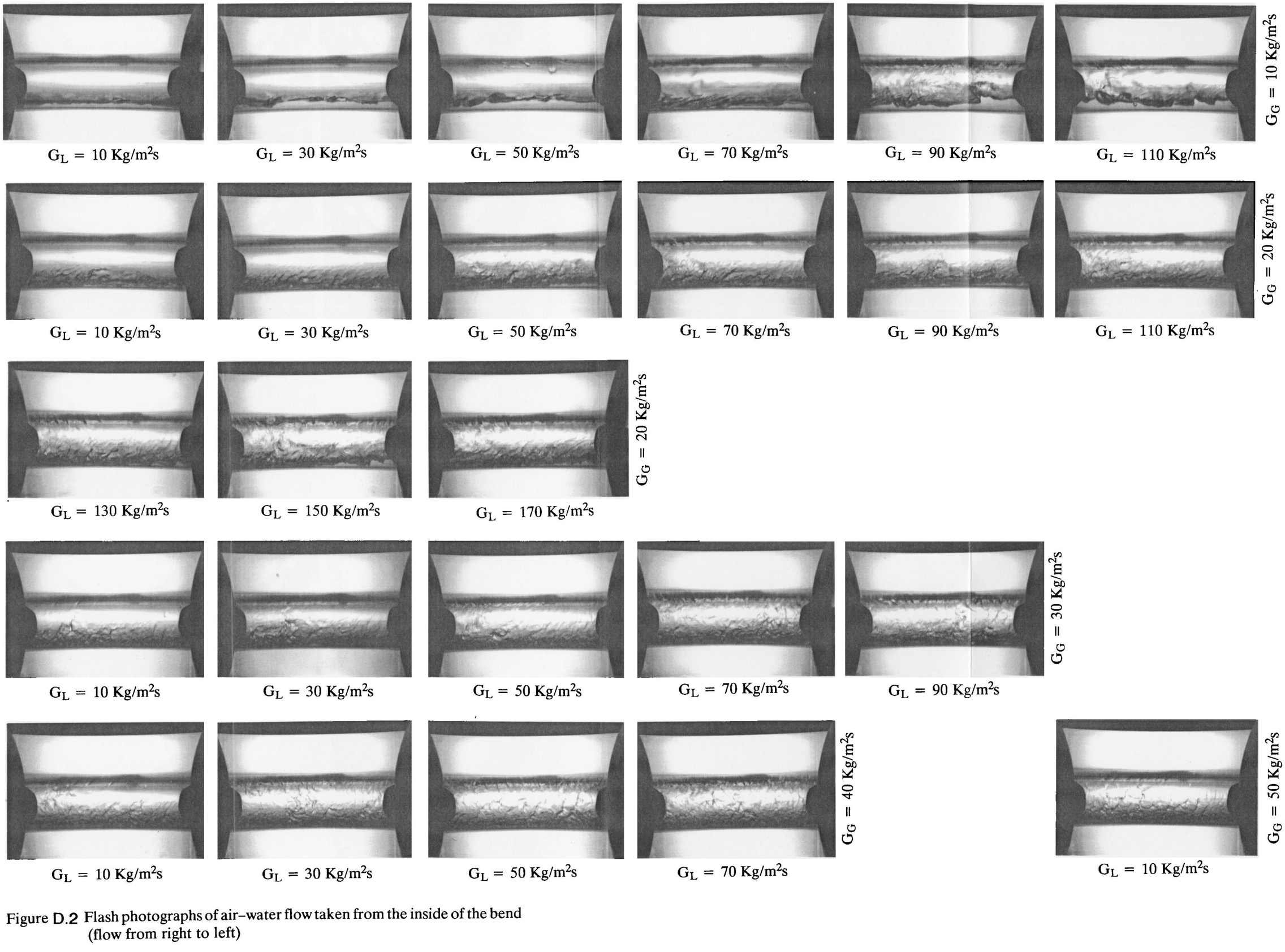

Figure D.2 Flash photographs of air–water flow taken from the inside of the bend (flow from right to left)

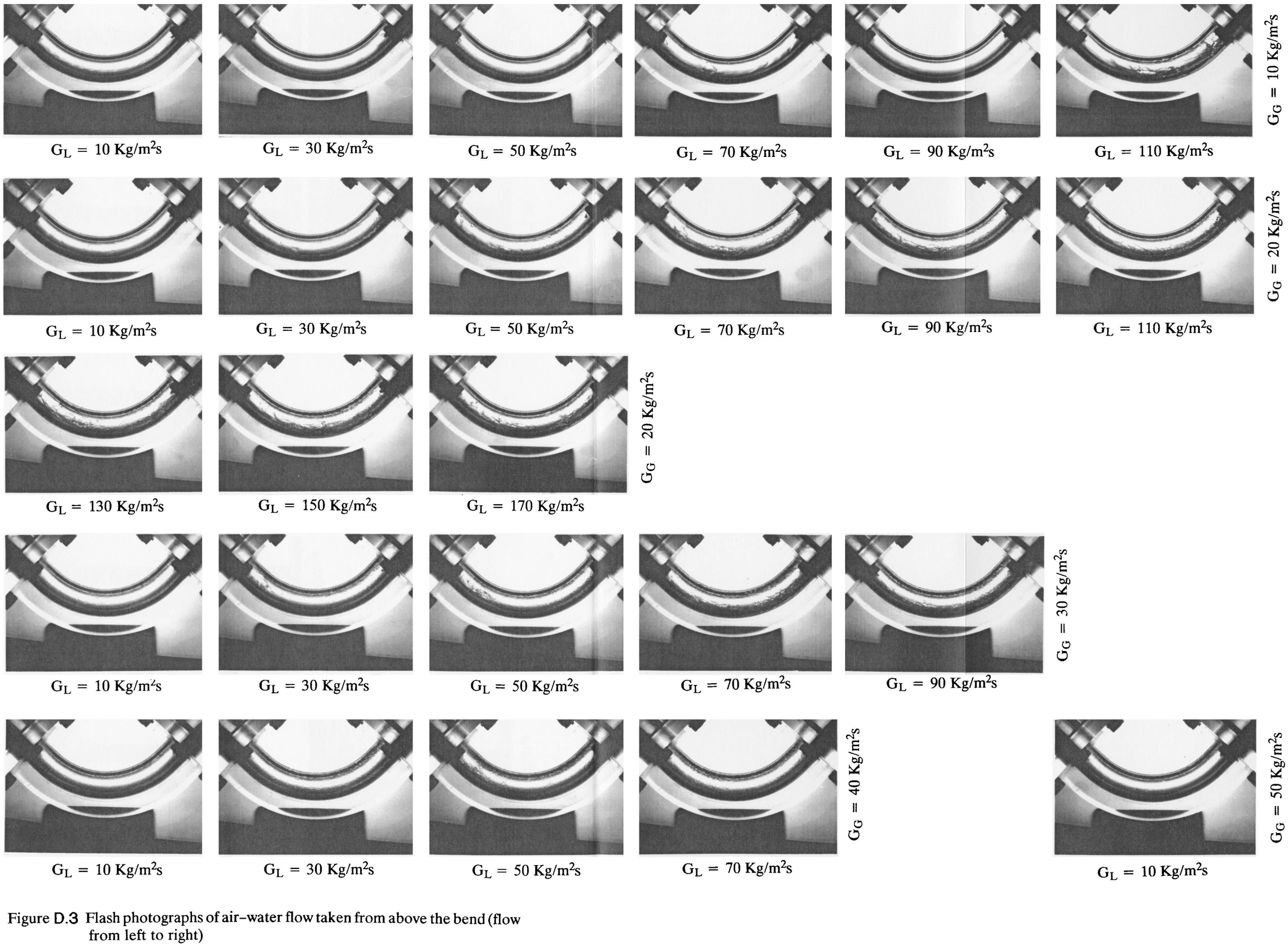

Figure D.3 Flash photographs of air–water flow taken from above the bend (flow from left to right)

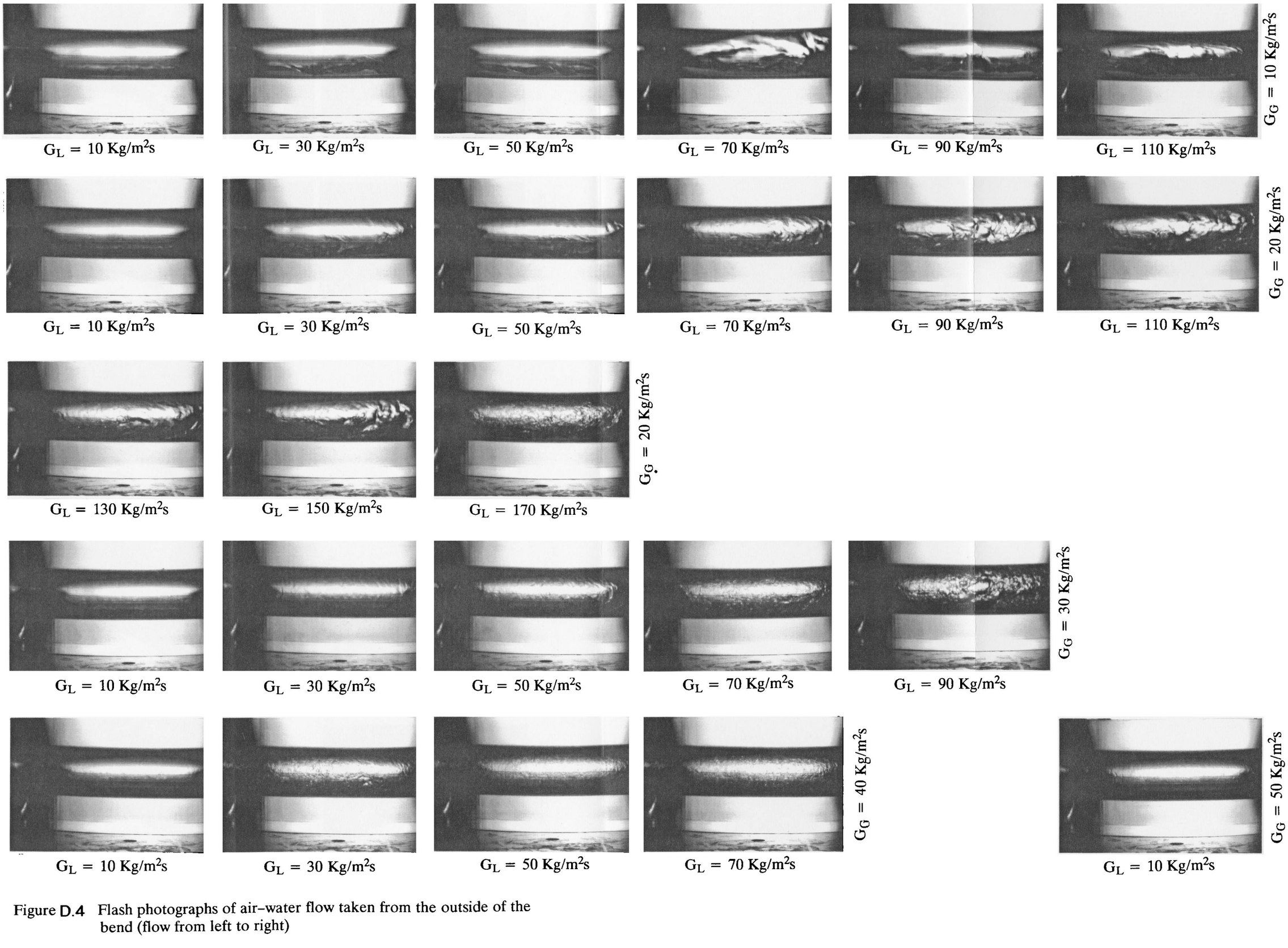

Figure D.4 Flash photographs of air–water flow taken from the outside of the bend (flow from left to right)

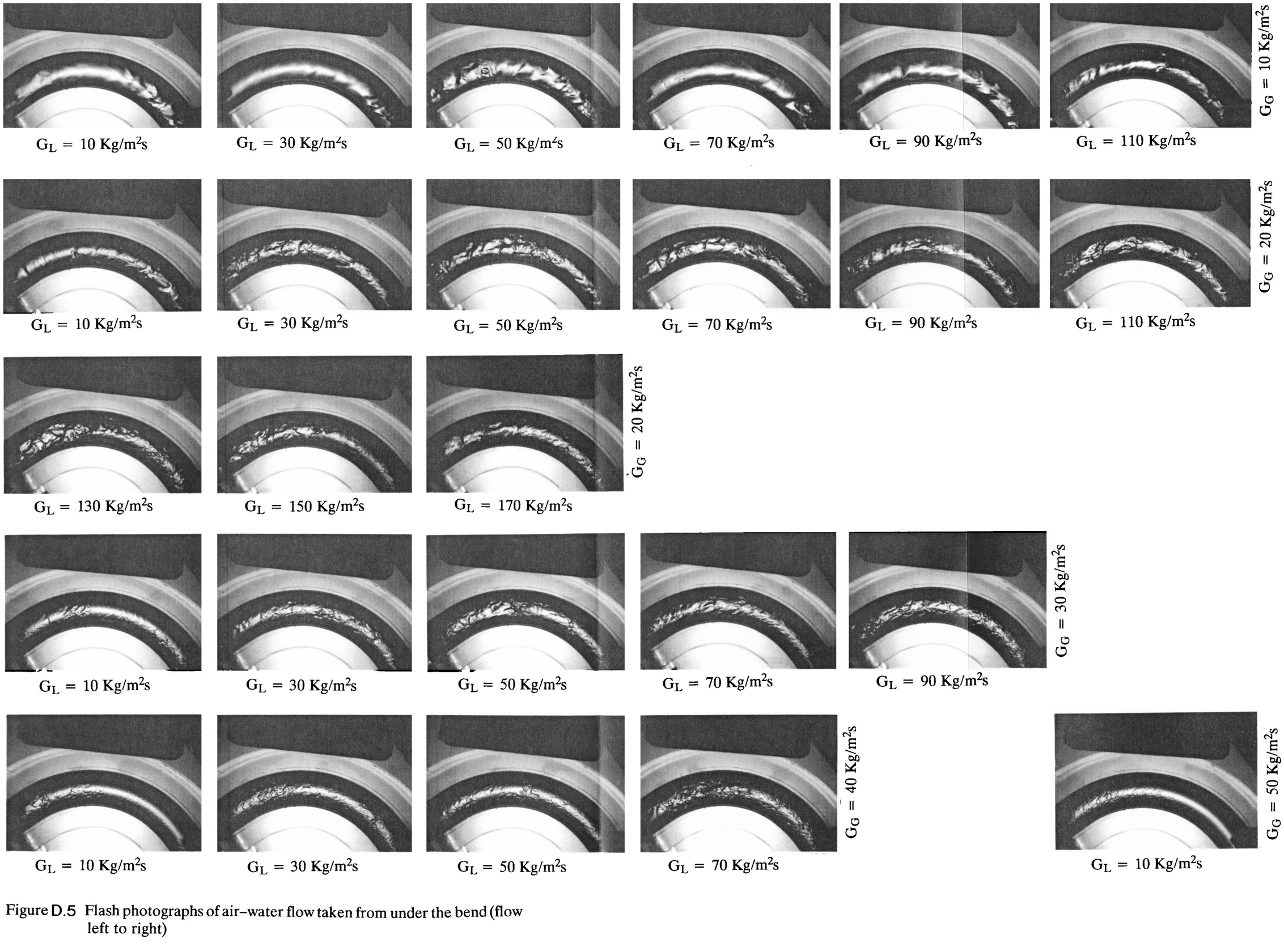

Figure D.5 Flash photographs of air–water flow taken from under the bend (flow left to right)

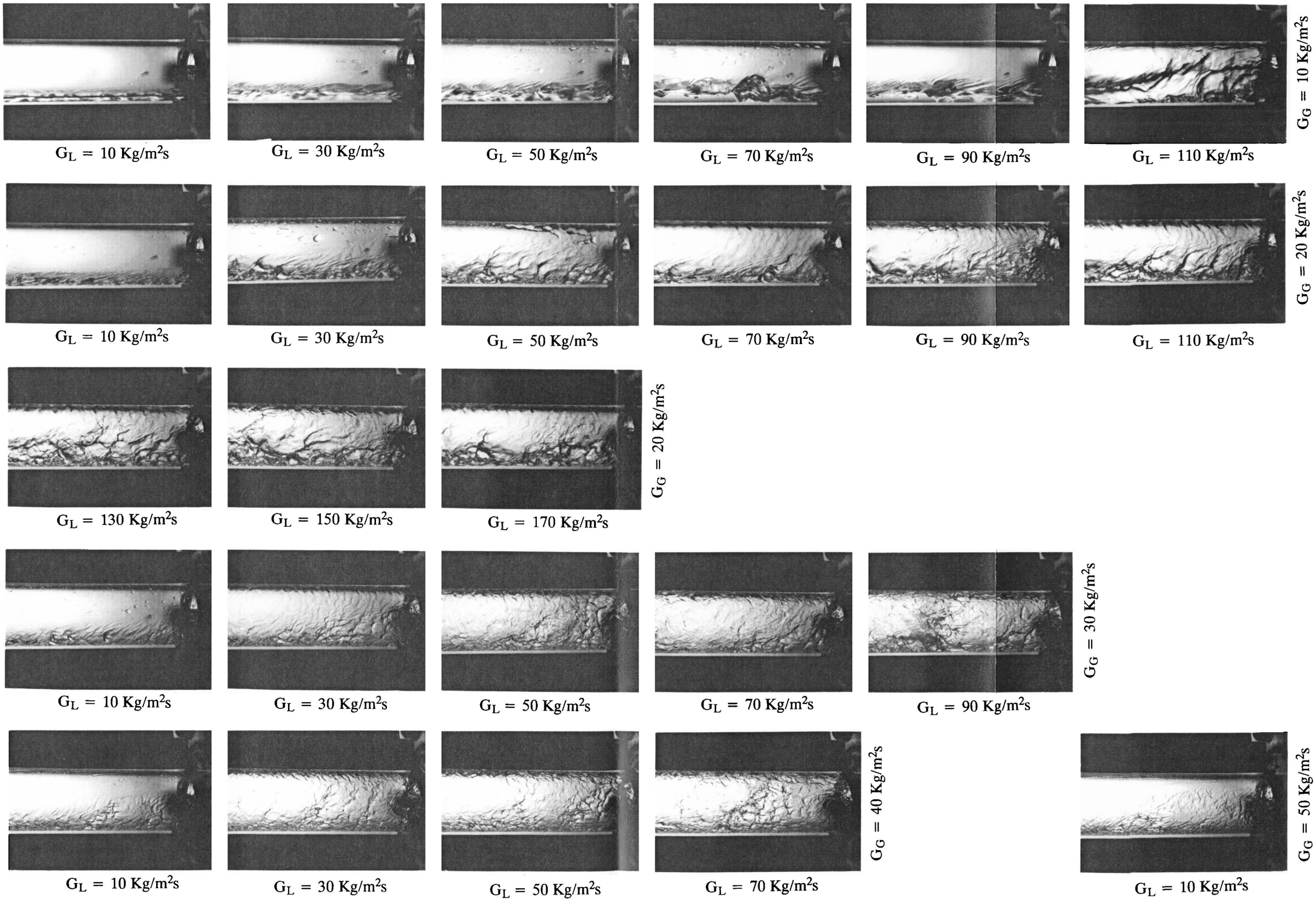

Figure D.6 Flash photographs of air–water flow taken downstream of the bend (flow from right to left)

Appendix E

CALCULATION OF LIQUID FILM THICKNESS IN HORIZONTAL ANNULAR FLOW

Laurinat et al (1984) proposed that a convenient method to calculate film thicknesses in horizontal tubes could be given by the relation:

$$\frac{m}{d_t} = \frac{6.59\ F_H}{[2.3^5 + (90\ F_H)^5]^{0.2}} \qquad \text{(E.1)}$$

The horizontal flow factor F_H is defined as:

$$F_H = \frac{\gamma_H(\mathrm{Re}_{LF})}{\mathrm{Re}_G^{0.9}} \frac{\mu_L}{\mu_G} \sqrt{\frac{\varrho_G}{\varrho_L}} \qquad \text{(E.2)}$$

where Re_G is the gas Reynolds number. The function $\gamma_H(Re_{LF})$ is given by:

$$\gamma_H(\mathrm{Re}_{LF}) = [(0.566\ \mathrm{Re}_{LF}^{0.5})^{2.5} + (0.0303\ \mathrm{Re}_{LF}^{0.9})^{2.5}]^{0.4} \qquad \text{(E.3)}$$

and Re_{LF} is the liquid film Reynolds number.

Equations (E.1) and (E.2) can be solved by successive substitution for m in (E.1) and Re_G in (E.2), starting with the estimate of $m = 0$.

This method was employed to calculate the average height of the film around the pipe circumference for the 0.032 m tube used in this investigation, allowing finally the calculation of actual velocities of the gas phase (U_G).

Appendix F

TIME FLIGHT OF A DROP

Once a drop is released from the liquid film, it is accelerated by the moving gas stream. To calculated the time required for a drop to reach a given velocity, a simple method was used. It was based on the same principles followed by Gibbons (1985), but modified accordingly, so it could be applied to horizontal conditions. The magnitude of the drag force is given by:

$$\varrho_L \frac{\pi\ D^3}{6} \frac{d\ v_{Dz}}{dt} = \frac{C_D}{2}\ \varrho_G\ (U_G - v_{Dz})^2\ \frac{\pi\ D^2}{4} \qquad \text{(F.1)}$$

where D is the drop diameter, U_G is the gas velocity, v_{Dz} is the axial drop velocity and C_D is the drag coefficient.

The drag coefficient was given by a correlation proposed by Lapple and Shepherd (1941), as:

$$C_D = \frac{24}{\mathrm{Re}_p} + 0.44 \qquad \text{(F.2)}$$

and the particle Reynolds number is defined by:

$$\mathrm{Re}_p = (U_G - v_{Dz})\ \frac{\varrho_G\ D}{\mu_G} \qquad \text{(F.3)}$$

Substituting equations (F.2) and (F.3) into equation (F.1):

$$\frac{d\ v_{Dz}}{dt} = \frac{18\ \mu_G}{\varrho_L\ D^2}\ (U_G - v_{Dz}) + \frac{0.33\ \varrho_G}{D\ \varrho_L}\ (U_G - v_{Dz})^2 \qquad \text{(F.4)}$$

If $X = U_G - v_{Dz}$, and U_G is a constant, then:

$$\frac{dX}{dt} = -\frac{dv_{Dz}}{dt} \qquad \text{(F.5)}$$

Substituting (F.5) in equation (F.4), gives:

$$-\frac{dX}{dt} = a\ X^2 + b\ X \qquad \text{(F.6)}$$

where

$$a = 0.336 \frac{\varrho_G}{\varrho_L D} \tag{F.7}$$

$$b = 18 \frac{\mu_G}{\varrho_L D^2} \tag{F.8}$$

By integration of equation (F.6):

$$[-t]_0^{T_0} = \left[\frac{1}{b} \ln \left| \frac{X}{X + \frac{a}{b}} \right| \right]_{X_0}^{X} \tag{F.9}$$

If the initial velocity of the drop is considered to be negligible, then $X_0 = U_G$, the time flight of a drop from the moment of its creation (T_0) can be finally calculated as:

$$-T_0 = \frac{1}{b} \ln \left(\frac{(U_G - v_{Dz})\ (U_G + b/a)}{U_G\ (U_G - v_{Dz} + b/a)} \right) \tag{F.10}$$

where a and b are given by (F.7) and (F.8), respectively.

A drop with a diameter of 0.5 mm travelling in a gas stream of $G_G = 20$ kg/m^{2}s at a pressure of 1.2 bar ($\varrho_G = 1.44$ kg/m^3) will take 0.67 s to reach a velocity of 12.5 m/s (= 0.9 U_G). In this case, the gas velocity was considered to be close to the superficial gas velocity ($U_{GS} = 13.9$ m/s).

Appendix G

EXPERIMENTAL RESULTS FOR VERTICAL TWO-PHASE FLOW

CONTENTS

TABLE G.1 - LIQUID FILM FLOW RATE MEASUREMENTS IN VERTICAL FLOW

G_G	G_L	G_{LF}	G_{LE}	Datum*	*PD*
		kg/m^{2}s			%
60	40	37.35	2.65	39.19	-4.93
	60	56.96	3.04	57.94	-1.72
	80	75.89	4.11	75.23	+2.62
	100	94.86	5.14	93.11	+1.84
	120	114.97	5.03	111.96	+2.62
80	40	36.81	3.19	37.33	-1.41
	60	52.45	7.55	53.26	-1.54
	80	70.44	9.56	69.77	+0.95
	100	86.77	13.23	85.49	+1.47
	120	103.08	16.92	102.41	+0.65
100	40	35.02	4.98	33.73	+3.68
	60	49.13	10.87	49.05	+0.16
	80	64.04	15.96	61.55	+3.89
	100	78.32	21.68	75.41	+3.71
	120	91.70	28.30	89.15	+2.78
120	40	31.71	8.29	32.28	+1.80
	60	42.96	17.04	45.26	-5.35
	80	57.58	22.42	-	-
	100	71.19	28.81	-	-
	120	81.22	38.78	-	-

* Calculated liquid film flow rate from Table 1 in Jepson et al (1989)

TABLE G.2 - DROP SIZE MEASUREMENTS IN VERTICAL FLOW

G_G	G_L	$\bar{D}_{32}$	Datum*	PD'
kg/m^{2}s		μm		%
80	40	45.18	43.59	+3.52
	60	42.54	41.41	-2.66
	80	41.50	43.12	-3.90
	100	40.76	42.57	-4.44
	120	41.02	44.38	-8.19
100	40	34.39	32.93	+4.24
	60	34.23	31.76	+7.22
	80	34.21	33.53	+2.00
	100	34.66	34.66	0
	120	33.26	35.76	+7.52
120	40	26.37	26.49	-0.45
	60	27.50	26.92	+2.11
	80	28.49	-	-
	100	29.11	-	-
	120	30.48	-	-

* Results from Table 1 in Jepson et al (1989)